

Cover Page



Universiteit Leiden

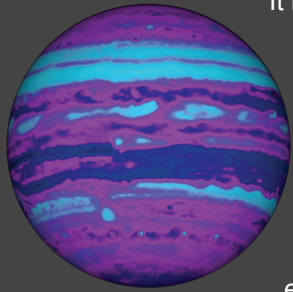


The handle <http://hdl.handle.net/1887/20830> holds various files of this Leiden University dissertation.

**Author:** Karalidi, Theodora

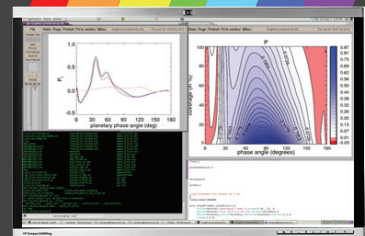
**Title:** Broadband polarimetry of exoplanets : modelling signals of surfaces, hazes and clouds

**Issue Date:** 2013-04-23



It is less than 20 years since astronomers discovered the first exoplanet orbiting a Sun-like star. In this short period more than 770 confirmed exoplanets have been detected. With so many exoplanets the next step is their characterization. What is their atmosphere made of? Does it contain water clouds? Is there water on the planetary surface? Could there be life on these planets? To answer all these questions good and reliable models are necessary for interpreting the signal we observe from the detected exoplanets.

In this thesis, Karalidi works with a numerical code to model the flux and polarization properties of starlight reflected by exoplanets with various forms of inhomogeneities. She shows that the rainbow, created by water clouds in the planetary atmosphere, is a powerful ally in our search for water clouds on other planets. In the upcoming years the detection of giant planets will be easier than the detection of terrestrial planets. For this reason Karalidi also describes the influence that various formations, such as zones, spots and polar hazes, have on the signal from Jupiter-like exoplanets.



ISBN 978-94-6108-416-3

T. Karalidi

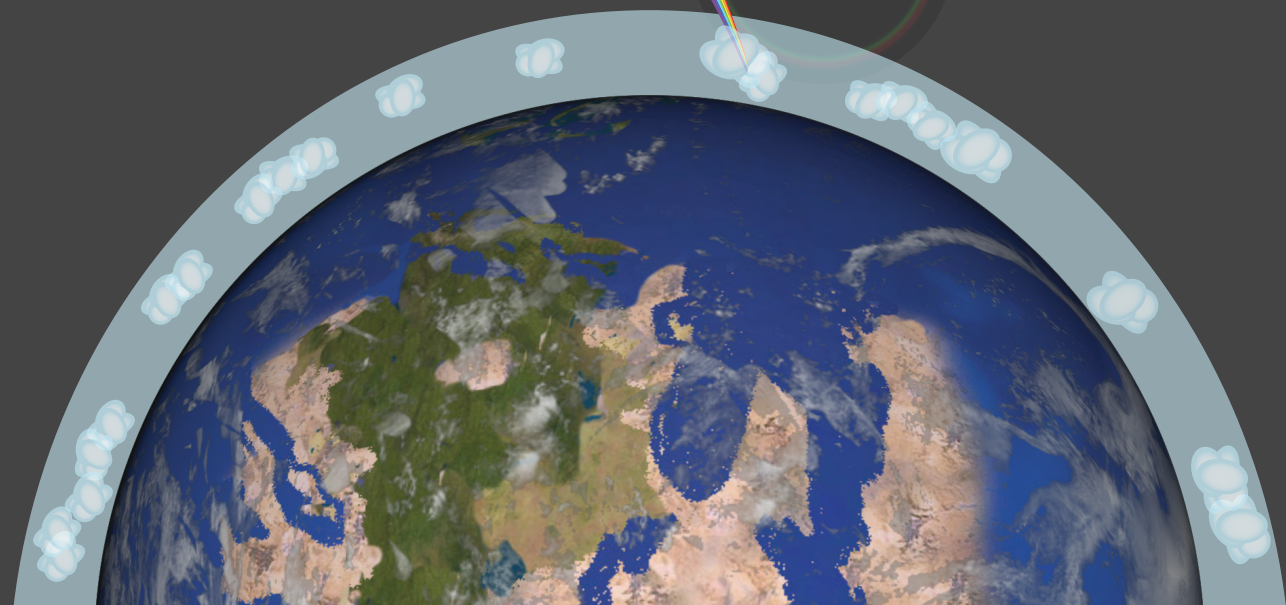


Broadband polarimetry of exoplanets - modelling signals of surfaces, hazes and clouds

# Broadband polarimetry of exoplanets

modelling signals of surfaces, hazes and clouds

THEODORA KARALIDI



*Propositions accompanying the thesis*

## ***Broadband polarimetry of exoplanets***

### ***Modelling signals of surfaces, hazes and clouds***

- $\alpha$ . The rainbow created by the water clouds of exoplanets is a mighty ally on our search for water on exoplanets.
- $\beta$ . The use of polarisation can help us characterise exoplanetary atmospheres and surfaces (*Chapter 2*).
- $\gamma$ . Using weighted averages of homogeneous models can lead to large errors on our interpretation of an exoplanetary signal (*Chapter 3*).
- $\delta$ . Looking for the rainbow of water clouds on exoplanets allows us to detect water on exoplanetary atmospheres, even when the latter contain lots of ice clouds (*Chapter 4*).
- $\epsilon$ . Spots, belts and polar hazes leave a distinctive trace on the disk-integrated exoplanetary signal (*Chapter 5*).
- $F$ . An instrument like LOUPE on the Moon will allow us to control our models and create benchmark observations for future characterization of Earth-like exoplanets (*Chapter 6*).
- $\zeta$ . Missions like JUICE, selected to fly to Jupiter and its moons, are very important, also for the field of exoplanetary research.
- $\eta$ . Polarization is a powerful means to decipher many of Nature's hidden messages.
- $\theta$ . Every scientist should be the most critical referee of his work.
- $\iota$ . A free-access and yet peer-reviewed way to publish research papers should be among the highest priority targets of the scientific community for the next decade.
- $\iota\alpha$ . Modern day democracy is a smartly disguised oligarchy.
- $\iota\beta$ . Relating the amount of funds a University receives to the number of students graduating every year, can only lead to a degradation of the quality of the provided education.
- $\iota\gamma$ . Feminism is a social movement that is being misused nowadays.

Cover Page



Universiteit Leiden



The handle <http://hdl.handle.net/1887/20830> holds various files of this Leiden University dissertation.

**Author:** Karalidi, Theodora

**Title:** Broadband polarimetry of exoplanets : modelling signals of surfaces, hazes and clouds

**Issue Date:** 2013-04-23

# **Broadband polarimetry of exoplanets**

**Modelling signals of surfaces, hazes and clouds**

© 2013 Theodora Karalidi  
Alle rechten voorbehouden

ISBN 978-94-6108-416-3

*Cover image:* An exoplanet with water clouds in its atmosphere creates a detectable rainbow feature. Using our models and observations we can characterize the exoplanetary atmosphere.

# **Broadband polarimetry of exoplanets**

**Modelling signals of surfaces, hazes and clouds**

Proefschrift

ter verkrijging van  
de graad van Doctor aan de Universiteit Leiden,  
op gezag van Rector Magnificus prof. mr. C. J. J. M. Stolker,  
volgens besluit van het College voor Promoties  
te verdedigen op dinsdag 23 april 2013  
klokke 15:00 uur

door

Theodora Karalidi  
geboren te Marousi Attikis  
in 1983

Promotor: prof. dr. C. U. Keller (Sterrewacht Leiden)

Co-promotor: dr. D. M. Stam (TU Delft, Faculty of Aerospace Engineering)

Promotiecommissie: prof. dr. H. Roettgering (Sterrewacht Leiden, WD, chair)  
prof. dr. C. U. Keller (Sterrewacht Leiden, Promotor)  
dr. D. M. Stam (TU Delft, Supervisor, Co-Promotor)  
prof. dr. K. H. Kuijken (Sterrewacht Leiden)  
prof. dr. I. Snellen (Sterrewacht Leiden)  
prof. dr. C. Dominik (University of Amsterdam)

*To my family,*



# Contents

---

<b>Contents</b>	<b>vii</b>
<b>1 Introduction</b>	<b>1</b>
1.1 A short history of exoplanets . . . . .	1
1.2 Detection methods of exoplanets . . . . .	3
1.3 Characteristic of the planets discovered so far . . . . .	5
1.4 Characterization of exoplanets . . . . .	8
1.5 Defining polarization . . . . .	9
1.6 Signals of Earth-like planets . . . . .	14
1.7 Modelling the signals of exoplanets . . . . .	18
1.8 Instruments for polarimetric studies of exoplanets . . . . .	20
<b>2 Water clouds on exoplanets</b>	<b>25</b>
2.1 Introduction . . . . .	26
2.2 Description of starlight that is reflected by an exoplanet . . . . .	30
2.3 Our model atmospheres . . . . .	32
2.4 Single scattering properties of water cloud particles . . . . .	36
2.5 Light that is reflected by planets . . . . .	41
2.6 Summary and discussion . . . . .	50
2.7 Future work . . . . .	53
<b>3 The numerical code</b>	<b>55</b>
3.1 Introduction . . . . .	55
3.2 Calculating reflected starlight . . . . .	59
3.3 Sensitivity to horizontal inhomogeneities . . . . .	62
3.4 Application to Earth-like planets . . . . .	70
3.5 Summary and conclusions . . . . .	75
<b>4 Looking for the rainbow</b>	<b>83</b>
4.1 Introduction . . . . .	83

4.2	Calculating flux and polarization signals . . . . .	87
4.3	The influence of the liquid water cloud coverage . . . . .	95
4.4	The influence of mixed cloud droplet sizes . . . . .	99
4.5	The influence of the ice cloud coverage . . . . .	102
4.6	Searching for the rainbow on Earth . . . . .	106
4.7	Summary and conclusions . . . . .	108
<b>5</b>	<b>Gaseous exoplanets</b>	<b>113</b>
5.1	Introduction . . . . .	113
5.2	Description of the numerical simulations . . . . .	116
5.3	Single scattering properties of the cloud and haze particles . . . . .	119
5.4	Reflected flux and polarization signals of the model planets . . . . .	123
5.5	Discussion and conclusions . . . . .	132
<b>6</b>	<b>Observing the Earth as an exoplanet with LOUPE</b>	<b>137</b>
6.1	Introduction . . . . .	137
6.2	Flux and polarization spectra of the Earth as an exoplanet . . . . .	140
6.3	The advantages of using the Moon as observation platform . . . . .	143
6.4	The LOUPE instrument . . . . .	146
6.5	Summary and conclusions . . . . .	147
<b>7</b>	<b>Nederlandse samenvatting</b>	<b>149</b>
7.1	Exoplaneten, een korte geschiedenis . . . . .	149
7.2	Het belang van polarisatie . . . . .	151
7.3	Dit proefschrift . . . . .	153
7.4	Samenvatting van dit proefschrift . . . . .	159
<b>8</b>	<b>Περίληψη</b>	<b>161</b>
8.1	Μια σύντομη ανασκόπηση . . . . .	161
8.2	Η σημαντική συνεισφορά της πόλωσης του φωτός στην μελέτη των εξωπλανητών . . . . .	163
8.3	Μοντέλα για την μελέτη των εξωπλανητών . . . . .	166
	<b>Bibliography</b>	<b>175</b>
	<b>Acknowledgments</b>	<b>187</b>
	<b>Curriculum Vitae</b>	<b>189</b>

*Ἐν οἶδα ὅτι οὐδέν οἶδα*  
Σωκράτης (469 πΧ – 399 πΧ)

*One thing I know, that I know nothing*  
Socrates (469 BC – 399 BC)



# Introduction

---

## 1.1 A short history of exoplanets

In this thesis our goal is to model the broadband polarimetric signal of exoplanets containing various forms of inhomogeneities, like for example continents and oceans, hazes, clouds etc. Some of these inhomogeneities, like water clouds in a planetary atmosphere are very important for the existence of life as we know it, and as we will see in this thesis tend to leave a characteristic signal on the planetary signal.

Man kind has been pondering for centuries over the possible existence of exoplanets, i.e. planets that orbit around a star other than our Sun, that could harbor life. Already in ancient Greece, philosophers like Democritus and Epicurus were speaking of the existence of infinite worlds, either like or unlike ours.

*“In some worlds there is no Sun and Moon, in others they are larger than in our world, and in others more numerous. In some parts there are more worlds, in others fewer (...); in some parts they are arising, in others failing. There are some worlds devoid of living creatures or plants or any moisture.”* - Democritus (460–370 B.C.)

Aristotle’s authority and opinion that there “cannot be more worlds than one”, shadowed any further advancement on the topic for centuries. Giordano Bruno and a couple of centuries later Christiaan Huygens among others will come back to this topic, and claim the existence of multiple worlds like ours.

*“Why should not every one of these stars or suns have as great a retinue as our sun, of planets, with their moons, to wait upon them?”*  
- Christiaan Huygens (1629–1695 A.D.)

Huygens performed the first documented effort to detect exoplanets (Κοσμοθεωρός, 1698). Any efforts though to detect exoplanets back then would be futile

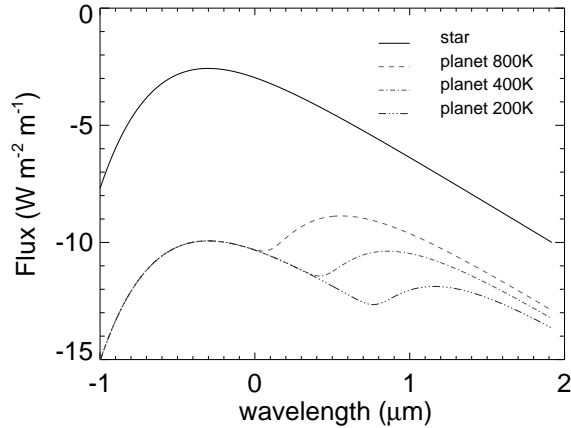


**Figure 1.1:** Solar flux of a Sun-like star as a function of the observation wavelength. The Star is set 4pc away from the observer. Over-plotted are the fluxes of a Jupiter-like planet lying 1A.U. from its parent star with a temperature of 200K (blue, dashed-triple-dotted line), 400K (green, dashed-dotted line) or 800K (red, dashed line). For giant planets the planet to star contrast ratio is of the order of  $10^{-9}$ , while for terrestrial planets this ratio can be of the order of  $10^{-11}$  in the visible.

since exoplanets are so faint in comparison to their parent stars (see Fig. 1.1) that with the means of that time their detection was impossible.

Some centuries later, astronomer P. van de Kamp using astrometry found a wobble in Barnard's star motion which he attributed to the existence of initially one and later two giant planets (van de Kamp 1969b,a). His findings have not been reconfirmed so far. The first official discovery of an exoplanet was done by Wolszczan & Frail (1992) who discovered an exoplanet orbiting around a pulsar. A pulsar – a highly magnetised, rotating neutron star that emits a beam of electromagnetic radiation – is not the ideal parent star for astronomers that seek our Earth's twin planet, but nevertheless this was the first time that the idea of the existence of planets outside our Solar System was reconfirmed.

A couple of years later the discovery of the first exoplanet orbiting a solar-like star by Mayor & Queloz (1995) inaugurated a new era in astronomy. In the less than two decades that have followed that discovery, more than 770 exoplanets have been detected up to today (source: The extrasolar planets encyclopedia). As we

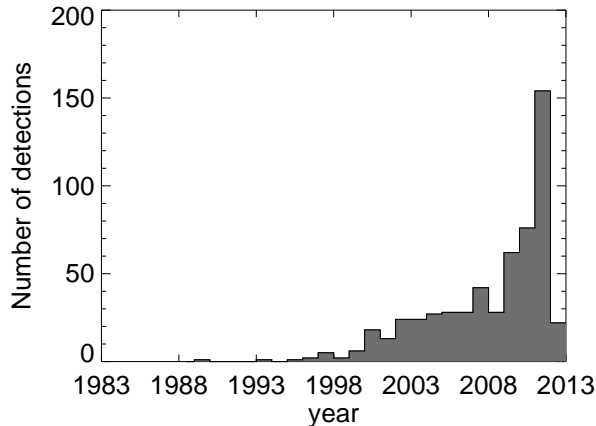


**Figure 1.2:** Number of exoplanets detected per year from 1983 up to 2012. As we can see, the number of exoplanet detections has been increasing almost exponentially in the past years thanks to instruments like HARPS, COROT and Kepler.

can see in Fig. 1.2 the number of exoplanet detections per year increases almost exponentially, mostly due to the improved instruments and detection techniques.

## 1.2 Detection methods of exoplanets

Since the first discovery of the first exoplanet orbiting a solar-like star by Mayor & Queloz (1995), using the radial velocity method a number of techniques have been developed for the detection and characterization of exoplanets. Most of these techniques are indirect, i.e. we never detect/ observe the planet itself, but we see the effect its existence has on the signal of its parent star. Here, we briefly present some of these techniques and the amount of information we can acquire with each one. Finally, in Table 1.1 we present the number of exoplanets detected with each method so far.

### 1.2.1 Indirect detection of exoplanets

The **radial velocity** (RV) method is the oldest technique used for the detection of exoplanets. It is to this technique that we owe the detection of the first exoplanet

orbiting a solar-like star (Mayor & Queloz 1995) and the start of the field of exoplanetary research. The RV method is based on the study of the Doppler shift of the parent star's light due to the rotation of the planet around it. The method is mostly sensitive to massive stars orbiting close to their parent star, since these planets have the largest radial velocities. Additionally, large orbits will require large observation times. Even though we owe the largest number of planetary detections to this method, we are close to reaching its limits.

The **planetary transit** method is the new method to which we owe a large number of exoplanet detections, and which is rapidly catching-up with the RV method thanks to new, space-born instruments like COROT (Convection, Rotation & planetary Transits) (Baglin et al. 2006) and Kepler (Koch et al. 1998). This method is based on measuring the dimming of the emitted light from the parent star as the planet transits, i.e. passes in front of the stellar disk, covering it partially and allowing less starlight to arrive to the observer. This method is sensitive to large planets that orbit close to their parent star<sup>1</sup>. These biases of the planetary transit method are the another reason why most of the exoplanets detected up to today are so-called hot Jupiters and not Earth-like planets.

Finally, the **microlensing** method uses the gravitational lensing phenomenon for the detection of exoplanets (Gould & Loeb 1992). When a foreground star passes close to the line of sight of a distant, background star, the foreground star will act as a lens and split the light of the background star in two, usually unresolved images. If the foreground star hosts a planet, whose plane of rotation lies close to the plane of observation, the latter will also act as a lens and introduce a short perturbation in the image that is a typical signature for the existence of a planet. The largest disadvantage of this method is that a detection can not be reconfirmed, since the alignment of the foreground star with a background star will probably not occur again, and the detected exoplanets are in systems very far away for other methods to observe them.

### 1.2.2 Direct detection of exoplanets

As the name suggests, direct detection of exoplanets concerns the direct depiction of an exoplanet on an image, separated from its parent star. The direct detection of exoplanets will be the best way to characterize the atmosphere and surface of an Earth-sized exoplanet, with the help of large, ground-based telescopes such

---

<sup>1</sup>It can be shown that the probability of a planet showing a transit is reversely proportional to its distance from its parent star. Additionally, it can be shown that the depth of the (primary) transit is proportional to the square of the planetary radius, implying that larger planets are easier to detect.

**Table 1.1:** Number of exoplanet detections by method up to May 2012. Source: The Extrasolar Planets Encyclopaedia (<http://exoplanet.eu/>).

Method	Number of detections	Number of planetary systems	Number of multiple planetary systems
Radial Velocity	708	563	96
Planetary Transits	231	197	30
Microlensing	15	14	1
Direct Detection	31	27	2

as the European Extremely Large Telescope (E-ELT) (Keller et al. 2010). Since though the planet to star contrast ratio is quite small (see Fig. 1.1), this method is quite challenging. With the aid of polarimetry, the planet to star contrast ratio can be increased by three to four orders of magnitude, making the detection of an exoplanet easier (Keller et al. 2010). Even when the contrast problem is overcome and we manage to observe the exoplanet, we are still faced with the challenge to characterize an exoplanet that is unresolved, i.e. it occupies a single pixel. If the planet resembles the Earth for example, that one single pixel will hold information on oceans, continents, vegetation coverage and cloud content of the planetary atmosphere.

### 1.3 Characteristic of the planets discovered so far

When we discover an exoplanet with the help of the radial velocity and transit methods, we can get information on its mass and radius and thus we can define its density ( $\rho \sim \text{mass}/\text{radius}^3$ ). The density and radius of a planet can give us an indication of whether this planet is a giant, gaseous planet like Jupiter ( $\rho_J \sim 1.33 \text{ gr}/\text{cm}^3$ ) and the rest giants planet of our Solar System or a terrestrial, rocky planet like Earth ( $\rho_E \sim 5.51 \text{ gr}/\text{cm}^3$ ) and the rest terrestrial planets of our Solar System.

Most of the exoplanets discovered up to now, are very massive planets, with masses up to a couple of times that of Jupiter, and tend to rotate in very tight orbits around their parent stars (see Fig. 1.3). Thankfully for the researchers interested in finding our Earth's twin, a planet with a size similar to our Earth that lies within its parent star's habitable zone, i.e. the region around the star within which a planet can sustain liquid water on its surface, provided it has an adequate atmosphere (see e.g. Kaltenegger & Sasselov 2011) (see Fig. 1.4), this is not a natural phenomenon making the terrestrial planets of our Solar System unique or special, but an observational bias, intrinsic to the methods and instruments used

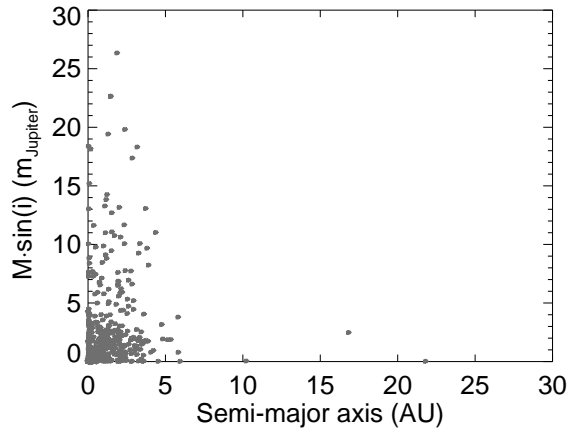


**Figure 1.3:** A scatter plot of the minimum estimated mass (in Jupiter masses) of the (confirmed) exoplanets detected up to today as a function of the semi-major axis of their orbit (in AU). As we can see, most exoplanets detected up to today are massive objects orbiting in tight orbits around their parent stars.

in the first years of exoplanetary research. In fact, Borucki et al. (2011) comparing the first data from Kepler with ground-based observations have shown that the smaller, terrestrial-like exoplanets should be a lot more common than the large planets, but due to the intrinsic biases of our ground-based methods we have not detected them yet. Recently, Cassan et al. (2012) have estimated that about 62% of the Milky Way stars should actually have an Earth-like planet. Up to today we have detected about five rocky planets, the smallest one of which has a minimum mass of  $1.9 M_{\oplus}$  (Mayor et al. 2009) and its year lasts about 3.15 days. Detecting, and most importantly characterizing even smaller Earth-like exoplanets, will not be possible with the currently used (indirect) methods (Kaltenegger & Traub 2009).

In order to detect and characterize smaller Earth-like exoplanets we need to turn to direct detection of exoplanets, and most particularly in polarization. The disk-integrated light coming to us from distant solar type stars is virtually unpolarized (Kemp et al. 1987). On the other hand, as we will see in Sections 1.5.1 and 1.5.2, the starlight that is reflected by the (exo-)planet will be polarized due to scattering and reflection processes in the planetary atmosphere and surface (when present). Thanks to this, polarization can be used to enhance the planet to star contrast

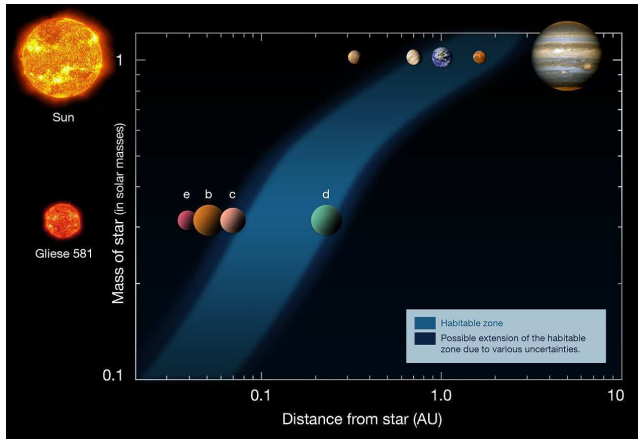


**Figure 1.4:** Habitable zones of our Sun and Gliese 581. As we can see the hotter the star is, the further away its habitable zone is. Credits: ESO.

ratio by up to three to four orders of magnitude (Keller et al. 2010).

In particular, assume we observe a planetary system in polarization using two mutually perpendicular set-ups of our polarimeter and then we subtract the two images. Since the starlight is unpolarized, its intensity in both images should be approximately the same, thus the subtraction of the two images should leave a (almost) zero signal in the position of the star. Since the planetary light is polarized on the other hand, its intensity will vary between the two images. Assuming that we have chosen the correct orientation for our polarimeter initially, such that the polarimeter is co-aligned with the planet's polarized signal, its perpendicular set-up will allow zero planetary signal passing through and thus the subtraction of the two images will give us the full polarized planetary signal. In this way we can in principal get rid of (most of) the starlight and detect easier the planetary signal (see e.g. Rodenhuis et al. 2011, for an application on a real instrument).

Concluding, in less than two decades thanks to the advancement of our methods and instruments we have detected more than 770 exoplanets. In the next couple of years the number of detected exoplanets will increase exponentially and soon we will find the first Earth-like planets lying in the habitable zone of its parent star. Still though, with the current means we will not be able to properly characterize that exoplanet and we will not be able to make any conclusive remarks on its potential habitability.

## 1.4 Characterization of exoplanets

With the detection of exoplanets being a routine procedure nowadays, the interest of the exoplanetary community shifts slowly from the plain detection of exoplanets to their characterization. Until the recent past, the planetary characterization involved only the determination of the physical characteristics of the exoplanet, such as its (minimum) mass, radius, density and distance from its parent star. Nowadays though, thanks to our improved instruments and with the aid of transit spectroscopy we can define the chemical content of planetary atmospheres (see e.g. Tinetti et al. 2007, Désert et al. 2011), its atmospheric temperature–pressure profile (see e.g. Huitson et al. 2012, Todorov et al. 2012, Snellen et al. 2010b) and more recently, we can even detect the existence of atmospheric patterns (see e.g. Snellen et al. 2010a).

In the near future, with the detection of the first Earth–like planets, our interest will, inevitably, be shifted towards the detection of signs of habitability. Our experience from our Solar System planets shows that habitability is intertwined with the existence of liquid water on a planetary atmosphere and surface. Detection of liquid water on a planetary atmosphere or surface can be achieved by the detection of the rainbow created by the water clouds on the exoplanetary atmosphere (see Chapters 2, 4 and 6 and references therein), or by the detection of the glint of starlight reflected on liquid surfaces, such as those of oceans, on the exoplanetary surface (see e.g. Williams & Gaidos 2008). In this effort the direct detection of exoplanets and most importantly the use of polarization will provide us with a crucial tool.

### 1.4.1 Polarization as a tool for the characterization of exoplanets

Polarization is a powerful tool for the characterization of planetary atmospheres and surfaces (Hansen & Travis 1974) that has been known and used in astronomical studies for more than a hundred years. Already in 1929 Lyot (Lyot 1929) was using polarization to study the atmospheres of Venus and Jupiter, while Hansen & Hovenier (1974) were able to derive the composition and size distribution of the droplets on the upper Venusian clouds, as well as the cloud top altitudes in the Venusian atmosphere, thanks to the ability of polarization to brake the degeneracies that the previous flux–only measurements had. In recent years, the power of polarization is generally accepted and applied in studies of Earth’s atmosphere and surface for e.g. characterizing aerosols and surfaces and determining the phase (liquid or ice) of water clouds.

Even in the case of the Solar System planets, polarization has proven a valuable

ally (see e.g. Hansen & Hovenier 1974, West et al. 1983, West & Smith 1991, Mishchenko 1993), thanks to its extreme sensitivity to the atmospheric (micro-) physical properties (refractive index of cloud droplets and size distribution, cloud optical thickness and top altitude etc) (Hansen & Travis 1974). This sensitivity being due to the fact that because of the generally low polarization of light that is multiple times scattered in the atmosphere, the main angular features observed in a polarized planetary signal will be due to single scattered light.

Unlike Solar System planets, in the case of exoplanets the planetary signal is disk-integrated. The question arises then if any atmospheric or surface related features can survive in the disk-integration and thus if we can still characterize the planets based on their flux and polarization signals. In the field of terrestrial exoplanets the pioneering work of Ford et al. (2001), and later follow up works of Seager et al. (2005), Stam (2008) and Williams & Gaidos (2008) for example, have shown that the disk integrated signal of exoplanets should preserve crucial information on the planetary composition such as the signal of the so-called red-edge and the ocean glint, while in cases of horizontally homogeneous exoplanets and weighted averaged inhomogeneous exoplanets (the polarization part of ) the signal could also hold information on the cloud content of the planetary atmosphere (Stam 2008). In this book, we will show that even in the case of realistically inhomogeneous exoplanets when for example clouds cover just fractions of the planetary surface, their signal can still survive in the disk-integrated polarization, allowing us to “see” their presence in the exoplanetary signal.

But what do we mean when we talk about polarization?

## 1.5 Defining polarization

Light consists of electric-magnetic waves made out of oscillating and mutually perpendicular electric and magnetic fields which are fully polarized. And while in the case of radio observations measuring waves is possible, the same does not hold for the optical regime studies where we measure photons. Natural, unpolarized light is characterized by the fact that the photons out of which it is made, are polarized in all possible angles, and thus within the normal observing times we cannot track down any “preferred” polarization direction. On the other extreme, a totally linearly polarized light will contain photons polarized all in one and only angle. Generally an arbitrary beam of light of total flux  $\pi F_{\text{tot}}$  will consist of two parts, an unpolarized part  $\pi F_{\text{unpol}}$  and a fully polarized part  $\pi F_{\text{pol}}$ , such that  $\pi F_{\text{tot}} = \pi F_{\text{unpol}} + \pi F_{\text{pol}}$ .

Broad-band polarized light can be created from natural light in four basic ways:

reflection, refraction, differential absorption and scattering. When we are interested in the polarization of starlight reflected of a planet, the reflection (on the planetary surface) and scattering (in the atmosphere) are the two most important processes we deal with.

### 1.5.1 Polarization due to reflection

When natural light reflects on a surface it will generally become polarized. The extent to which polarization will occur depends on two factors: the angle of incidence (in other words the angle with which the light approaches the surface of the material relevant to the perpendicular) and the material of the surface. For example, most non-metallic surfaces reflect light with one vibrational direction, more efficiently than others (in particular there is a preference to the plane perpendicular to the plane of incidence), thus resulting in polarized light.

When the reflection is regular at the boundary between two media of different refractive indices (for example the atmosphere and the surface) we can describe it using the so-called Fresnel equations (Fresnel 1819).

In general, a surface tends to reflect the incident flux  $\pi F_{\text{in}}$  anisotropically. The function that is used to describe the way that a surface reflects incident light at various directions is called the *Bidirectional Reflectance Distribution Function* (*BRDF*) and the function that describes the way the reflected light is polarized at various directions is called the *Bidirectional Polarization Distribution Function* (*BPDF*). For modelling Earth surfaces for example, the most common *BPDF* model is that of Nadal & Breon (1999), while a number of models exist for the *BRDFs* (see e.g. Litvinov et al. 2010). These functions tend to take into account the existence of variations on the reflecting surfaces due to e.g. the existence of waves, leaves causing shadowing etc.

A simplified version of the *BRDF* is that of a Lambertian reflector, in which case we assume that the surface reflects the light in the same way in all directions (see Fig. 1.5). The Lambertian approximation, even though not satisfied by any real reflector, is a convenient approximation for many diffuse reflectors (Lenoble 1993).

A basic “disadvantage” of a Lambertian surface is that it is totally depolarizing, i.e. not only it does not polarize light falling on it like surfaces normally do, but even when polarized light falls on it, it will become unpolarized. Studies of the influence of a Lambertian assumption on retrieval algorithms of Earth’s atmosphere show that it leads to minor errors (see e.g. O’Dell et al. 2011), but it could introduce some errors in our results when the polarization of reflected light is of interest.

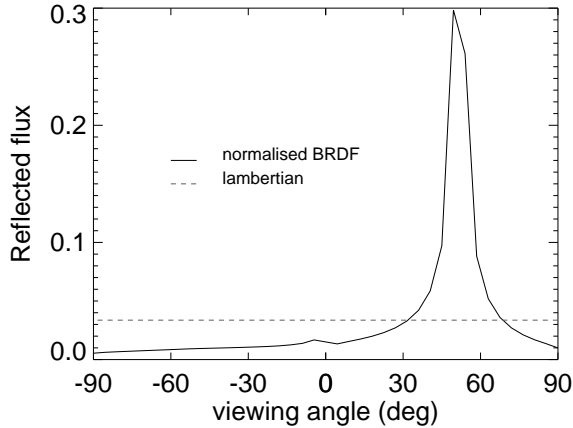


**Figure 1.5:** Normalized BRDF of a surface versus its lambertian reflection. The input parameters used for the calculation of the BRDF and the albedo of the surface was taken from MODIS data. The normalization of the BRDF is such that the total reflected flux is equal to that of the lambertian case. The solar zenith angle is taken equal to  $35^\circ$ .

### 1.5.2 Polarization due to scattering

Unpolarized light that travels through an atmosphere and scatters on a particle, generally gets polarized. The reason for this is that as the photons collide with the atoms of the particles it will set them into vibration. In their turn, the vibrating atoms will emit photons that will be radiated in all directions. These waves now can collide with other atoms of the particle, which will reproduce in their turn new photons. In this way the light will be scattered about the medium. This scattered light is polarized (Leroy 2001). The polarization characteristics of the scattered light due to its creation mechanism depends largely on the properties of the scattering particles (in particular its chemical composition, shape, size) and they are wavelength dependent (Stam et al. 2006b).

Assume a beam of light that enters an atmosphere and on its way encounters a particle. If we assume that it undergoes single scattering on it we will get the following pattern for the degree of polarization as a function of the angle. In the back-scattering and forward-scattering directions the degree of polarization will be zero. As we proceed to the perpendicular direction the degree of polarization will increase to higher values, reaching a 100% polarization on the perpendicular

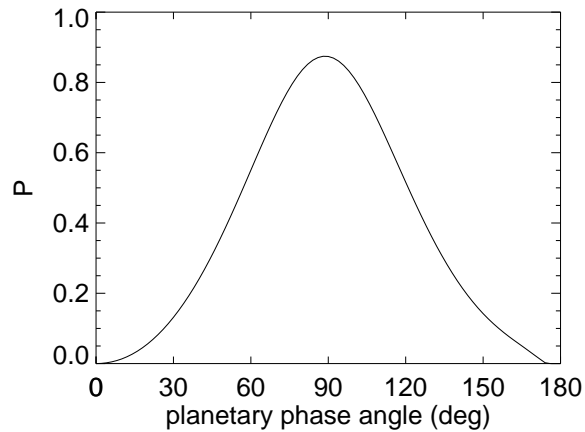


**Figure 1.6:**  $P$  of light reflected by a clear planetary atmosphere keeps the characteristics of the single scattering properties of the atmospheric molecules. Here, we plot  $P$  of an ocean planet with a clear, Earth-like atmosphere at  $0.65 \mu\text{m}$ .

(50% if the radiation wavelength is larger than the characteristic dimensions of the scattering particles).

In reality, since the particles are somewhat irregular in shape, and we can be dealing with anisotropic radiation and multiple scattering, the degree of polarization never reaches 100%. This behavior defines to a large degree the “picture” of polarization we get when viewing from above a planetary atmosphere as we can see in Fig. 1.6, where we plot the degree of polarization  $P$  as function of the planetary phase angle ( $\alpha$ ) for an ocean planet with a clear, Earth-like atmosphere.

### 1.5.3 Stokes formalism

George Gabriel Stokes introduced in 1852 a new way to describe the polarization state of light in the optical regime through intensity measurements, in terms of its total flux ( $\pi F$ ), fractional degree of polarization ( $P(\lambda)$ ) and the shape parameters of the polarization ellipse. The Stokes parameters are combined into the Stokes

vector:

$$\pi\vec{F} = \pi \begin{pmatrix} F \\ Q \\ U \\ V \end{pmatrix}, \quad (1.1)$$

which spans the space of all the polarization states of light (namely unpolarized, partially polarized and fully polarized)(Collett 1992). The  $\pi F$  component represents the incoherent sum of the signal (there are no interference effects), the  $\pi Q$  and  $\pi U$  are the differences in linear polarization states at two perpendicular planes and the  $\pi V$  factor represents the circular polarization. In this way for example a light with a Stokes vector of  $\pi\vec{F} = (1, 0, 0, 0)$  would be completely unpolarized, while a  $\pi\vec{F} = (1, 0, 0, 1)$  would be right-handed, circularly polarized (with respect to the positive  $x$ -axis, clockwise as seen by the observer (del Toro Iniesta 2003)).

In the case we are dealing with fully polarized light the total flux will be:

$$F = \sqrt{Q^2 + U^2 + V^2}, \quad (1.2)$$

or in case we are dealing with partial polarized light we will have:

$$F \geq \sqrt{Q^2 + U^2 + V^2}. \quad (1.3)$$

The Degree of polarization ( $P$ ), the ratio of the flux of the polarized light to the flux of the unpolarized light, as a function of the Stokes parameters is given by:

$$P = \frac{\sqrt{Q^2 + U^2 + V^2}}{F}, \quad (1.4)$$

which in case that  $V = 0$  (no circular but only linear polarization) transforms in the degree of linear polarization ( $P_L$ ) that has the form :

$$P_L = \frac{\sqrt{Q^2 + U^2}}{F}. \quad (1.5)$$

When additionally  $U = 0$  we define the degree of linear polarization as

$$P_S = -\frac{Q}{F}. \quad (1.6)$$

Based on this we see why as we mentioned earlier, when we have a Stokes vector  $\pi\vec{F} = (1, 0, 0, 0)$  we are dealing with unpolarized light, since then we have  $P = 0$ .

The corresponding Angle of linear polarization ( $\chi$ ) is:

$$\chi = \frac{1}{2} \arctan\left(\frac{U}{Q}\right) \quad (1.7)$$

(Hansen & Travis 1974).

## 1.6 Signals of Earth-like planets

One of the biggest challenges of the field of exoplanets will be the detection and characterization of an Earth-like exoplanet. Particularly, when the first exoplanet with the correct mass and in the correct distance from its parent star is found we will be interested in finding whether this planet has continents and oceans on its surface, and whether there are water clouds in its atmospheres. But how can we figure out what the planetary atmosphere and surface contains?

To decipher the signal of a directly detected exoplanet, we will need numerical models that can simulate single pixel signals of exoplanets with inhomogeneous atmospheres and surfaces (if present). Such models will be essential for the design and optimization of telescope instruments and mission profiles (which are the necessary spectral bands and resolution for characterizing a given object, for how long should we observe etc). Additionally, once the first observations are available, these models can be used to interpret these observations. In order to control our models' ability to characterize an Earth-like exoplanet we need to test them against a planet that has continents, oceans and water clouds on its atmosphere, i.e. our Earth. But what can we expect when we will observe an Earth-like exoplanet?

In Fig. 1.7 we present calculated disk-integrated flux and polarization spectrum of our Earth as an exoplanet for a phase angle of  $46^\circ$  or  $90^\circ$  and for various Earth configurations. The continuum features we see in Fig. 1.7, which as we see vary with the phase angle, are due to the various surface and atmospheric features of Earth. For example, we notice that the lower albedo of the ocean surface when the Pacific is in the center of our field of view, leads to a lower reflected flux (and correspondingly higher polarization) than in the case Eurasia and Africa are on the center of our field of view.

In the latter case we notice a bump for wavelengths longer than  $0.65 \mu\text{m}$ , which is the so-called red-edge caused by the vegetation that is in our field of view. Unlike what our eyes would tell us, vegetation on Earth tends to reflect a lot more light around  $0.7 \mu\text{m}$  (the near infrared part of the spectrum) than around  $0.5 \mu\text{m}$ , the wavelength area that gives plants their distinctive green color. In particular, if we would plot the vegetational reflectivity as a function of wavelength, the region of

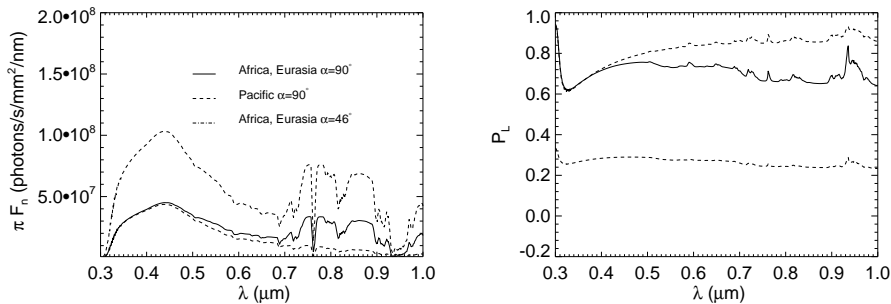


**Figure 1.7:** Calculated flux  $\pi F$  (left) and degree of linear polarization  $P_L$  (right) of sunlight reflected by the Earth as functions of  $\lambda$ , for  $\alpha = 90^\circ$ : with Africa and Eurasia in view and no clouds (solid lines), with the Pacific ocean in view and no clouds (dashed lines) and for for  $\alpha = 46^\circ$  with Africa and Eurasia in view (dashed-dotted lines).

the visual spectrum from about  $0.6\mu\text{m}$  onwards would present an increase up to five times or more in comparison to the  $0.5\mu\text{m}$  region. This sudden increase in the reflectivity is called the *red edge*. The exact location and intensity of this red edge depends on the nature of the vegetation and its environment (see Seager et al. 2005, and references therein).

In Fig. 1.7 we have treated the ocean surface as a black surface, and thus the only effect it has on our signal is due to its lower albedo. In reality though the ocean surface can have a larger influence to the total planetary signal at specific phase angles through the so-called *glint*. In particular, a liquid surface such as a planet's oceans can reflect light in a mirror-like way causing the glint. In case the liquid surface is flat (e.g. a non-waved ocean) the angle of reflectance equals the angle of incidence and we have a normal *specular reflection*. Specular reflection of starlight on a planetary ocean can affect its polarization properties, making the light highly polarized. In case the liquid surface is wavy, foamy etc, things can be more complicated but a number of analytical solutions exist to describe the flux and polarization properties of the reflected light (Nadal & Breon 1999, Martin 2004).

The high spectral resolution features that we see in both flux and polarization are due to gaseous absorption bands. At the shortest wavelengths light is absorbed by the atmospheric  $\text{O}_3$ , causing a dip in the reflected flux and a corresponding increase in the degree of polarization around  $0.3\mu\text{m}$ . Between  $\sim 0.5\mu\text{m}$  and  $\sim 0.7\mu\text{m}$  we notice, especially in the case we observe areas with high surface albedo

(here, the case of Africa and Eurasia), a dip in the reflected flux, which is the so-called Chappuis absorption band of  $O_3$ . Around  $0.76 \mu\text{m}$  we notice a deep absorption band which is the famous oxygen A-band, the easiest identifiable  $O_2$  band in our atmosphere. The oxygen A-band is useful for the characterization of planetary atmospheres, since its depth compared to the continuum, can help us determine the cloud top heights in a planetary atmosphere (see e.g. Wu 1985, and references therein).

In polarization, we notice that the spectrum of our planet looks similar to that in flux, only now the absorption lines have transformed into “emission” lines, i.e. there is a local increase in the degree of polarization where an absorption line lies. The reason for this is that the absorption of light in a band decreases the amount of multiple scattered light and we see mostly light that is singly scattered ((normally) with a higher degree of polarization) in the atmosphere.

The general increase in polarization that we observe with wavelength is due to the decrease in the optical thickness of the atmosphere with wavelength, which leads to a small(er) amount of multiple scattering. In this way, in the case we observe the Pacific region, since the ocean surface is almost black the polarization reaches almost as high as the single scattering value of the atmosphere. In the case we observe the Africa–Eurasia area on the other hand, a number of photons will have managed to reach as low as the surface and get reflected. At the longer wavelengths, where the atmosphere is less opaque the number of photons that have managed to penetrate the atmosphere and reflect on the surface is (getting) comparable to the number of singly scattered photons on the upper atmosphere and the degree of polarization decreases.

### 1.6.1 Looking for the rainbow

*“It’s a trick of the light”*

– Mike Oldfield, *Discovery*, 1984

An important feature to look for when we are interested in the detection of water clouds on exoplanets is the *rainbow* (see e.g. Bailey 2007, and references therein). The rainbow of water clouds is formed by light that has been refracted and reflected one or more times inside their water particles (see van de Hulst 1957, Adam 2002, Bailey 2007). The dispersion of the colors in a rainbow is due to the different refractive index that materials exhibit for photons of different wavelengths, a phenomenon known as (*chromatic*) *dispersion*. Short-wavelength (blue) light is refracted at a greater angle than long-wavelength (red) light.

The rainbow that we are all most familiar with, is the result of two refractions and one reflection inside the water droplets and is known as the *primary rainbow*. Due to the reflection of the light inside the droplet, the blue light will emerge at a smaller angle to the incident white light than the red light, causing blue to be on the inside of a rainbow arc and red on the outside. A less frequently observed rainbow, is that caused by light that has been reflected twice inside the water particles, the so-called *secondary rainbow*. Due to the second reflection its colors are reversed in comparison to the primary rainbow, i.e. the red color appears on the inside of the rainbow-arc and the blue color on the outside. Due to the angle of (incidence or) reflection being equal to the Brewster angle in the case of water droplets, the reflected light will be (almost) completely perpendicularly polarized, giving the primary and secondary rainbows high degrees of polarization (the primary rainbow can reach a  $P = 96\%$  and the secondary rainbow a  $P = 90\%$  (see Adam 2002, and references therein)). In principal, more than two internal reflections can take place inside each droplet, causing the so-called tertiary, quaternary and higher order rainbows (Adam 2002).

Rainbows' angular position depends strongly on the refractive index of the scattering particles and slightly on their radius ( $r_{\text{eff}}$ ) (see Chapter 2 and Adam (2002)). In Fig. 1.8, we plot the degree of linear polarization ( $P_S$ ) of starlight scattered by a planetary atmosphere as a function of wavelength ( $\lambda$ ) and the planetary phase angle ( $\alpha$ ). The color coding indicates the various values of  $P_S$ . In the left plot our model planet has a cloud deck of water clouds in its atmosphere and on the right plot a cloud deck of sulfuric acid ( $\text{H}_2\text{SO}_4$ ), like Venus. The bump of higher  $P_S$  around  $\alpha = 30^\circ - 40^\circ$  that we see in the left plot is the primary rainbow (notice how the location of the peak changes as a function of  $\lambda$ ). As we can see a similar feature does not appear in the case of  $\text{H}_2\text{SO}_4$ .

In this book we will look for the rainbow on exoplanets with cloud decks and cloud patches. Especially in Chapter 4 we will try to find the limits within which the rainbow can still give us insight on the existence of water on the planetary atmosphere, depending on the cloud coverage and the existence of ice clouds in the planetary atmosphere.

We should finally note here, that while the rainbow we are all most familiar with on Earth is caused by large, water drops, the rainbows we are interested in in this book are made by the interaction of starlight with water cloud particles, whose size many times does not exceed  $10 \mu\text{m}$  (0.00001 meters).

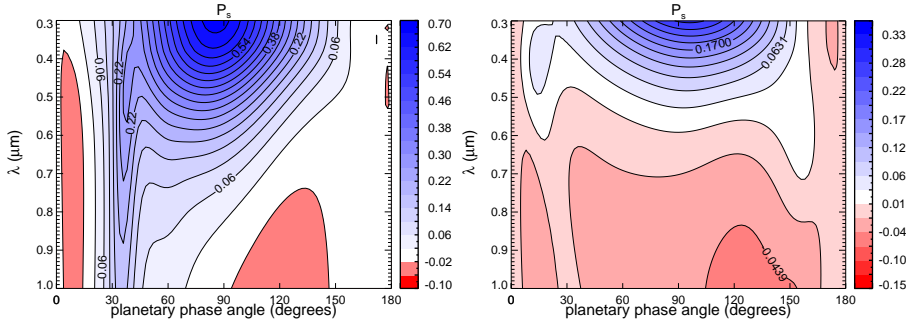


**Figure 1.8:** Degree of polarization  $P_S$  as function of the planetary phase angle  $\alpha$  and the wavelength  $\lambda$  for two cloud decked planets. Left plot: the cloud deck is made of water clouds, Right plot: the cloud deck is made of sulfuric acid. The primary rainbow (that we can see as an increase in  $P_S$  between  $\alpha = 30^\circ$  and  $\alpha = 40^\circ$ ) is apparent in the case of the water clouds, but non visible in the case of the sulfuric acid clouds.

## 1.7 Modelling the signals of exoplanets

As we previously mentioned, to decipher the signal of a directly detected exoplanet, we will need numerical models that can simulate single pixel signals of exoplanets with inhomogeneous atmospheres and surfaces (if present). Such models will be essential for the design and optimization of telescope instruments and mission profiles (which are the necessary spectral bands and resolution for characterizing a given object, for how long should we observe etc). Additionally, once the first observations are available, these models can be used to interpret these observations.

A number of models exist today that are used to calculate the signals of starlight reflected by gaseous and terrestrial exoplanets (see e.g. Ford et al. 2001, Tinetti 2006, Williams & Gaidos 2008, Stam 2008). Most of them treat only the flux and ignore the polarization, a fact that can introduce large errors in our interpretation of our observations (see e.g. Stam & Hovenier 2005). In a few cases that the models do take polarization into account, they tend to do it over-simplified (for example ignoring multiple scattering), or if they take polarization properly into account they treat homogeneous only planets.

Most of the planets of our Solar System though, exhibit some form of inhomogeneity or another (oceans, continents, (liquid or ice) water clouds, ammonia ice clouds, zones, belts and spots etc.). To mimic this inhomogeneity, some of the models that treated homogeneous-only planets used methods like the *weighted*

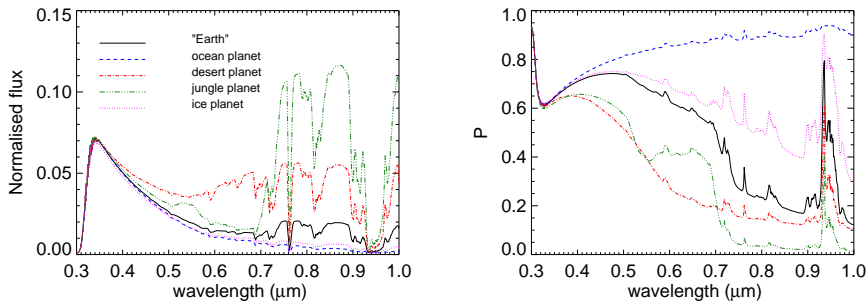


**Figure 1.9:** An example of how the weighted averaging method works. Our simplified Earth-as-an-exoplanet is covered by  $\sim 72\%$  by ocean,  $\sim 10\%$  by desert,  $\sim 9.4\%$  by forest and  $\sim 8.6\%$  by ice. Our model “Earth” is observed at a phase angle of  $90^\circ$ .

*averaging* (Stam 2008), in which the flux and polarization signals of a number of homogeneous planets are (weighted) summed up to create the inhomogeneous planetary signal. The weight given to each one of the homogeneous models depends on the percentage coverage on the planet of the feature treated in the model. For example, to model the signal of a simplified and cloudless Earth-as-an-exoplanet, we would need to use a model of an ocean world (a planet covered completely by water), a desert world, a jungle world and an ice world. Then knowing that at a random time the Earth is covered by e.g.  $\sim 72\%$  by ocean,  $\sim 10\%$  by desert,  $\sim 9.4\%$  by forest and  $\sim 8.6\%$  by ice we can produce the total Earth-as-an-exoplanet signal by adding  $0.72 \cdot (\text{ocean world signal}) + 0.10 \cdot (\text{desert world signal}) + 0.094 \cdot (\text{jungle world signal}) + 0.086 \cdot (\text{ice world signal})$  (see Fig. 1.9). Of course, the question arises how good is this approximation, and which are the limits within which we can use it without large deviations from the “truth”.

In this book, we will present a new numerical code that can deal with truly horizontally and vertically inhomogeneous exoplanets and can produce their full, disk-integrated flux and polarization signal as a function of the observational wavelength and the planetary phase angle (i.e. where the planet lies on its orbit around its parent star). Our code is based on the same efficient and accurate adding-doubling algorithm as Stam et al. (2004) and can take polarization properly into account (all orders of scattering, all kinds of different clouds, surface reflection etc). As we will show later on this book, the results from our “truly” inhomogeneous planets show that the *weighted averaging* cannot be used for the complete characterization of exoplanets, unless the latter are almost homogeneous. In par-

ticular, the lack of information that the *weighted averaging* method has on the geographical distribution of inhomogeneities on the planet affects to a large degree the predicted flux and polarization spectra of the model exoplanets.

## 1.8 Instruments for polarimetric studies of exoplanets

A number of instruments are being planned that will use polarimetry as a method to detect and characterize exoplanets. In the next couple of years the Spectro-Polarimetric High-contrast Exoplanet Research (SPHERE) (see Beuzit et al. 2006) instrument on the Very Large Telescope (VLT) of ESO in Chile will increase the number of directly detected (giant) exoplanets. SPHERE consists of three instruments, IRDIS (Infra-Red Dual-beam Imager and Spectrograph), IFS (Infra-red Integral Field Spectrograph) and ZIMPOL (Zurich IMaging POLarimeter). The first two instruments will work on detecting exoplanets in the infrared part of the spectrum (above  $0.95 \mu\text{m}$ ), while ZIMPOL will work on characterizing detected exoplanets with the help of polarization in the visible part of the spectrum ( $0.6 \mu\text{m}$  to  $0.9 \mu\text{m}$ ) (Povel et al. 1994). IRDIS includes a dual polarimetric imaging mode (DPI) for imaging extended stellar environments (e.g. detecting disks of dust).

Another instrument that should see light within the next years is the Gemini Planet Imager (GPI) (Macintosh et al. 2006), which will target the characterization of giant planets observing between  $0.9 \mu\text{m}$  and  $2.4 \mu\text{m}$ . GPI will use polarization measurements to measure the polarization of light to see faint disks of dust from other solar systems' comet and asteroid belts (Perrin et al. 2010).

In the further future the Exoplanet Imaging Camera and Spectrograph (EPICS) (see Kasper et al. 2010) and its polarization instrument EPOL (Exoplanet Polarimeter) on the European Extremely Large Telescope (E-ELT) will push the limits of the lowest mass of *directly* detected and characterized exoplanets down to massive terrestrial objects and will aim to detect terrestrial planets located in the habitable zone of their parent star (see Kasper et al. 2010, Keller et al. 2010). EPOL will operate in the visible part of the spectrum between  $0.6 \mu\text{m}$  (target  $0.5 \mu\text{m}$ ) and  $0.9 \mu\text{m}$ .

An innovative concept for the direct detection and characterization of exoplanet is that of the New Worlds Observer (NWO) (Cash & New Worlds Study Team 2010). NWO plans on using a large occulter in front of a space telescope to block the light of nearby stars in order to observe their orbiting planets. Another instrument moving along similar lines is the Telescope for Habitable Earth and Interstellar/Intergalactic Astronomy (THEIA) (Seager et al. 2009). THEIA is designed to be a multi-instrument space-telescope concept for a 4-m diffraction-

limited telescope operating at UV/visible wavelengths. While NWO will use polarization for the detection and characterization of exoplanets similar plans do not exist for THEIA so far.

We should note here that the use of polarimetry in missions like these is important not only because it can help us detect an exoplanet easier (Keller et al. 2010), but also because it helps us *correctly* characterize an exoplanet. In particular, experience from Earth observations shows that not taking polarization into account, even when we are interested in flux only measurements, can introduce large errors in our interpretations of our observations (see e.g. Natraj et al. 2007, Sromovsky 2005).

As preparation for these missions and to test our models to a first order, we perform Earthshine observations, i.e. we study the light that gets reflected by the day side Earth on the Moon and back to us (see e.g. Turnbull et al. 2006, Sterzik et al. 2012). Unfortunately though, while such measurements are helpful there may still be some intrinsic biases that we cannot properly correct for (like for example the exact effect of the lunar surface on the polarization properties of the reflected Earthlight). For a proper control of our models we would ideally need direct observations of Earth as an exoplanet.

An interesting instrument concept that can help us on this, and that we will discuss further in Chapter 6 is that of LOUPE, the Lunar Observer for Unresolved Polarimetry of Earth. LOUPE is a small, lightweight instrument that could be placed on a lunar lander to observe the Earth as if it were an exoplanet. Thanks to the monthly orbit of the Moon around the Earth and its tidal locking with respect to the Earth, an instrument like LOUPE on a Lunar Lander could observe the whole of the Earth, all of the time and at all phase angles, from about  $0^\circ$  (i.e. a fully illuminated Earth disk), up to about  $180^\circ$  (i.e. a fully dark Earth disk). In this way, already in a months time LOUPE would see the Earth going through all the variations that (almost) any other Earth-like exoplanet that we could observe and characterize would go through. Ideally, the mission should last long enough to cover all seasons and capture the effects of seasonal changes (local solar zenith angles, weather and cloud patters, surface albedos, polar nights etc). An instrument like LOUPE would create a benchmark dataset against which we could test our retrieval models and which could be used for reference on every future Earth-like exoplanet characterization.

## This thesis is organized as follows:

In Chapter 2 we study the case of horizontally homogeneous planets, completely covered by liquid water clouds. Our planets are vertically inhomogeneous, i.e. every atmospheric layer can have a different composition of the other ones. We study the effect of a number of cloud micro- and macro-physical properties on the planetary flux and polarization signal. Our aim in this chapter is to explore the information content of the spectropolarimetric signal of cloudy planets and the wavelength and phase angle ranges that can provide use with most information on the atmospheric content.

In Chapter 3 we present the code we developed that can treat horizontally and vertically inhomogeneous planets. We test our code against the previously well-tested horizontally homogeneous code we used in Chapter 2. We then study the validity of the previously used *weighted averaging* method (see Chapter 1.7). We find that while the latter method can give us a feeling for the nature of inhomogeneities met on a planet (for example through the rainbow and its location), it can lead to errors on the characterization of the exoplanet since it holds no information on the location of inhomogeneities on the planetary surface. We apply our new code to some first test cases, using terrestrial exoplanets with atmospheric and/or surface inhomogeneities.

In Chapter 4 we study horizontally and vertically inhomogeneous planets with patchy water clouds and try to look for signs of the rainbow under various coverage and multi-cloud-layer conditions. We see that the rainbow is visible in polarization for planets with a cloud coverage above 10% for observation at  $0.55 \mu\text{m}$  (20% for observation at  $0.865 \mu\text{m}$ ), while the existence of ice clouds can mask the existence of water clouds (and the rainbow) only for the cases the ice clouds overcast more than half of the water clouds. Using MODIS/Aqua data for Earth, we model a simplified exo-Earth with liquid water and ice clouds and test whether an alien observer would notice the liquid water clouds in our planetary atmosphere.

In Chapter 5 we modify our code to study the effect of various inhomogeneities on the signal of gaseous, giant (exo-)planets. We study the effect that various inhomogeneities that occur on the giant planets of our Solar System (bands, spots, polar haze etc) have on the planetary signal. We notice that polarization is more sensitive than flux to the existence of these inhomogeneities. For example, while the variation in the signal of a Jupiter-like planet due to the diurnal rotation of a spot is non measurable in flux, in polarization it leaves a distinctive trace. In some cases more than one inhomogeneities could cause a similar variation on the planetary signal. The existence of multi-wavelength observations could help us distinguish between the various cases.

In Chapter 6 we use our code to study a model of Earth-as-an-exoplanet and present LOUPE, the Lunar Observatory for Unresolved Polarimetry of Earth. LOUPE is a small and lightweight instrument that could be placed on a lunar lander like ESA's Lunar Lander that will be launched in 2018 (if selected). From the Moon LOUPE will be able to make benchmark observations of Earth as if it were an exoplanet, that will be very valuable for future characterization of Earth-like exoplanets.

Finally, in Chapters 7 and 8 we present a summary of the research presented in this thesis in Dutch and Greek.



# Water clouds on exoplanets

---

Based on:

T. Karalidi, D. M. Stam and J. W. Hovenier, *Flux and polarization spectra of water clouds on exoplanets*, *Astronomy & Astrophysics*, volume 530, id A69, 2011, reproduced with permission ©ESO

**Abstract** *Context.* A crucial factor for a planet's habitability is its climate. Clouds play an important role in planetary climates. Detecting and characterizing clouds on an exoplanet is therefore crucial when addressing this planet's habitability. *Aims.* We present calculated flux and polarization spectra of starlight that is reflected by planets covered by liquid water clouds with different optical thicknesses, altitudes, and particle sizes, as functions of the phase angle  $\alpha$ . We discuss the retrieval of these cloud properties from observed flux and polarization spectra. *Methods.* Our model planets have black surfaces and atmospheres with Earth-like temperature and pressure profiles. We calculate the spectra from 0.3 to 1.0  $\mu\text{m}$ , using an adding–doubling radiative transfer code with integration over the planetary disk. The cloud particles' scattering properties are calculated using a Mie-algorithm. *Results.* Both flux and polarization spectra are sensitive to the cloud optical thickness, altitude and particle sizes, depending on the wavelength and phase angle  $\alpha$ . *Conclusions.* Reflected fluxes are sensitive to cloud optical thicknesses up to  $\sim 40$ , and the polarization to thicknesses up to  $\sim 20$ . The shapes of polarization features as functions of  $\alpha$  are relatively independent of the cloud optical thickness. Instead, they depend strongly on the cloud particles' size and shape, and can thus be used for particle characterization. In particular, a rainbow strongly indicates the presence of liquid water droplets. Single scattering features such as rainbows, which can be observed in polarization, are virtually unobservable in reflected fluxes, and fluxes are thus less useful for cloud particle characterization. Fluxes are sensitive to cloud top altitudes mostly for  $\alpha < 60^\circ$  and wavelengths  $< 0.4 \mu\text{m}$ , and the polarization for  $\alpha$  around  $90^\circ$  and wavelengths between 0.4 and 0.6  $\mu\text{m}$ .

## 2.1 Introduction

Since the discovery of the first exoplanet orbiting a solar-type star more than a decade ago (Mayor & Queloz 1995), the quest for signs of habitable exoplanets has started. And while many scientists intertwine habitability with the existence of liquid water on the planetary surface, another key factor for habitability is the planetary climate (Kasting et al. 1993). Clouds are among the major factors that affect a planetary climate.

Regarding the Earth, Goloub et al. (2000) presented an extended series of studies of the Earth's climate both at an observational as well as at a modelling level, which clearly indicates the crucial and diverse roles of clouds. In particular, clouds are responsible for the modulation of both the shortwave radiation (from the sun) as well as the long-wave radiation (from the planet) budgets of the Earth (Kim & Ramanathan 2008, Ramanathan et al. 1989, Cess et al. 1992, Malek 2007, and others). Additionally, by modulating the solar radiation clouds affect the atmospheric photolysis rates, which change the atmospheric photochemistry and chemical composition (Pour Biazar et al. 2007). And clouds are responsible for the storage of atmospheric volatiles, such as the organic volatiles that are indicators of the existence of bio and fossil-masses, which can damage the soil and groundwater and can react with sunlight to create tropospheric  $O_3$  (Klouta et al. 1996). Because of their roles in the climate, clouds on Earth have been subjected to intense study for the past five decades, both from a theoretical/modelling point of view, as well as from an observational point of view (from the ground as well as from space). The effects of clouds on the Earth's climate have been shown to depend on the sizes and shapes (i.e. thermodynamical phase) of the cloud particles, and on the optical thickness and vertical extension of a cloud.

In this Chapter, we present results of numerical simulations of flux and especially polarization spectra of starlight that is reflected by cloudy exoplanets, and discuss the sensitivity of these spectra to the size of the cloud particles, the cloud optical thickness and the cloud top altitude. In general, the composition of a cloud or cloud layer in a planetary atmosphere will depend on the ambient chemical composition, and the pressure and temperature profiles (the latter themselves will of course also be influenced by the presence of clouds). It is well known that clouds have strong effects on flux spectra of planets in the Solar System and beyond. Examples of simulated flux spectra of exoplanets with water clouds can be found in Marley et al. (1999), Tinetti et al. (2006c), Kaltenegger et al. (2007). Far less work has been done regarding polarization spectra of cloudy planets. Examples of simulated polarization spectra of exoplanets with liquid water clouds can be found in Stam (2008). In this Chapter we extend this work to different types of clouds, at various

altitudes.

Terrestrial liquid water clouds are in general comprised of particles with radii ranging from  $\sim 5 \mu\text{m}$  to  $\sim 30 \mu\text{m}$  (Han et al. 1994), and their optical thickness varies typically from  $b \sim 1$  to  $b \sim 40$  or more (van Deelen et al. 2008). There appears to be a correlation between the cloud particle sizes and the cloud optical thickness (Han et al. 1994, and references therein), that could originate in the properties of the condensation nuclei that the cloud particles condense on, but it is not a strong one (Stephens et al. 2008). Knowing the sizes of cloud particles is important for understanding a cloud's influence on a planetary climate, because it determines how a cloud particle scatters and absorbs incident light and thermal radiation (see e.g. Chapman et al. 2009, and references therein). How a particle scatters the light depends in particular on the size parameter, i.e. the ratio of  $2\pi$  times the particle radius to the wavelength (see Eq. 2.9). We will consider size parameters ranging from less than 1 up to  $\sim 120$ , covering the so-called Rayleigh regime, where the scattering particles are much smaller than the wavelength, to the geometric optics regime, where particles are large with respect to the wavelength. The cloud's optical thickness (which, when assuming spherical particles, is the product of the column number density and the extinction cross-section of the cloud particles) depends on the cloud particles' sizes, shapes, and composition, and hence also on the wavelength of the radiation. We will use cloud optical thicknesses ranging from 0.5 to 60 (at  $0.55 \mu\text{m}$ ) and spherical water particles.

Another cloud parameter that is not only important for the radiation field, but also for the thermo- and hydro-dynamical processes that take place in planetary atmospheres is the altitude or pressure of the top of the cloud. Cloud top altitudes and pressures are routinely determined in Earth remote-sensing and regularly in planetary observations (e.g. Wark & Mercer 1965, Weigelt et al. 2009, Peralta et al. 2007, Garay et al. 2008, Matcheva et al. 2005). In Earth and planetary observations, knowledge of cloud top altitudes is also essential for accurate derivations of mixing ratios of atmospheric trace gases from the depths of gaseous absorption bands in planetary spectra, since clouds will change the band depths. For example, in Earth observation, cloud top altitudes are used in the retrieval of the trace gas ozone ( $\text{O}_3$ ). These cloud top altitudes are usually derived from the depth of the so-called A absorption band of the well-mixed gas oxygen (the  $\text{O}_2$  A band is located around  $0.76 \mu\text{m}$ ) (e. g. Yamamoto & Wark (1961) and Fischer & Grassl (1991)). Note that in case an absorbing gas is not well-mixed and its vertical distribution is not known, its absorption bands cannot be used to provide absolute cloud tops.

Clouds on Earth are found at a wide range of altitudes. Most clouds are located in the troposphere, the lowest portion of the atmosphere, where the temperature generally decreases with altitude. On average, the top of the troposphere decreases

with increasing latitude, and with that the maximum cloud top altitude, from about 20 km in the tropics, to about 10 km in the polar regions. The tops of the highest clouds will usually contain ice particles. The thin, wispy clouds commonly known as cirrus clouds, are composed entirely of water ice crystals. Since above the tropopause, the atmosphere contains relatively little water vapour, most types of clouds are confined to the troposphere. The few cloud types that can be found above the tropopause are thin ice clouds, such as polar stratospheric clouds and noctilucent clouds.

We will limit ourselves to clouds that are composed entirely of liquid water droplets, and hence limit the cloud top altitudes in our model atmospheres to about 4 km (where the temperatures are still high enough to exclude the presence of ice particles). Our main reason to exclude clouds with ice particles is that the single scattering properties of ice (crystal) particles are usually very different from those of liquid (spherical) particles (see e.g. Goloub et al. 2000), and as a result, their presence will influence the light that is reflected by a cloud (in particular the polarized signal). Modelling and analysing this influence (which will depend on absolute and relative ice particle number densities, ice particle sizes and shapes, and orientation) will be the subject of further research.

In this Chapter, we present not only numerically simulated flux spectra, but especially polarization spectra. Polarimetry, i.e. measuring the direction and degree of polarization of light, is considered to be a powerful tool for the direct detection of exoplanets (Keller 2006, Keller et al. 2010, Stam et al. 2004). The reason for this is that, when integrated over the stellar disk, starlight of solar type stars will be virtually unpolarized (Kemp et al. 1987), while starlight that has been reflected by an exoplanet will generally be polarized, due to scattering and reflection processes in the planetary atmosphere and on the surface (if present). Polarimetry can thus enhance the contrast between a planet and its star by a factor of  $\sim 10^4 - \sim 10^5$  (Keller et al. 2010), and thus facilitate the direct detection of an exoplanet. Another advantage of polarimetry for exoplanet detection is that it enables the direct confirmation of a detection, since the degree and direction of polarization of a detected object will exclude it being a background star.

The real strength of polarimetry for exoplanet research is, however, that it cannot only be used for the direct detection of exoplanets, but also for the characterization of the physical properties of these planets. The reason is that the state of polarization of starlight that is reflected by a planet is very sensitive to the composition and structure of the planetary atmosphere and surface (if present) (see Hansen & Travis 1974, Hovenier et al. 2004, Mishchenko et al. 2010, and references therein). An early example of this application of polarimetry is the derivation of the composition and size distribution of the droplets forming the upper Venusian

clouds as well as the cloud top altitudes from Earth-based, disk-integrated Venus observations by Hansen & Hovenier (1974).

The application of polarization for the detection and characterization of exoplanets has been shown for gaseous exoplanets by e.g. Seager et al. (2000), Saar & Seager (2003), Stam (2003), Stam et al. (2004) and for terrestrial planets by Stam (2008). Note that in the first two papers, planets are considered that are too close to their star to be spatially resolved. The observable degree of polarization for these systems is thus the ratio of the polarized flux of the planet to the total flux of the star (plus that of the planet), and consequently, very small. In the latter three papers, the planet is assumed to be spatially resolvable from its star. In that case, the observable degree of polarization is thus the degree of polarization of the planet itself (apart from a contribution of unpolarized background starlight), which can be several tens of percents. In this Chapter, we will consider spatially resolvable planets. Our results can straightforwardly be applied to spatially unresolvable planets by scaling them with the stellar flux.

The simulations we present in this Chapter are useful for the design, development, and optimisation of instruments for the direct detection of exoplanets. Since the presence of water-clouds is not restricted to terrestrial planets, these can be instruments for the detection of gaseous planets and/or terrestrial planets, and both for ground- and space-based telescopes. An example of such an instrument is SPHERE (Spectro-Polarimetric High-contrast Exoplanet Research), a second generation planetfinder instrument for the European Southern Observatory's (ESO) Very Large Telescope (VLT). For SPHERE, first light is expected in 2012. SPHERE has broadband polarimetric capabilities in the I-band (0.6 - 0.9  $\mu\text{m}$ ). EPICS (Exoplanet Imaging Camera and Spectrograph) has been proposed as the planetfinder instrument for ESO's Extremely Large Telescope (ELT), and will also have a polarimeter to detect and characterize exoplanets. EPICS is still in its design and optimisation phase, and first light is expected not earlier than 2020. An example of a space telescope concept for exoplanet research that would be ideally suited to observe both the flux and the state of polarization of starlight that is reflected by exoplanets is the New Worlds Observer (NWO) that has been and will be proposed to NASA (Oakley & Cash 2009, Cash & New Worlds Study Team 2010). An example of a space-telescope with polarimetric capabilities for exoplanet research that has been proposed to the European Space Agency in response to its Cosmic Vision 2015-2020 call for a medium sized mission (M3), is Spectro-Polarimetric Imaging and Characterization of Exo-planetary Systems, or SPICES.

This Chapter is organized as follows. In Sect. 2.2, we give a general description of light, including polarization, and present the radiative transfer algorithm we use

2.3, we describe our model atmospheres and in Sect. 2.4 the flux and degree of polarization of light that has been singly scattered by the model cloud particles. In Sects. 2.5.1 and 2.5.2, we show the results of our numerical simulations of the flux and degree of polarization of reflected starlight for different cloud particle microphysical properties, and in Sect. 2.5.3, for different cloud top pressures. Finally, in Sects. 2.6 and 2.7 we summarise and discuss our results and future work.

## 2.2 Description of starlight that is reflected by an exoplanet

Light that has been reflected by an exoplanet can be fully described by a flux vector  $\pi\vec{F}$ , as follows:

$$\pi\vec{F} = \pi \begin{bmatrix} F \\ Q \\ U \\ V \end{bmatrix}, \quad (2.1)$$

where parameter  $\pi F$  is the total reflected flux, parameters  $\pi Q$  and  $\pi U$  describe the linearly polarized flux and parameter  $\pi V$  the circularly polarized flux (see e.g. Hansen & Travis 1974, Hovenier et al. 2004, Stam 2008). All four parameters are wavelength dependent and their dimensions are  $\text{W m}^{-2}\text{m}^{-1}$ . Parameters  $\pi Q$  and  $\pi U$  are defined with respect to the so-called *planetary scattering plane*, i.e. the plane through the centers of the planet, the host star and the observer (see Stam 2008).

The degree of polarization  $P$  is defined as the ratio of the polarized flux to the total flux, as follows:

$$P = \frac{\sqrt{Q^2 + U^2 + V^2}}{F}. \quad (2.2)$$

In case a planet is mirror-symmetric with respect to the planetary scattering plane, and for unpolarized incoming stellar light, the disk integrated fluxes  $\pi U$  and  $\pi V$  of the reflected light will equal zero due to symmetry (see Hovenier 1970) and we can use the following, alternative, definition of the degree of polarization that includes the direction of polarization

$$P_s = -\frac{Q}{F}. \quad (2.3)$$

For  $P_s > 0$  (i.e.  $Q < 0$ ), the light is polarized perpendicular to the reference plane, while for  $P_s < 0$  (i.e.  $Q > 0$ ) the light is polarized parallel to the reference plane.

The flux vector  $\pi\vec{F}$  of stellar light that has been reflected by a spherical planet with radius  $r$  at a distance  $d$  from the observer ( $d \gg r$ ) is given by (Stam et al. 2006a)

$$\pi\vec{F}(\lambda, \alpha) = \frac{1}{4} \frac{r^2}{d^2} \vec{S}(\lambda, \alpha) \pi\vec{F}_0(\lambda). \quad (2.4)$$

Here,  $\lambda$  is the wavelength of the light and  $\alpha$  the planetary phase angle, i. e. the angle between the star and the observer as seen from the center of the planet. Furthermore,  $\vec{S}$  is the  $4 \times 4$  planetary scattering matrix (Stam et al. 2006a) and  $\pi\vec{F}_0$  is the flux vector of the incident stellar light. For a solar type star, the stellar flux can be considered to be unpolarized when integrated over the stellar disk (Kemp et al. 1987). Further assuming that the stellar light is unidirectional, we can thus describe  $\pi\vec{F}_0$  as (see Eq. 5.1)

$$\pi\vec{F}_0(\lambda) = \pi F_0(\lambda) \vec{1}, \quad (2.5)$$

with  $\pi F_0$  the flux of the stellar light that is incident on the planet measured perpendicular to the direction of incidence, and  $\vec{1}$  the unit column vector.

For unpolarized incident stellar light (see Eq. 2.5) and for a planet that is mirror-symmetric with respect to the planetary scattering plane, the degree of polarization  $P_s$  (Eq. 2.3) of the light that is reflected by the planet depends on only two elements of the scattering matrix, as follows

$$P_s(\lambda, \alpha) = -\frac{b_1(\lambda, \alpha)}{a_1(\lambda, \alpha)} \quad (2.6)$$

(for a derivation see Stam 2008). Since the degree of polarization is a relative measure, it has no dependence on planetary and stellar radii, distances, nor on the incident stellar flux.

In this Chapter, we present numerically simulated flux and polarization spectra of planets that are completely covered by water clouds as functions of the planetary phase angle  $\alpha$ . Even though such a model is probably not very realistic, in this first study we will use it in order to limit the number of parameters we need to study in our models, and to get some first idea on the important features we need to investigate in planetary signals. We assume that the ratio of the planetary radius  $r$  and the distance to the observer  $d$  is equal to one, and that the incident stellar flux  $\pi F_0$  is equal to  $1 \text{ W m}^{-2} \text{ m}^{-1}$ . The hence normalized flux  $\pi F_n$  that is reflected by a planet is thus given by

$$\pi F_n(\lambda, \alpha) = \frac{1}{4} a_1(\lambda, \alpha) \quad (2.7)$$

(see Stam 2008), and corresponds to the planet's geometric albedo  $A_G$  if  $\alpha = 0^\circ$  ( $A_G$  is defined as the ratio of the total flux  $\pi F$  that is reflected by the planet at  $\alpha = 0^\circ$ , to the flux  $\pi F_L$  that is reflected by a Lambertian surface subtending the same solid angle on the sky). Our normalized fluxes  $\pi F_n$  can straightforwardly be scaled for any given planetary system using Eq. 4.4 and inserting the appropriate values for  $r$ ,  $d$  and  $\pi F_0$ . As mentioned above, the degree of polarization  $P_s$  is independent of  $r$ ,  $d$  and  $\pi F_0$ , and will thus not require any scaling.

To calculate the planetary scattering matrix elements  $a_1$  and  $b_1$  of the reflected stellar light, we employ the algorithm described in Stam et al. (2004), which consists of an efficient and accurate adding–doubling algorithm (de Haan et al. 1987) in combination with a fast, numerical, disk integration algorithm, to calculate the radiative transfer in the locally plane–parallel planetary atmosphere, and to integrate the reflected light across the illuminated and visible part of the planetary disk.

### 2.3 Our model atmospheres

The model planetary atmospheres we use in our numerical simulations are composed of stacks of horizontally homogeneous and locally plane–parallel layers, which contain gas molecules and, optionally, cloud particles. We create vertically inhomogeneous atmospheres simply by stacking different, homogeneous layers. Each atmosphere is bounded below by a flat, homogeneous surface. We base our atmospheric temperature and pressure profiles on representative ones of the Earth's atmosphere (McClatchey et al. 1972). Here, we use only four atmospheric layers (see Table 2.1 for the pressures and temperatures at the tops of these layers) and a black planetary surface. The molecular or Rayleigh scattering optical thickness, of each atmospheric layer and its spectral variation is calculated as described in Stam (2008) assuming an atmospheric gas composition of the model atmospheres that is similar to that of the Earth. For our simulations of the flux and polarization spectra, we focus on the continuum, and we ignore absorption by atmospheric gases (such as  $O_2$ ,  $H_2O$  and  $O_3$ ). Even though we use pressure and temperature profiles and a gas composition that are typical for an Earth–like planet, most of our results are also applicable to other planets, e.g. gas giants with high altitude water clouds.

We will use a clear model atmosphere, i.e. without clouds, and cloudy model atmospheres. In the latter, one of the atmospheric layers contains cloud particles in addition to the gas molecules. To study the dependence of the flux and degree of polarization of the starlight that is reflected by the model planet on the altitude of

**Table 2.1:** The altitude (in km), pressure (in bar), and temperature (in K) at the bottom and top of each layer of our model atmosphere (McClatchey et al. 1972).

Altitude	pressure	temperature
0.0	1.013	294.0
2.0	0.802	290.0
3.0	0.710	279.0
4.0	0.628	273.0
100.0	$3.0 \cdot 10^{-7}$	210.0

the top of the cloud layer, we will use the following three cases: a low cloud layer, with its top at an ambient pressure of 0.802 bar (corresponding to an altitude of 2 km on Earth), a middle cloud layer, with its top at 0.710 bar (3 km on Earth), and a high cloud layer, with its top at 0.628 bar (4 km on Earth). Unless stated otherwise the geometrical thickness of the cloud layer is 1 km.

Optical thicknesses of clouds on Earth show a huge variation on daily and monthly timescales and from place to place. In particular, the optical thickness in completely cloudy cases can reach values up to 40 (van Deelen et al. 2008) or more. The optical thickness  $b$  of our cloud layers is chosen to range between 0.5 and 60 (at  $\lambda = 0.55 \mu\text{m}$ ). Our standard cloud layer has an optical thickness of 10 (at  $\lambda = 0.55 \mu\text{m}$ ), which appears to be an average value. The spectral variation of the cloud layer's optical thickness depends on the microphysical properties of the cloud particles, such as their composition, shape and size (see below).

Our model cloud layers are composed of liquid, spherical water particles. Water cloud observations on Earth show a large variation in droplet sizes that is attributed to, amongst others, a variation in the number density and composition of cloud condensation nuclei (Han et al. 1994, Martin et al. 1994, Segal & Khain 2006). In particular, typical cloud particle radii range from about  $5 \mu\text{m}$  to  $15 \mu\text{m}$ , with a global mean value of about  $8.5 \mu\text{m}$  above continental areas, and  $11.8 \mu\text{m}$  above maritime areas (Han et al. 1994). On the lower limit, sizes down to  $2 \mu\text{m}$  have been reported from satellite measurements (Minnis et al. 1992), and on the upper limit, sizes up to  $25 \mu\text{m}$  (Goloub et al. 2000).

We describe the sizes of our cloud particles by a standard size distribution (Hansen & Travis 1974), as follows

$$n(r) = C r^{(1-3v_{\text{eff}})/v_{\text{eff}}} e^{-r/v_{\text{eff}}r_{\text{eff}}}, \quad (2.8)$$

where  $C$  is a normalisation constant,  $n(r)dr$  is the number of particles with radii between  $r$  and  $r+dr$  per unit volume, and  $r_{\text{eff}}$  and  $v_{\text{eff}}$  are the effective radius

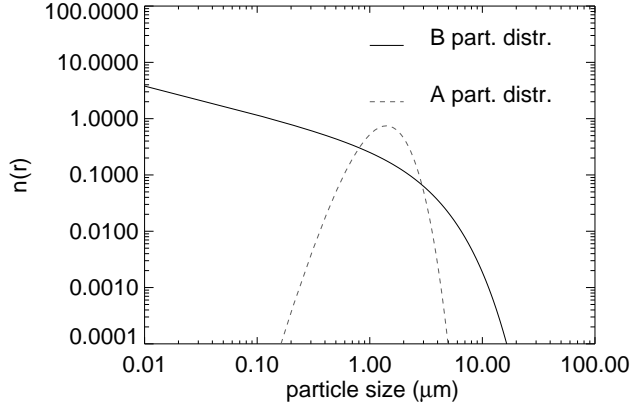


**Figure 2.1:** Particle size distributions (see Eq. 2.8) for model A particles ( $r_{\text{eff}} = 2.0 \mu\text{m}$ ,  $v_{\text{eff}} = 0.1$ ; red, dashed line) and model B particles ( $r_{\text{eff}} = 6.0 \mu\text{m}$ ,  $v_{\text{eff}} = 0.4$ ; black, solid line). Each size distribution has been normalised such that the integral over all sizes equals 1.

and variance, respectively (see Hansen & Travis 1974). The units of  $r_{\text{eff}}$  are [ $\mu\text{m}$ ], while  $v_{\text{eff}}$  is dimensionless.

The scattering properties of particles often depend strongly on the ratio of the radius of the particles to the wavelength of the light. This so-called effective size parameter,  $x_{\text{eff}}$ , that will be used later in this Chapter, is defined as

$$x_{\text{eff}} = \frac{2\pi r_{\text{eff}}}{\lambda} \quad (2.9)$$

(see Hansen & Travis 1974). For  $x_{\text{eff}} \ll 1$ , the scattering is usually referred to as Rayleigh scattering, and for  $x_{\text{eff}} \gg 1$ , we get into the regime where light scattering can be described with geometrical optics.

Our cloud layers are composed of either small model A particles with  $r_{\text{eff}} = 2.0 \mu\text{m}$  and  $v_{\text{eff}} = 0.1$  (Stam 2008), or larger model B particles with  $r_{\text{eff}} = 6.0 \mu\text{m}$  and  $v_{\text{eff}} = 0.4$ . The latter are similar to those used by van Diedenhoven et al. (2007), who consider this to represent an average terrestrial water cloud. Figure 2.1 shows the size distributions of the particles of the two standard models used further in this Chapter (A and B particles). To study the influence of a size distribution's

**Table 2.2:** The effective radius  $r_{\text{eff}}$  (in  $\mu\text{m}$ ) and variance  $v_{\text{eff}}$  of the standard size distributions (see Hansen & Travis 1974, and Eq. 15) that describe our model cloud particles.

Particle	$r_{\text{eff}}$	$v_{\text{eff}}$
A	2.0	0.1
A <sub>2</sub>	2.0	0.4
B	6.0	0.4
B <sub>2</sub>	6.0	0.1

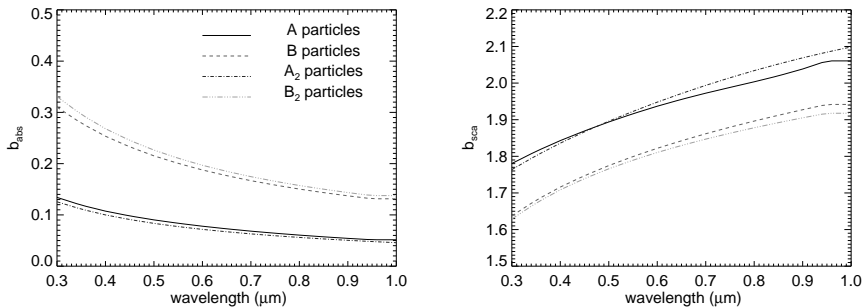


**Figure 2.2:** Spectral variation of the absorption (left panel) and scattering (right panel) optical thicknesses,  $b_{\text{abs}}$  and  $b_{\text{sca}}$ , of cloud layers composed of the following model particles (see Table 2.2): A ( $r_{\text{eff}} = 2.0 \mu\text{m}$ ,  $v_{\text{eff}} = 0.1$ ; black, solid line), A<sub>2</sub> ( $r_{\text{eff}} = 2.0 \mu\text{m}$ ,  $v_{\text{eff}} = 0.4$ ; blue, dashed–dotted line), B ( $r_{\text{eff}} = 6.0 \mu\text{m}$ ,  $v_{\text{eff}} = 0.4$ ; red, dashed line), and B<sub>2</sub> ( $r_{\text{eff}} = 6.0 \mu\text{m}$ ,  $v_{\text{eff}} = 0.1$ ; orange, dashed–triple–dotted line). The total optical thickness ( $b = b_{\text{sca}} + b_{\text{abs}}$ ) of each cloud layer is 2.0 at  $\lambda = 0.55 \mu\text{m}$ .

effective variance  $v_{\text{eff}}$  on the reflected light, we will also use model A<sub>2</sub> particles with  $r_{\text{eff}} = 2.0 \mu\text{m}$  and  $v_{\text{eff}} = 0.4$ , and model B<sub>2</sub> particles with  $r_{\text{eff}} = 6.0 \mu\text{m}$  and  $v_{\text{eff}} = 0.1$  (see Table 2.2).

The real part of the refractive index of water in the wavelength region of our interest is slightly wavelength dependent. It varies from 1.344 at  $\lambda = 0.4 \mu\text{m}$ , to 1.320 at  $1.0 \mu\text{m}$  (Daimon & Masumura 2007, van Diedenhoven et al. 2007). The imaginary part of the refractive index is small but varies strongly (Pope & Fry 1997), from about  $10^{-8}$  at  $0.3 \mu\text{m}$ , to about  $10^{-5}$  at  $1.0 \mu\text{m}$ , with a minimum of  $8 \times 10^{-10}$  at  $0.5 \mu\text{m}$ . We use a constant refractive index that is equal to  $1.335 \pm 0.00001i$ . We checked that our results are virtually insensitive to the assumption of a constant value of the refractive index.

Given the wavelength, refractive index, effective radius  $r_{\text{eff}}$  and variance  $v_{\text{eff}}$ , we calculate the cloud particles' extinction cross-section, single scattering albedo, and the expansion coefficients of the single scattering matrix in generalized spherical functions (see Hovenier et al. 2004) using Mie theory (van de Hulst 1957, de Rooij & van der Stap 1984). With the hence obtained extinction cross-sections, we calculate the cloud layer's optical thickness at wavelengths other than  $0.55 \mu\text{m}$ . Figure 2.2 shows the spectral variation of the absorption and scattering optical thicknesses of four cloud layers, each with a total optical thickness of 2.0 at  $\lambda = 0.55 \mu\text{m}$ , that are composed of the model A,  $A_2$ , B and  $B_2$  particles, respectively. As can be seen in the figure, the effective variance  $v_{\text{eff}}$  plays only a minor role in determining the cloud's scattering and absorption optical thicknesses.

## 2.4 Single scattering properties of water cloud particles

The degree of polarization of the starlight that is reflected by a planet is very sensitive to the single scattering properties of the atmospheric particles (see e.g. Hansen & Travis 1974). The reason for this is that due to the generally low degree of polarization of multiple-scattered light, the main angular features observed in a polarized planetary signal will be due to single scattered light. The contribution of the multiple scattered light to the signal is mostly to decrease the overall degree of polarization, not to change the shape or angular distribution of the features. Thus, in order to understand the features observed in starlight that is reflected by a planet, as presented in Sect. 2.5, knowledge of the single scattered light is essential.

In this section, we therefore present and discuss the flux and degree of polarization of incident unpolarized light  $P_s$  that is singly scattered by our model liquid water cloud particles as functions of the single scattering angle  $\Theta$  and the wavelength  $\lambda$ . The flux as a function of  $\Theta$  is usually referred to as the (flux) *phase function*, and we will refer to  $P_s$  as a function of  $\Theta$  as the *polarized phase function*.

Figure 2.3 shows the flux and  $P_s$  of the four model cloud particles A, B,  $A_2$  and  $B_2$  (see Table 2.2 for their sizes) as functions of the scattering angle  $\Theta$  at  $\lambda = 0.55 \mu\text{m}$ . For comparison, we have also added the phase function of the gas molecules (Rayleigh scattering) using an Earth-like depolarization factor, i.e. 0.028 (Bates 1984). The flux phase functions are normalized such that their average over all scattering directions equals unity; they thus do not include the particles' single scattering albedo.

As can be seen in Fig. 2.3,  $P_s$  of light that is singly scattered by the gas molecules and by the model cloud particles equals zero at  $\Theta = 0^\circ$  (forward scat-

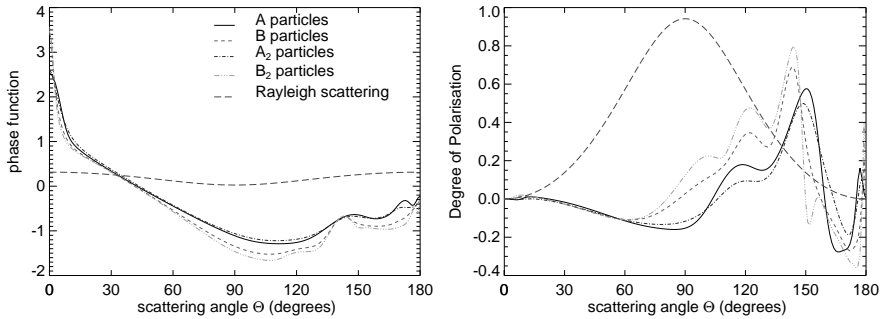


**Figure 2.3:** Phase function on a logarithmic scale (left panel) and degree of polarization  $P_s$  (right panel) for incident unpolarized light at  $\lambda = 0.55 \mu\text{m}$  that is singly scattered by our model water cloud particles (see Table 2.2) as functions of the scattering angle  $\Theta$ : model A (black, solid lines), model B (red, dashed lines), model  $A_2$  (blue, dashed-dotted lines) and model  $B_2$  (orange, dashed-triple-dotted lines). For comparison, the phase function and  $P_s$  are also shown for gas molecules (i.e. Rayleigh scattering) (purple, long-dashed lines).

tering) and  $180^\circ$  (backward scattering). The reason for this is that the incoming light is unpolarized and that at these scattering angles, the scattering process is symmetric with respect to the incoming and the scattered light. The phase function and  $P_s$  of Rayleigh scattered light is smooth and symmetric around  $\Theta = 90^\circ$ . The maximum value of  $P_s$  of this light is 0.94 (i.e. 94 %).

The flux phase functions of all four types of cloud particles have a strong peak in the forward scattering direction due to light that is diffracted by the particles and the so-called glory in the backscattering direction (cf. Hansen & Travis 1974). The polarization phase functions of the cloud particles have several interesting features. In particular, for each particle type,  $P_s$  changes sign (thus direction), several times between  $\Theta = 0^\circ$  and  $180^\circ$ . For  $\Theta \lesssim 50^\circ$ , the angular features of  $P_s$  appear to be insensitive to the particle size, while for larger scattering angles, the features depend clearly on  $r_{\text{eff}}$  and  $v_{\text{eff}}$ .

Between  $\Theta = 135^\circ$  and  $150^\circ$ , the phase functions of all four types of cloud particles show a local maximum that is usually referred to as the (primary) rainbow, which is formed by light that has been reflected once inside the particles (see van de Hulst 1957, Hansen & Travis 1974). These rainbows are clear indicators of the spherical shape of the scattering particles, and their angular position depends strongly on the composition (refractive index) of the scattering particles

(see Hansen & Travis 1974) and slightly on  $r_{\text{eff}}$  of the particles (see below). While especially for the small cloud particles (models A and A<sub>2</sub>), the primary rainbow is hardly visible in the flux phase function (see Fig. 2.3), in  $P_s$  it is the strongest and most prominent angular feature for each of the four cloud particle types. Note that the rainbows that are seen in the Earth's sky during showers are not formed in cloud particles, but in raindrops. On Earth, raindrops have radii on the order of millimeters, corresponding to  $x_{\text{eff}} \gg 1000$  at visible wavelengths.

For  $r_{\text{eff}} = 2 \mu\text{m}$  (particles A and A<sub>2</sub>), the rainbow is located at  $\Theta \approx 148^\circ$ . For  $r_{\text{eff}} = 6 \mu\text{m}$  (particles B and B<sub>2</sub>), the rainbow is more pronounced and shifted to slightly smaller scattering angles, i.e. to  $\Theta \approx 143^\circ$ . The strength of the primary rainbow in  $P_s$  depends on  $r_{\text{eff}}$  and on  $v_{\text{eff}}$ ; the smaller  $r_{\text{eff}}$ , the smaller the maximum value of  $P_s$  in the primary rainbow, and the smaller  $v_{\text{eff}}$ , the larger this maximum value. In particular, for  $r_{\text{eff}} = 2.0 \mu\text{m}$  and  $v_{\text{eff}} = 0.1$  (model A),  $P_s$  of the primary rainbow is 0.58 (58 %), while for  $r_{\text{eff}} = 2.0 \mu\text{m}$  and  $v_{\text{eff}} = 0.4$  (A<sub>2</sub>), it is 0.50. For  $r_{\text{eff}} = 6.0 \mu\text{m}$  and  $v_{\text{eff}} = 0.1$  (B),  $P_s$  of the primary rainbow is 0.80, and for  $r_{\text{eff}} = 6.0 \mu\text{m}$  and  $v_{\text{eff}} = 0.4$  (B<sub>2</sub>),  $P_s = 0.69$ . The scattering angle of the primary rainbow ( $\Theta$  where  $P_s$  is maximum) depends mostly on  $r_{\text{eff}}$ : at  $\lambda = 0.55 \mu\text{m}$ , the angle is  $150^\circ$  for  $r_{\text{eff}} = 2.0 \mu\text{m}$  (A and A<sub>2</sub>) and  $143^\circ$  for  $r_{\text{eff}} = 6.0 \mu\text{m}$  (B and B<sub>2</sub>).

For the large particles, a secondary peak in the flux phase function is visible around  $\Theta \approx 120^\circ$ . This peak is the secondary rainbow, which is formed by light that has been reflected twice inside the particles. While in the phase function this rainbow is hardly visible, and only for the largest particles,  $P_s$  clearly shows the secondary rainbow for all four cloud particle types: for  $r_{\text{eff}} = 6.0 \mu\text{m}$  (B and B<sub>2</sub>) around  $\Theta = 120^\circ$ , and for the smaller particles at slightly smaller angles. Noteworthy is the minor peak around  $155^\circ$  in  $P_s$  of the large B<sub>2</sub> particles; this is a supernumerary arc (see e. g. Dave 1969). For the same particles we see a peak around  $\Theta \sim 100^\circ$ , which could also be a supernumerary arc. Supernumerary arcs are interference features, which explains their washing out with increasing  $v_{\text{eff}}$ .

The effects of  $r_{\text{eff}}$  and  $v_{\text{eff}}$  on the singly scattered light are even more clear from Figs. 2.4 and 2.5, which show the scattered flux and  $P_s$  as functions of  $\Theta$  and the effective size parameter  $x_{\text{eff}}$  (cf. Eq. 2.9) for  $v_{\text{eff}} = 0.1$  (A and B<sub>2</sub>) and  $v_{\text{eff}} = 0.4$  (A<sub>2</sub> and B), respectively. Similar graphs for other size distributions and refractive indices can be found in, for example, Hansen & Travis (1974) and Hansen & Hovenier (1974). The curves shown in Fig. 2.3 correspond to horizontal cuts in Figs. 2.4 and 2.5, at  $x_{\text{eff}} = 23$  ( $r_{\text{eff}} = 2 \mu\text{m}$  and  $\lambda = 0.55 \mu\text{m}$ ; particles A and A<sub>2</sub>) and  $x_{\text{eff}} = 69$  ( $r_{\text{eff}} = 6 \mu\text{m}$  and  $\lambda = 0.55 \mu\text{m}$ ; particles B and B<sub>2</sub>), respectively.

Comparing the graphs of the flux phase functions in Figs. 2.4 and 2.5, it is

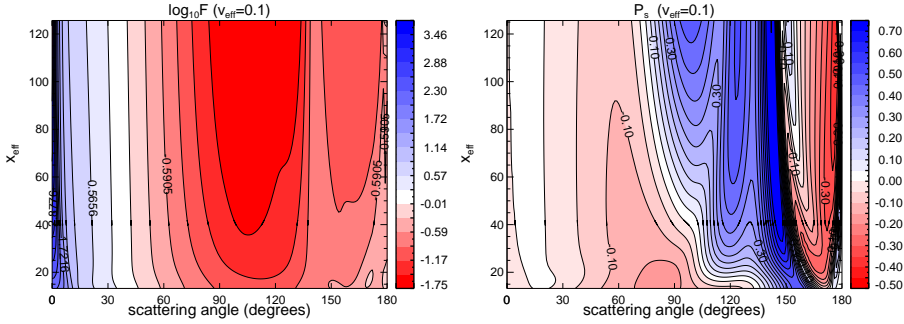


**Figure 2.4:** Phase function on a logarithmic scale (left panel) and degree of polarization  $P_s$  (right panel) for incident unpolarized, singly scattered light as functions of the scattering angle  $\Theta$  and the effective size parameter  $x_{\text{eff}} = 2\pi r_{\text{eff}}/\lambda$  for model cloud particles with  $v_{\text{eff}} = 0.1$ , i.e. models A and B<sub>2</sub>. For model A (with  $r_{\text{eff}} = 2.0 \mu\text{m}$ ), the curves shown in Fig. 2.3 correspond to  $x_{\text{eff}} = 23$ , while for model B<sub>2</sub> (with  $r_{\text{eff}} = 6.0 \mu\text{m}$ ), they correspond to  $x_{\text{eff}} = 69$ .

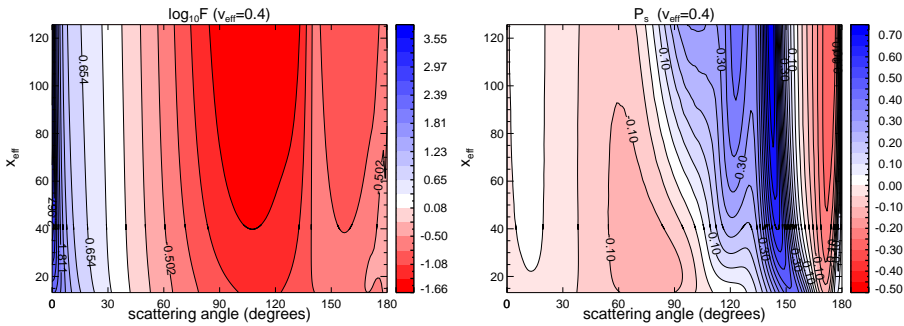


**Figure 2.5:** Similar to Fig. 2.4, except for particles with  $v_{\text{eff}} = 0.4$ , i.e. models A<sub>2</sub> and B. For model A<sub>2</sub> (with  $r_{\text{eff}} = 2.0 \mu\text{m}$ ), the curves shown in Fig. 2.3 correspond to  $x_{\text{eff}} = 23$ , while for model B (with  $r_{\text{eff}} = 6.0 \mu\text{m}$ ), they correspond to  $x_{\text{eff}} = 69$ .

clear that the phase function depends mostly on  $x_{\text{eff}}$ , thus on the ratio  $2\pi r_{\text{eff}}/\lambda$ , and that it is not very sensitive to  $v_{\text{eff}}$ , which mostly determines the smoothness of the phase function, i. e. the larger  $v_{\text{eff}}$ , the more subdued the angular variation in the phase function (for a given  $x_{\text{eff}}$ , see Hansen & Travis 1974). Additionally, we see that  $P_s$  appears to be somewhat more sensitive to  $v_{\text{eff}}$  than the flux phase

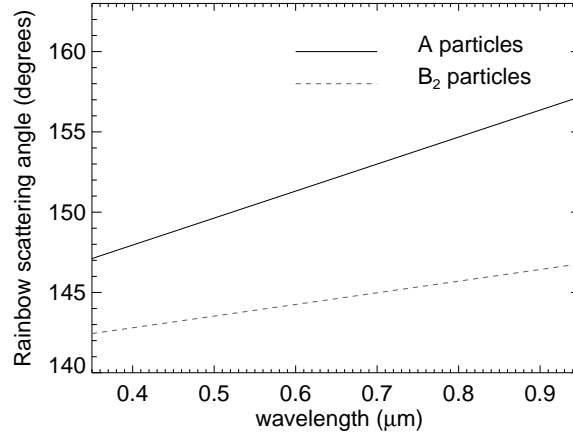


**Figure 2.6:** Scattering angle  $\Theta$  where the primary rainbow in  $P_s$  occurs as a function of the wavelength for the model A ( $r_{\text{eff}} = 2.0 \mu\text{m}$ ) and B<sub>2</sub> ( $r_{\text{eff}} = 6.0 \mu\text{m}$ ) particles.

function, but the overall appearance of  $P_s$  is the same for the two values of  $v_{\text{eff}}$ . In particular, for  $\Theta < 20^\circ$ , both figures show a peninsula with small values of  $P_s$ . As can also be seen in Hansen & Travis (1974) and Hansen & Hovenier (1974) the shape of this peninsula is sensitive to  $v_{\text{eff}}$  for small values of  $x_{\text{eff}}$ .

In both Figs. 2.4 and 2.5, the primary rainbow (just below  $\Theta = 150^\circ$ ) is only a slight crest in the flux phase functions, but by far the strongest feature in the polarization phase functions. The strength of the polarized primary rainbow increases with increasing  $x_{\text{eff}}$ . In other words, for particles with a given  $r_{\text{eff}}$ , the strength of the rainbow increases towards the blue, and/or at a given wavelength, the strength of the rainbow increases with increasing  $r_{\text{eff}}$ . Interesting to note is that for small values of  $x_{\text{eff}}$  (i.e.  $\leq 60$ ), the primary rainbow shifts to larger values of  $\Theta$  with decreasing  $x_{\text{eff}}$ , i.e. for a given effective particle radius  $r_{\text{eff}}$ , the rainbow shifts to larger values of  $\Theta$  towards the red. Consequently, when observed with polarimetry, the rainbow in visible light that is scattered by small water cloud particles should be inverted in colour, compared to the rainbow of light that is scattered by water raindrops (this can not be observed in the flux since the rainbow is virtually unobservable in the flux of light scattered by small cloud particles).

This colour inversion is shown more clearly in Fig. 2.6, where the scattering

angle of the primary rainbow in  $P_s$  is plotted as a function of  $\lambda$  for the model A and B<sub>2</sub> particles. For the smallest particles, the rainbow angle increases from 147° at  $\lambda = 0.3 \mu\text{m}$ , to 157° at  $\lambda = 1.0 \mu\text{m}$ . From these and other numerical simulations (not shown) it appears that  $d\Theta/d\lambda$  decreases with increasing  $r_{\text{eff}}$  until  $r_{\text{eff}} \approx 20 \mu\text{m}$ . Indeed, for particles with  $x_{\text{eff}} \sim 100$  whitish rainbows (so-called *fogbows*), are observed in flux (Adam 2002). For much larger particles, such as rain drops,  $d\Theta/d\lambda$  becomes negative and decreases further with increasing  $r_{\text{eff}}$ . We checked that the behavior of  $d\Theta/d\lambda$  that we calculated is not affected by our choice of using a wavelength independent refractive index, nor by our choice of the particle size distribution.

Our single scattering results suggest that in particular observing the dispersion of the primary rainbow in polarization would be a useful tool in the retrieval of cloud particle shapes and sizes in exoplanetary atmospheres. To evaluate the usefulness of this tool, numerical simulations of multiple scattered light are required. Results of such simulations are presented and discussed in Sect. 2.5.

## 2.5 Light that is reflected by planets

In the previous section we have presented the single scattering phase functions of our model cloud particles. Here, we present the normalised flux  $\pi F_n$  and the degree of polarization  $P_s$  of (single and multiple scattered) starlight that is reflected by a planet as a whole, thus integrated over the illuminated and visible part of the planetary disk. We show the dependence of  $\pi F_n$  and  $P_s$  on the cloud optical thickness in Sect. 2.5.1, on the size of the cloud particles in Sect. 2.5.2, and on the cloud top pressure in Sect. 2.5.3. We show  $\pi F_n$  and  $P_n$  as functions of the planetary phase angle  $\alpha$ , which equals  $180^\circ - \Theta$ , with  $\Theta$  the single scattering angle.

### 2.5.1 The effects of the cloud optical thickness

Figure 2.7 shows  $\pi F_n$  and  $P_s$  of light reflected by cloudy planets as functions of the phase angle  $\alpha$ . At  $\alpha = 0^\circ$ , the planet's illuminated side is fully visible, and at  $\alpha = 180^\circ$ , we see the planet's night side. The cloud layer on each planet is composed of model A particles (see Table 2.2), and the cloud top pressure is 0.628 bar (on Earth this would correspond to a cloud top altitude of 4 km, see Table 2.1). At  $0.55 \mu\text{m}$ , the molecular scattering optical thickness of the whole model atmosphere is 0.098, and that of the gaseous atmosphere above the cloud 0.06. In the figure, the cloud optical thickness varies from 0 (i.e. no cloud at all) to 60 (at  $\lambda = 0.55 \mu\text{m}$ ). Note that a cloud optical thickness of 60 appears to

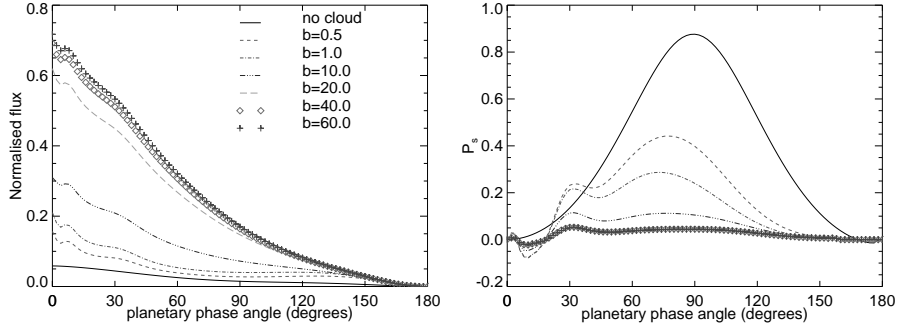


**Figure 2.7:** Normalised flux  $\pi F_n$  (left panel) and  $P_s$  (right panel) at  $\lambda = 0.55 \mu\text{m}$ , as functions of the planetary phase angle  $\alpha$  for model planets with a cloudfree atmosphere (black solid line) and with atmospheres containing a cloud layer ranging from 3 to 4 km, composed of model A cloud particles, with the following cloud optical thicknesses  $b$  (at  $\lambda = 0.55 \mu\text{m}$ ): 0.5 (red, dashed lines), 1.0 (green, dash-dotted lines), 10.0 (blue, dash-triple-dotted lines), 20.0 (orange, long-dashed lines), 40.0 (pink, diamond lines), and 60.0 (purple, cross lines).

be very large for a 1 km thick cloud. We have included this large value in our simulations for the purpose of comparison.

As can be seen in Fig. 2.7, the quasi-monochromatic geometric albedo  $A_G$  of the cloudfree planet is as small as 0.063, which is due to the black surface and the small atmospheric (molecular) scattering optical thickness. The normalized flux  $\pi F_n$  decreases smoothly with  $\alpha$ . The degree of polarization  $P_s$  of the cloudfree planet is zero at  $\alpha = 0^\circ$  (due to symmetry) and  $180^\circ$  (due to first order scattering, see Hovenier & Stam (2007)) (cf. Fig. 2.3). In between these phase angles,  $P_s$  varies smoothly with  $\alpha$ , and is positive except for  $\alpha \gtrsim 168^\circ$ . These negative values, which indicate that the light is polarized parallel instead of perpendicular to the reference plane (as it is at the smaller phase angles), are due to second order scattered light. The maximum degree of polarization of the cloudfree planet is 0.87 (87%) and occurs at  $\alpha = 90^\circ$ .

Figure 2.7 also shows that  $\pi F_n$  generally increases with increasing cloud optical thickness, and converges rapidly for  $b \gtrsim 40$ . With such large optical thicknesses, the cloud layer appears to be semi-infinite, making  $\pi F_n$  insensitive to further increases of  $b$ . The sensitivity of  $\pi F_n$  to  $b$  decreases with increasing phase angle, and in particular for  $\alpha > 150^\circ$ ,  $\pi F_n$  hardly changes with  $b$ , since in this limb viewing geometry most of the reflected starlight has been scattered in the layers

above the cloud layer or by the highest cloud particles and did not penetrate deep into the layer.

The normalized flux  $\pi F_n$  shows a few angular features. At  $\alpha \sim 30^\circ$  ( $\Theta \sim 150^\circ$ ), the primary rainbow (cf. Fig. 2.3) is slightly visible, and the local maximum in  $\pi F_n$  at  $\alpha \sim 8^\circ$  can be traced back to the cloud particles' single scattering feature at  $\Theta \approx 170^\circ$  in Fig. 2.3.

The degree of polarization  $P_s$  of the cloudy planets is a mixture of the degree of polarization of light that is scattered by the atmospheric gases and of light that is scattered by the cloud particles (and includes, of course, light that has been scattered by both). In particular, for an atmosphere with a cloud with a total optical thickness  $b$  of only 0.5 (at  $\lambda = 0.55 \mu\text{m}$ ), the maximum  $P_s$  still clearly shows the angular features of a Rayleigh scattering atmosphere, with a maximum of 0.46 around  $\alpha \approx 78^\circ$ . At most phase angles,  $|P_s|$  decreases with increasing value of  $b$  due to the increasing contribution of light with a low degree of polarization that has been multiple scattered within the cloud layer. The degree of polarization converges rapidly for  $b \gtrsim 20$ . It does not necessarily converge to zero, because even for the thickest cloud,  $P_s$  is determined by the degree of polarization of light that has been singly scattered within the upper parts of the cloud and the nearly unpolarized flux from the deeper parts, which converges for large values of  $b$ .

Indeed, even for optically thick clouds,  $P_s$  of the planet shows the traces of the degree of polarization of the singly scattered light. For example, the negative values of  $P_s$  of the cloudy planets around  $\alpha \approx 10^\circ$  can be traced back to the single scattering feature of the cloud particles at  $\Theta \approx 170^\circ$  (see Fig. 2.3). The maximum in  $P_s$  around  $\alpha \approx 30^\circ$  is the primary rainbow. Increasing  $b$  decreases  $P_s$  of this rainbow because multiple scattering increases the unpolarized total flux: for  $b = 0.5$ ,  $P_s = 0.24$  (24%), while for  $b = 20$ ,  $P_s = 0.06$  (6%). The detection of the primary rainbow in starlight that is reflected by an exoplanet would indicate that the cloud particles are made of liquid water (this was also pointed out by e.g. Hansen & Travis 1974, Liou & Takano 2002, except for individual clouds not for whole planets), and if the phase angle of the rainbow could be determined accurately, it would hold information on the particle sizes. For cloudy exoplanets (with a disk integrated signal), this rainbow was also discussed by Bailey (2007) (whose radiative transfer calculations do not include multiple scattering), and clearly shows up in the numerical simulations (that do include multiple scattering) by Stam (2008). The latter uses only the smallest of our cloud particle sizes (i.e. with  $r_{\text{eff}} = 2 \mu\text{m}$ ) and a relatively thick cloud layer ( $b = 10$  at  $\lambda = 0.55 \mu\text{m}$ ), which results in a rather subdued rainbow ( $P_s = 0.10$  at  $\lambda = 0.44 \mu\text{m}$ ). The secondary rainbow that was seen in Fig. 2.3, does not show up in Fig. 2.7, because for small cloud optical thicknesses  $b$ , it vanishes in the contribution of the Rayleigh scattered

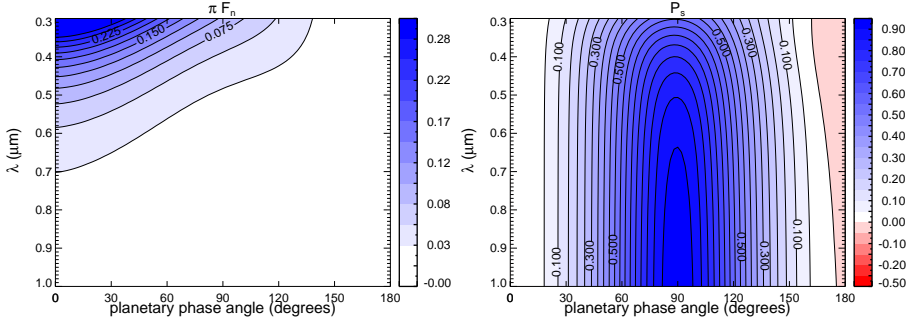


**Figure 2.8:** Normalized flux  $\pi F_n$  (left panel) and  $P_s$  (right panel) as functions of the planetary phase angle  $\alpha$  and wavelength  $\lambda$  for the cloudfree model planet.

light, while for large values of  $b$ , it is suppressed by nearly unpolarized, multiple scattered light.

The normalized flux and degree of polarization of the reflected starlight depend not only on phase angle  $\alpha$ , but also on wavelength  $\lambda$ . In Fig. 2.8 we show  $\pi F_n$  and  $P_s$  of light that is reflected by a cloudfree ( $b = 0$ ) planet as functions of  $\alpha$  and  $\lambda$ . The atmospheric molecular scattering optical thickness ranges from 1.1 at  $\lambda = 0.3 \mu\text{m}$  to 0.009 at  $\lambda = 1.0 \mu\text{m}$ . Clearly,  $\pi F_n$  is largest at the smallest values of  $\lambda$  and  $\alpha$ , where the atmospheric optical thickness is largest and where most of the illuminated hemisphere of the planet is visible, and decreases smoothly with increasing  $\lambda$  and  $\alpha$ . The degree of polarization  $P_s$  shows the strong maximum around  $\alpha = 90^\circ$  that is due to Rayleigh scattering. The general increase of  $P_s$  with  $\lambda$  is due to the decrease of the atmospheric optical thickness, and hence the multiple scattering which usually decreases  $P_s$ , with  $\lambda$ . The decrease of the atmospheric optical thickness also explains why the phase angle region where  $P_s$  is negative narrows with increasing  $\lambda$ : the smaller the optical thickness, the longer the path through the atmosphere, and hence the larger the phase angle required to have enough second order scattered light to change the sign of  $P_s$ .

Figure 2.9 is similar to Fig. 2.8 except for an atmosphere that contains a cloud layer composed of model A particles, with  $b = 10.0$  (at  $\lambda = 0.55 \mu\text{m}$ ), and with its top at 0.628 bar. The cloud layer strongly increases  $\pi F_n$ , except at large values of  $\alpha$ , where the observed light has not penetrated deep enough into the atmosphere to encounter the cloud. The features seen at  $\alpha \approx 10^\circ$  were also seen in Fig. 2.7, and trace back to the single scattering features at  $\Theta \approx 170^\circ$  in Fig. 2.3. Like in Fig. 2.7, the primary rainbow is hardly visible in the fluxes shown in Fig. 2.9.

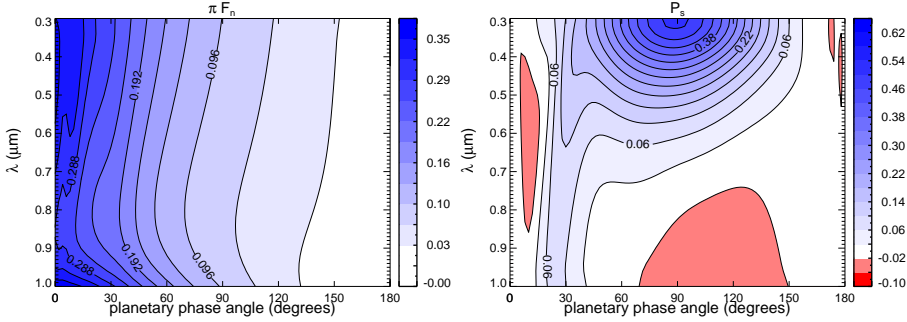


**Figure 2.9:** Similar to Fig. 2.8, except for a model planet with a cloud layer with  $b = 10.0$  (at  $\lambda = 0.55 \mu\text{m}$ ) with its top at 0.628 bar that is composed of model A particles ( $r_{\text{eff}} = 2.0 \mu\text{m}$ ).

Adding a cloud layer to the model atmosphere strongly decreases  $P_s$ , especially at longer wavelengths, as can be seen from comparing Figs. 2.9 and 2.8. At the shortest wavelengths, the Rayleigh scattering maximum of  $P_s$  (around  $\alpha = 90^\circ$ ) is still visible, because there, the molecular scattering optical thickness above the cloud layer is still significant. With increasing  $\lambda$ , this optical thickness decreases, and the contribution of light that is reflected by the cloud layer increases. In particular, the ridge in  $P_s$  near  $\alpha = 35^\circ$  at  $0.5 \mu\text{m}$  and extending towards  $\alpha = 25^\circ$  at  $1.0 \mu\text{m}$ , is the primary rainbow. The strength of this rainbow decreases with increasing  $\lambda$ , from about 0.15 (15 %) at  $\lambda = 0.3 \mu\text{m}$  to about 0.07 (7 %) at  $\lambda = 1.0 \mu\text{m}$ .

The branch of negative values of  $P_s$  in Fig. 2.9 that appears from  $\lambda = 0.4$  to  $0.85 \mu\text{m}$  for  $\alpha \lesssim 20^\circ$ , corresponds to the branch of negative values of  $P_s$  for light that has been single scattered by the model A cloud particles for  $150^\circ < \Theta < 180^\circ$  (see Fig. 2.4). The negative values of  $P_s$  in Fig. 2.9 that appear for  $\lambda > 0.7 \mu\text{m}$  and for intermediate phase angles are related to the band of negative values of the single scattering  $P_s$  for  $\Theta < 90^\circ$  (see Fig. 2.4).

### 2.5.2 The effects of the cloud particle sizes

To study the effects of the cloud particle sizes on  $\pi F_n$  and  $P_s$  of the reflected starlight, we replace the model A particles in our cloud layer with model B particles, while keeping the cloud top pressure at 0.628 bar and its optical thickness  $b$  equal to 10 (at  $\lambda = 0.55 \mu\text{m}$ ). The resulting  $\pi F_n$  and  $P_s$  are shown in Fig. 2.10. For

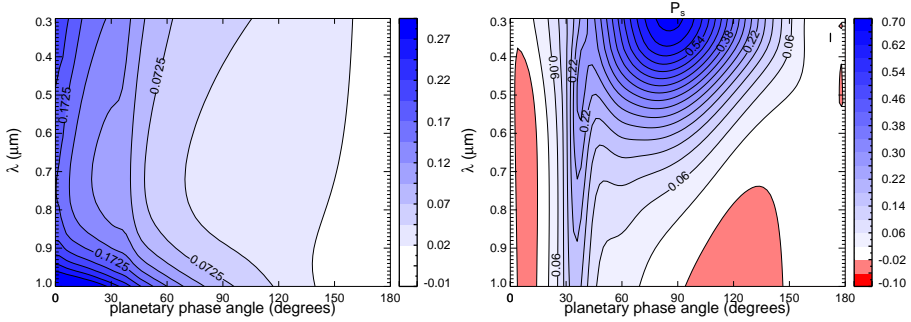


**Figure 2.10:** Similar to Fig. 2.9, except for a cloud layer that is composed of model B particles ( $r_{\text{eff}} = 6.0 \mu\text{m}$ ).

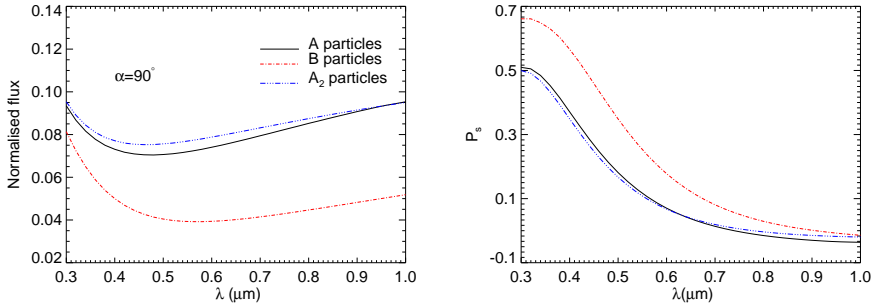


**Figure 2.11:** Cross-sections through Figs. 2.9 and 2.10 at  $\alpha = 90^\circ$  to show the spectral effects of the particle size on the reflected normalized flux and degree of polarization: model A particles (black, solid line; Fig. 2.9), and model B particles (red, dot-dashed line; Fig. 2.10). Also included: model  $A_2$  particles (blue, triple-dot-dashed line).

comparison, Fig. 2.11 shows a cross-section of Figs. 2.9 and 2.10 at a phase angle of  $90^\circ$ , and includes lines for clouds composed of model  $A_2$  particles.

Comparing Figs. 2.10 and 2.9, we can see that the introduction of the larger cloud particles in our model atmosphere leaves clear traces in the reflected  $\pi F_n$  and  $P_s$ . Figure 2.11 shows, for  $\alpha = 90^\circ$ , that the effect of the cloud particle variance on  $\pi F_n$  and  $P_s$  is negligibly small. Indeed, the particle effective radius appears to be the parameter that influences the reflected signals most.

In Figs. 2.10 and 2.9, normalized flux  $\pi F_n$  is significantly lower with the larger particles except for the largest values of  $\lambda$  and  $\alpha$ . The lower values of  $\pi F_n$  are explained by the smaller single scattering albedo of the model B cloud particles (see Fig. 2.2). Indeed, while the albedo of the model A particles equals  $\sim 1$  across the wavelength range under consideration, the albedo of the model B particles varies from 0.84 at  $0.3 \mu\text{m}$ , to 0.90 at  $0.55 \mu\text{m}$ , and 0.94 at  $1.0 \mu\text{m}$ . The differences between the reflected normalized fluxes at the largest phase angles are relatively small, because there, most of the reflected starlight has been scattered in the layers above the cloud.

With the model B cloud particles,  $\pi F_n$  of the light that is reflected by the planet shows a somewhat stronger primary rainbow than with the smaller model A particles (Fig. 2.9). This is explained by the difference in strength of the primary rainbow in the single scattering phase functions of both particle types (Fig. 2.3).

With the model B cloud particles (Fig. 2.10),  $P_s$  shows stronger angular features than with the smaller model A particles (Fig. 2.9). In particular, the maximum around  $\alpha = 90^\circ$  is higher, which is due to the lower single scattering albedo of the model B particles: because more light is absorbed within the cloud layer, there is less multiple scattering, and less (little polarized) light is scattered upward by the cloud layer. With increasing  $\lambda$ , the maximum in  $P_s$  shifts towards smaller phase angles, because there the Rayleigh scattering feature blends with the strong features in the single scattering  $P_s$  of the model B particles that can be seen for  $\Theta > 100^\circ$  in Figs. 2.3 and 2.5.

Furthermore, as expected from the single scattering polarization phase function (Fig. 2.3), and as in the case of  $\pi F_n$ , the primary rainbow is a much more prominent feature in  $P_s$  of the reflected starlight with the model B particles, than with the model A particles. In particular, at  $\lambda = 0.55 \mu\text{m}$ , with the model A particles,  $P_s$  in the rainbow is about 0.12, while with the model B particles,  $P_s$  in the rainbow reaches a value as high as 0.26. The latter value is comparable to the case in which the atmosphere contains a cloud layer of model A particles with an optical thickness of only  $b = 0.5$  (see Fig. 2.7). In observations, the two cases should be separable because with the model B particles, the primary rainbow peak is the global maximum across the entire  $\alpha$  regime, while in the case of the thinner cloud made out of model A particles, it is just a local maximum, since  $P_s$  in the Rayleigh scattering peak is as large as 0.44.

### 2.5.3 The effects of the cloud top pressure

To study the effects of the cloud top pressure on  $\pi F_n$  and  $P_s$ , we use a cloud composed of model A particles, with  $b = 10$  (at  $\lambda = 0.55 \mu\text{m}$ ), and place it with

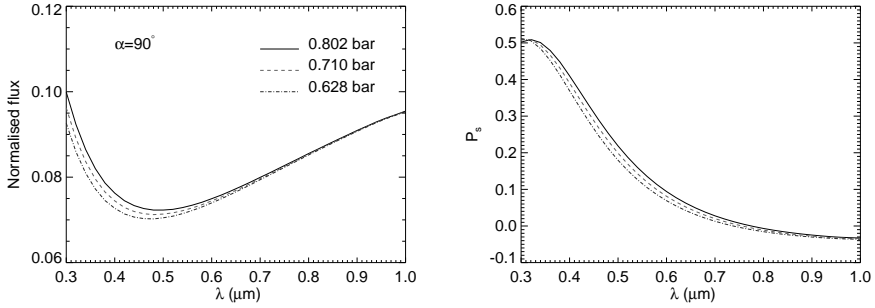


**Figure 2.12:** Normalised flux  $\pi F_n$  (left panel) and  $P_s$  (right panel) as functions of the wavelength  $\lambda$  for model planets with cloud layers with cloud top pressures  $p_{\text{top}}$  equal to 0.802 bar (solid line), 0.710 bar (dashed line) and 0.628 bar (dashed–dotted line). The cloud layer has an optical thickness  $b = 10$  (at  $0.55 \mu\text{m}$ ), and is composed of model A particles. The planetary phase angle  $\alpha$  is  $90^\circ$ .

its top at three different pressures  $p_{\text{top}}$  in the model atmosphere. The geometrical thickness of each cloud is 1 km. We use a low cloud, with  $p_{\text{top}} = 0.802$  bar (corresponding to 2 km on Earth), a middle cloud, with  $p_{\text{top}} = 0.710$  bar (3 km on Earth), and a high cloud, with  $p_{\text{top}} = 0.628$  bar (4 km on Earth). The corresponding cloud top temperatures on Earth are 285, 279, and 273 K, respectively (see Tab. 2.1). These cloud top pressures are chosen to correspond with terrestrial liquid water clouds.

Figure 2.12 shows  $\pi F_n$  and  $P_s$  as functions of  $\lambda$ , at  $\alpha = 90^\circ$ , for the three values of  $p_{\text{top}}$ . At wavelengths shorter than about  $0.6 \mu\text{m}$ ,  $\pi F_n$  increases with increasing  $p_{\text{top}}$ , because of the increasing amount of gaseous molecules, and hence molecular scattering optical thickness, above of the cloud layer. With increasing wavelength, the sensitivity of  $\pi F_n$  to  $p_{\text{top}}$  vanishes, because of the decreasing molecular scattering optical thickness above the cloud layer. The increase of  $\pi F_n$  with increasing  $\lambda$  that occurs for all three values of  $p_{\text{top}}$  is due to the corresponding increase of the scattering optical thickness of the cloud layer and the decrease of its absorption optical thickness (see Fig. 2.2).

As can be seen in Fig. 2.12,  $P_s$  increases with increasing  $p_{\text{top}}$  at almost all wavelengths, because of the increasing amount of molecules, which scatter light with a relatively high degree of polarization, above the cloud layer. In Fig. 2.12, the largest increase in  $P_s$  is 0.044 at  $\lambda = 0.44 \mu\text{m}$  when  $p_{\text{top}}$  increases from 0.628 bar to 0.802 bar. The change of  $P_s$  with  $p_{\text{top}}$  vanishes at the shortest and longest

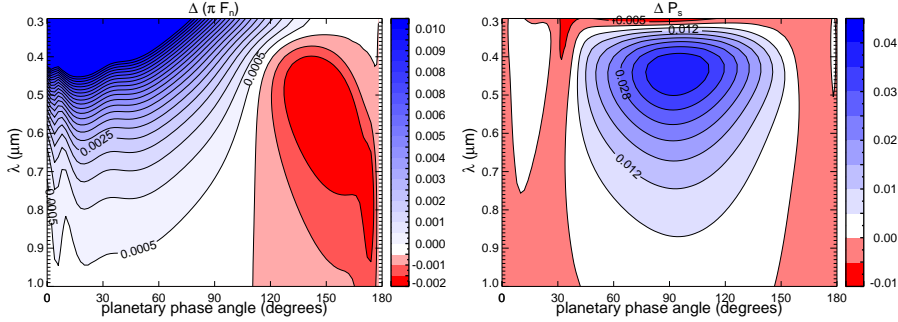


**Figure 2.13:** Differences  $\pi F_n(p_{\text{top}} = 0.802) - \pi F_n(p_{\text{top}} = 0.628)$  (left panel) and  $P_s(p_{\text{top}} = 0.802) - P_s(p_{\text{top}} = 0.628)$  (right panel) as functions of  $\lambda$  and  $\alpha$  for a model planet with a cloud layer with  $b = 10$  (at  $\lambda = 0.55 \mu\text{m}$ ) that is composed of model A particles.

wavelengths. When  $\lambda \lesssim 0.32 \mu\text{m}$ ,  $P_s$  actually decreases slightly with increasing  $p_{\text{top}}$ , because here the increasing amount of molecules leads to an increase of multiple scattered, little polarized light. At the longest wavelengths, the molecular scattering optical thickness of the atmosphere above the cloud layer is too small for each of the three values of  $p_{\text{top}}$  to significantly influence  $P_s$ .

The dependence of  $\pi F_n$  and  $P_s$  on  $p_{\text{top}}$  varies not only with  $\lambda$ , but also with  $\alpha$ . In Fig. 2.9, we presented  $\pi F_n$  and  $P_s$  as functions of  $\alpha$  and  $\lambda$  for a cloud layer with  $p_{\text{top}} = 0.628$  bar. To get a better view of the change of  $\pi F_n$  and  $P_s$  with  $p_{\text{top}}$ , Fig. 2.13 shows  $\pi F_n(p_{\text{top}} = 0.802) - \pi F_n(p_{\text{top}} = 0.628)$  and  $P_s(p_{\text{top}} = 0.802) - P_s(p_{\text{top}} = 0.628)$  as functions of  $\alpha$  and  $\lambda$ . As can be seen in Fig. 2.13,  $\pi F_n$  increases with increasing  $p_{\text{top}}$ , except for  $\alpha \gtrsim 110^\circ$  and  $\lambda \gtrsim 0.32 \mu\text{m}$ . The changes of  $\pi F_n$  with  $p_{\text{top}}$  from 0.802 to 0.628 bar are very small: at maximum  $\sim 3.3\%$  for  $\lambda = 0.3 \mu\text{m}$  and  $\alpha \sim 10^\circ$ . In particular at the phase angles around  $90^\circ$ , where an exoplanet will be easiest to observe directly because it will be relatively far from its star, the sensitivity of  $\pi F_n$  to  $p_{\text{top}}$  is extremely small, making the derivation of cloud top pressures in this range using flux measurements practically impossible.

Regarding the polarization plot of Fig. 2.13, increasing  $p_{\text{top}}$  yields the largest increases in  $P_s$  for  $\lambda \gtrsim 0.35 \mu\text{m}$  and  $\alpha \approx 90^\circ$ . As was also explained for Fig. 2.12,  $P_s$  increases with increasing  $p_{\text{top}}$  because of the increase of the amount of molecules above the cloud layer. In particular, the largest change in  $P_s$  is 0.05, at  $\lambda = 0.44 \mu\text{m}$  and  $\alpha = 94^\circ$ .

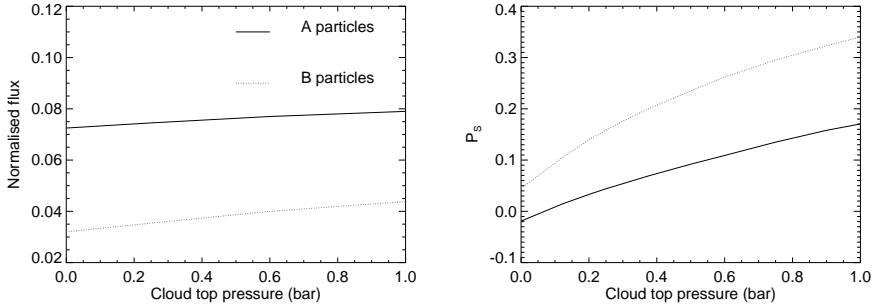


**Figure 2.14:** Normalised flux  $\pi F_n$  (left panel) and  $P_s$  (right panel) at  $\lambda = 0.55 \mu\text{m}$ , as functions of  $p_{\text{top}}$  for model cloud layers with  $b = 10$  (at  $\lambda = 0.55 \mu\text{m}$ ) that are composed of model A or model B particles. The planetary phase angle  $\alpha$  is  $90^\circ$ .

In Fig. 2.14, finally, we present  $\pi F_n$  and  $P_s$  as functions of  $p_{\text{top}}$ , for a cloud layer with an optical thickness of 10 (at  $0.55 \mu\text{m}$ ), consisting of A or B particles, for  $\lambda = 0.55 \mu\text{m}$  and  $\alpha = 90^\circ$ . Not surprisingly, both  $\pi F_n$  and  $P_s$  vary smoothly with  $p_{\text{top}}$ . The normalised flux increases with  $p_{\text{top}}$ , for both cloud particle types. In particular, for the model A (B) particles,  $\pi F_n$  increases from about 0.072 (0.032) at  $p_{\text{top}} = 0$  bar to 0.079 (0.044) at  $p_{\text{top}} = 1$  bar. At this wavelength, the degree of polarization  $P_s$  increases with  $p_{\text{top}}$ , as well; for the model A particles,  $P_s$  increases from  $-0.015$  at  $p_{\text{top}} = 0$  bar to about  $0.17$  at  $p_{\text{top}} = 1$  bar, and for the model B particles,  $P_s$  increases from  $0.045$  at  $p_{\text{top}} = 0$  bar to about  $0.34$  at  $p_{\text{top}} = 1$  bar. The negative values of  $P_s$  for the model A particles and  $p_{\text{top}} < 0.1$  bar are explained by the single scattering properties of these particles at  $\Theta = 90^\circ$  (see Fig. 2.3).

## 2.6 Summary and discussion

We have presented numerically simulated normalized flux ( $\pi F_n$ ) and polarization ( $P_s$ ) spectra from  $0.3$  to  $1.0 \mu\text{m}$  of exoplanets that are completely covered by liquid water clouds. We studied the effects of the cloud optical thickness, the size of the cloud particles, and the cloud top altitude on the spectra as functions of the planetary phase angle. Knowing the microphysical properties of cloud particle on a planet is important for our understanding of the cloud's influence on the planetary climate. In particular, from Earth studies we know that the cloud particle sizes strongly influence the cloud radiative forcing (see e.g. Chapman et al. 2009,

Kobayashi & Adachi 2009, and references therein), since they change the way cloud particles scatter and absorb incident sunlight and thermal radiation.

Given the huge number of free parameters in systems like this, our aim was not to cover the whole parameter space, but rather to explore the information content of, in particular, the degree of polarization of starlight that is reflected by a planet, and the spectral and phase angle ranges that would provide this information. Although we used atmospheric temperature and pressure profiles that are typical for an Earth-like planet, our results can also be used to represent liquid water clouds on gaseous planets, except that the cloud top pressures are likely to be different.

The cloud's optical thickness  $b$  strongly influences the normalized flux and polarization spectra of our model planets. In particular, up to about  $b = 40$ , an increase of  $b$  leads to an increase of  $\pi F_n$ . For larger optical thicknesses, the cloud layer appears to be semi-infinite and the normalized flux spectra no longer change significantly. In polarization, increasing  $b$  lowers the (polarization) continuum, because it increases the amount of multiple scattered light, with usually a low degree of polarization, to the total amount of reflected light. While multiple scattering subdues the angular features in the polarization, even for the largest values of  $b$ ,  $P_s$  as a function of the planetary phase angle still carries the angular features that are representative for light that was singly scattered by the cloud particles in the upper layers of the cloud. In particular, the locations of maxima and so-called zero-points (where  $P_s$  equals zero), are characteristic for the particle size, shape, and composition.

Changing the effective radius  $r_{\text{eff}}$  of the size distribution of the water cloud particles changes their single scattering properties, and hence both the normalized flux and polarization spectra of the reflected starlight. As an example, increasing  $r_{\text{eff}}$  from  $2 \mu\text{m}$  to  $6 \mu\text{m}$  (keeping  $v_{\text{eff}}$  constant), increases  $P_s$  by  $\sim 0.20$  in the blue for a cloud with  $b = 10$ , a cloud top pressure of 0.628 bar and at  $\alpha = 90^\circ$  (Fig. 2.11). The effective variance  $v_{\text{eff}}$  has an almost negligible effect on the normalized flux and polarization spectra, and can thus not be derived from such observations.

Because  $P_s$  preserves the angular features of the singly scattered light, the detection of the primary rainbow in  $P_s$  at planetary phase angles around  $30^\circ$ , would be a clear indicator of the presence of liquid water clouds. This rainbow is present across a wide range of particle sizes, but is only detectable in  $P_s$ , not in  $\pi F_n$  (rainbows seen 'in scattered flux' on the Earth originate in rain droplets, which are much larger than cloud droplets). Interestingly, our simulations show that for small water cloud droplets ( $1 \mu\text{m} \leq r_{\text{eff}} \lesssim 10 \mu\text{m}$ ), the dispersion of the polarized 'cloud' rainbows is opposite to that found for 'rain' rainbows: at  $\lambda = 0.56 \mu\text{m}$ ,

the maximum of the polarized rainbow is located at  $\alpha \sim 32^\circ$  (corresponding to a single scattering angle  $\Theta$  of  $148^\circ$ ), while for  $\lambda = 1.0 \mu\text{m}$ , the largest  $P_s$  is found at  $\alpha \sim 24^\circ$  ( $\Theta = 156^\circ$ ). For 'rain' rainbows,  $\Theta$  decreases with increasing  $\lambda$ . Our simulations show that the dispersion for the 'cloud' rainbows decreases with increasing particle size. Indeed, in case our model cloud consists of the larger model B particles, the maximum polarized rainbow is found at  $\alpha \sim 38^\circ$  ( $\Theta = 142^\circ$ ) for  $\lambda = 0.56 \mu\text{m}$  and at  $\alpha \sim 36^\circ$  ( $\Theta = 144^\circ$ ) for  $\lambda = 1.0 \mu\text{m}$  (see Fig. 2.10).

The inverse dispersion of a polarized 'cloud' rainbow should be observable for terrestrial clouds, e.g. when measured looking down towards a cloud layer from an airplane. As far as we know, such observations have not been done yet.

In order to use the polarized rainbow feature for determining the composition and shape of cloud particles, an exoplanet should be observed across the appropriate phase angle range (from about  $30^\circ$  to  $40^\circ$ ) and with an appropriate angular resolution (about  $10^\circ$ ). To also derive the cloud particle size, an angular resolution of a few degrees ( $2^\circ - 5^\circ$ ) would be required across the rainbow phase angle range. We expect that if an exoplanet were found that could have liquid water clouds and that would be directly observable, a dedicated observing campaign to search for the rainbow would be conceivable.

The strength of rainbows and other angular features will depend slightly on the cloud top altitude, because the latter is related to the scattering optical thickness of the gaseous atmosphere above the clouds. Our simulations show that the lower the cloud (hence the larger the cloud top pressure), the larger the reflected  $\pi F_n$  (in the absence of gaseous absorption). The increase of  $\pi F_n$  with decreasing cloud top altitude decreases with increasing wavelength: above about  $0.6 \mu\text{m}$ ,  $\pi F_n$  appears to be independent of the cloud top altitude. This is due to the decrease of the molecular scattering cross-section, hence the gaseous scattering optical thickness, with increasing wavelength. The sensitivity of  $\pi F_n$  depends strongly on the planetary phase angle. In particular, around  $\alpha = 90^\circ$ , the sensitivity is very small:  $\pi F_n$  changes by at most  $\sim 1\%$  for a cloud top pressure increase of the order of  $\sim 0.17$  bar (on Earth, this corresponds to a cloud top altitude drop of  $\sim 2$  km). The sensitivity of  $\pi F_n$  to the cloud top altitude seems to increase slightly with decreasing phase angle. However, with decreasing phase angle, the difficulty for measuring the normalized flux that is reflected by the planet increases because of the interfering starlight.

The degree of polarization of the reflected starlight is most sensitive to the cloud top altitude at wavelengths between  $0.4$  and  $0.5 \mu\text{m}$ , and around  $\alpha = 90^\circ$ . Around this phase angle and wavelength range,  $P_s$  shows a maximum due to Rayleigh scattered light, and increasing the cloud top pressure (lowering the cloud) leads to an increase of  $P_s$ , because of the increase of light that has been singly scattered by

the gas molecules above the cloud. In this regime, increasing the cloud top pressure by  $\sim 0.18$  bar, typically increases  $P_s$  by 0.05 (5 %). At shorter wavelengths, multiple Rayleigh scattering is significant, and increasing the cloud top pressure results in an increase of multiple scattering and hence a (small) decrease of  $P_s$ . At longer wavelengths, the gaseous scattering optical thickness is too small to change  $P_s$  significantly.

## 2.7 Future work

The simulated signals that we showed in this Chapter all pertain to planets with a homogeneous cloud layer, i.e. there are no variations in cloud particle composition and/or size and/or shape in the clouds. In real planetary atmospheres, we expect variations. On Earth, for example, particle sizes usually show some variation with altitude within the cloud. Such variations could influence the retrieval of cloud particle properties and should be investigated. As an example, in Fig. 2.15, we show  $\pi F_n$  and  $P_s$  of starlight reflected by a model planet covered by two homogeneous cloud layers on top of each other. The lower cloud layer contains model B particles and has its top at 0.710 bar and the upper cloud layer contains model A particles and its top is located at 0.628 bar. For comparison, we also show  $\pi F_n$  and  $P_s$  for the cases in which both layers contain particles B or A, respectively. The total optical thickness of the two cloud layers is 2.0 (at  $\lambda = 0.55 \mu\text{m}$ ) for each case, but the ratio of the optical thicknesses of the two layers varies.

The curves in Fig. 2.15 clearly show that even when the upper cloud has a relatively small optical thickness,  $P_s$  of the planet is mainly determined by the properties of the upper cloud particles. This is due to the fact that the angular features of  $P_s$  are mostly due to singly scattered light, which originates mostly in the upper part of a cloud. Combining polarization observations at a range of wavelengths, e.g. from the UV to the near-infrared, or even the infrared (where polarization signatures would be due to scattered thermal radiation), would probably help probing various depths in the cloud layers, since cloud optical thicknesses depend on the wavelength.

Another interesting extension to the work presented in this Chapter, would be to study the influence of variations in particle shape within the clouds. In this Chapter, we placed the clouds at altitudes where the ambient temperatures ensure that the cloud particles are liquid, and hence, spherical in shape. With increasing cloud top altitude and decreasing ambient temperatures, clouds will contain more and more ice particles. The single scattering flux and polarization phase functions of ice cloud particles will differ strongly from those of liquid water particles because

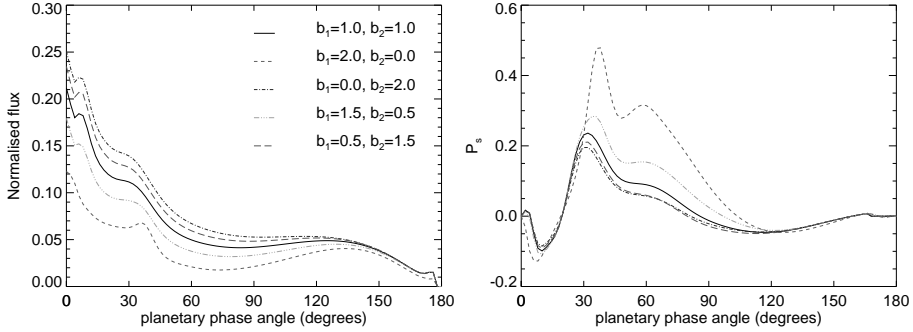


**Figure 2.15:** The normalised flux ( $\pi F_n$ ) and degree of polarization ( $P_s$ ) of starlight reflected by a planet covered by two cloud layers; the lower (upper) one composed of model particles B (A). The top of the upper cloud is at 0.628 bar, and for these calculations, the cloud layers themselves do not contain any gas molecules. The lines pertain to different combinations of cloud optical thicknesses (at 0.55 microns): upper cloud  $b_2=0.5$ , lower cloud  $b_1=1.5$  (orange, dashed–triple-dotted line); upper cloud  $b_2=1.0$ , lower cloud  $b_1=1.0$  (black, solid line); upper cloud  $b_2=1.5$ , lower cloud  $b_1=0.5$  (green, long–dashed line). For comparison, we also included the cases in which both cloud layers contain particles B with total  $b_1=2.0$  (red, dashed line), and particles A with total  $b_2=2.0$  (blue, dashed–dotted line).

of the non-spherical, possibly crystalline shape of the ice particles. We can thus expect that ice particles will significantly influence the polarization spectrum of a cloudy planet. Using Earth-observation data, Goloub et al. (2000) showed that the strength of the primary rainbow polarization peak that is characteristic for liquid water cloud particles decreases when the column number density of overlaying ice particles increases. For a full retrieval of cloud parameters, we will thus have to take into account the polarization characteristics of ice particles. Knowledge of the phase (liquid or solid) of cloud particles gives valuable information on the ambient atmospheric temperatures, especially when combined with knowledge of cloud top altitudes. Flux and polarization signatures of ice and mixed clouds will be the subject of further study.

Furthermore, the model planets that we used in this Chapter have horizontally homogeneous atmospheres. We will adapt our numerical radiative transfer and disk integration code to investigate the influence of horizontally inhomogeneities of cloud layers (e.g. partial cloud coverage or Jupiter-like cloud belts and zones) on the flux and polarization spectra, and on the retrieved cloud parameters.

# The numerical code

---

Based on:

T. Karalidi and D. M. Stam, *Modelled flux and polarization signals of horizontally inhomogeneous exoplanets applied to Earth-like planets*, *Astronomy & Astrophysics*, volume 546, id A56, 2012, reproduced with permission ©ESO

**Abstract** *Context.* We present modelled flux and linear polarization signals of starlight that is reflected by spatially unresolved, horizontally inhomogeneous planets and discuss the effects of including horizontal inhomogeneities on the flux and polarization signals of Earth-like exoplanets. *Methods.* Our code is based on an efficient adding–doubling algorithm, which fully includes multiple scattering by gases and aerosol/cloud particles. We divide a model planet into pixels that are small enough for the local properties of the atmosphere and surface (if present) to be horizontally homogeneous. Given a planetary phase angle, we sum up the reflected total and linearly polarized fluxes across the illuminated and visible part of the planetary disk, taking care to properly rotate the polarized flux vectors towards the same reference plane. *Results.* We compared flux and polarization signals of simple horizontally inhomogeneous model planets against results of the weighted sum approximation, in which signals of horizontally homogeneous planets are combined. Apart from cases in which the planet has only a minor inhomogeneity, the signals differ significantly. In particular, the shape of the polarization phase function appears to be sensitive to the horizontal inhomogeneities. The same holds true for Earth-like model planets with patchy clouds above an ocean and a sandy continent. Our simulations clearly show that horizontal inhomogeneities leave different traces in flux and polarization signals. Combining flux with polarization measurements would help retrieving the atmospheric and surface patterns on a planet.

## 3.1 Introduction

Since Mayor & Queloz (1995) discovered the first planet orbiting another main sequence star almost two decades ago, the rapid improvement of detection methods and instruments has yielded hundreds of exoplanets, including several tens of so-called super-Earths (see e.g. Léger et al. 2011, Charbonneau et al. 2009,

Miller-Ricci & Fortney 2010, Beaulieu et al. 2006), and many more will follow in the coming years. The next step in exoplanet research is the characterization of the atmospheres and surfaces (if present) of detected exoplanets: what is their composition and structure?

Currently, exoplanet atmospheres are being characterized using the *transit method* (see e.g. Beaulieu et al. 2010, Miller-Ricci & Fortney 2010). This method is based on measurements of the wavelength dependence of starlight that filters through the upper planetary atmosphere during the primary transit, or of the planetary flux just before or after the secondary eclipse. The transit method is mostly applied to gaseous planets that orbit close to their star. The chances to catch gaseous planets in wide orbits, such as Jupiter and Saturn in our Solar System, transiting their star are extremely small, because their orbital plane should be perfectly aligned with our line of sight and because their transits are very rare. Earth-sized exoplanets in the habitable zone of a solar-type star are probably too small and transit too seldom to reach a sufficient signal-to-noise ratio to do transit spectroscopy (Kaltenegger & Traub 2009).

A promising method to characterize atmospheres and surfaces (if present) of exoplanets that are small and/or in wide orbits, is *direct detection*, in which the starlight that a planet reflects and/or the thermal radiation that a planet emits is measured separately from the stellar light (except for some background starlight). Some instruments that are being designed for such direct detections are SPHERE (for the VLT) and EPICS (for the European Extremely Large Telescope, or E-ELT). An example for a space telescope for direct detection is the New Worlds Observer (NWO) (Cash & New Worlds Study Team 2010), which is under study by NASA. Through direct detections, broadband images and/or spectra of various types of exoplanets will become available in the near future.

Knowing the Solar System planets, it is to be expected that exoplanets that will be observed are horizontally inhomogeneous, e.g. with clouds and hazes in patches, such as on Earth and Mars, or in banded structures, such as, for example, on Jupiter and Saturn. And there will undoubtedly be solid exoplanets with significant local variations in surface reflection properties and texture, such as the Earth with its continents and oceans. Although the lack of spatial resolution in near future exoplanet observations will merge all spatial variation into a single image pixel and/or spectrum, accounting for the existence of horizontal inhomogeneities will be important when trying to retrieve planet characteristics. For example, efforts to identify spectral signatures of life on other planets will face various challenges, such as clouds masking or mimicking the signatures of vegetation (Tinetti et al. 2006b, and references therein). The cloud coverage will also influence the retrieval of mixing ratios of atmospheric gases, such as water vapour and oxygen, from reflected

light spectra. In particular, the larger the fraction of clouds across an exoplanetary surface, the smaller the depth of gaseous absorption bands. Absorption band depths are, however, also influenced by the cloud top altitudes, with higher clouds yielding shallower absorption bands (for examples, see Stam 2008). The distribution of cloud top altitudes across a planet will thus also be a parameter to take into account.

Horizontal inhomogeneities can have large effects on the flux of starlight that is reflected by a planet. In particular, Ford et al. (2001) have shown that an Earth analogue planet without clouds would show diurnal flux variations of up to 150% due to the variation of the albedo of different regions on the planet. In full agreement, Oakley & Cash (2009) have calculated that in absence of an atmosphere, the flux of an Earth-like exoplanet would show a clear diurnal variability as different continents would rotate in and out of the field of view of an observer. The presence of clouds in the Earth's atmosphere significantly complicates the characterization of various surface types. Ford et al. (2001) show, for example, that an Earth-like cloud pattern would suppress the diurnal flux variations to as little as 20%, while Oakley & Cash (2009) indicates that characterizing the surface of the planet is possible only for cloud coverages significantly lower than the average coverage on Earth ( $\lesssim 25\%$  versus  $\sim 60\%$ ). To quantitatively estimate the effects of horizontal inhomogeneities due to clouds or surface features on observed spectra, and to be able to account for such variations in the retrieval of planet characteristics from future observations, numerical codes are essential tools.

In this Chapter, we present our numerical code to calculate spectra of starlight that is reflected by spatially unresolved, horizontally inhomogeneous exoplanets. The main difference with other codes for horizontally inhomogeneous planets (such as those used by Ford et al. 2001, Oakley & Cash 2009, Tinetti et al. 2006b) is that it can be used to calculate not only the flux of reflected starlight but also its state (degree and direction) of polarization. Polarimetry promises to play an important role in exoplanet research both for exoplanet detection and characterization. In particular, because the direct starlight is unpolarized, while the starlight that is reflected by a planet will usually be polarized (see e. g. Zuger et al. 2010, Stam et al. 2006a, 2004, Saar & Seager 2003, Seager et al. 2000), polarimetry can increase the planet-to-star contrast ratio by 3 to 4 orders of magnitude (Keller et al. 2010), thus facilitating the detection of an exoplanet that might otherwise be lost in the glare of its parent star. Polarimetry will not only help to detect a planet, it will also confirm the status of the object, since background objects will usually be unpolarized.

The importance of polarimetry for studying planetary atmospheres and surfaces has been shown many times using observations of the Earth and other Solar Sys-

tem planets (see for example Hansen & Hovenier 1974, Hansen & Travis 1974, Mishchenko 1990, Tomasko et al. 2009), as well as by modeling of Solar System planets or giant exoplanets (e. g. Madhusudhan & Burrows 2012, Stam 2008, 2003, Stam et al. 2004, Saar & Seager 2003, Seager et al. 2000). In particular the sensitivity of polarization to the microphysical properties of the scatterers in the planetary atmosphere, make it a crucial tool for braking degeneracies that flux only observations can have.

The radiative transfer calculations in our code are based on an efficient adding-doubling algorithm (de Haan et al. 1987) which fully includes multiple scattering by gases and aerosol/cloud particles, that was used before for flux and polarization calculations for gaseous and terrestrial exoplanets by Stam (2003), Stam et al. (2004), Stam (2008) and Chapter 2. These authors, however, assumed each exoplanet to be horizontally homogeneous, such that it could be treated as a single starlight scattering 'particle', which allowed for a very fast integration of the reflected flux and polarization signals across the planet's disk for the whole planetary phase angle range (see Stam et al. 2006a, for a description of this disk-integration algorithm). With this horizontally homogeneous code, the signals of horizontally inhomogeneous planets can be simulated using the so-called weighted sum approximation: signals of homogeneous planets are multiplied by a weighting factor and summed to yield the final signal. We, on the other hand, divide a horizontally inhomogeneous model planet into pixels that are small enough for the local properties of the atmosphere and surface (if present) to be horizontally homogeneous. For each type of pixel, we perform adding-doubling radiative transfer calculations (de Haan et al. 1987) and, given the planetary phase angle, we sum up the reflected total and polarized fluxes across the illuminated and visible part of the planetary disk. Our code for horizontally inhomogeneous planets allows investigating the applicability of the weighted sum approximation, and the effects of horizontal inhomogeneities on the flux and in particular the polarization signals of exoplanets.

This Chapter is organized as follows. In Sec. 3.2, we describe our numerical method to calculate the flux and polarization of starlight that is reflected by a horizontally inhomogeneous planet, and in Sec. 3.3, we present simulations of flux and polarization for different types of horizontal inhomogeneities. In Sec. 3.4, we present flux and polarization signals of horizontally inhomogeneous Earth-like planets and compare them to signals for horizontally homogeneous planets. Finally, in Sec. 3.5, we discuss and summarize our results. Appendix A contains the results of testing our code for horizontally inhomogeneous planets against an existing code for horizontally homogeneous planets.

### 3.2 Calculating reflected starlight

Light can fully be described by a flux vector  $\pi\vec{F}$ , as follows

$$\pi\vec{F} = \pi \begin{bmatrix} F \\ Q \\ U \\ V \end{bmatrix}, \quad (3.1)$$

with  $\pi F$  the total,  $\pi Q$  and  $\pi U$  the linearly and  $\pi V$  the circularly polarized fluxes (see e.g. Hansen & Travis 1974, Hovenier et al. 2004, Stam 2008). Parameters  $\pi F$ ,  $\pi Q$ ,  $\pi U$  and  $\pi V$  depend on the wavelength  $\lambda$ , and have dimensions  $\text{W m}^{-2}\text{m}^{-1}$ . Parameters  $\pi Q$  and  $\pi U$  are defined with respect to a reference plane, for which we choose the planetary scattering plane, i.e. the plane through the centers of the planet, star and observer. Note that this plane is usually not the same as the planetary orbital plane; only for orbits that are seen edge-on, the two planes coincide at all phase angles. In the following, we will ignore  $\pi V$ , because it is usually very small (Hansen & Travis 1974), and because the errors in calculated values of  $\pi F$ ,  $\pi Q$ , and  $\pi U$  due to ignoring  $\pi V$  are negligible (Stam & Hovenier 2005).

The degree of polarization  $P$  of vector  $\pi\vec{F}$  is defined as

$$P = \frac{\sqrt{Q^2 + U^2}}{F}, \quad (3.2)$$

which is independent of the choice of reference plane. For planets that are mirror-symmetric with respect to the planetary scattering plane (i.e. horizontally homogeneous planets), Stokes parameter  $U$  equals zero. In that case, we can use an alternative definition of the degree of polarization

$$P_s = -\frac{Q}{F}, \quad (3.3)$$

with the sign indicating the direction of the polarization, i.e. if  $P_s > 0$  ( $P_s < 0$ ) the light is polarized perpendicular (parallel) to the planetary scattering plane. The absolute value of  $P_s$  is just equal to  $P$ .

We calculate the flux vector of starlight that has been reflected by a spherical planet with radius  $r$  at a distance  $d$  from the observer using ( $d \gg r$ ) as (see Stam et al. 2006a)

$$\pi\vec{F}(\alpha) = \frac{1}{4} \frac{r^2}{d^2} \vec{S}(\alpha) \pi\vec{F}_0, \quad (3.4)$$

with  $\alpha$  the planetary phase angle, i.e. the angle between the star and the observer as seen from the planet's center. Furthermore,  $\pi\vec{F}_0$  is the flux vector of the incident starlight and  $\vec{S}$  the  $4 \times 4$  planetary scattering matrix. In the following, we normalize Eq. 4.4 assuming  $r = 1$  and  $d = 1$ .

As described in Stam et al. (2006a), the planetary scattering matrix  $\vec{S}$  can be calculated by integrating local reflection matrices  $\vec{R}$  across the illuminated and visible part of the planetary disk, as follows

$$\vec{S}(\alpha) = \frac{4}{\pi} \int_{\mathcal{D}} \mu \mu_0 \vec{L}(\beta_2) \vec{R}(\mu, \mu_0, \Delta\phi) \vec{L}(\beta_1) dO, \quad (3.5)$$

where  $dO$  is a surface element on the planet, and  $\vec{R}$  is the local reflection matrix, which describes how starlight that is incident on a given location of the planet is reflected towards the observer. The reference planes for  $\vec{R}$  are the local meridian planes, which contain the direction of propagation of the incident and reflected light, respectively, and the local vertical direction. The matrices  $\vec{L}$  are so-called rotation matrices (see Hovenier et al. 2004, Hovenier & van der Mee 1983) that are used to rotate from the planetary scattering plane to the local meridian planes and back:

$$\vec{L}(\beta) = \begin{bmatrix} 1 & 0 & 0 & 0 \\ 0 & \cos 2\beta & \sin 2\beta & 0 \\ 0 & -\sin 2\beta & \cos 2\beta & 0 \\ 0 & 0 & 0 & 1 \end{bmatrix}, \quad (3.6)$$

Angle  $\beta$  is measured in the anti-clockwise direction from the old to the new reference plane when looking in the direction of propagation of the light.

In Eq. 3.5, we assume that the planetary atmosphere and surface (if present) are *locally* plane-parallel and rotationally symmetric with respect to the local vertical direction. Therefore, each matrix  $\vec{R}$  depends on  $\mu_0 = \cos \theta_0$ , with  $\theta_0$  the angle between the local zenith and the direction towards the star, on  $\mu = \cos \theta$ , with  $\theta$  the angle between the local zenith and the direction towards the observer, and on  $\Delta\phi = \phi - \phi_0$ , the angle between the azimuthal angles of the incident and the reflected light, respectively. Azimuthal angles are measured rotating clockwise when looking up from an arbitrary, local vertical plane towards the local vertical plane containing the direction of propagation of the light.

For *horizontally homogeneous* planets, Stam et al. (2006a) present an efficient method for evaluating Eq. 3.5 that uses an adding-doubling radiative transfer algorithm (de Haan et al. 1987) to calculate the coefficients of the expansion of the local reflection matrix (which is the same across the planet) into a Fourier series.

These coefficients are then used to compute coefficients of the expansion of matrix  $\vec{S}$  into generalized spherical functions. With these expansion coefficients,  $\vec{S}$  can be calculated rapidly for any phase angle  $\alpha$ . Since with this method, a planet is basically treated as a single light-scattering particle, it cannot be used for horizontally inhomogeneous planets.

To calculate  $\vec{S}$  for *horizontally inhomogeneous* planets, we divide a planet into pixels small enough for the local atmosphere and surface (if present) to be considered both plane-parallel and horizontally homogeneous. For each type of pixel (a combination of surface and atmosphere properties), we first calculate the coefficients of the expansion of the local reflection matrix  $\vec{R}$  into a Fourier series, using the adding-doubling algorithm (de Haan et al. 1987). Then, for each given planetary phase angle and each pixel, we use the respective Fourier coefficients to calculate the local reflection matrices (see de Haan et al. 1987). The local matrices are summed up according to

$$\vec{S}(\alpha) = \frac{4}{\pi} \sum_{i=1}^N \mu_i \mu_{0i} \vec{L}(\beta_{2i}) \vec{R}_i(\mu_i, \mu_{0i}, \Delta\phi_i) \vec{L}(\beta_{1i}) dO_i, \quad (3.7)$$

with  $N$  the total number of pixels on the illuminated and visible part of the planetary disk.

In the following, we assume unpolarized incident starlight, since integrated over the stellar disk, light of solar-type stars can be assumed to be unpolarized (Kemp et al. 1987). In this case,  $\pi\vec{F}_0 = \pi F_0 \vec{I}$ , with  $\vec{I}$  the unit column vector and  $\pi F_0$  the total incident stellar flux (measured perpendicular to the propagation direction of the light), for which we assume a normalized value of  $1 \text{ W m}^{-2} \text{ m}^{-1}$ . Thanks to the assumption of unpolarized incident starlight, rotation matrix  $\vec{L}(\beta_{1i})$  can be ignored in Eq. 3.7.

Because of the normalizations and the assumption of unpolarized incident light, the total flux that is reflected by a planet (cf. Eq. 4.4) is given by

$$\pi F_n(\lambda, \alpha) = \frac{1}{4} a_{11}(\lambda, \alpha), \quad (3.8)$$

with  $a_{11}$  the (1,1)-element of matrix  $\mathbf{S}$  (see Stam (2008) and Chapter 2). The subscript  $n$  indicates the normalization. When  $\alpha = 0^\circ$ , the hence normalized total flux equals the planet's geometric albedo  $A_G$ . Our normalized total and polarized fluxes  $\pi F_n$ ,  $\pi Q_n$  and  $\pi U_n$  can straightforwardly be scaled to any given planetary system using Eq. 4.4 and inserting the appropriate values for  $r$ ,  $d$  and  $\pi F_0$ . The degree of polarization ( $P$  or  $P_s$ ) is independent of  $r$ ,  $d$  and  $\pi F_0$ , and would thus not require any scaling.

We have tested our disk-integration code by comparing its results with those of the code for horizontally homogeneous planets by Stam et al. (2006a) (see Appendix 3.5). We have not compared it against other codes for modelling signals of horizontally inhomogeneous planets (see e.g. Ford et al. 2001, Oakley & Cash 2009, Tinetti et al. 2006b), because these codes ignore polarization, which is the most interesting feature of our code. A comparison between calculated total fluxes would require us to disable the polarization calculations in our adding-doubling code, since ignoring polarization introduces errors of up to several percent in total flux calculations (Stam & Hovenier 2005). From the comparison with the code for horizontally homogeneous planets applied to horizontally inhomogeneous planets using the weighted sum approximation, in which weighted sums of flux vectors reflected by horizontally homogeneous planets are used to approximate the flux vectors of horizontally inhomogeneous planets (see Appendix 3.5), we conclude that our code is accurate enough for application to horizontally inhomogeneous planets, provided enough pixels are used across the disk, not only for resolving the spatial variations but also the variations in illumination and viewing angles across pixels.

### 3.3 Sensitivity to horizontal inhomogeneities

In this section, we present flux and polarization (degree and angle) signals of planets with different types of horizontal inhomogeneities on their surfaces as calculated using our code to show the signatures of inhomogeneities and the differences with signatures of horizontally homogeneous planets with similar surface albedos. Unless stated otherwise, each planet has a gaseous, Rayleigh scattering atmosphere with a total optical thickness of  $\sim 0.1$  (no absorption), and a flat surface. For the surface albedo, we choose the extreme values of 0.0 (black) and 1.0 (white), since they give the largest contrast in flux and polarization.

Establishing which types of inhomogeneities could still be handled with e.g. a weighted sum approximation and which would need a full scale horizontally inhomogeneous approach with e.g. our code (from hereon: the HI-code), is interesting for saving computing time when possible. The disadvantage of our HI-code is namely the large amount of computing time it requires as compared to the horizontally homogeneous code of Stam et al. (2006a) (from hereon: the HH-code). For example, the HI-code takes about  $10^5$  times more time than the HH-code for calculating the flux vectors of a horizontally homogeneous planet covered by a cloud layer with optical thickness 2, for phase angles  $\alpha$  from  $0^\circ$  to  $180^\circ$  in steps of  $2^\circ$ , with the planet having been divided into pixels of  $2^\circ \times 2^\circ$ , and for a single

wavelength.

The difference in computation times would be irrelevant if the computing time of the HI-code were negligible. Unfortunately this is not the case. This time depends strongly on the properties of the model atmosphere, especially on the absorption and scattering optical thickness of the gases and particles in the atmosphere and on the angular variation of the single scattering properties of the scattering particles. In particular adding polarization to the flux calculations increases the time by at least an order of magnitude, and of course, the timing increases almost linearly with the number of wavelengths at which calculations are required (since these calculations are independent of each other, they could easily be done in parallel). For the cloudy model planet calculations described in the previous paragraph, the HH-code takes about a minute on an average workstation.

The difference in computing time is not spent in the radiative transfer calculations themselves, since the two codes use the same adding-doubling radiative transfer algorithm (based on de Haan et al. 1987) and were run with the same numerical accuracy. Also, because both planets were horizontally homogeneous, the radiative transfer calculation had to be performed only once for each code. Indeed, in the HI-code, the additional computing time is mostly spent in the integration of the flux vectors across the planetary disk. In particular, for  $\alpha = 0^\circ$ , the number of  $2^\circ \times 2^\circ$  pixels across the disk is more than 8000. For each pixel, the appropriate Fourier coefficients have to be determined from the list of calculated coefficients, they have to be summed to calculate the local reflection matrix, and with that the locally reflected flux vectors. Then, the locally reflected flux vectors have to be rotated to the planetary scattering plane in order to be summed up to calculate the reflected flux vector of the planet. Even though the computing time per pixel can be relatively small, the mere number of pixels (which of course depends on the planetary phase angle) can result in long computing times.

### 3.3.1 Planets with spots

The first type of horizontally inhomogeneous planets have black surfaces with homogeneously distributed white spots. We start with spots consisting of single white pixels that cover 4% of the planet's surface, and let the area of each spot grow until the spots cover 68% of the surface. Figure 3.1 shows  $\pi F_n$  and  $P_s$  (see Eq. 3.3) as calculated using the HI-code as functions of the planetary phase angle  $\alpha$  for these planets. As can be seen, increasing the percentage of white pixels from 4% to 68%, increases  $\pi F_n$  smoothly from 0.09 to 0.58 at  $\alpha = 0^\circ$ , while  $P_s$  decreases from 0.6 to 0.08 at  $\alpha = 90^\circ$  (this phase angle does not coincide with the maximum of  $P_s$ ). With increasing surface brightness, the peak value of  $P_s$  shifts

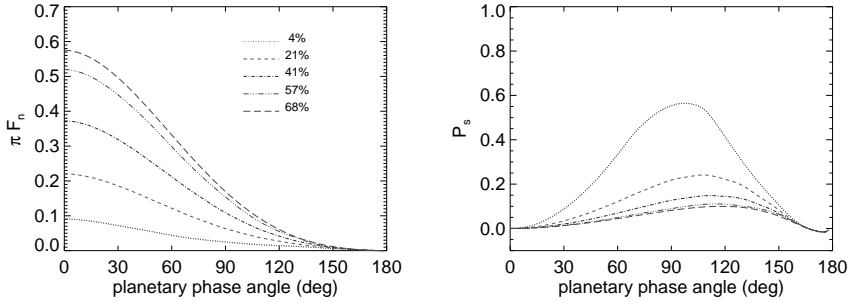


**Figure 3.1:**  $\pi F_n$  and  $P_s$  as functions of  $\alpha$  for black, cloud-free planets with white spots occupying 4% (red, dotted line), 21% (green, dashed line), 41% (blue, dashed-dotted line), 57% (grey, dashed-triple-dotted line) and 68% (purple, long-dashed line) of the planet.

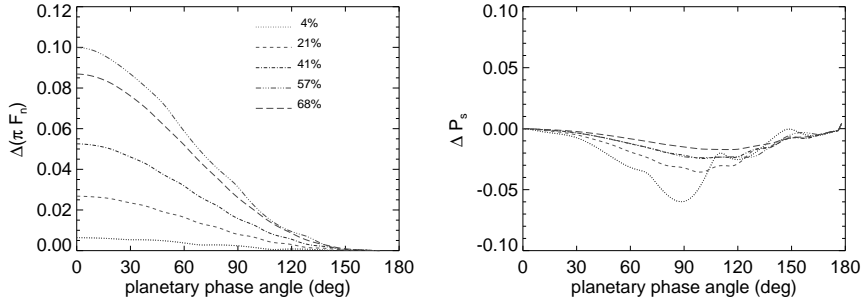
from  $\alpha = 98^\circ$  (4% white) to  $\alpha = 116^\circ$  (68% white).

Figure 3.2 shows the difference between the results from the HI-code and those from the HH-code (the latter combined with with the weighted sum approximation, as described in Appendix 3.5). In Fig. 3.2, it is clear that when the planet is almost horizontally homogeneous (only 4% covered by white pixels), the maximum relative difference in flux,  $\Delta\pi F_n$  is very small ( $\sim 0.64\%$  for  $\alpha = 0^\circ$ ), with the HI-code giving the slightly higher values. With increasing coverage,  $\Delta\pi F_n$  increases, showing a maximum value of 10% for 57% coverage in Fig. 3.2, to decrease again when the planet is almost homogeneously white.

Because the degree of polarization is itself a relative measure, we show the differences in  $P_s$  between the HI-code and the HH-code as absolute differences. As can be seen in Fig. 3.2, the absolute difference  $\Delta P_s$  is largest ( $\sim -6\%$  percent point around  $90^\circ$ ) for the darkest planet and decreases towards the whiter planets. The HH-code produces at (almost) all phase angles a larger  $P_s$  than the HI-code. Interestingly, the polarization phase curve of the darkest planet is significantly less symmetrical when horizontal inhomogeneities are accurately taken into account (HI-code) than with the HH-code and the weighted sum approximation.

### 3.3.2 Planets with center continents

The second type of horizontally inhomogeneous planets have black surfaces and a circular “continent” of white pixels at the center of the planetary disk facing



**Figure 3.2:** Relative difference  $\Delta\pi F_n$  and the absolute difference  $\Delta P_s$  between the flux and polarization phase functions of the white spotted planets of Fig. 3.1 as calculated using the HI-code and the HH-code. The coverage of white spots is 4% (red, dotted line), 21% (green, dashed line), 41% (blue, dashed–dotted line), 57% (grey, dashed–triple–dotted line) and 68% (purple, long–dashed line).

the observer (rotation of the planet, hence the rotation of the continent in and out of the field-of-view is not taken into account here). Figure 3.3 shows  $\pi F_n$  and  $P_s$  as functions of  $\alpha$  for planets with continents that cover from 5% to 98% of the disk. Both for the flux and the polarization, the curves for 80% and 98% coverage virtually overlap, because in these cases, the black pixels are all located along the limb of the planet and hardly contribute to the total signal. The flux phase functions in Fig. 3.3 have very similar shapes as those in Fig. 3.1, although the latter are darker for the same surface coverage of white pixels, which is not surprising since they have more black pixels on the front side of the disk. The polarization phase curves in Fig. 3.3 clearly have different, more asymmetrical shapes than those in Fig. 3.1, except for the largest coverages. The peak in the polarization phase curves indicates the phase angle where the continent disappears into the planet’s nightside.

Comparing the flux and polarization signals of the planets with white continents as calculated with our HI-code to the signals calculated using the HH-code (Fig. 3.4), it is obvious that the differences  $\Delta\pi F_n$  and  $\Delta P_s$  are smallest when the planetary disk is almost completely covered by the continent. In Fig. 3.4, the largest difference in the flux is about 33%, for a coverage of 32% and at  $\alpha = 0^\circ$ , with the HI-code giving the higher fluxes. The difference in polarization,  $\Delta P_s$ , clearly shows the strong asymmetry around  $\alpha = 90^\circ$  of  $P_s$  when calculated with the HI-code.

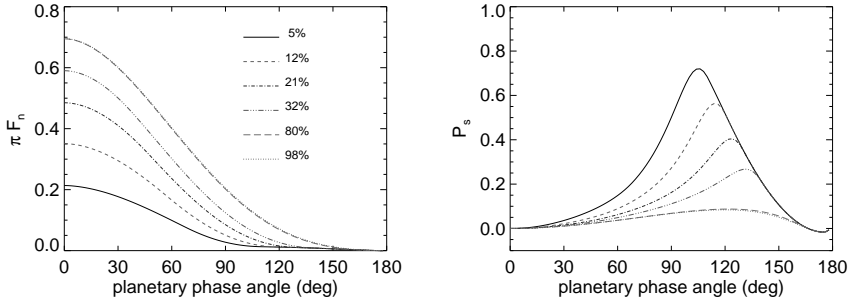


**Figure 3.3:**  $\pi F_n$  and  $P_s$  as functions of  $\alpha$  for black, cloud-free planets with a white continent on the center of the planetary disk facing the observer, for different coverages of the continent: 5% (black, solid line), 12% (red, dashed line), 21% (blue, dashed-dotted line), 32% (green, dashed-triple-dotted line), 80% (magenta, long-dashed line) and 98% (gray, dotted line).

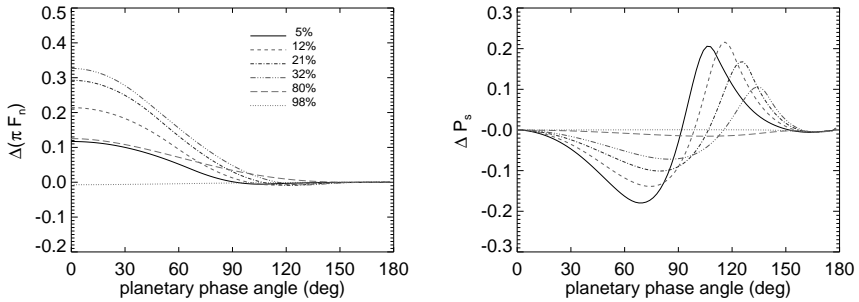


**Figure 3.4:**  $\Delta\pi F_n$  and  $\Delta P_s$  between the phase functions of the white continent planets of Fig. 3.3 as calculated using the HI-code and the HH-code. The coverage of the continents is: 5% (black, solid line), 12% (red, dashed line), 21% (blue, dashed-dotted line), 32% (green, dashed-triple-dotted line), 80% (magenta, long-dashed line) and 98% (gray, dotted line) of the planetary disk.

Figure 3.5 shows  $\Delta\pi F_n$  and  $\Delta P_s$  for the same planets except with a white surface and a black continent. Not surprisingly, for these planets, at most phase angles,  $\pi F_n$  is smaller when calculated with the HI-code than with the HH-code for each percentage of coverage at most phase angles, because of the concentration

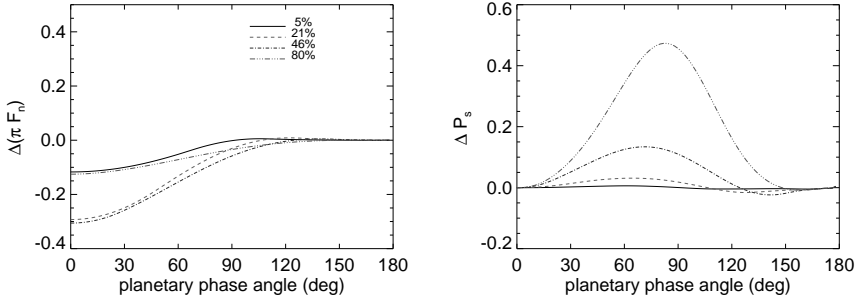


**Figure 3.5:** Similar to Fig. 3.4, except for white, cloud-free planets with black continents. The coverage of the continents is: 5% (black, solid line), 21% (red, dashed line), 46% (blue, dashed–dotted line), and 80% (green, dashed–triple–dotted line) of the planetary disk.

of black pixels in the centre of the disk. The difference  $\Delta P_s$  is less asymmetric than for the black planets with white continents (cf. Fig. 3.3). The polarization phase functions as calculated using the two codes are thus similarly shaped. The maximum of the polarization phase function, however, does depend strongly on the code, and is thus sensitive to the distribution of pixels across the disk, with the HI-code yielding much higher maximum values of  $P_s$  than the HH-code, except for the smallest coverages. Indeed, for a white planet with a black continent covering 80% of the disk,  $P_s$  is almost 50% higher (around  $\alpha = 80^\circ$ ) calculated with the HI-code than with the HH-code. Note that for this coverage, the difference in flux is relatively small ( $\sim -10\%$ ) and similar to that for a coverage of 5%. The difference in sensitivity to the spatial distribution of albedo across the planetary disk between flux and polarization clearly illustrates the strengths of combined flux and polarization measurements.

### 3.3.3 Planets with hemispherical caps

The third type of horizontally inhomogeneous planets have black surfaces and two, equally sized white caps on opposing sides of the planet. We will present results for three locations of the caps:  $0^\circ$  (the caps cover the “north” and the “south” poles of the planet),  $45^\circ$ , and  $90^\circ$  (the caps are on the “eastern” and “western” sides of the planetary disk). Planets with caps at  $45^\circ$  are not mirror-symmetric with respect to the planetary scattering plane. Therefore, Stokes parameter  $U$  will

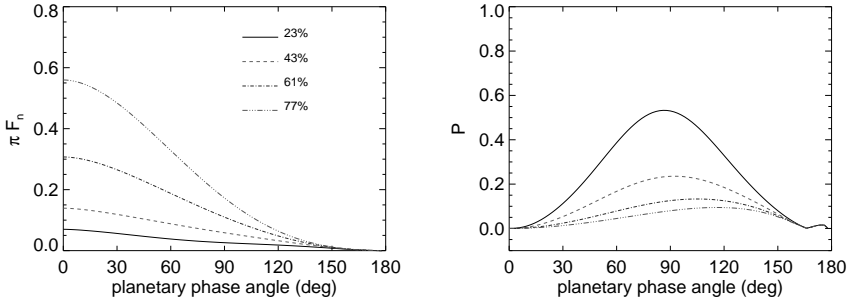


**Figure 3.6:**  $\pi F_n$  and  $P$  as functions of  $\alpha$  for black, cloud-free planets with hemispherical caps occupying 23% (black, solid line), 43% (red, dashed line), 61% (blue, dashed-dotted line), and 77% (green, dashed-triple-dotted line) of the planet. The caps are located at the 'north' and 'south' poles of the planet.

usually not be zero. In the following, we will therefore use Eq. 5.2 to define the degree of linear polarization instead of Eq. 3.3.

First, we'll discuss the signals of planets with the caps covering the poles of the planets. Figure 3.6 shows  $\pi F_n$  and  $P$  for different coverages of the caps as calculated using the HI-code. The shape of the flux phase function is very smooth, and at  $\alpha = 0^\circ$ ,  $\pi F_n$  increases from 0.07 for 23% coverage, to 0.56 for 77% coverage. In the latter case, the planet is basically white with a black, equatorial belt (for a completely white planet,  $\pi F_n$  would equal 0.7, see Fig. 3.15). The polarization phase function is quite symmetric for small caps, and  $P$  decreases from almost 0.55 for 23% coverage to 0.08 for 77% coverage at  $\alpha = 90^\circ$  (note that the maxima of the polarization phase functions occur at somewhat smaller and larger phase angles, respectively).

In Fig. 3.7, we show  $\Delta\pi F_n$  and  $\Delta P$  for the planets in Fig. 3.6 when calculated using the HI-code and the HH-code. The difference in flux is negative for all values of  $\alpha$ : the HI-code thus gives smaller fluxes than the HH-code for the same coverage. At  $\alpha = 0^\circ$ ,  $\Delta\pi F_n$  is -0.14 for 23% coverage, increases up to -0.21 for 43% coverage, and decreases again to -0.07 for 77% coverage. In differences in polarization show that for small coverages, the HI-code gives significantly higher values of  $P$  than the HH-code. The reason is of course that for small coverages, the white pixels are mostly located near the limb of the planetary disk, where they contribute little to the total signal.

Figure 3.8 shows  $\pi F_n$  and  $P$  for planets with caps covering 23% of the disk

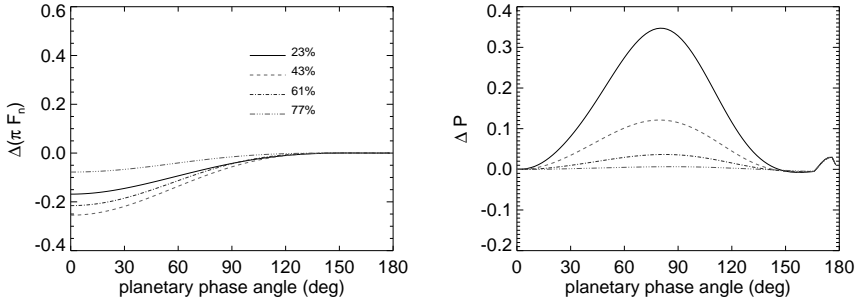


**Figure 3.7:**  $\Delta\pi F_n$  and  $\Delta P_s$  between the phase functions of the capped planets of Fig. 3.6 as calculated using the HI-code and the HH-code. The caps occupy 23% (black, solid line), 43% (red, dashed line), 61% (blue, dashed-dotted line) and 77% (green, dashed-triple-dotted line) of the planet.

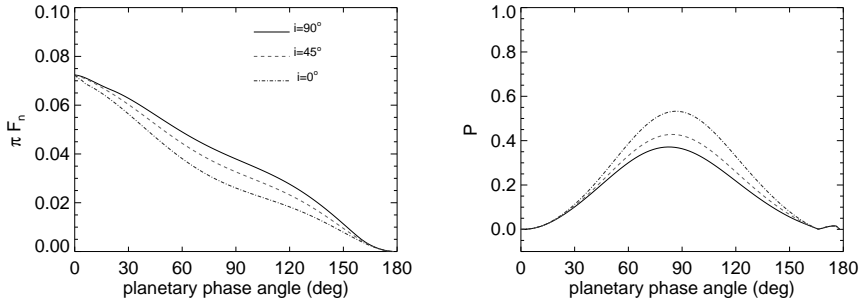


**Figure 3.8:**  $\pi F_n$  and  $P$  as functions of  $\alpha$  for black, cloud-free planets with white, hemispherical caps that occupy 23% of the planet. The locations of the caps are:  $0^\circ$  (black, solid line), indicating the caps are on the 'north' and 'south' poles of the planet,  $45^\circ$  (red, dashed line), and  $90^\circ$  (blue, dashed-dotted line), with the caps on the 'eastern' and 'western' sides of the planetary disk.

for three different locations of the caps. The three different flux phase functions show the relatively small effects of different fractions of the caps being visible at a given phase angle. The polarization phase functions are all fairly symmetric around  $\alpha = 90^\circ$ , especially for the planet with its caps at the poles of the planet.

Figure 3.9 shows  $\Delta\pi F_n$  and  $\Delta P$  for the three model planets of Fig. 3.8 as

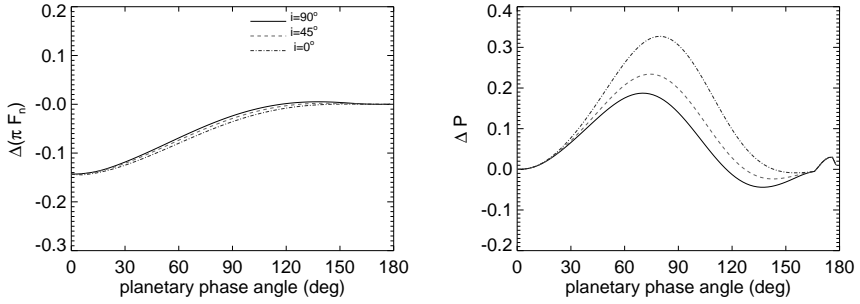


**Figure 3.9:**  $\Delta\pi F_n$  and  $\Delta P_s$  between the phase functions of the capped planets of Fig. 3.8 as calculated using the HI-code and the HH-code. The cap locations are:  $0^\circ$  (black, solid line),  $45^\circ$  (red, dashed line), and  $90^\circ$  (blue, dashed–dotted line).

calculated using the HH-code and the HI-code. As can be seen, the  $\Delta\pi F_n$  are fairly independent of the caps' position angle. This implies that it would be difficult to retrieve information about the position of the caps from the flux alone. polarization appears to be more sensitive to the location of the caps. In particular, the  $\Delta P$  are several percentage points depending on the location and on  $\alpha$ . Around  $\alpha = 90^\circ$ , where exoplanets have a relatively high chance of being observed with direct detection methods, the differences in  $\Delta P$  are about 0.12 for the planet with the eastern and western caps, implying that the accuracy of the polarimetry should be larger than 0.10 to be able to establish their existence.

### 3.4 Application to Earth–like planets

In this section, we present flux and polarization signals of planets with horizontally inhomogeneous Earth–like surface coverages and patchy cloud layers. In reality, the Earth exhibits a large variation in atmospheric temperature and pressure profiles, cloud properties (both on macro- and micro-scales) and surface properties. To avoid introducing too many variables, we assume a single temperature and pressure profile across our model planet, the so–called mid–latitude summer profile from (McClatchey et al. 1972), a single type of cloud particles and cloud properties (optical thickness and vertical distribution), and a surface that is covered by either ocean or sand (a continent).

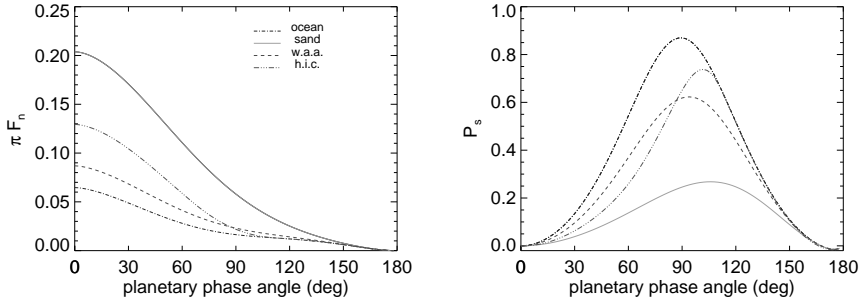


**Figure 3.10:**  $\pi F_n$  and  $P_s$  as functions of  $\alpha$  for a model planet covered by ocean and with a center continent of sand between  $\pm 22^\circ$  longitude and  $\pm 50^\circ$  latitude. (green, dashed–triple-dotted line). Also plotted: the functions for a homogeneous ocean planet (blue, dashed–dotted line), a homogeneous sand planet (orange, solid line) and a weighted sum of these with  $\sim 16\%$  sand and  $\sim 84\%$  ocean (gray, dashed line).

### 3.4.1 Surface inhomogeneities

First, we present the signals of a planet with a sandy continent surrounded by ocean. The continent extends between longitudes of  $\pm 22^\circ$  and latitudes of  $\pm 50^\circ$  (measured with respect to the subobserver point). The sand surface reflects Lambertian (unpolarized and isotropically) with an albedo of 0.25. This albedo is taken from the ASTER spectral library and should be representative for a sand surface on Earth at  $\lambda = 0.55 \mu\text{m}$ . The ocean is black. The planetary atmosphere is cloud-free, with a total gas optical thickness of 0.1 (no absorption), which corresponds to a wavelength of  $0.55 \mu\text{m}$ .

Figure 3.10 shows  $\pi F_n$  and  $P_s$  as functions of  $\alpha$  for the model planet as calculated with our HI-code and the HH-code (combined with the weighted averages method), and, to compare, for model planets that are completely covered by sand or ocean. Both in  $\pi F_n$  and in  $P_s$ , there are significant differences between the signals from the HI-code and the HH-code, depending on the phase angle. At  $\alpha = 0^\circ$ , the difference  $\Delta\pi F_s$  is  $\sim 30\%$ . With increasing phase angle, the fraction of the continent on the planet's nightside increases, and  $\pi F_n$  calculated with the HI-code decreases faster than that calculated with the HH-code. The polarization phase function calculated using the HI-code is more asymmetric than that calculated using the HH-code. The largest absolute difference between the two curves is  $\sim 0.14$  (14%) at  $\alpha = 106^\circ$ .

Incidentally, for this planet, the flux and polarization signals calculated using the HI-code and the HH-code are virtually equal at  $\alpha = 90^\circ$ . At this phase angle, flux and polarization observations would thus not help to establish the existence of the continent. However, interpreting flux observations at smaller (larger) phase angles using the HH-code would result in an overestimation (underestimation) of the coverage with sand, while interpreting only polarization observations at smaller (larger) phase angles using the HH-code would result in an underestimation (overestimation) of the coverage with sand. The interpretation of the combined flux and polarization observations using the HH-code would fail and thus reveal that assuming a homogeneous mixture of sand and ocean pixels is not realistic.

### 3.4.2 Atmospheric inhomogeneities

The next model planet has a black surface, a gaseous atmosphere with optical thickness of 0.1 (no absorption), and a patchy cloud layer with an optical thickness of 2.0. The clouds are composed of liquid water particles described in size by the standard distribution of Hansen & Travis (1974), with an effective radius of  $2.0 \mu\text{m}$  and an effective variance equal to 0.1 (model A particles of Chapter 2). The single scattering albedo of our particles at  $0.55 \mu\text{m}$  is 0.999534. For a detailed description of the single scattering properties of our cloud particles see Chapter 2. The cloud layer is patchy (the clouds are composed of fully cloud covered pixels that cluster in random manner across the planetary surface) in the horizontal direction, but its vertical extension is the same all over the planet, namely from 3 km to 4 km in Earth's atmosphere (279 K to 273 K).

Figure 3.11 shows  $\pi F_n$  and  $P$  as functions of phase angle  $\alpha$  of the model planet for different cloud coverages as calculated using the HI- and the HH-code. The flux phase functions for the different cloud coverages have different strengths, but very similar shapes. The phase functions as calculated using the HH-code have slightly sharper features near  $\alpha = 0^\circ$ . Note that the bump in the curves near  $\alpha = 30^\circ$  is the signature of the primary rainbow (see e.g. Chapter 2): light that is scattered once by the cloud particles. As expected, the difference between the fluxes calculated with the two codes are small for small and large percentages of cloud coverage. For an intermediate, almost Earth-like, coverage of 42.3%,  $\Delta\pi F_n$  is as large as 15% at  $\alpha = 0^\circ$ . In this case, using the HH-code to interpret the flux reflected by the patchy cloudy planet near  $\alpha = 0^\circ$  would yield a cloud coverage of  $\sim 53\%$ .

The polarization phase functions clearly show the different contributions of the light that is Rayleigh scattered by the gas molecules above and in particular between the patches of clouds (the strong values around  $\alpha = 90^\circ$ ) and that of the light

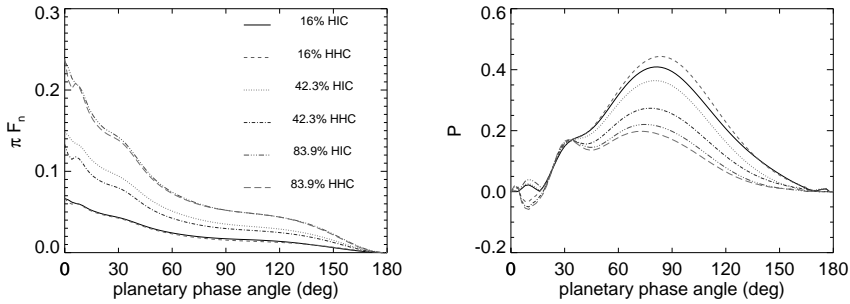


**Figure 3.11:**  $\pi F_n$  and  $P_s$  as functions of  $\alpha$  for a model ocean planet with patchy clouds that cover 16%, 42.3%, or 83.9% of the planet. The curves as calculated using the HH-code and the weighted sum approximation are also shown.

that is scattered by the cloud articles (the primary rainbow). Clearly, the larger the coverage of the clouds, the smaller the contribution of the purely Rayleigh scattered light to the total signal. Adding clouds to our model planet decreases the amount of purely Rayleigh scattered light, and thus decreases  $P$  around  $\alpha = 90^\circ$ . The strength of the primary rainbow in  $P$  is insensitive to the cloud coverage because adding clouds does not change the fraction of multiply scattered light within the clouds (the clouds have the same optical properties), which mostly determines the strength of the rainbow on these planets. The Rayleigh scattering polarization maximum around  $\alpha = 90^\circ$  does influence the contrast of the rainbow feature: for low cloud coverages it forms a shoulder on the Rayleigh scattering maximum, while for high coverages, it is a local maximum..

For small and large percentages of cloud coverage, the differences in the polarization phase functions due to using either the HI- or the HH-code are at most a few percent points around  $\alpha = 90^\circ$  ( $\sim 4\%$  for 16%, and  $\sim 3\%$  for 83.9% coverage). The differences are largest for the intermediate cloud coverage: about 10% for 42.3% coverage. In this case, using the HH-code to interpret the polarization reflected by the patchy cloudy planet near  $\alpha = 90^\circ$ , would yield a cloud coverage of  $\sim 25\%$ . The degree of polarization calculated with the HI-code, and thus  $\Delta P$  too, depends not only on the cloud coverage, but also on the locations of the clouds across the planet. Not surprisingly, this sensitivity is highest for intermediate cloud coverages.

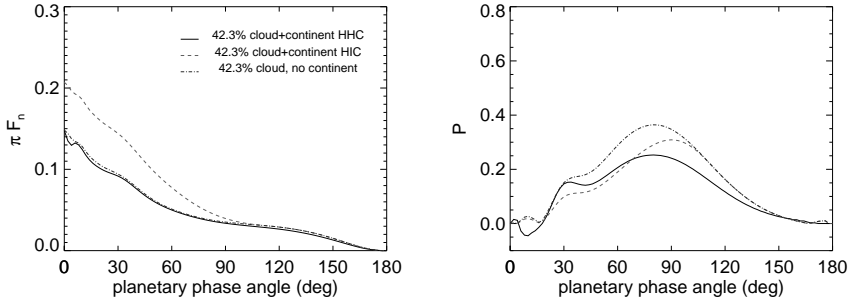


**Figure 3.12:**  $\pi F_n$  and  $P_s$  as functions of  $\alpha$  for a model ocean planet with a central sandy continent and 42.3% cloud coverage as calculated using the HI-code (red, dashed line) and the HH-code and the weighted sum approximation (black, solid line). For comparison, the curves for a model ocean planet without the continent and with 42.3% cloud coverage are also shown (blue, dashed–dotted line).

### 3.4.3 Atmospheric and surface inhomogeneities

Finally, we present the flux and polarization signals of planets with patchy clouds (see Sect. 3.4.2), and a sandy continent in the middle of a black ocean (see Sect. 3.4.1). Figure 3.12 shows  $\pi F_n$  and  $P$  as functions of  $\alpha$  for 42.3% cloud coverage. The phase functions as calculated using the HH-code and the HI-code results for a cloudy planet without a continent are also shown.

The continent strongly increases  $\pi F_n$ . The increase will usually depend on the location of the clouds and the continent. In this case, the continent is located in the middle of the planetary disk, and thus has a large influence. Since only a small fraction ( $\sim 8\%$ ) of the pixels on the disk contain sand, the flux calculated with the HH-code is only marginally higher than that calculated with the HI-code and without a continent (see Fig. 3.11). Inversely, if the HH-code would be used to interpret the flux signal of the cloudy planet with the continent, a 55% continental coverage and 24% clouds would be found.

The presence of the Lambertian reflecting continent below the clouds decreases the polarization phase function and shifts the maximum  $P$  towards larger  $\alpha$ , when compared to the polarization phase function of the cloudy ocean planet. The primary rainbow is still visible in the phase function, albeit more like a shoulder than a local maximum.

Using polarimetry only, a straightforward fit to the polarization phase function

with the HH-code would estimate the continental coverage at about 17% and the cloud coverage at 24%. When both  $\pi F_n$  and  $P$  are taken into account the best fit is acquired for the case of 22% continental coverage and 19% cloud coverage.

### 3.5 Summary and conclusions

We have presented a numerical code that can be used to calculate disk integrated total and polarized fluxes of starlight that is reflected by horizontally inhomogeneous exoplanets, e.g. planets that are covered by oceans and continents, and/or overlaid by a patchy cloud deck.

For most types of model planets, our code for horizontally inhomogeneous planets (the HI-code) is computationally much more expensive than the code for horizontally homogeneous planets by Stam et al. (2006a) combined with the so-called weighted sum approximation to simulate fluxes of horizontally inhomogeneous planets (the HH-code). In the latter method, total and polarized flux signals of different horizontally homogeneous planets are summed using weighting factors depending on which fraction of the illuminated and visible part of the horizontally inhomogeneous planet is represented by each type of planet. Only for planets with a large variation of horizontal inhomogeneities, such as a large number of different surface and cloud coverages, the computing time for the HH-code approaches that for the HI-code.

The main advantage of using the HI-code instead of the HH-code is obviously the ability to simulate signals of horizontally inhomogeneous planets. Other advantages of the HI-code are that since every pixel on the planet is treated separately, it allows taking into account effects of e.g. the non-sphericity of a planet, shadowing by planetary rings, and a spatial extension of the illuminating source.

Since for most model planets, our HI-code consumes much more computing time than the HH-code (Stam et al. 2006a), it is interesting to investigate the influences of horizontal inhomogeneities on the total and polarized fluxes of starlight that is reflected by a planet. For three types of horizontally inhomogeneous planets covered by black and white surface pixels and overlaid by a gaseous atmosphere, we have calculated the fluxes and the degree of polarization as functions of the planetary phase angle  $\alpha$  and compared them with results from the HH-code assuming the same percentage of black and white surface pixels and the same model atmosphere. Horizontal inhomogeneities can leave significant traces in both the reflected total flux  $\pi F_n$  and the degree of linear polarization. However, while horizontal inhomogeneities appear to mostly influence the total amount of reflected flux and not so much the shape of the planet's flux phase functions, they can

strongly change the planet's polarization phase functions in shape and strength. Indeed, fitting a planet's polarization phase function using the HH-code would yield very different fractions of disk coverage (up to several tens of percent).

We also used the HI-code to calculate flux and polarization signals of Earth-like planets with surface and/or patchy clouds. These calculations confirmed that the shape of a planet's flux phase function is fairly independent of the horizontal inhomogeneities. Obviously, the absolute values of the flux phase function does depend on the inhomogeneities, but it will also depend on the radius of the planet (in this Chapter we assumed a planetary radius equal to one), which thus would have to be known accurately to fit the flux phase function. The polarization phase function appears to be rather sensitive to the inhomogeneities, both its absolute values and the shape of the curve (e.g. location maximum value). Because the degree of polarization is a ratio, it is independent of the radius of a planet. The flux and polarization signals of planets are wavelength dependent (see e.g. Stam 2008), therefore the observability of horizontal inhomogeneities will also depend on the wavelength. In particular, at short wavelengths, the gas optical thickness is larger than at longer wavelengths, and will thus hamper the observations of the surface. Future studies could focus on which spectral bands should be combined to optimize retrieval schemes.

In the presence of liquid water clouds, the strength of the primary rainbow in the flux phase functions of Earth-like planets increases with increasing cloud coverage. Whether or not it would be detectable depends strongly on the sensitivity and stability of the observing instrument. In the polarization phase function, the strength of the rainbow is almost independent of the cloud coverage as long as the planet's surface is very dark (i.e. does not add too much unpolarized flux to the total signal). A bright surface, such as a sandy continent, decreases the strength of the rainbow feature.

Properly accounting for horizontal inhomogeneities appears to significantly influence reflected fluxes and polarization signals, and should eventually be applied to interpret observations of horizontally inhomogeneous exoplanets or e.g. observations of Earth-shine (Sterzik et al. 2012). The HH-code (horizontally homogeneous planets combined with the weighted sum approximation), however, is still a strong tool for simulating signals to be used for the design and optimization of exoplanet observations, because its simulations cover the range of total and polarized fluxes that we can expect to observe. Because flux and polarization phase functions have different sensitivities to the inhomogeneities, a combination of flux and polarization observations would help to retrieve the actual planetary parameters.

Our results, and especially the differences between the fluxes and degrees of polarization of the reflected starlight, indicate which accuracies should be reached

with flux and/or polarization observations in order to detect horizontal inhomogeneities on a planet. As such they can drive the design of instruments for exoplanet characterization. Assuming a super-Earth exoplanet (with a radius of  $1.5 r_{\oplus}$ ) orbiting a Sun-like star at 1 pc from the observer at a 40-meter telescope (such as the E-ELT), a back-of-the-envelope calculation shows that a few nights of integration time (a total of 20 hours) could yield an accuracy of  $10^{-3}$ . The phase angle of a planet in an Earth-like orbit would change by  $\sim 3^\circ$  during that time. For this calculation we ignored the influence of stellar background light on the observation, and we didn't include any actual instrument parameters, such as spectral bandwidths. Until results such as ours are combined with a realistic instrument and telescope simulator, the integration time estimate should thus be considered as a rough value.

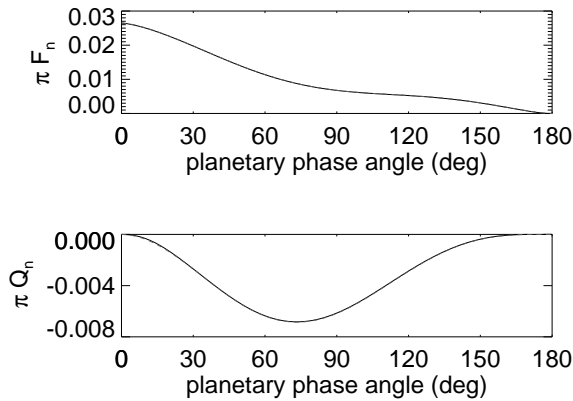


**Figure 3.13:** Normalised reflected fluxes  $\pi F_n$  and  $\pi Q_n$  as functions of the planetary phase angle  $\alpha$  for a black planet with a gaseous atmosphere as calculated using the HH-code (solid lines) and the HI-code (dashed lines). The solid and dashed lines coincide.

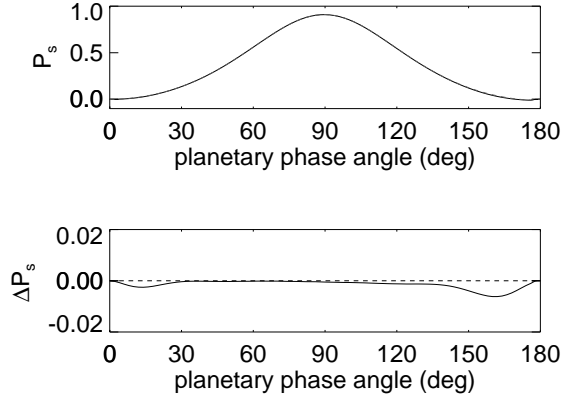


**Figure 3.14:** The degree of polarization  $P_s$  corresponding to the fluxes shown in Fig. 3.13 (the two lines coincide) and the absolute difference between the two lines.

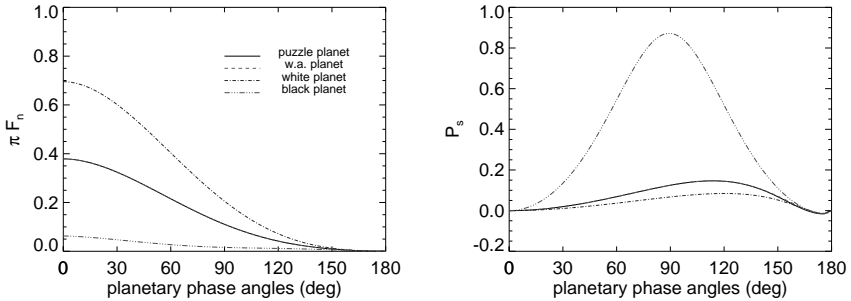


**Figure 3.15:**  $\pi F_n$  and  $P_s$  as functions of  $\alpha$  for a black planet (gray, dashed–triple–dotted line), a white planet (blue, dashed–dotted line), and a planet with a gaseous atmosphere and its surface covered by alternating black and white pixels (black, solid line). The latter curves coincide with those calculated using horizontally homogeneous planets and a weighted sum approximation (red, dashed line). All planets are cloud-free.

## A. Testing our numerical code

Here, we present the results of testing our numerical code for horizontally inhomogeneous planets (from hereon the HI-code). We have tested our code by comparing it to results of the code for horizontally homogeneous planets Stam et al. (2006a) (from hereon the HH-code).

### A1. Horizontally homogeneous planets

For the first comparison between our HI-code and the HH-code, we used both codes to calculate the light reflected by a model planet with a black surface and a gaseous, Rayleigh scattering atmosphere with a total optical thickness of about 0.1. For the HI-code, the planet was divided into pixels of  $2^\circ \times 2^\circ$  (latitude  $\times$  longitude). Figure 3.13 shows the excellent agreement between the reflected fluxes  $\pi F_n$  and  $\pi Q_n$  as functions of phase angle  $\alpha$  calculated using the two codes (because the planet is mirror-symmetric with respect to the reference plane,  $\pi U_n = 0$ ). The absolute difference between the fluxes calculated by the two codes is smaller than  $10^{-5}$ . Figure 3.14 shows the degree of polarization  $P_s (= -Q/F)$  (see Eq. 3.3) calculated using both codes, and the absolute difference  $\Delta P_s$  between the curves.  $\Delta P_s$  is largest around small ( $15^\circ$ ) and large ( $160^\circ$ ) phase angles, which is due to the size of the pixels. Since in the HI-code, we use one set of angles  $\theta_0$ ,  $\theta$ ,  $\Delta\phi$ , and  $\beta_2$  for each pixel, the larger a pixel, the less this set of angles represents the range of angles across the pixel. The error is largest for pixels along the planetary limb and terminator, and thus for the large and small phase angles (at the small angles, the degree of polarization in the centre of the disk is close to zero, making the contribution of the limb pixels thus significant). At  $\alpha = 0^\circ$  and  $180^\circ$ ,  $P_s$  of the planet is zero and thus  $\Delta P_s$ , too.

For a model planet with a gaseous atmosphere, the differences between the results of the two codes appear to be fairly independent of the albedo of a (Lambertian reflecting) surface: with a white surface, the absolute differences in  $\pi F_n$  and  $\pi Q_n$ , and  $\Delta P_s$  are similar to those with a black surface.

For a model planet with a horizontally homogeneous cloud layer of optical thickness 1, composed of the model A cloud particles of Chapter 2, and a surface albedo of 0.1, the absolute difference in the fluxes increased slightly to a maximum value of  $5 \times 10^{-5}$  and the maximum  $\Delta P_s$  increased to  $\sim 0.0062$ . These differences didn't change significantly when other (e.g. larger) cloud particles were used.

The comparison with the HH-code shows that the integration across the disk by our HI-code is accurate enough for application to horizontally homogeneous planets, provided small enough pixels are used across the disk.

## A2. Horizontally inhomogeneous planets

For a second test of our HI-code, we used model planets with surfaces covered by two types of  $2^\circ \times 2^\circ$  pixels that alternate in longitude and latitude (they thus look like chess boards). The equator of each planet coincides with the planetary scattering plane. The planetary atmospheres are gaseous, Rayleigh scattering and have an optical thickness of 0.1. While our HI-code can handle these types of planets, the HH-code cannot. Therefore, as in Stam (2008), weighted sums of flux vectors reflected by horizontally homogeneous planets are used to approximate the flux vectors of horizontally inhomogeneous planets. The flux vector of a planet covered by  $J$  different types of pixels (with a different atmosphere and/or surface) is thus calculated using

$$\pi\vec{F}(\alpha) = \sum_{j=1}^J w_j \pi\vec{F}_j(\alpha) \quad \text{with} \quad \sum_{j=1}^J w_j = 1 \quad (3.9)$$

with  $\pi F_j$  the flux vector of starlight reflected by a planet that is completely covered by type  $j$  pixels, and with  $w_j$  the fraction of type  $j$  pixels on the horizontally inhomogeneous planet.

Figure 3.15 shows  $\pi F_n$  and  $P_s$  as functions of phase angle  $\alpha$  for a planet with its surface covered by alternating black and Lambertian reflecting white pixels as calculated with the HI-code and the HH-code (the latter combined with the weighted sum approximation, see Eq. 3.9). For comparison,  $\pi F_n$  and  $P_s$  are also shown for horizontally homogeneous black and white planets.

The absolute difference between the fluxes of starlight reflected by the black-and-white planet as calculated using the HI-code and the HH-code is smaller than  $7 \times 10^{-5}$ , and between the degrees of polarization smaller than 0.005 across the whole phase angle range. It appears that the differences between the results of the two codes depend slightly on the surface albedo: decreasing the albedo of pixels from 1.0 to 0.24 (which is typical for a sand surface at  $0.55 \mu\text{m}$ ), the difference in the flux decreases to  $5 \times 10^{-5}$  and in the polarization to 0.004.

The comparison with the HH-code applied to horizontally homogeneous planets and using the weighted sum approximation shows that our HI-code is accurate enough for application to horizontally inhomogeneous planets, provided enough pixels are used across the disk.



# Looking for the rainbow

---

Based on:

T. Karalidi, D. M. Stam and J. W. Hovenier, *Looking for the rainbow on exoplanets with liquid and icy water clouds*, *Astronomy & Astrophysics*, volume 548, id A90, 2012, reproduced with permission ©ESO

**Abstract** *Aims.* Looking for the primary rainbow in starlight that is reflected by exoplanets appears to be a promising method to search for liquid water clouds in exoplanetary atmospheres. Ice water clouds, that consist of water crystals instead of water droplets, could potentially mask the rainbow feature in the planetary signal by covering liquid water clouds. Here, we investigate the strength of the rainbow feature for exoplanets that have liquid and icy water clouds in their atmosphere, and calculate the rainbow feature for a realistic cloud coverage of Earth. *Methods.* We calculate flux and polarization signals of starlight that is reflected by horizontally and vertically inhomogeneous Earth-like exoplanets, covered by patchy clouds consisting of liquid water droplets or water ice crystals. The planetary surfaces are black. *Results.* On a planet with a significant coverage of liquid water clouds only, the total flux signal shows a weak rainbow feature. Any coverage of the liquid water clouds by ice clouds, however, dampens the rainbow feature in the total flux, and thus the discovery of liquid water in the atmosphere. On the other hand, detecting the primary rainbow in the polarization signal of exoplanets appears to be a powerful tool for detecting liquid water in exoplanetary atmospheres, even when these clouds are partially covered by ice clouds. In particular, liquid water clouds covering as little as 10%–20% of the planetary surface, with more than half of these covered by ice clouds, still create a polarized rainbow feature in the planetary signal. Indeed, calculations of flux and polarization signals of an exoplanet with a realistic Earth-like cloud coverage, show a strong polarized rainbow feature.

## 4.1 Introduction

The discovery of the first exoplanet orbiting a main sequence star almost two decades ago (Mayor & Queloz 1995) inaugurated a new era in astronomy. As

of today, more than 700 exoplanets have been detected (source: The extrasolar planets encyclopaedia). Telescope instruments and satellite missions, like for example COROT (CONvection, ROTation & planetary Transits) (Baglin et al. 2006), NASA's Kepler mission (Koch et al. 1998), HARPS (High Accuracy Radial Velocity Planet Searcher) (e.g. Pepe et al. 2004), Super-WASP (Deming et al. 2012), and, in the near future, GPI (Gemini Planet Imager) (Macintosh et al. 2008) on the Gemini observatory (first on the telescope on the southern hemisphere) and SPHERE (Spectro-Polarimetric High-Contrast Exoplanet Research) (e.g. Dohlen et al. 2008, Roelfsema et al. 2011) on ESO's Very Large Telescope (VLT), to name a few, will rapidly increase the number of detected exoplanets.

The detection methods used and the accuracy of our instruments result in most of the exoplanets detected up to today being giants, even though in recent years the lower mass limit of our detections has been pushed down allowing for the detection of more than 30 super-Earth planets. With an increasing possibility for the detection of the first Earth-like planets in the next decade, an important factor to consider is how ready our models will be to interpret the observations.

An important factor that needs to be taken into account for future efforts to detect signatures of life on other planets is the possible inhomogeneity of the planetary surface and atmosphere (Tinetti et al. 2006b, and references therein). The existence of continents, oceans and variable atmospheric patterns (cloud patches etc), as well as their distributions across the planetary surface can have a large impact on the observed signal. For this reason, the models that we use to interpret the observations should be able to handle inhomogeneous planets.

There exist a number of models that deal with the brightness of inhomogeneous exoplanets (Ford et al. 2001, Tinetti 2006, Montañés-Rodríguez et al. 2006, Pallé et al. 2008, to name a few). All of the models show the importance of planetary inhomogeneity and temporal variability on the modelled planetary signal. The pioneering work of Ford et al. (2001) as well as later studies (e.g. Oakley & Cash 2009), show a clear diurnal variability of the modelled Earth-as-an-exoplanet signal due to areas of different albedo passing in and out of the observational field of view.

Among the factors that influence the planetary signal, clouds have a prominent role. Observations of earthshine for example, have shown that clouds can induce a considerable daily variation in the planetary signal. The amount of variability observed differs slightly among the observations ( $\sim 10\%$  for Pallé et al. (2004),  $\sim 5\%$  for Goode et al. (2001) and a few percent for Cowan et al. (2009)). Cloud coverage and variability can also influence to a large degree the interpretation of the observations. Oakley & Cash (2009) for example find that mapping the planetary surface is only possible for cloud coverages smaller than the mean Earth one. Even in the case of giant planets or dwarf stars, clouds play a crucial role in defining the

atmospheric thermal profile and eventually spectra (Marley et al. 2010).

At present, the characterization of exoplanets is mainly done using planetary transits with instruments on e.g. the Hubble and Spitzer Space Telescopes (see e.g. Ehrenreich et al. 2007, Deming et al. 2011, Tinetti & Griffith 2010), and for some planets, even with ground-based instrumentation (see e.g. Snellen et al. 2010b, Brogi et al. 2012, de Mooij et al. 2012). With the transit method though, during the primary transit, the observed starlight has only penetrated the upper layers of the planetary atmosphere. Cloud layers at lower altitudes could for example block out the signal from lower atmospheric layers or a possible planetary surface. Even with the help of secondary transits, the characterisation of Earth-like exoplanets in the habitable zone of a solar-type star would not be possible, since these planets would yield too weak a signal (Kaltenegger & Traub 2009). Direct observations of reflected starlight from the planet could solve this problem, since then information from the lower atmospheric layers and surface could survive in the observed planetary signal. The combination in these cases of flux and polarization observations could provide us with a crucial tool to break any possible retrieval degeneracies (for example, such as between optical thicknesses and single scattering albedo's or cloud particle sizes) that flux only measurements may present. A first detection of an exoplanet using polarimetry was claimed by Berdyugina et al. (2008). Subsequent polarization observations by Wiktorowicz (2009) could, however, not confirm this detection. In 2011 Berdyugina et al. (2011) presented another detection of the same planet at shorter wavelengths, which still awaits confirmation by follow-up observations. Telescope instruments like GPI (Macintosh et al. 2008) and SPHERE (e.g. Dohlen et al. 2008, Roelfsema et al. 2011), which have polarimetric arms that have been optimized for exoplanet detection, are expected to detect and characterize exoplanets with polarimetry in the near future.

The power of polarization in studying planetary atmospheres and surfaces has been shown multiple times in the past through observations of Solar System planets (including Earth itself)(see for example Hansen & Hovenier 1974, Hansen & Travis 1974, Mishchenko 1990, Tomasko et al. 2009), as well as by modeling of solar system planets or giant and Earth-like exoplanets (e.g. Stam (2003), Stam et al. (2004), Saar & Seager (2003), Seager et al. (2000), Stam (2008) and Chapter 2). Polarization provides us with a unique tool for the detection of liquid water on a planetary atmosphere and surface. Williams & Gaidos (2008) e.g. use polarization to detect the glint of starlight reflected on liquid surfaces (oceans) of exoplanets and Zuger et al. (2010, 2011) conclude that the existence of an atmosphere as thick as Earth's would hide any polarization signature of the underlying oceans. Probably the most interesting feature to look for in the polarization signal of exoplanets is the rainbow.

The rainbow is a direct indication of the presence of liquid water droplets in a planetary atmosphere (see e.g. Bailey (2007) and Chapter 2). Its angular position depends strongly on the refractive index of the scattering particles and slightly on their effective radius (see Chapter 2 and references therein). Its existence, most pronounced in polarization observations, can be masked by the existence of ice clouds (Goloub et al. 2000). The latter are often located above thick liquid water clouds and can dominate the appearance of the reflected polarization signal for ice cloud optical thicknesses larger than 2 (Goloub et al. 2000).

In Chapter 3, we calculated flux and polarization signals for horizontally homogeneous model planets that were covered by liquid water clouds. The polarization signals of these planets clearly contained the signature of the rainbow. The polarization signals of the quasi horizontally inhomogeneous planets (where weighted sums of horizontally homogeneous planets are used to approximate the signal of a horizontally inhomogeneous planet) as presented by Stam (2008) also show the signature of the rainbow. However, to confirm that realistically horizontally inhomogeneous planets, with patchy liquid water clouds, and with patchy liquid water clouds covered by patchy ice clouds, also show the signature of the rainbow, the algorithm for horizontally inhomogeneous planets as described in Chapter 3 is required. In this Chapter we will do exactly that: using the algorithm of Chapter 3 to look for the rainbow on horizontally inhomogeneous planets, that are covered by different amounts of liquid and icy water clouds.

This Chapter is organized as follows. In Sect. 4.2, we give a short description of polarized light and our radiative transfer algorithm, and present the model planets and the clouds we use. In Sect. 4.3, we investigate the influence of the liquid water cloud coverage on the strength of the rainbow feature of a planet in flux and polarization. In Sects. 4.4 and 4.5 we investigate the influence of different clouds layers, respectively with different droplet sizes and with different thermodynamic phases (liquid or ice), on the strength of the rainbow feature. An interesting test case for the detection of a rainbow feature is of course the Earth itself. In Sect. 4.6, we use realistic cloud coverage, optical thickness and thermodynamic phase data from the MODIS satellite instrument to investigate whether the rainbow feature of water clouds would appear in the disk integrated sunlight that is reflected by the Earth. Finally, in Sect. 4.7, we present a summary of our results and our conclusions.

## 4.2 Calculating flux and polarization signals

### 4.2.1 Defining flux and polarization

We describe starlight that is reflected by a planet by a flux vector  $\pi\vec{F}$ , as follows

$$\pi\vec{F} = \pi \begin{bmatrix} F \\ Q \\ U \\ V \end{bmatrix}, \quad (4.1)$$

where parameter  $\pi F$  is the total flux, parameters  $\pi Q$  and  $\pi U$  describe the linearly polarized flux and parameter  $\pi V$  the circularly polarized flux (see e.g. Hansen & Travis 1974, Hovenier et al. 2004, Stam 2008). All four parameters depend on the wavelength  $\lambda$ , and their dimensions are  $\text{W m}^{-2}\text{m}^{-1}$ . Parameters  $\pi Q$  and  $\pi U$  are defined with respect to a reference plane, and as such we chose here the planetary scattering plane, i.e. the plane through the center of the star, the planet and the observer. Parameter  $\pi V$  is usually small (Hansen & Travis 1974), and we will ignore it in our numerical simulations. Ignoring  $\pi V$  will not introduce significant errors in our calculated total and polarized fluxes (Stam & Hovenier 2005).

The linearly polarized flux,  $\pi F_P$  of flux vector  $\pi\vec{F}$  is independent of the choice of the reference plane and is given by

$$\pi F_P = \pi\sqrt{Q^2 + U^2}, \quad (4.2)$$

while the degree of (linear) polarization  $P$  is defined as the ratio of the linearly polarized flux to the total flux, as follows

$$P = \frac{F_P}{F} = \frac{\sqrt{Q^2 + U^2}}{F}. \quad (4.3)$$

For a planet that is mirror-symmetric with respect to the planetary scattering plane, parameter  $U$  will be zero. In this case we use the *signed* degree of linear polarization  $P_s = -Q/F$ , which includes the direction of polarization: if  $P_s > 0$  ( $P_s < 0$ ), the light is polarized perpendicular (parallel) to the plane containing the incident and scattered beams of light. A planet with patchy clouds will usually not be mirror-symmetric with respect to the planetary scattering plane, and hence  $U$  will usually not equal zero.

The flux vector  $\pi\vec{F}$  of stellar light that has been reflected by a spherical planet with radius  $r$  at a distance  $d$  from the observer ( $d \gg r$ ) is given by (Stam et al.

2006a)

$$\pi\vec{F}(\lambda, \alpha) = \frac{1}{4} \frac{r^2}{d^2} \vec{S}(\lambda, \alpha) \pi\vec{F}_0(\lambda). \quad (4.4)$$

Here,  $\lambda$  is the wavelength of the light and  $\alpha$  the planetary phase angle, i. e. the angle between the star and the observer as seen from the center of the planet. Furthermore,  $\vec{S}$  is the  $4 \times 4$  planetary scattering matrix (Stam et al. 2006a) with elements  $a_{ij}$  and  $\pi\vec{F}_0$  is the flux vector of the incident stellar light. For a solar type star, the stellar flux can be considered to be unpolarized when integrated over the stellar disk (Kemp et al. 1987).

We assume that the ratio of the planetary radius  $r$  and the distance to the observer  $d$  is equal to one, and that the incident stellar flux  $\pi F_0$  is equal to  $1 \text{ W m}^{-2} \text{ m}^{-1}$ . The hence normalised flux  $\pi F_n$  that is reflected by a planet is thus given by

$$\pi F_n(\lambda, \alpha) = \frac{1}{4} a_{11}(\lambda, \alpha) \quad (4.5)$$

(see Stam (2008), Chapter 2), and corresponds to the planet's geometric albedo  $A_G$  when  $\alpha = 0^\circ$ . The corresponding normalized polarized flux is given by

$$\pi F_{n,P}(\lambda, \alpha) = \frac{1}{4} \sqrt{a_{21}(\lambda, \alpha)^2 + a_{31}(\lambda, \alpha)^2}, \quad (4.6)$$

with  $a_{21}$  and  $a_{31}$  elements of the planetary scattering matrix. Our normalized fluxes  $\pi F_n$  can straightforwardly be scaled for any given planetary system using Eq. 4.4 and inserting the appropriate values for  $r$ ,  $d$  and  $\pi F_0$ . The degree of polarization  $P$  is independent of  $r$ ,  $d$  and  $\pi F_0$ , and will thus not require any scaling.

## 4.2.2 The radiative transfer calculations

The code that we use to calculate the total and polarized fluxes of starlight that is reflected by a model planet fully includes single and multiple scattering, and polarization. It is based on the same efficient adding-doubling algorithm (de Haan et al. 1987) used by Stam et al. (2006a), Stam (2008). To calculate flux and polarization signals of horizontally inhomogeneous planets, we divide a model planet in pixels with a size such that we can assume that the surface and atmospheric layers are locally plane parallel and horizontally homogeneous. We then use the code for horizontally inhomogeneous planets, as presented in Chapter 3: the contribution of every illuminated pixel that is visible to the observer to the planet's total and

polarized flux are calculated separately, the polarized fluxes are rotated to the common reference plane, and then all fluxes are summed up to get the disk-integrated planetary total and polarized fluxes. From these fluxes, the disk-integrated degree of linear polarization  $P$  is derived (Eq. 5.2).

As before (Chapter 3), we divide our model planets in plane-parallel, horizontally homogeneous (but vertically inhomogeneous) pixels of  $2^\circ \times 2^\circ$ . Our pixels are large enough to be able to ignore adjacency effects, i.e. light that is scattered and/or reflected within more than one pixel (e.g. light that is reflected by clouds in one pixel towards the surface of another pixel). These effects, that make the fluxes emerging from a given type of pixel dependent on the properties of the surrounding pixels, show up for higher spatial resolutions, for example, with pixels that are smaller than about  $1 \times 1 \text{ km}^2$  (Marshak et al. 2008).

### 4.2.3 The model planets

All model planets have a vertical inhomogeneous atmosphere on top of a black surface. The assumption of a black surface is a very good approximation for an ocean surface (without the glint), which covers most of the Earth's surface. We'll discuss the effects of brighter surfaces on our results where necessary. All model atmospheres have a pressure and temperature profile representative for a mid-latitude atmosphere (McClatchey et al. 1972) (see Fig. 4.1). We divide each model atmosphere in the same 16 layers. The total gaseous (Rayleigh) scattering optical thickness of the atmosphere is 0.097 at  $\lambda = 0.550 \mu\text{m}$  and 0.016 at  $\lambda = 0.865 \mu\text{m}$ . We do not include gaseous absorption, which is a good assumption at the wavelengths of our interest.

The flux and polarization signals of our model planets are fairly insensitive to the pressure and temperature profiles, but they are sensitive to the horizontal and vertical distribution of the clouds, and to the microphysical properties of the cloud particles. We will use two types of clouds: the first type consisting of liquid water droplets, and the second type consisting of water ice particles. The details of these particles will be discussed in Sect. 4.2.4. The liquid water clouds will be located below an altitude of 4 km (i.e. at pressures lower than 0.628 bars, which corresponds to temperatures higher than 273 K) and the ice clouds above that altitude.

We create our cloud maps by using an ISCCP yearly cloud map which we filter according to the clouds' optical thicknesses. Figure 4.2 shows a sample map for a model planet with a single cloud layer that covers  $\sim 25\%$  of the planet. As shown in Chapter 3, the precise location of clouds can influence in particular the polarized phase function of a planet (i.e. the degree of polarization of the reflected starlight

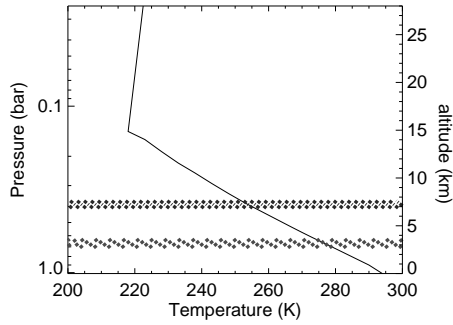


**Figure 4.1:** The atmospheric pressure and altitude as functions of the temperature for the model planets. The liquid water clouds are located below 4 km (for example in between 3 km and 4 km as in the gray, dotted area), and the ice clouds between 7 km and 8 km (blue, dashed–dotted area).

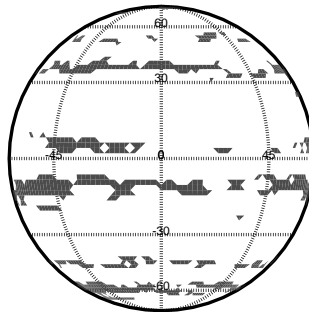


**Figure 4.2:** A sample map of our model planets. Here, the planetary atmosphere contains a single layer with clouds that cover  $\sim 25\%$  of the planet (the dark regions are the clouds).

as a function of the planetary phase angle). To avoid changes in  $\pi F_{n,P}$  and  $P$  due to the location of clouds when the coverage increases, we increase the cloud coverage of a planet by letting existing clouds grow in size. Cloudy regions thus remain cloudy, while surface patches are getting cloudy.

#### 4.2.4 The cloud particles

The liquid water cloud particles are spherical, with the standard size distribution given by (Hansen & Travis 1974)

$$n(r) = Cr^{(1-3v_{\text{eff}})/v_{\text{eff}}} e^{-r/r_{\text{eff}}v_{\text{eff}}}, \quad (4.7)$$

with  $n(r)dr$  the number of particles per unit volume with radius between  $r$  and  $r+dr$ ,  $C$  a constant of normalization,  $r_{\text{eff}}$  the effective radius and  $v_{\text{eff}}$  the effective variance of the distribution. Terrestrial liquid water clouds are in general composed of droplets with radii ranging from  $\sim 5 \mu\text{m}$  to  $\sim 30 \mu\text{m}$  (Han et al. 1994). We use either small droplets (type A), with  $r_{\text{eff}} = 2.0 \mu\text{m}$  and  $v_{\text{eff}} = 0.1$ , or larger droplets (type B) with  $r_{\text{eff}} = 6.0 \mu\text{m}$  and  $v_{\text{eff}} = 0.4$  (see also Chapter 2). The latter are similar to those used by van Diedenhoven et al. (2007) as average values for terrestrial water clouds. We use a wavelength independent refractive index of  $1.335+0.00001i$  (see Chapter 2 and references therein) For a given wavelength, and values of  $r_{\text{eff}}$  and  $v_{\text{eff}}$ , we calculate the extinction cross-section, single scattering albedo and the single scattering matrix using Mie-theory (de Rooij & van der Stap 1984) and normalized according to Eq. 2.5 of Hansen & Travis (1974).

Ice crystals in nature present a large variety of shapes, depending on the temperature and humidity conditions during their growth (Hess 1998). Even though the variety of shapes is large, Magono & Lee (1966) showed that only a small number of classes suffice for the categorization of most natural ice crystals. Until recently most researchers used perfect hexagonal columns and plates in order to model the light scattered by natural ice crystals, including halo phenomena. However, when these particles are oriented, they give rise to halos, which are rarely observed (Macke et al. 1996, Hess 1998). For this reason a number of models were created to model the signal of ice crystals without halo phenomena (Hess & Wiegner 1994, Macke et al. 1996, Hess 1998). In this Chapter we use an updated version of the model crystals of Hess (1998). Finally, we should mention that the sizes of most atmospheric ice crystals are considerably larger than the visible wavelengths we will use in this Chapter (Macke et al. 1996). In particular, the crystals we use in this Chapter range in size from  $\sim 6 \mu\text{m}$  up to  $\sim 2 \text{mm}$ , with a size distribution based on (Heymsfield & Platt 1984).

Figure 4.3 shows the total flux, the polarized flux and the degree of linear polarization of light that has been singly scattered by the cloud droplets and the ice particles at a wavelength  $\lambda$  equal to  $0.550 \mu\text{m}$ , when the incident light is unpolarized. The curves for scattering by gas molecules (Rayleigh scattering) have also been added. All curves have been plotted as functions of the phase angle  $\alpha$  instead of of the more common single scattering angle  $\Theta$  to facilitate the comparison

with the signals of the planets. Since for single scattering by the spherical cloud particles or by the ensemble of randomly oriented ice crystals, the scattered light is oriented parallel or perpendicular to the scattering plane (the plane containing the directions of propagation of the incident and the scattered light), we use the *signed* degree of linear polarization  $P_s$  in Fig. 4.3: when  $P_s$  is larger (smaller) than 0, the direction of polarization is perpendicular (parallel) to the scattering plane. The absolute value of  $P_s$  equals  $P$ .

The curves for Rayleigh scattering by gas clearly show the nearly isotropic scattering of the total flux, the symmetry of the polarization phase function and the high polarization values around  $\alpha = 90^\circ$ . The curves for the total flux scattered by both types of liquid water droplets have a strong forward scattering peak at the largest values of  $\alpha$  (the smallest single scattering angles), which is due to refraction and depends mostly on the size of the scattering particles, and not so much on their shape (Mishchenko et al. 2010). Another characteristic of the flux phase function of the droplets is the primary rainbow, that is due to light that has been reflected once inside the particles. For a given wavelength, the precise location of the rainbow depends on the particle size: for the small type A particles, it is found close to  $\alpha = 30^\circ$ , while for the larger type B particles, it is close to  $\alpha = 40^\circ$ . The primary rainbow also shows up in the scattered polarized flux and very strongly in the degree of polarization  $P_s$ . The direction of polarization across the primary rainbow is perpendicular to the planetary scattering plane. The polarized flux and  $P_s$  go through zero, thus change direction, a few times between phase angles of  $0^\circ$  and  $180^\circ$ . These particular phase angles are usually referred to as *neutral points* and, like the rainbow, they depend on the particle properties and the wavelength. At  $0.550 \mu\text{m}$ , the type A particles have neutral points at  $5^\circ$ ,  $20^\circ$ ,  $76^\circ$  and  $158^\circ$ , and the type B particles at  $2^\circ$ ,  $22^\circ$ ,  $94^\circ$ , and  $160^\circ$ .

The total flux scattered by the ice particles (Hess & Wiegner 1994, Hess 1998) has a smooth appearance without a feature such as the rainbow but with a strong forward scattering peak at the largest values of  $\alpha$ . The polarized flux and the degree of polarization of the ice particles are also smooth functions of  $\alpha$ . The neutral point of the ice particles is around  $\alpha = 140^\circ$ .

Fig. 4.4 shows the degree of linear polarization  $P_s$  for the type B liquid water droplets and the ice particles at  $\lambda = 0.550, 0.660$  and  $0.865 \mu\text{m}$ . The ice particles are relatively large, and therefore their scattering properties are virtually insensitive to  $\lambda$  across the wavelength region of our interest (the visible). The scattering properties of the liquid cloud particles vary slightly with the wavelength: with increasing  $\lambda$ , the strengths of the primary and secondary rainbows decreases slightly, and the neutral point around intermediate phase angles shifts towards smaller phase angles. With increasing  $\lambda$ , the primary rainbow also shifts towards smaller

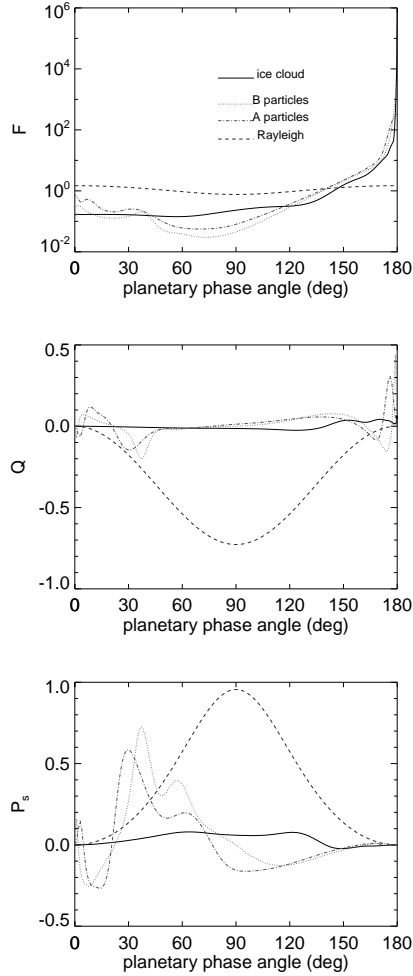


**Figure 4.3:** Phase function  $F$ , linearly polarized flux  $Q$ , and degree of linear polarization  $P_s$  as functions of the phase angle  $\alpha$  ( $\alpha = 180^\circ - \Theta$ , with  $\Theta$  the single scattering angle). Linearly polarized flux  $U$  equals zero, and  $P_s$  is defined as  $-Q/F$ . Curves are shown for liquid water droplets type A ( $r_{\text{eff}} = 0.2 \mu\text{m}$ ,  $v_{\text{eff}} = 0.1$ ), type B ( $r_{\text{eff}} = 6.0 \mu\text{m}$ ,  $v_{\text{eff}} = 0.4$ ), and water ice particles (Hess & Wiegner 1994, Hess 1998), all calculated at  $\lambda = 0.550 \mu\text{m}$ . For comparison, the curves for Rayleigh scattered light are also shown.

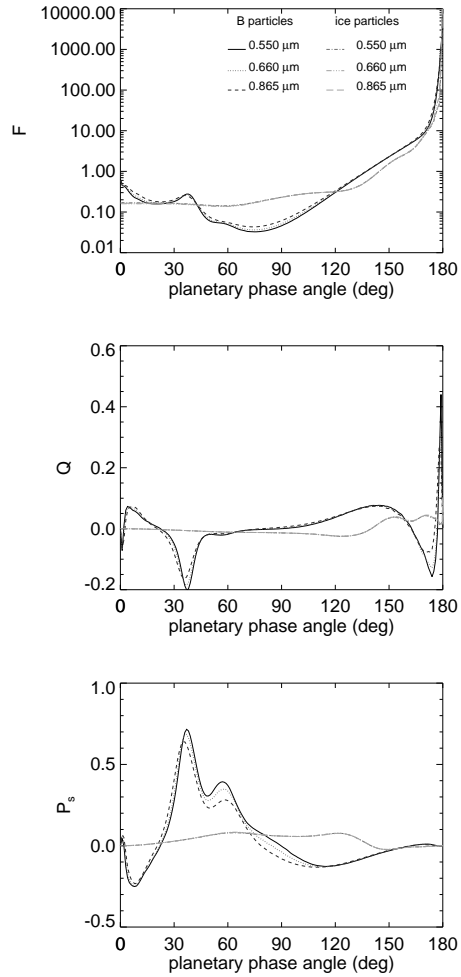


**Figure 4.4:** Singly scattered  $F$ ,  $Q$ , and  $P_s$  as functions of  $\alpha$  for the liquid water droplets type B and the ice particles at  $\lambda = 0.550, 0.660$  and  $0.865 \mu\text{m}$ . The curves for the ice particles overlap each other.

phase angles (larger single scattering angles). As also discussed in Chapter 2, the dispersion of the primary rainbow depends on the size of the particles that scatter the incident starlight: in large particles, such as rain droplets, the dispersion shows the opposite behavior, with the primary rainbow shifting towards larger phase angles with increasing  $\lambda$ . This latter shift gives rise to the well-known primary rainbow seen in the rainy sky with the red bow on top and the violet bow at the bottom.

### 4.3 The influence of the liquid water cloud coverage

In this section, we explore the strength of the primary rainbow feature as a function of the liquid water cloud coverage. All clouds have the same optical thickness, i.e. 2.0 (at  $0.550 \mu\text{m}$ ), and the same altitudes of their bottoms and tops, i.e. 3 and 4 km, respectively (see Fig. 4.1). The clouds consist of type A droplets.

Figure 4.5 shows the total reflected flux  $\pi F_n$ , the polarized reflected flux  $\pi F_{n,P}$ , and the degree of polarization  $P$  at  $0.550 \mu\text{m}$ , as functions of the phase angle  $\alpha$  and the percentage of cloud coverage. Horizontal cuts through Fig. 4.5 at a number of coverages are shown in Fig. 4.6. Because the model planets are not mirror-symmetric with respect to the planetary scattering plane, we use Eq. 5.2 to define the degree of polarization instead of the  $P_s$  used in the previous section.

Clearly, as the cloud coverage increases, the flux and polarization features converge smoothly towards the signals for completely cloudy planets (see also Chapter 2 for flux and polarization signals of completely cloudy planets). At small coverages,  $P$  has a strong maximum around  $\alpha = 90^\circ$ , which is due to scattering by the gas molecules above and between the patchy clouds. The Rayleigh scattering optical thickness above the clouds is 0.06 at  $\lambda = 0.550 \mu\text{m}$ , and between the clouds, it is 0.097 (see Sect. 4.2.3). As expected from the single scattering curves (Fig. 4.3), the primary rainbow feature is located close to  $\alpha = 30^\circ$ . The precise rainbow phase angle depends on the size of the particles and the wavelength, but, as expected, it does not depend on the cloud coverage.

In the total flux  $\pi F_n$ , the rainbow is difficult to discern regardless of the cloud coverage (Fig. 4.5), as can also be seen in Fig. 4.6. In the polarized flux, the rainbow shows up as a local maximum for coverages of about 30% or more. In the degree of polarization,  $P$ , the rainbow feature is a shoulder on the Rayleigh scattering maximum from a cloud coverage of  $\sim 20\%$ . For a cloud coverage larger than about 40%, the rainbow causes a local maximum in  $P$ , because the Rayleigh scattering maximum decreases with increasing cloud coverage. A reflecting (i.e. non-black) surface underneath our atmosphere would increase the contrast of the (primary) rainbow peak by lowering the intensity of the Rayleigh scattering peak

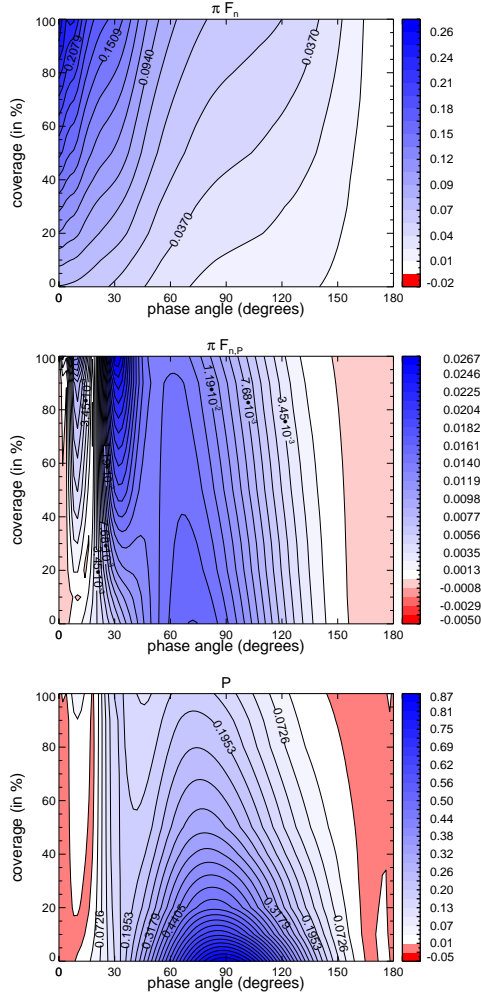


**Figure 4.5:** Total flux  $\pi F_n$ , the polarized flux  $\pi F_{n,P}$ , and the degree of polarization  $P$  as functions of the phase angle  $\alpha$  for liquid water cloud coverages from 0% up to 100%. Wavelength  $\lambda$  is  $0.550 \mu\text{m}$ , the optical thickness of the clouds is 2.0, and their top is at 4 km. The clouds are composed of type A droplets.

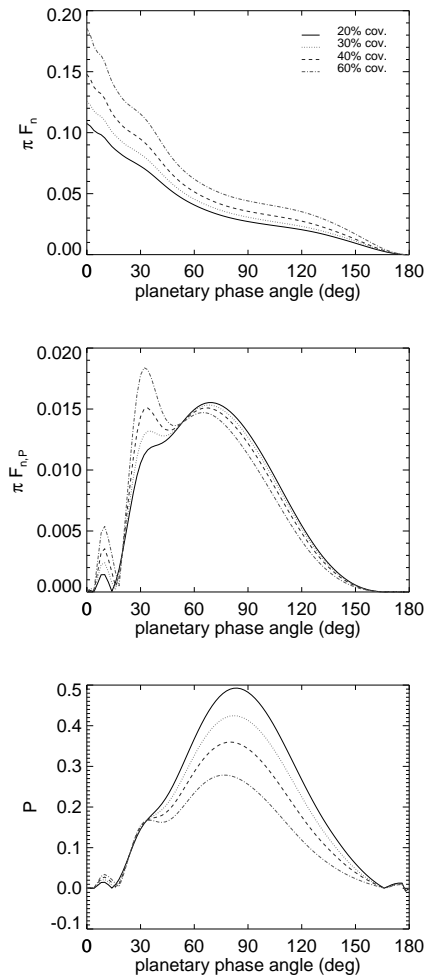


**Figure 4.6:** Horizontal cuts through the panels of Fig. 4.5 for cloud coverages of 20%, 30%, 40%, and 60%.

due to the increase of light with a generally low degree of polarization.

At phase angles near  $20^\circ$ ,  $\pi F_{n,P}$  and  $P$  are close to zero, fairly independent of

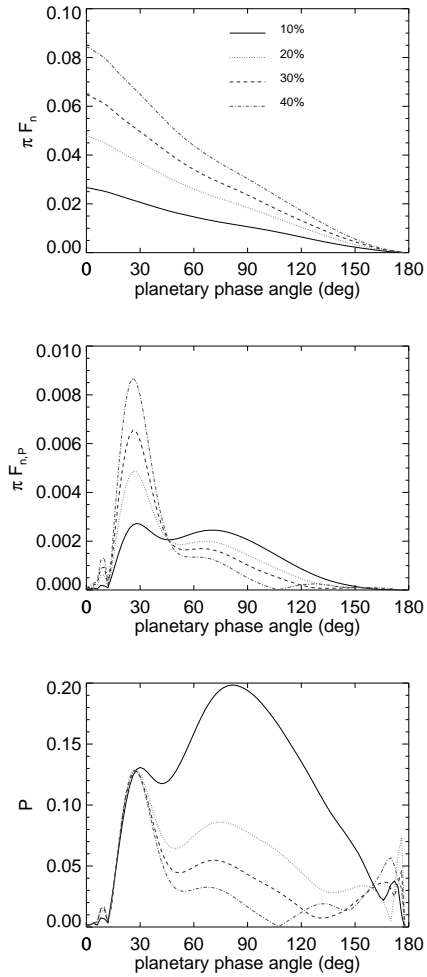


**Figure 4.7:** Similar to Fig. 4.6, except for  $\lambda = 0.865 \mu\text{m}$ .

the cloud coverage (see Fig. 4.6). This phase angle corresponds to a neutral point in the single scattering polarization phase function (Fig. 4.3). The type A cloud particle's neutral point near  $76^\circ$  is lost in the Rayleigh scattering contribution to  $P$ .

The neutral point near  $5^\circ$  yields the near-zero polarization region at the smallest phase angles, while the neutral point near  $158^\circ$  and the generally low polarization values at those phase angles (see Fig. 4.3) show up as the broad low  $P$  region at the largest phase angles in Fig. 4.5. Note that at these largest phase angles, the planet is almost in front of its star, and will be extremely difficult to detect directly anyway.

Figure 4.7 shows the same as Fig. 4.6, except for  $\lambda = 0.865 \mu\text{m}$ . At this wavelength, the Rayleigh scattering optical thickness above the clouds is 0.01, while between the clouds it is 0.016 (see Sect. 4.2.3). The optical thickness of the clouds at  $0.865 \mu\text{m}$  is 2.1. The differences in reflected fluxes and the degree of polarization between Fig. 4.7 and Fig. 4.6 are due to the difference in Rayleigh optical thickness above and between the clouds and to the difference in scattering properties of the cloud particles at the different wavelengths. Note that the effects of lowering the Rayleigh scattering optical thickness above the clouds are similar to increasing the altitude of the clouds.

At  $0.865 \mu\text{m}$ , the reflected total flux  $\pi F_n$  is a very smooth function of  $\alpha$ , almost without even a hint of the rainbow. This smoothness is due to the smoother single scattering phase function of the small type A particles at this relatively long wavelength. The degree of polarization shows a very strong rainbow signature, especially for cloud coverages larger than 10%. The reason that the rainbow is so strong is mostly due to the small Rayleigh scattering optical thickness above the clouds, which suppresses the strong polarization maximum around  $90^\circ$ . The strength of the rainbow appears to be fairly independent of the percentage of coverage (all clouds have the same optical thickness). Around  $\alpha = 108^\circ$ ,  $P$  is virtually zero for a coverage of 40%. These low values of  $P$  (also in the graphs for the 20% and 30% coverage, but then around  $\alpha = 135^\circ$  and  $130^\circ$ , respectively) are due to the direction of polarization of the light scattered by the cloud particles (cf. Figs. 4.3 and 4.4) that is opposite to that of light scattered by the gas molecules. Because at  $0.865 \mu\text{m}$ , the Rayleigh scattering optical thickness is small, the single scattering polarization signatures of the ice particles dominate the polarization signature of the planet.

#### 4.4 The influence of mixed cloud droplet sizes

In the previous section, all clouds were composed of the same type of liquid water cloud droplets. In reality, cloud droplet sizes vary across the Earth. Typically, droplets above continents are smaller than those above oceans, due to different types of condensation nuclei and different amounts of condensation nuclei. In

particular, typical cloud particle radii range from about  $5 \mu\text{m}$  to  $30 \mu\text{m}$ , with a global mean value of about  $8.5 \mu\text{m}$  above continental areas, and  $11.8 \mu\text{m}$  above maritime areas (Han et al. 1994). Also within clouds, droplet size distributions will vary, depending e.g. on internal convective updrafts or downdrafts that influence droplet growth through condensation and collisions (see e.g. Stephens & Platt 1987, Spinhirne et al. 1989). Here, we will present the influence of clouds with different liquid water droplet size distributions on the flux and polarization signals of a model planet.

Our model planet has two layers of clouds, with the lower clouds located between 1 and 3 km (0.902 and 0.710 bar) and the upper clouds between 3 and 4 km (0.710 and 0.628 bar) (cf. Fig. 4.1). The lower clouds are composed of the type B droplets ( $r_{\text{eff}} = 6.0 \mu\text{m}$ ,  $v_{\text{eff}} = 0.4$ ) and have a coverage of 42.3%. The upper clouds are composed of the smaller, type A droplets ( $r_{\text{eff}} = 2.0 \mu\text{m}$ ,  $v_{\text{eff}} = 0.1$ ) and have a coverage of 16%. The maps for the upper and the lower clouds were generated separately and hence there are regions with only lower clouds, or only upper clouds, or both.

Figure 4.8 shows the reflected total flux  $\pi F_{\text{n}}$ , the polarized flux  $\pi F_{\text{n,P}}$ , and the degree of polarization  $P$  for our model planet at  $\lambda = 0.550 \mu\text{m}$  for different values of the cloud optical thickness,  $b$ . Because the two types of cloud particles have slightly different locations of the rainbows, the rainbow in the total flux in the presence of two cloud layers appears to be somewhat broadened, as compared to the curves for the fluxes of single layers of clouds (the curves in Fig. 4.8 where one of the cloud optical thicknesses equals zero).

In  $P$ , the strength of the rainbow feature appears to depend on the properties of the highest cloud layer: adding a lower cloud layer mainly decreases the strength of the Rayleigh scattering maximum by adding more low polarized light at these phase angles.  $P$  is fairly insensitive to the optical thickness of this lower cloud layer (i.e. 2 or 10): increasing the thickness of this cloud slightly increases  $\pi F_{\text{n}}$ , but also slightly increases  $\pi F_{\text{n,P}}$ . This latter effect can also be seen in the rainbow feature in the curves for a planet with a single, lower cloud layer: with increasing  $b$ ,  $\pi F_{\text{n}}$  increases, but  $\pi F_{\text{n,P}}$  increases, too! At larger phase angles ( $\alpha > 55^\circ$  in Fig. 4.8), increasing  $b$  of the lower cloud layer increases  $\pi F_{\text{n}}$  but does not increase  $\pi F_{\text{n,P}}$  significantly, which can be attributed to the single scattering properties of the cloud droplets (see Fig. 4.3).

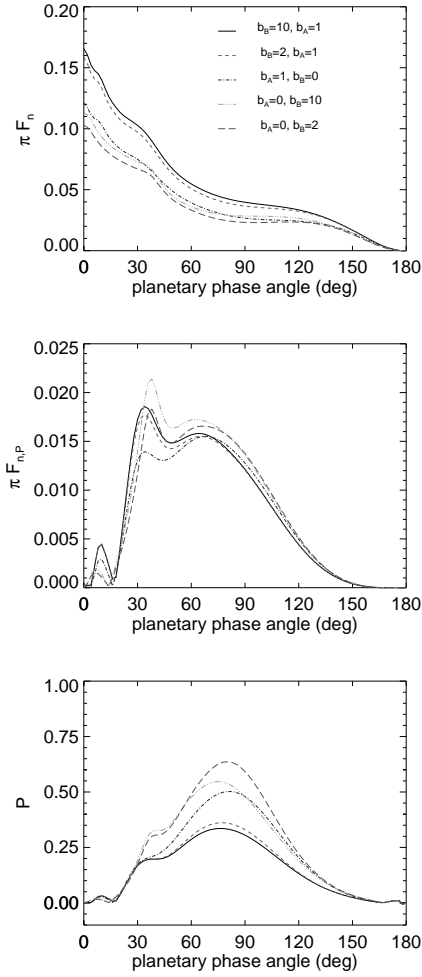


**Figure 4.8:**  $\pi F_n$ ,  $\pi F_{n,P}$ , and  $P$  as functions of  $\alpha$  for a planet with a lower, type B liquid water cloud that covers  $\sim 42.3\%$  and an upper, type A liquid water cloud layer that covers  $\sim 16\%$  of the planet for various values of the cloud optical thicknesses.

## 4.5 The influence of the ice cloud coverage

On Earth, liquid water clouds can be overlaid by water ice clouds. These latter clouds can be entirely separate (such as high-altitude cirrus clouds) or the upper parts of vertically extended clouds that have lower parts consisting of liquid water droplets. The amount of ice cloud coverage on Earth depends strongly on the latitude. Cirrus clouds for example, have an annual mean coverage of  $\sim 20\%$  in the tropics, while at northern mid-latitudes the annual mean coverage goes down to  $\sim 12\%$ . Globally, cirrus clouds cover  $\sim 14\%$  of the Earth's upper troposphere (Eleftheratos et al. 2007). As mentioned in Sect. 4.1, water ice particles come in various sizes and shapes that yield single scattering properties that differ from those of liquid water droplets. In particular, light that has been singly scattered by ice cloud particles does not show a rainbow feature between phase angles of  $30^\circ$  and  $40^\circ$  (i.e. between single scattering angles of  $140^\circ$  and  $150^\circ$ ).

To investigate the influence of water ice clouds on the strength of the rainbow feature of liquid water clouds, we used model planets with two layers of clouds: a lower layer of optical thickness 10, consisting of type B liquid water droplets and an upper layer containing water ice particles Hess & Wiegner (1994), Hess (1998). The lower layer is located between 279 and 273 K (3 and 4 km, or 0.710 and 0.628 bar) and the upper layer between 253 and 248 K (7 and 8 km, or 0.426 and 0.372 bar) (c.f. Fig. 4.1). The single scattering properties of the water ice particles clouds have been calculated using the code of Hess & Wiegner (1994), Hess (1998). The singly scattered total and polarized flux and the degree of polarization of our ice cloud particles are shown in Fig. 4.3 for  $\lambda = 0.550 \mu\text{m}$  and in Fig. 4.4 for  $\lambda = 0.660$  and  $0.865 \mu\text{m}$ .

Our first model planets have a liquid water cloud layer that covers  $\sim 42.3\%$  of the surface, and an ice cloud layer that covers  $\sim 16\%$ . About 4.5% of the liquid water clouds is covered by ice clouds (i.e.  $\sim 12\%$  of the ice clouds is covering a liquid water cloud). Figure 4.9 shows  $\pi F_n$  and  $P$  of our model planets as functions of  $\alpha$  for various optical thicknesses of the ice clouds.

Adding a thin ice cloud (with  $b = 0.5$ ) to the cloudy planet lowers  $\pi F$  at the smallest phase angles (cf. Fig. 4.8), because the ice particles are less strong backward scattering than the liquid water droplets (cf. Fig. 4.3). At intermediate phase angles (around  $\alpha = 90^\circ$ ), the thin ice clouds brighten the planet, because at those angles, their single scattering phase function is higher than that of the liquid water droplets (cf. Fig. 4.3). Clearly, with increasing ice cloud optical thickness the reflected flux increases across the whole phase angle range (which is difficult to see at phase angles larger than about  $150^\circ$ ).

The total flux  $\pi F_n$  does not show any evidence of a rainbow feature, not even

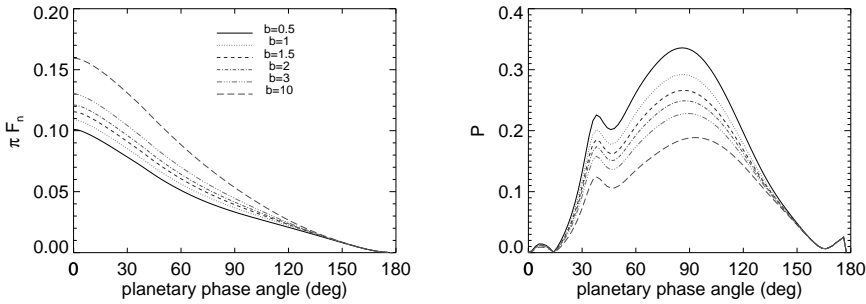


**Figure 4.9:**  $\pi F_n$  and  $P$  as functions of  $\alpha$  at  $\lambda = 0.550 \mu\text{m}$ , for a planet with a lower liquid water cloud with  $b = 10$  that covers  $\sim 42.3\%$  of the planet and an upper ice cloud layer that covers  $\sim 16\%$  of the planet, and  $\sim 11\%$  of the liquid water clouds.

for the thinnest ice cloud. The degree of polarization  $P$ , however, clearly shows the signature of the rainbow, even for large optical thicknesses of the ice cloud particles (cf. Fig. 4.9). The rainbow shows up in  $P$  despite the overlaying ice clouds, because the ice particles themselves have a very low polarization signature especially in the phase angle region of the rainbow (see Fig. 4.3), so the only polarized signals arise from scattering by the liquid cloud particles and the gas molecules (which yields the maximum in  $P$  around  $90^\circ$ ). Increasing the ice cloud optical thickness, decreases  $P$  across all phase angles because it increases the amount of mostly unpolarized reflected light.

In Fig. 4.10, we have plotted  $\pi F_n$ ,  $\pi F_{n,P}$  and  $P$  for the same model planet as used for Fig. 4.9, except for an ice cloud optical thickness of 2.0, and for  $\lambda = 0.660$  and  $0.865 \mu\text{m}$ . For comparison, the  $\lambda = 0.550 \mu\text{m}$  curves (see Fig. 4.9) are also shown. With increasing wavelength, the total reflected flux decreases, mainly because the Rayleigh scattering optical thickness above and between the clouds decreases. The decrease of the Rayleigh scattering optical thickness is also apparent from the decrease of the maximum in  $P$  around  $90^\circ$ , and the stronger influence of the single scattering polarization phase function of the liquid water cloud droplets. The ice particles leave no obvious feature in the polarization phase function at longer wavelengths, except that they decrease  $P$  somewhat as compared to  $P$  of a planet with only a liquid cloud (cf. the 40% coverage curve in Fig. 4.7).

To investigate the influence of the ice cloud coverage over liquid water clouds on the reflected flux and polarization, we used a model planet with lower liquid water clouds with  $b = 10$  and a coverage of  $\sim 25\%$ , and upper ice clouds with

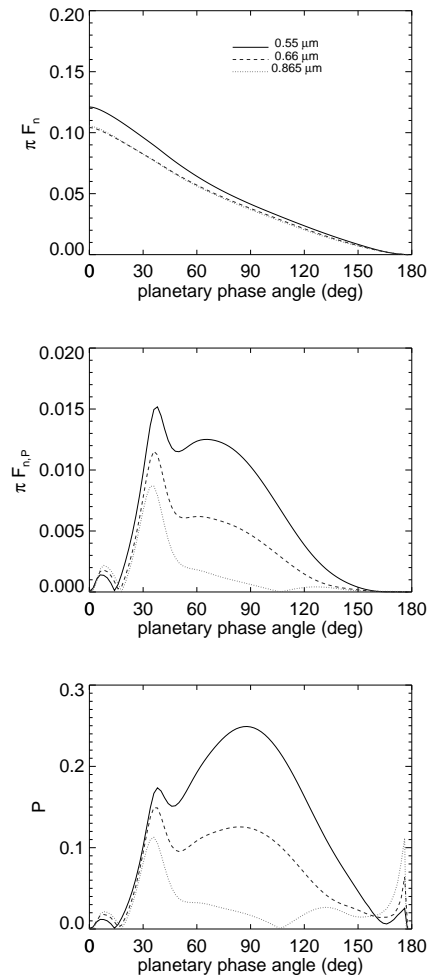


**Figure 4.10:** Similar to Fig. 4.9, except for an ice cloud with  $b = 2.0$ , and for  $\lambda = 0.550$ ,  $0.660$ , and  $0.865 \mu\text{m}$ . The  $\pi F$  curves for  $0.660$  and  $0.865 \mu\text{m}$  overlap.

$b = 4$  right above the liquid water clouds. Figure 4.11 shows the planet's flux and polarization phase functions at  $\lambda = 0.550 \mu\text{m}$  for various ice cloud coverages of

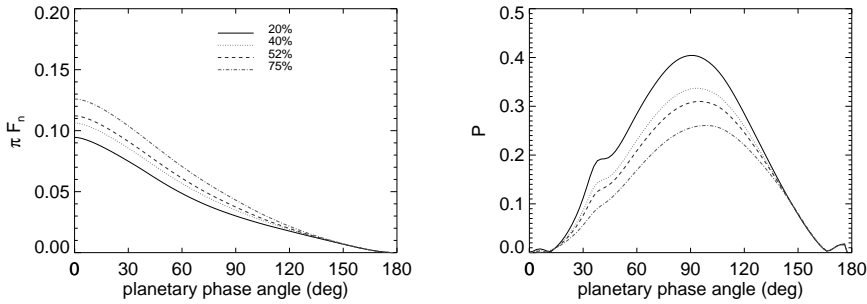


**Figure 4.11:** Similar to Fig. 4.9, except for a lower liquid water cloud that covers  $\sim 25\%$  of the planet and an upper ice cloud with  $b = 4.0$ . The ice cloud coverage is varied from 20% to 75% of the water clouds.

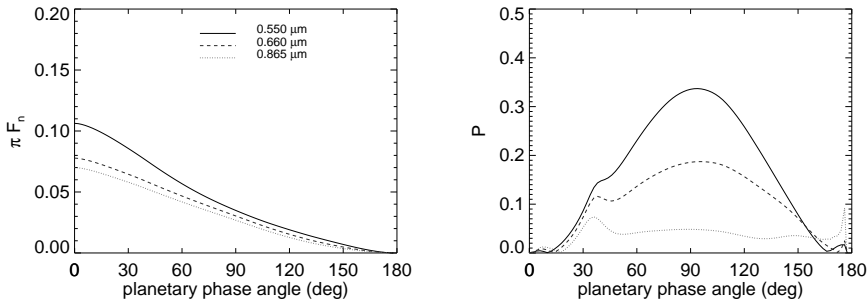


**Figure 4.12:** Similar to Fig. 4.11, for ice clouds covering 40% of the liquid water clouds, and for  $\lambda = 0.550$ , and  $0.865 \mu\text{m}$ .

the liquid water clouds (thus, an ice cloud coverage of 75% of the liquid water clouds, equals an ice cloud coverage of  $\sim 16\%$  of the planet).

Even with ice clouds covering as little as 20% of the liquid water clouds (5% of the planet, but only above the liquid water clouds), the total flux phase function fails to show a hint of the rainbow. This was also apparent from Fig. 4.9, where 11% of the liquid water clouds was covered by an ice cloud. The polarization phase function does show the rainbow feature, but up from an ice cloud coverage of 40% (a coverage of 10% of the planet) in Fig. 4.9, the feature is increasingly weak such

**Table 4.1:** The cloud optical thicknesses  $b$  (at  $\lambda = 0.550 \mu\text{m}$ ) from the MODIS/Aqua data from April 25, 2011. To avoid having to include too many different values of  $b$ , we have binned the optical thicknesses as shown below. Ice clouds with  $b \geq 20$  are ignored.

Liquid water cloud		Ice water cloud	
$b_{\text{MODIS}}$	$b_{\text{model}}$	$b_{\text{MODIS}}$	$b_{\text{model}}$
$0 < b < 1$	0.5	$0 < b < 1$	0.5
$1 \leq b < 10$	5	$1 \leq b < 2$	1.5
$5 \leq b < 20$	15	$2 \leq b < 5$	3
$20 \leq b < 50$	35	$5 \leq b < 10$	7.5
$50 \leq b < 80$	65	$10 \leq b < 20$	15

that it disappears into the Rayleigh scattering polarization maximum around  $90^\circ$ . At longer wavelengths, such as  $0.865 \mu\text{m}$ , where the Rayleigh scattering optical thickness above and between the clouds is smaller, the rainbow feature is still clearly visible in  $P$  when ice clouds cover 40% of the liquid water clouds. This can be seen in Fig. 4.12.

## 4.6 Searching for the rainbow on Earth

Figure 4.11 shows us that liquid water clouds on a planet can be detected using polarization measurements of the reflected starlight, even when the liquid water clouds are (partly) covered by water ice clouds. The question arises whether the rainbow would be visible for a distant observer of the Earth. As far as we know, the only polarization observations of the Earth have been done by the POLDER instrument (POLARization and Directionality of the Earth's Reflectances) a version of which is currently flying onboard the PARASOL satellite (for a description of the instrument, see Deschamps et al. 1994). Locally, POLDER has indeed observed the primary rainbow above liquid water clouds (see Goloub et al. 2000). However, since PARASOL is in a low-Earth-orbit, the POLDER measurements are not representative for polarization observations of the whole (disk-integrated) Earth observed from afar.

In the absence of real polarization observations, we have simulated the total flux and polarization of light reflected by the whole Earth using cloud properties derived from observations by MODIS (Moderate Resolution Imaging Spectroradiometer), onboard NASA's Aqua satellite. We used MODIS' cloud coverage (the horizontal distribution of the clouds), cloud thermodynamic phase (liquid or ice), and the

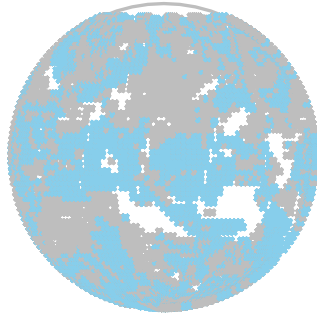


**Figure 4.13:** The cloud map of the Earth on April 25th, 2011, based on MODIS/Aqua data. The planet is covered by  $\sim 63\%$  liquid water clouds (gray regions) and  $\sim 36\%$  ice clouds (blue regions). About 28% of the planet is covered by two layers of clouds.

cloud optical thickness as measured on April 25th, 2011, to build a model Earth. To limit the number of (time-consuming) calculations, we binned the measured optical thicknesses according to Table 4.1. Ice clouds with an optical thicknesses larger than 20 (at  $\lambda = 0.550 \mu\text{m}$ ) were ignored, so as to include only cirrus/cirrostratus ice clouds in our sample (according to the ISCCP categorization) and to avoid deep convection clouds. We assume that the liquid water clouds consist of the type B droplets and for the ice particles, we use the models of Hess & Wiegner (1994) and Hess (1998). Finally, our ice clouds are positioned at altitudes with temperatures lower than 253 K, so that we avoid mixed-phase clouds (in which droplets and crystals exist side-by-side). The surface is assumed to be black as an ocean.

Figure 4.13 shows the cloud map of our model Earth. On April 25th, 2011, about 85% of the planet was covered by clouds (liquid and/or ice), about 14% was covered by both liquid and ice clouds, about 63% of the planet was covered by liquid water clouds and about 36% by water ice clouds.

In Fig. 4.14, we show the calculated  $\pi F_n$  and  $P$  of our model Earth at  $\lambda = 0.550 \mu\text{m}$  and  $0.865 \mu\text{m}$ . The total reflected flux at  $\alpha = 0^\circ$  equals the planet's geometric albedo, which is very similar at the two wavelengths and equals  $\sim 0.22$  at  $\lambda = 0.55 \mu\text{m}$ . This value is slightly smaller than the one found in literature for Earth's geometric albedo (0.33 (Brown 2005)) and is due to our use of a black surface on our planet. It is clear that the total reflected flux does not show a rainbow feature, while the degree of polarization does. The maximum  $P$  in the rainbow feature is 0.08 (8% in polarization) at  $\lambda=0.55 \mu\text{m}$ , and the absolute difference with the nearby local minimum around  $\alpha = 50^\circ$ , is 0.02 in  $P$  (an absolute

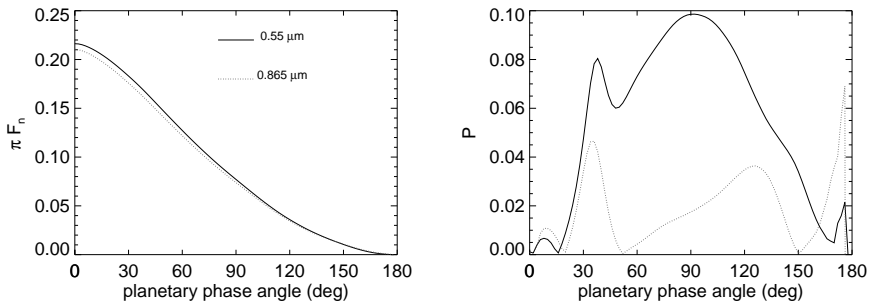


**Figure 4.14:**  $\pi F_n$  and  $P$  as functions of  $\alpha$  for the model Earth with clouds as shown in Fig. 4.13.

difference of 2% in polarization). At  $\lambda = 0.865 \mu\text{m}$ , the rainbow feature is even more pronounced in  $P$ , with an absolute difference with its surroundings of more than 4%. Interestingly,  $P$  reaches zero around the rainbow feature (which indicates a change of direction of the polarization), which should facilitate measuring the strength of the rainbow feature.

Bailey (2007) derived the disk-integrated polarization signature of the partly-cloudy Earth from remote-sensing data and predicted degrees of polarization of  $\sim 12.7\%$  to  $\sim 15.5\%$  in the rainbow peak at wavelengths between about 0.5 to 0.8 microns. These values are higher than our values of 4% to 8% as shown in Fig. 4.14. The differences are, however, small when considering the estimations by Bailey (2007) on the influence of multiple scattering and ice clouds on the polarization.

## 4.7 Summary and conclusions

The flux and degree of linear polarization of sunlight that is scattered by cloud particles and that is reflected back to space depend on the phase angle. Close to a phase angle of  $40^\circ$ , the flux and degree of polarization of unpolarized incident light that is singly scattered by spherical water cloud droplets, shows the enhancement that is known as the primary rainbow. The multiple scattering of light within clouds dilutes the primary rainbow feature both in flux and in polarization. In Earth-observation, with a spatial resolution of a few kilometers, the detection of the polarized rainbow feature is used to discriminate between liquid water clouds and

ice clouds (Goloub et al. 2000). Light that is scattered by ice cloud particles, such as hexagonal crystals, does not show the rainbow feature. Knowledge of the cloud properties (thermodynamical phase, optical thickness, microphysical properties etc) are crucial for studies of global climate change on Earth (Goloub et al. 2000).

In Chapter 2, we used horizontally homogeneous model planets to investigate the strength of the rainbow feature in flux and polarization for various model atmospheres of terrestrial exoplanets. In that Chapter, we briefly discussed the influence of a second atmospheric layer containing clouds on top of another one and the implications that that could have on our ability to characterize the planetary atmosphere. We concluded that even when the upper cloud has a relatively small optical thickness, the polarization signal of the planet is mainly determined by the properties of the upper cloud particles. Here, in Sects. 4.4 and 4.5 we extended this research on horizontally inhomogeneous exoplanets and for various cloud cases.

We noticed that in case the cloud layers contain clouds of similar nature (for example liquid water clouds) and when the cloud particles present a size stratification with altitude it is the top cloud layer that will define the total planetary signal, as was also the case in Chapter 2. On the other hand if the clouds are made out of the same nature and size particles it is the (optically) thickest clouds that will define to a largest extent the planetary signal.

In case the upper cloud layer contains ice clouds, we noticed that the characteristics of the planetary signal can depend on either one of the cloud layers, depending on their overcast and the optical thickness of the ice cloud layer. Using our homogeneous planet code we have seen that for  $b_{\text{ice}} \gtrsim 3$  the existence of any lower cloud on the observed planetary pixel will be masked. When the overcast of the two cloud layers is small the existence of the ice cloud layer does not seem to be able to cover the existence of the water cloud layer (i.e. the rainbow), even for high values of the optical thickness (see Fig. 4.9).

Even in case the ice cloud layer has an optical thickness large enough to mask the existence of the underlying liquid water cloud, the rainbow feature of the liquid water cloud survives for the case the ice cloud layer covers slightly more than half the water clouds (see Fig. 4.11). So unless our observed exoplanet contains a very large number of ice clouds in its atmosphere, the rainbow of the water clouds will still be visible in the planetary  $P$  signal.

An interesting test-case for the detection of the rainbow is our own Earth. To test whether a distant observer would be able to detect a rainbow due to Earth's liquid water clouds partly covered by water ice clouds, we modeled the Earth's cloud coverage using MODIS/Aqua data from April 25, 2011. These data contained the location and optical thickness of ice and water clouds across the planet. We binned the cloud optical thicknesses in a limited number (5) of optical thickness values

(to avoid too many time-consuming computations), as tabulated in Table 4.1, and modelled the scattering properties of the liquid water cloud droplets using Mie-scattering and those of the water ice crystals using the models of Hess (1998).

Our calculations for the disk-integrated flux and polarization signals of this model Earth as functions of the planetary phase angle and at  $\lambda = 0.550 \mu\text{m}$  and  $0.865 \mu\text{m}$ , show that the flux does not have the primary rainbow feature. Flux observations as a function of the phase angle would thus not provide an indication of the liquid water clouds on Earth. In the polarization signal, however, the rainbow is clearly visible, especially at the longer wavelengths ( $\lambda = 0.865 \mu\text{m}$ ). Polarimetry as a function of the planetary phase angle would thus establish the existence of liquid water clouds on our planet.

The results presented in this Chapter were for a black planetary surface. A bright surface that reflects light with a low degree of polarization would not significantly affect the reflected polarized flux, but it would increase the total flux, and hence decrease the degree of polarization. If a planet were thus covered by a bright surface and few clouds, the rainbow feature would be less strong than presented here (with increasing cloud coverage, the influence of the surface would decrease), although P at other phase angles would also be subdued. For example, comparing our results for a planet with a mean Earth cloud coverage completely covered by a sandy surface with an albedo of 0.243 (at  $0.55 \mu\text{m}$ ), polarization in the rainbow would be about 15.39%, compared to 41.7% for a planet completely covered by a black surface. Detailed calculations for planets with realistically inhomogeneous surfaces and inhomogeneous cloud decks, preferably including the variations of the cloud deck in time, would help to study the effects of the surface reflection. With an ocean surface with waves, one could also expect the glint of starlight to contribute to the reflected flux and polarization (Williams & Gaidos 2008). How often this glint would be visible through broken clouds and its effect on the rainbow of starlight that is scattered by cloud particles, when it is indeed visible, will be subject to further studies.

Summarizing, the primary rainbow of starlight that has been scattered by liquid water clouds should be observable for modest coverages (10% - 20%) of liquid clouds, and even when liquid water clouds are partly covered by water ice clouds. The total flux of the reflected starlight as a function of the planetary phase angle does not show the rainbow feature due to the presence of ice clouds. The degree of linear polarization of this light as a function of the phase angle will usually show the rainbow feature, even when a large fraction (up to  $\sim 50\%$ ) of the liquid water clouds are covered by ice clouds. Polarimetry of starlight that is reflected by exoplanets, thus provides a strong tool for the detection of liquid water clouds in the planetary atmospheres.

## **Acknowledgments**

We would like to thank Dr. Michael Hess for providing us with the new data set of the scattering properties of the ice crystals we use in this Chapter. The authors acknowledge the MODIS mission scientists and associated NASA personnel for the production of the data used in this research effort.



# Gaseous exoplanets

---

Based on:

T. Karalidi, D. M. Stam and D. Guirado, *Flux and polarization signals of spatially inhomogeneous gaseous exoplanets*, submitted in *Astronomy & Astrophysics*, 2013

**Abstract** *Context.* We present numerically calculated, disk-integrated, spectropolarimetric signals of starlight that is reflected by vertically and horizontally inhomogeneous giant exoplanets. We have included a number of spatial features that the giant planets in our Solar System show, such as spots, belts and zones, and polar hazes, to test whether such spatial features leave a trace in the disk-integrated flux and polarization signals. *Methods.* We calculate flux and polarization signals of giant exoplanets using a numerical radiative transfer code that is based on an efficient adding-doubling algorithm, and that fully includes single and multiple scattering and polarization. The atmospheres of the model planets can contain gas molecules and cloud and/or aerosol particles, and they can be horizontally and vertically inhomogeneous. *Results.* The existence of zones and spots on an exo-Jupiter could leave a detectable trace on the planetary signal. The location of these features on the planetary disk and the total coverage of the latter by the features define their detectability. We find that e.g. with a favorable observational geometry, the Great Red Spot should leave a distinctive trace on the integrated-planetary signal. The existence of polar haze finally, is found to leave a trace on the disk-integrated planetary signal, even though the flux and polarization curves do not acquire any distinctive feature, probably making the characterisation of a haze-containing exo-Jupiter degenerate.

## 5.1 Introduction

Since the discovery of the first exoplanet orbiting a main sequence star by Mayor & Queloz (1995), more than 850 exoplanets have been detected up to today. The refinement of the detection methods and the instrumentation, such as the highly successful space missions CoRoT (CONvection, ROTation & planetary Transits) (Baglin et al. 2006) and Kepler (Koch et al. 1998), and ground-based telescope

instruments like HARPS (High Accuracy Radial Velocity Planet Searcher) (Pepe et al. 2004) have led to an almost exponential increase of the number of planets that are detected per year.

The next step of exoplanet research is the characterization of detected exoplanets: what is the composition and structure of their atmospheres and their surface (for rocky exoplanets). In the near future, instruments like SPHERE (Spectro-Polarimetric High-Contrast Exoplanet Research) on the VLT (Very Large Telescope) (Dohlen et al. 2008, Roelfsema et al. 2011), GPI (Gemini Planet Imager) on the Gemini North telescope (Macintosh et al. 2008) and EPICS (Exoplanet Imaging Camera and Spectrograph) on the E-ELT (Kasper et al. 2010) will further increase the detections and help pushing the lower mass limit of our detections closer to Earth-like objects.

Observations of our Solar System planets show that a common feature of almost all planets is inhomogeneity. Oceans, continents, cloud patches and rings are only some of the forms of inhomogeneities we meet on our Solar System planets. The existence of inhomogeneities on a planet can have a large impact on the observed planetary signal. The existence for example of continents and cloud patches on an Earth-like planet, and the way they are distributed across the planetary disk could influence, mask, or even mimic the existence of life on the planet (see e.g. Tinetti et al. 2006b).

Even in the cases we are interested in the characterization of giant exoplanets, inhomogeneity is a factor we should take into account. In our Solar System the gaseous planets tend to have some form of inhomogeneity, either it is in the form of zones and bands like in Jupiter, or in the form of spots like the Great Red Spot of Jupiter or the Great Dark Spot of Neptune. In most cases these features are considered to originate from various up- and down-welling processes in the planetary atmospheres and have cloud decks of various densities and altitudes (see for example Simon-Miller et al. 2001, for the case of Jupiter), making the planetary atmospheres both horizontally, as well as vertically inhomogeneous.

Polarization observations of the giant planets of our Solar System show another form of inhomogeneity. As early as 1929, Lyot (Lyot 1929) had observed a strong positive polarization on Jupiter's poles and a small polarization signal from Saturn (most predominant is the polarization signal of its' ring system). Later Earth-based observations of Jupiter and Saturn (see e.g. Schmid et al. 2011, and references therein), as well as spacecraft observations (see e.g. West et al. 1983, Smith & Tomasko 1984) have confirmed these observations. West & Smith (1991) have shown that this strong polarization signals can be explained by the existence of aggregate, high altitude, haze particles on the planetary atmosphere. Photochemical reactions of complex hydrocarbon molecules and PAHs have been suggested

as the source of these haze particles (see e.g. Wong et al. 2000, Friedson et al. 2002).

In flux there exist a number of models that deal with inhomogeneous exoplanets (Ford et al. 2001, Tinetti 2006, Montañés-Rodríguez et al. 2006, Pallé et al. 2008, to name a few). All of the models show the importance of planetary inhomogeneity and temporal variability on the modelled planetary signal. Unfortunately, most of these models either ignore polarization, or do not take it properly into account, a fact that could lead to errors on the derived properties of the observed exoplanet (see e.g. Stam 2008, and references therein).

The power of polarization in studying planetary atmospheres and surfaces has been shown multiple times in the past through observations of Solar System planets (including Earth itself)(see for example Hansen & Hovenier 1974, Hansen & Travis 1974, Mishchenko 1990, Tomasko et al. 2009), as well as by modeling of solar system planets or giant and Earth-like exoplanets (e.g. Stam (2003), Stam et al. (2004), Saar & Seager (2003), Seager et al. (2000), Stam (2008) and Chapter 2).

So far, in the field of exoplanet research, when polarization is treated properly, “true” inhomogeneities are ignored. The study of inhomogeneous planets is done mostly through the use of weighted averages of homogeneous planets, for the creation of “quasi inhomogeneous” planetary signals (Stam 2008). In the few cases that inhomogeneity is taken into account polarization is handled in an over-simplistic way, for example dealing only with Rayleigh scattering (Zugger et al. 2010).

In Chapter 3 we presented our code that can model flux and polarization signals of realistically inhomogeneous planets. After comparing it against the “quasi inhomogeneous” planet method we concluded the importance of using our “truly” inhomogeneous planetary model, especially in the cases that we are interested in the location of planetary inhomogeneities, like for example in the case of planetary mapping.

In Chapter 4 we presented applications of our code to terrestrial planets. In this Chapter we will present more results from our newly developed code and study in more detail the effect that atmospheric inhomogeneities have on the modelled planetary signal of (exo-) planets. In particular, we will study the case of (exo-) giant planets and our ability to detect possible inhomogeneities on their atmospheres (zones, bands, spots etc) based on planetary flux and polarization spectra.

This Chapter is organized as follows. In Sec. 5.2, we give a short description of polarized light, our radiative transfer algorithm, and our planetary model atmospheres. In Sec. 5.3, we present the single scattering properties of the cloud and haze particles in our model atmospheres. In Sec. 5.4, we present the calculated flux and polarization signals of different types of spatially inhomogeneous model

planets: with zones and belts, cyclonic spots, and polar hazes. Section 5.5, finally, contains a discussion and our conclusions.

## 5.2 Description of the numerical simulations

### 5.2.1 Definitions of flux and polarization

Starlight that has been reflected by a planet can be described by a flux vector  $\pi\vec{F}$ , as follows

$$\pi\vec{F} = \pi \begin{bmatrix} F \\ Q \\ U \\ V \end{bmatrix}, \quad (5.1)$$

where parameter  $\pi F$  is the total flux, parameters  $\pi Q$  and  $\pi U$  describe the linearly polarized flux and parameter  $\pi V$  the circularly polarized flux (see e.g. Hansen & Travis 1974, Hovenier et al. 2004). Although not explicitly written out in Eq. 5.1, all four parameters depend on the wavelength  $\lambda$ , and their dimensions are  $\text{W m}^{-2}\text{m}^{-1}$ . Parameters  $\pi Q$  and  $\pi U$  are defined with respect to a reference plane, and as such we chose the planetary scattering plane, i.e. the plane through the centers of the star, the planet and the observer (see Chapter 2). Finally, parameter  $\pi V$  is generally small (Hansen & Travis 1974) and in the rest of the Chapter we will ignore it. This can be done without introducing significant errors in our calculated total and polarized fluxes (Stam & Hovenier 2005).

The degree of (linear) polarization  $P$  of flux vector  $\pi\vec{F}$  is defined as the ratio of the (linearly) polarized flux to the total flux, as follows

$$P = \frac{\sqrt{Q^2 + U^2}}{F}, \quad (5.2)$$

which is independent of the choice of our reference plane.

Unless stated otherwise, we assume unpolarized incident stellar light (Kemp et al. 1987) and planets that are mirror-symmetric with respect to the planetary scattering plane. In that case, parameter  $\pi U$  equals zero, and we can use an alternative definition for the degree of polarization, namely

$$P_s = -\frac{Q}{F}. \quad (5.3)$$

If  $P_s$  is positive (negative), the reflected starlight is polarized perpendicular (parallel) to the reference plane.

We will present calculated fluxes that are normalized such that at a planetary phase angle  $\alpha$  equal to  $0^\circ$  (i.e. seen from the middle of the planet, the angle between the star and the observer equals  $0^\circ$ ), the total reflected flux  $\pi F$  equals the planet's geometric albedo  $A_G$  (see e.g. Stam et al. 2004). We will indicate the hence normalized total flux by  $\pi F_n$  and the associated linearly polarized fluxes by  $\pi Q_n$  and  $\pi U_n$ . The normalized fluxes that we present in this Chapter can straightforwardly be scaled to absolute fluxes of a particular planetary system by multiplying them with  $r^2/d^2$ , where  $r$  is the spherical planet's radius and  $d$  the distance between the planet and the observer, and with the stellar flux that is incident on the planet. In our calculations, we furthermore assume that the distance between the star and the planet is large enough to assume that the incident starlight is uni-directional. Since the degree of polarization  $P$  (or  $P_s$ ) is a relative measure, it doesn't require any scaling.

Our calculations cover phase angles  $\alpha$  from  $0^\circ$  to  $180^\circ$ . Of course, the range of phase angles an exoplanet exhibits as it orbits its star, depends on the orbital inclination angle. Given an orbital inclination angle  $i$  (in degrees), one can observe the exoplanet at phase angles ranging from  $90^\circ - i$  to  $90^\circ + i$ . Thus, an exoplanet in a face-on orbit ( $i = 0^\circ$ ) would always be observed at a phase angle equal to  $90^\circ$ , while the phase angles of an exoplanet in an edge-on orbit ( $i = 90^\circ$ ) range from  $0^\circ$  to  $180^\circ$ , the complete range that is shown in this Chapter. Note that the actual range of phase angles an exoplanet can be observed at will depend strongly on the observational technique that is used, and e.g. on the angular distance between a star and its planet.

### 5.2.2 Our radiative transfer code

Our radiative transfer code to calculate the total and polarized fluxes that are reflected by model planets is based on the efficient adding-doubling algorithm described by de Haan et al. (1987). It fully includes single and multiple scattering and polarization, and assumes that locally, the planetary atmosphere is plane-parallel. In this Chapter, we will use a version of the code that applies to horizontally homogeneous planets, as used by Stam et al. (2006a), Stam (2008), and a (more computing-time-consuming) version that applies to horizontally inhomogeneous planets, such as with zones and belts, as described by Chapter 3. In the latter code, a model planet is divided into pixels that are small enough to be considered horizontally homogeneous. Reflected stellar fluxes are then calculated for all pixels that are both illuminated and visible to the observer and then summed up to acquire the disk-integrated total and polarized reflected fluxes. Since the adding-doubling code uses the local meridian plane (which contains both the local zenith direc-

and the propagation direction of the reflected light) as the reference plane, we have to rotate locally calculated flux vectors to the planetary scattering plane before summing them up. Following Chapter 3, we divide our model planets into pixels of  $2^\circ \times 2^\circ$  (latitude  $\times$  longitude).

### 5.2.3 Our model planets

The atmospheres of our model planets consist of homogeneous, plane-parallel layers that contain gases and, optionally, clouds or hazes. Here, we use the term 'haze' for optically thin layers of submicron-sized particles, while 'clouds' are thicker and composed of larger particles. The model atmospheres are bounded below by black surfaces, i.e. no light is entering the atmospheres from below. The ambient atmospheric temperature and pressure profiles are representative for midlatitudes on Jupiter (see Stam et al. 2004). Given the temperatures and pressures across an atmospheric layer, and the wavelength  $\lambda$ , the gaseous scattering optical thickness of each atmospheric layer is calculated according to Stam et al. (1999), using a depolarization factor that is representative for hydrogen-gas, namely 0.02 (see Hansen & Travis 1974). At  $\lambda = 0.55 \mu\text{m}$ , the total gaseous scattering optical thickness of our model atmosphere is 5.41. We ignore absorption by methane, and choose wavelengths in the continuum for our calculations. In particular, when broad band filters are being used for the observations, the contribution of reflected flux from continuum wavelengths will contribute most to the measured signal.

The physical properties of the clouds and hazes across a planet like Jupiter vary in time (for an overview, see e.g. West et al. 2004). Here, we use a simple atmosphere model that suffices to show the effects of clouds and hazes on the flux and polarization signals of Jupiter-like exoplanets. Our model atmospheres have an optically thick tropospheric cloud layer that is composed of ammonia ice particles (their properties are presented in Sect. 5.3). The bottom of this cloud layer is at a pressure of 1.0 bar. We vary the top of the cloud between 0.1 and 0.5 bars. The cloud top pressure of 0.1 bars is representative for the so-called zonal bands on Jupiter. In the zones, the clouds typically rise up higher into the atmosphere than in the adjacent belts where the cloud top pressures can be up to a few hundred mbar higher (see Ingersoll et al. 2004). On Jupiter, the clouds are overlaid by a stratospheric, photochemically produced haze layer. The haze layers over in particular both polar regions, provide strong polarization signals indicating that they consist of small aggregated particles (West & Smith 1991). To avoid introducing too many variables, we only use haze layers over the polar regions of our model planets.

We will present results for horizontally homogeneous model planets and for

model planets with bands of clouds divided into zones and belts that run parallel to the equator, which lies in the planet's equatorial plane. Our banded model planets are mirror-symmetric: measured from the equator in either the northern or the southern direction, we chose the latitudes that bound the belts and zones as follows:  $0^\circ$ – $8^\circ$  (zone),  $8^\circ$ – $24^\circ$  (belt),  $24^\circ$ – $40^\circ$  (zone),  $40^\circ$ – $60^\circ$  (belt),  $60^\circ$ – $90^\circ$  (zone). These latitudes correspond roughly to the most prominent cloud bands of Jupiter (see e.g. de Pater & Lissauer 2001). The jovian tropospheric cloud can finally be overlaid by a haze layer on the poles consisting of aggregated particles (West & Smith 1991). The northern and southern polar hazes extend upward, respectively downward, from a latitude of  $60^\circ$ . Vertically these hazes extend between  $\sim 0.0075$  bar and  $\sim 0.0056$  bar, and we give them an optical thickness of 0.2 (at  $0.55 \mu\text{m}$ ).

### 5.3 Single scattering properties of the cloud and haze particles

#### 5.3.1 Tropospheric cloud particles

Thermodynamic models of the jovian atmosphere indicate that the upper tropospheric cloud layers should consist of ammonia ice particles (see for example Sato & Hansen 1979, Simon-Miller et al. 2001, de Pater & Lissauer 2001). Galileo NIMS and Cassini CIRS data, however, indicated that spectrally identifiable ammonia ice clouds cover only very small regions on the planet (see, respectively Baines et al. 2002, Wong et al. 2004). As put forward by e.g. Atreya et al. (2005), this apparent contradiction could be explained if the ammonia ice particles are coated by in particular hydrocarbon haze particles settling from the stratosphere. Thus, only the highest and freshest ammonia ice clouds would show identifiable spectral features. Atreya et al. (2005) also mention that the strength of the spectral features would depend on the sizes and shapes of the ice crystals. In this Chapter, we assume that the upper tropospheric clouds in our model atmospheres are indeed composed of ammonia ice particles, without modelling specific spectral features.

Our ammonia ice particles are assumed to be spherical with a refractive index of  $n = 1.48 + 0.01i$  (assumed to be constant across the spectral region of our interest) (as adopted from Gibson et al. 2005, Romanescu et al. 2010) and with their sizes described by a standard size distribution (see Hansen & Travis 1974) with an effective radius  $r_{\text{eff}}$  of  $0.5 \mu\text{m}$ , and an effective variance  $v_{\text{eff}}$  of 0.1 (Stam et al. 2004). We calculate the single scattering properties of the ammonia ice particles using Mie theory as described by de Rooij & van der Stap (1984).

Figure 5.1 shows the flux and degree of linear polarization  $P_s$  of unpolarized

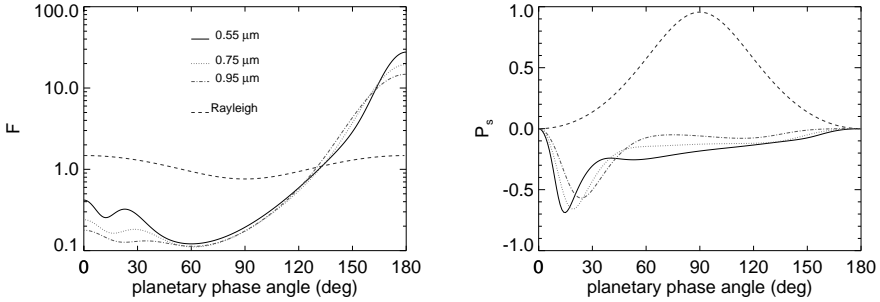


**Figure 5.1:** Single scattering  $F$  and  $P_s$  of our ammonia ice particles as functions of the planetary phase angle  $\alpha$  at  $0.55 \mu\text{m}$  (black, solid line),  $0.75 \mu\text{m}$  (red, dotted line) and  $0.95 \mu\text{m}$  (green, dashed–dotted line). The Rayleigh scattering curves (blue, dashed line) at  $0.55 \mu\text{m}$  are over plotted for comparison.

incident light with  $\lambda = 0.55 \mu\text{m}$ ,  $0.75 \mu\text{m}$ , and  $0.95 \mu\text{m}$ , respectively, that is singly scattered by the ice particles as functions of the planetary phase angle  $\alpha$ . Note that  $\alpha = 180^\circ - \Theta$ , with  $\Theta$  the conventional single scattering angle, defined as  $\Theta = 0^\circ$  for forward scattered light. All scattered fluxes have been normalized such that their average over all scattering directions equals one (see Eq. 2.5 of Hansen & Travis 1974). At  $\alpha = 0^\circ$  ( $180^\circ$ ) the light is scattered in the backward (forward) direction. For comparison, we have added the curves for (Rayleigh) scattering by gas molecules at  $\lambda = 0.55 \mu\text{m}$  (these curves are fairly wavelength independent). As can be seen in the figure, our spherical ice particles are moderately forward scattering and the scattered fluxes show a prominent feature (a local minimum) around  $\alpha = 12^\circ$  at  $\lambda = 0.55 \mu\text{m}$ , around  $20^\circ$  at  $0.75 \mu\text{m}$ , and (much less pronounced) around  $25^\circ$  at  $0.95 \mu\text{m}$ .

The degree of polarization  $P_s$  of the light that is singly scattered by our ammonia ice particles is negative across almost the whole phase angle range. The light is thus polarized parallel to the scattering plane, which contains both the incident and the scattered beams. The local minima in scattered fluxes have associated local minima in  $P_s$  (at slightly shifted values of  $\alpha$ ).

### 5.3.2 Polar haze particles

By combining flux and polarization observations, West & Smith (1991) argue that the stratospheric haze covering Jupiter’s polar regions should consist of aggregated

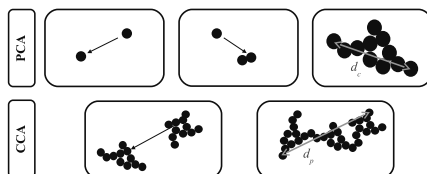


**Figure 5.2:** Models of aggregation to build the particles. For PCA, identical monomers are stuck together sequentially to the aggregate until the maximum distance between two monomers is larger than a certain limit  $d_c$ . For CCA, several PCA aggregates are joined together until the maximum distance between two monomers of the particle becomes larger than  $d_p$ .

particles.

We model Jupiter’s polar haze particles as randomly oriented aggregates of equally sized spheres. To generate the aggregates (needed for calculating the single scattering properties of these particles), we use a cluster–cluster aggregation (CCA) method that starts with the formation of particle–cluster aggregates (PCA) by sequentially adding spheres from random directions to an existing cluster, as shown in the upper part of Fig. 5.2. Next, we combine several PCA–particles, as shown in the lower part of Fig. 5.2). For both PCA and CCA, the coagulation process finishes when the maximum distance between any pair of monomers of the aggregate exceeds a certain limit (in Fig. 5.2:  $d_c$  for PCA and  $d_p$  for CCA). With the later assumption, we limit the size of the generated particle, which is convenient due to the computational limitations of the T-matrix method. CCAs are used instead of PCAs because they produce higher values of  $P_s$ , which we need to reproduce our results.

Figure 5.3 shows a model aggregate haze particle that we generated and for which we calculated the single scattering matrices and other optical properties. The particle consists of 94 spherical monomers. The radius of each monomer is approximately  $0.035 \mu\text{m}$ , and the volume-equivalent-sphere radius of the whole particle  $0.16 \mu\text{m}$ . Calculations of the single scattering matrix and other optical properties of these particles were performed using the T-matrix theory combined with the superposition theorem (Mackowski & Mishchenko 2011), at  $\lambda = 0.55$ ,  $0.75$  and  $0.95 \mu\text{m}$ , and adopting a refractive index of  $1.5+i0.001$  (corresponding to benzene, see Friedson et al. 2002). In Fig. 5.1 we show the flux and polarization of unpolarized incident light that is singly scattered by the haze particles at the three different wavelengths, together with the Rayleigh curves at  $\lambda = 0.55 \mu\text{m}$ .

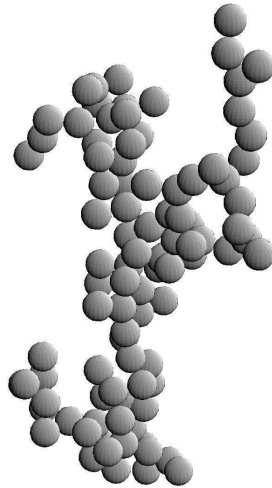


**Figure 5.3:** A depiction of the model aggregate we generated and used for our calculations.

From comparing the different lines in Fig. 5.1, it is clear that the haze particles are more forward scattering than the ammonia ice particles, and that their scattered flux shows less angular features. The degree of linear polarization of the light scattered by the haze particles is very different from that of the cloud particles: it is positive at almost all phase angles (hence the light is polarized perpendicular to the scattering plane), and it reaches values larger than 0.7 (70 %) near  $\alpha = 90^\circ$ . The main reason that the polarization phase function of the haze particles differs strongly from that of the cloud particles while their flux phase functions are quite similar, is that the latter depends mostly on the size of the whole particle, while the polarization phase function depends more on the size of the smallest scattering particles, which have radii of about  $0.035 \mu\text{m}$ , in the case of the aggregate particles.

The maximum single scattering polarization of our aggregate particles is slightly

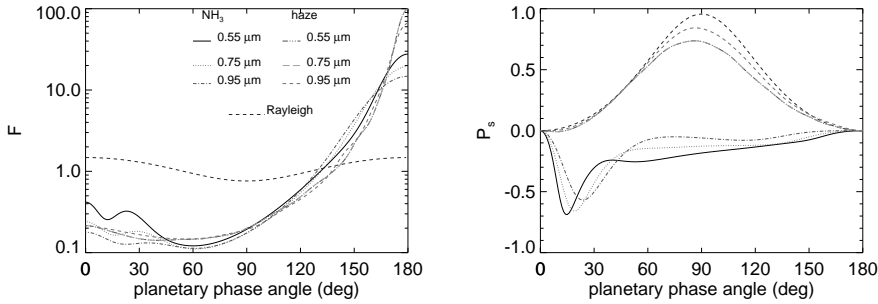


**Figure 5.4:** Single scattering  $F$  and  $P_s$  of light that is single scattered by our haze particles at 0.55  $\mu\text{m}$  (black, solid line), 0.75  $\mu\text{m}$  (red, dotted line) and 0.95  $\mu\text{m}$  (green, dashed–dotted line) and by our  $\text{NH}_3$  ice particles (0.55  $\mu\text{m}$ : grey, dashed–triple–dotted; 0.75  $\mu\text{m}$ : orange, long–dashed line and 0.95  $\mu\text{m}$ : magenta, dashed line). The Rayleigh scattering curves (blue, dashed line) at 0.55  $\mu\text{m}$  are over plotted for comparison.

higher than that derived by West & Smith (1991). This is due to the shape and sizes of our particles: our monomers are smaller than those used by West & Smith (1991), which have radii near 0.06  $\mu\text{m}$ , sometimes mixed with monomers with radii of 0.03  $\mu\text{m}$ . In addition, the particles in West & Smith (1991) were generated using the diffusion-limited aggregation (DLA) method, in which monomers follow random paths towards the aggregate, and which yields more compact particles than those produced by our CCA–method Meakin (see 1983).

## 5.4 Reflected flux and polarization signals of the model planets

In this section, we present fluxes and degrees of linear polarization for three different types of spatial inhomogeneities that occur on gaseous planets in the Solar System: zones and belts (Sect. 5.4.1), cyclonic spots (Sect. 5.4.2), and polar hazes (Sect. 5.4.3). We will compare the flux and polarization signals of the spatially inhomogeneous planets with those of horizontally homogeneous planets to investigate whether or not such spatial inhomogeneities would be detectable.

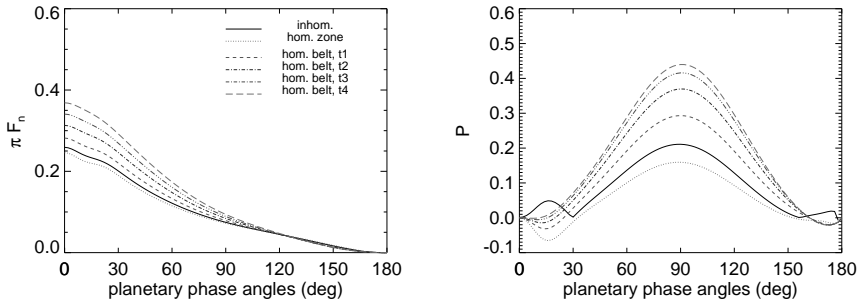
### 5.4.1 Zones and belts

The model atmospheres in this section contain only clouds, no hazes. Figures 5.5–5.10 show the flux  $\pi F_n$  and the degree of linear polarization  $P_s$  as functions of  $\alpha$  at  $\lambda = 0.55 \mu\text{m}$  (Fig. 5.5),  $0.75 \mu\text{m}$  (Fig. 5.9), and  $0.95 \mu\text{m}$  (Fig. 5.10), for horizontally homogeneous planets with the bottom of the cloud layer at 1.0 bar, and the top at 0.1, 0.2, 0.3, 0.4, or 0.5 bar. Also shown in these figures, are  $\pi F_n$  and  $P_s$  for a model planet with a cloud top pressure of 0.1 bar in the zones and 0.2 bar in the belts. The latitudinal borders of the zones and belts have been described in Sect. 5.2.3.

For each model planet and each wavelength, total flux  $\pi F_n$  at  $\alpha = 0^\circ$  equals the planet's geometric albedo  $A_G$ . With increasing wavelength,  $A_G$  decreases slightly, because of the decreasing cloud optical thickness with  $\lambda$ , and the decreasing single scattering phase function in the backscattering direction (see Fig. 5.1). With increasing  $\alpha$ ,  $\pi F_n$  decreases smoothly for all model atmospheres. The angular feature around  $\alpha = 12^\circ$  for the horizontally homogeneous planets with the highest cloud layers, can be retraced to the single scattering phase function (Fig. 5.1). The strength of the feature in the planetary phase functions decreases with  $\lambda$ , just like that in the single scattering phase functions. The decrease of the feature with increasing cloud top pressure is due to the increasing thickness of the gas layer overlying the clouds. With increasing  $\lambda$ , the difference between the total fluxes reflected by the model atmospheres decreases, mostly because of the decrease of Rayleigh scattering above the clouds with  $\lambda$ .

Interestingly,  $\pi F_n$  is insensitive to the cloud top pressure around  $\alpha = 125^\circ$  at  $\lambda = 0.55 \mu\text{m}$  (Fig. 5.5). With increasing  $\lambda$ , the phase angle where this insensitivity occurs decreases: from about  $110^\circ$  at  $\lambda = 0.75 \mu\text{m}$  (Fig. 5.9), to about  $90^\circ$  at  $\lambda = 0.95 \mu\text{m}$  (Fig. 5.10). Thus precisely across the phase angle range where exoplanets are most likely to be directly detected because they are furthest from their star, reflected fluxes do not give access to the cloud top altitudes.

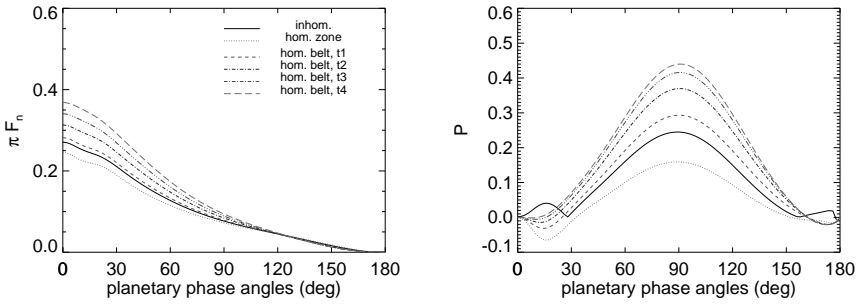
The degree of linear polarization,  $P_s$ , shows the typical bell-shape around approximately  $\alpha = 90^\circ$ , that is due to Rayleigh scattering of light by gas molecules (Fig. 5.5). With increasing cloud top altitude, hence decreasing Rayleigh scattering optical thickness above the clouds, the features of the single scattering phase function of the cloud particles become more prominent. This is especially obvious at the longer wavelengths, i.e. at  $0.75 \mu\text{m}$  and  $0.95 \mu\text{m}$ , where the Rayleigh scattering optical thickness above the clouds is smaller by factors of about  $(0.55/0.75)^4$  and  $(0.55/0.95)^4$ , respectively (Figs. 5.9 and 5.10). In particular, the negative polarized feature below  $\alpha = 30^\circ$ , that is due to light singly scattered by the cloud particles (see Fig. 5.1) becomes more prominent.



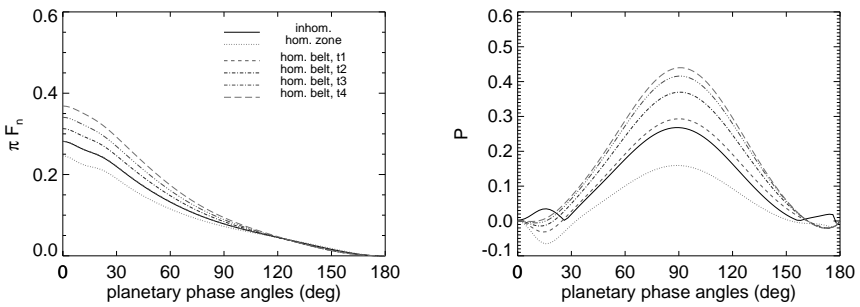
**Figure 5.5:**  $\pi F_n$  and  $P$  of starlight reflected by a giant planet with zones and belts at  $0.55 \mu\text{m}$  (black, solid line). The belt top pressure is set at 0.2 bar. All zones and belts contain  $\text{NH}_3$  ice clouds. The signal of homogeneous planets with top pressure of the  $\text{NH}_3$  ice cloud deck at 0.1 bar (zone model; red, dotted line), 0.2 bar (belt model t1; green, dashed line), 0.3 bar (belt model t2; blue, dashed-dotted line), 0.4 bar (belt model t3; grey, dashed-triple-dotted line) and 0.4 bar (belt model t4; magenta, long-dashed line) are over-plotted for comparison.

Figure 5.5 clearly shows that, unlike the reflected flux,  $P_s$  is sensitive to cloud top altitudes across planetary phase angles that are important for direct detections. The reason is that  $P_s$  is very sensitive to the Rayleigh scattering optical thickness above the clouds, as has been known for a long time from observations of Solar System planets, such as the ground-based observations of Venus (Hansen & Hovenier 1974), and remote-sensing observations of the Earth by instruments such as POLDER on low-orbit satellites (Knibbe et al. 2000). As expected, with increasing  $\lambda$ , the sensitivity of  $P_s$  to the cloud top altitude decreases (see Figs. 5.9 and 5.10).

Figures 5.5–5.10 also show  $\pi F_n$  and  $P_s$  of horizontally inhomogeneous planets with zones and belts. In all figures, the cloud top pressure of the zones is 0.1 bar while that at the top of the belts varies from 0.2 bar (Figs. 5.5, 5.9, and 5.10) to 0.5 bar (Fig. 5.8). The shapes of the flux and polarization phase functions of these horizontally inhomogeneous planets are very similar to those of the horizontally homogeneous planets: one could easily find a horizontally homogeneous model planet with a cloud top pressure between 0.1 and 0.3 bar that would fit the curves pertaining to the horizontally inhomogeneous planets. The cloud top pressure that would provide the best fit would be slightly different when fitting the flux or the polarization curves. For example, fitting the flux reflected by an inhomogeneous



**Figure 5.6:** Same as in Fig. 5.5, but now for a belt top pressure of 0.3 bar.



**Figure 5.7:** Same as in Fig. 5.5, but now for a belt top pressure of 0.4 bar.

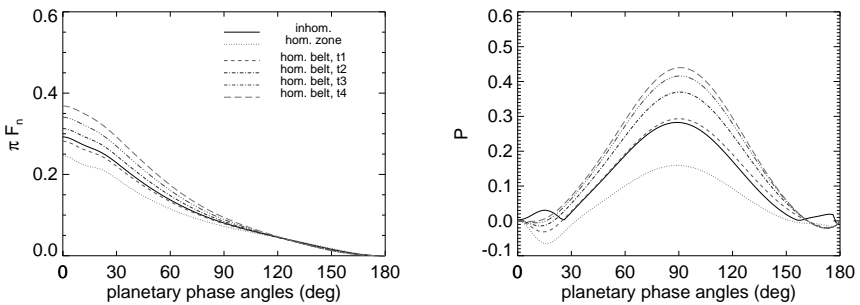


**Figure 5.8:** Same as in Fig. 5.5, but now for a belt top pressure of 0.5 bar.

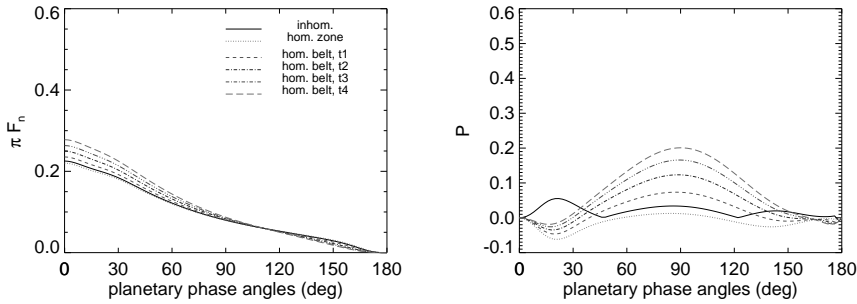


**Figure 5.9:** Same as in Fig. 5.5, but now for  $\lambda = 0.75 \mu\text{m}$ .

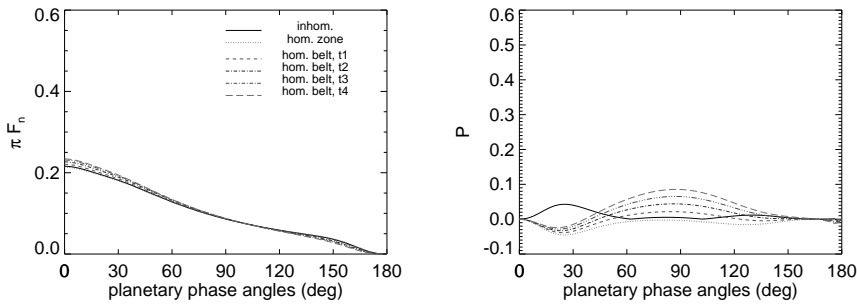


**Figure 5.10:** Same as in Fig. 5.5, but now for  $\lambda = 0.95 \mu\text{m}$ .

planet with cloud top pressures in the belts at 0.4 bar (Fig. 5.7) would require a homogeneous planet with its cloud top pressure at 0.2 bar, while fitting the polarization would require a cloud top pressure of about 0.18 bar. Such small differences would most likely disappear in the measurement errors. With increasing  $\lambda$ , the effects of the cloud top pressure decrease, in particular in  $\pi F_n$ . Covering a broad spectral region would thus not help in narrowing the cloud pressures down.

### 5.4.2 Cyclonic spots

Other spatial features on giant planets in our Solar System are (anti-)cyclonic storms that present themselves as oval-shaped spots. Famous examples are Jupiter's

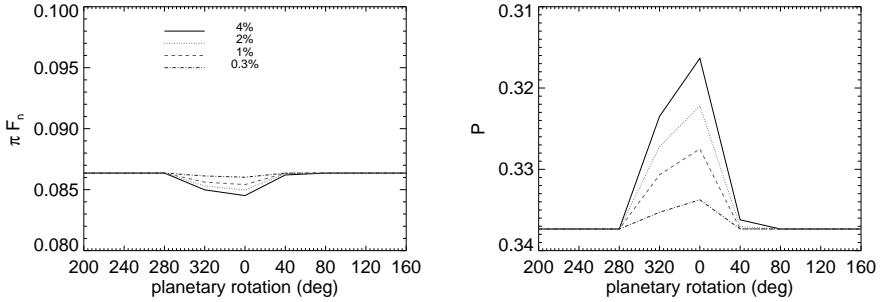


**Figure 5.11:**  $\pi F_n$  and  $P$  as functions of the angle of rotation (in degrees) of the planet around its own axis, for a Jupiter-like model planet with a spot (similar to Jupiter GRS). Different surface coverage cases are studied (0.3%: blue, dashed-dotted line, 1%: red, dashed line, 2%: green, dotted line and 4%: black, solid dashed line) in order to study the effect of the spot on the total planetary signal as a function of the surface coverage. All lines are plotted for  $\lambda = 0.55 \mu\text{m}$  and for  $\alpha \sim 90^\circ$ .

Great Red Spot (GRS) that appears to have been around for several hundreds of years and Neptune's Great Dark Spot (GDS) that was discovered in 1989 by Voyager-2, but that seems to have disappeared (Hammel et al. 1995). Recent spots on Uranus were presented by Hammel et al. (2009), Sromovsky et al. (2012). To study the effect of localized spots on reflected flux and polarization signals of exoplanets, we use a Jupiter-like model atmosphere with a spot of  $\text{NH}_3$  ice clouds extending between 0.75 and 0.13 bar. The clouds in the spot have an optical thickness of 36 at  $\lambda = 0.75 \mu\text{m}$  (Simon-Miller et al. 2001). We model the spot as a square of  $26^\circ$  in longitude by  $24^\circ$  in latitude.

Additionally, our model planet has zones and belts spatially distributed across the planet as described before, extending between 0.56 to 0.18 bar in the zones, and from 0.5 to 0.18 bar in the belts. The cloud optical thickness in the belts is 6.1, and in the zones 21 at  $\lambda = 0.75 \mu\text{m}$ .

Figure 5.11 shows reflected fluxes  $\pi F_n$  and degree of polarization  $P_s$  at  $\lambda = 0.55 \mu\text{m}$ , as functions of the planet's rotation angle. The planet's phase angle is  $90^\circ$ . The spot is on the planet's equator (which coincides with the planetary scattering plane). Recall that both Jupiter and Saturn have rotation periods on the order of 10 hours, while Uranus and Neptune rotate in about 17 and 16 hours, respectively. With a 10-hour rotation period and  $\alpha = 90^\circ$ , a small spot would cross the illuminated and visible part of the disk in about 2.5 hours. Curves are shown

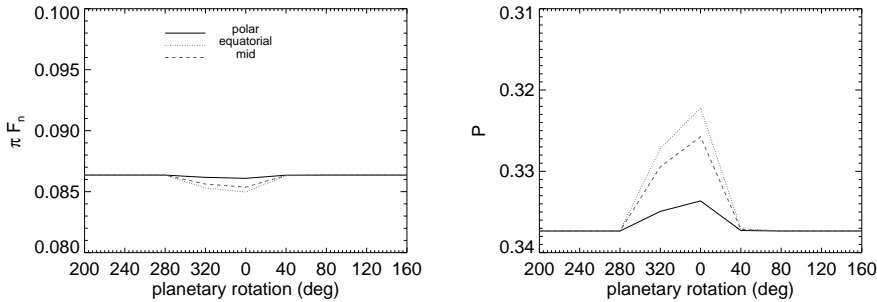


**Figure 5.12:**  $\pi F_n$  and  $P$  as functions of the angle of rotation (in degrees) of the planet around its own axis, for a model planet with a spot located at high latitudes (black, solid line), mid latitudes (red, dashed line) or low (equatorial) latitudes (green, dotted line).

for different sizes of the spot: covering at maximum 0.3 %, 1%, 2%, or 4% of the planet's disk, respectively. For comparison: the GRS covers about 6 % of Jupiter's disk. Each spot covers  $26^\circ$  in longitude, with its latitudinal coverage depending on the spot size. Note that the calculations for Fig. 5.11 have been done per  $40^\circ$  rotation of the planet, due to computational restrictions.

As can be seen in Fig. 5.11, the reflected fluxes  $\pi F_n$  hardly change upon the passage of the spot across the illuminated and visible part of the planetary disk: even for the largest spot located at the equator, the maximum change in  $\pi F_n$  is a few percent. In  $P_s$ , the transiting spots also leave a change of at most a few percent (absolute, since  $P_s$  is a relative measure itself). For spots located at higher latitudes of the planet, the effects are even smaller. With increasing wavelength, the sensitivity of both  $\pi F_n$  and  $P_s$  to the cloud top altitude decreases. At longer wavelengths, the effects of a spot would thus be smaller than shown in Fig. 5.11.

### 5.4.3 Polar hazes

The poles of both Jupiter and Saturn are covered by stratospheric hazes. In particular, when seen under phase angles around  $90^\circ$ , Jupiter's polar hazes yield strongly polarized signals. This high polarization can be explained by haze particles that consist of aggregates of particles that are small compared to the wavelength, and that polarize the incident sunlight as Rayleigh scatterers West & Smith (1991), with a high degree of polarization at scattering angles around  $90^\circ$ . We are interested in whether strongly polarized polar hazes will leave a trace in the disk-integrated

polarization signal of a planet.

We use a Jupiter-like model planet with belts and zones as in Sect. 5.4.1. The cloud top pressure of the belts is 0.3 bar. Starting at latitudes of  $\pm 60^\circ$ , the north and south poles of each model planet are covered by polar haze particles as described in Sect. 5.3.2. The optical thickness of the haze is 0.2 at  $\lambda = 0.55 \mu\text{m}$ .

In Figs. 5.13 and 5.14, we show, respectively  $\pi F_n$  and  $P$  at  $\lambda = 0.55 \mu\text{m}$ , across the visible and illuminated part of the planetary disk for  $\alpha = 0^\circ$  and for  $\alpha = 90^\circ$ . In flux, the differences between the zones and the belts are clearly visible, especially around the center of the planetary disk (for both angles  $\alpha$ ). The reflected fluxes due to the polar hazes do not stand out against those due to the clouds.

On the contrary, in polarization the variation of  $\alpha$  varies also the structure of our “map”. At high latitudes the polar haze produces a strong signal at  $\alpha \sim 90^\circ$ . In particular, at a latitude of  $\sim 80^\circ$ ,  $35\% \lesssim P \lesssim 60\%$ , while at  $\alpha \sim 0^\circ$   $P \lesssim 10\%$ . We repeat the calculations of our jovian planet at  $0.75 \mu\text{m}$  and  $0.95 \mu\text{m}$  (not shown here). At  $0.75 \mu\text{m}$  and for  $\alpha = 0^\circ$  our polar hazes produce a fractional  $Q/F$  polarization signal of  $\sim 6\%$ , which is close to the observations of Schmid et al. (2011).

In Fig. 5.15 we plot the disk integrated signal of our model planet at  $0.55 \mu\text{m}$  (black, solid line),  $0.75 \mu\text{m}$  (red, dotted line) and  $0.95 \mu\text{m}$  (green, dashed line). For comparison we also plot the disk integrated signal of our model planet without polar hazes ( $0.55 \mu\text{m}$ : blue, dashed-dotted line,  $0.75 \mu\text{m}$ : grey, dashed-triple-dotted line and  $0.95 \mu\text{m}$ : magenta, long-dashed line). In flux the influence of the polar hazes on the disk integrated planetary signal is not measurable ( $\Delta F \lesssim 0.3\%$  for  $\alpha = 90^\circ$ ). In polarization  $\Delta P_{0.55\mu\text{m}} \sim 1.3\%$  around  $\alpha = 90^\circ$ , while at the longer wavelengths  $\Delta P \lesssim 0.2\%$ .

We have tested the dependence of our results on the refractive index of our haze particles. We increased the refractive index ( $n$ ) of our particles to  $1.629 + i0.11$ . The variation of our hazes’  $n$  affects only slightly our jovian planet’s signal, and mostly at longer wavelengths. Finally, we have tested the dependence of our results on the “fluffiness” of our haze particles by modelling a more compact haze particle made of 112 spheres. The less fluffy hazes increase  $P$  of our model planets on the poles, especially at longer wavelengths.

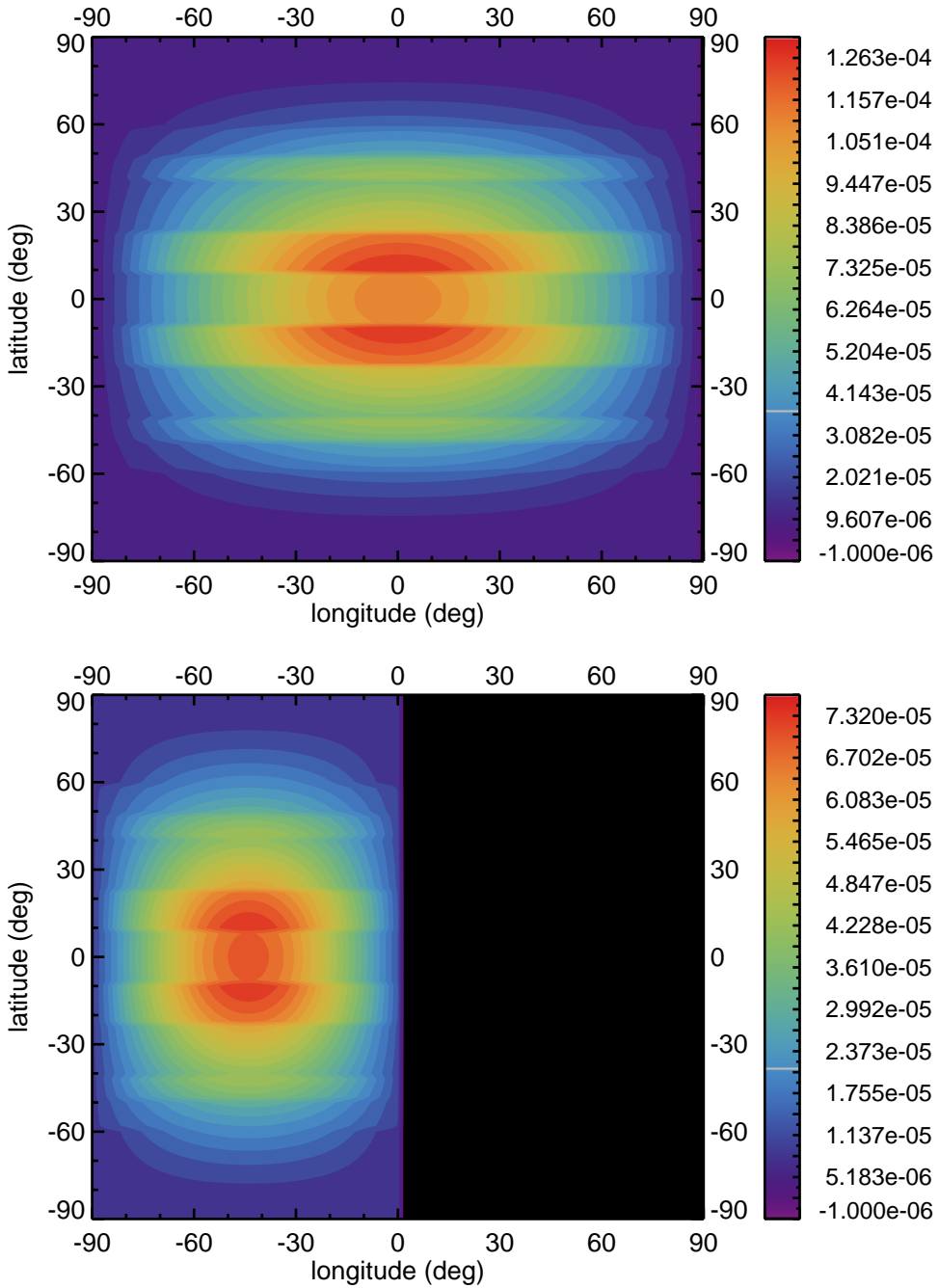


**Figure 5.13:**  $\pi F_n$  at  $0.55 \mu\text{m}$  of every pixel on the planetary disk for a jupiter like planet at  $\alpha = 0^\circ$  (top panel) and  $90^\circ$  (bottom panel). Our model planet contains zones, belts and polar haze between  $60^\circ$  and  $90^\circ$  of latitude.

## 5.5 Discussion and conclusions

A closer look at the planets of our Solar System reveals that inhomogeneity of one form or another is an intrinsic property of planets. Apart from Earth, which is by far the most inhomogeneous planet in our Solar System, all rocky planets and moons have some inhomogeneities (e.g. polar ice caps and dust storms on Mars), and even the giant planets with their various clouds and hazes exhibit some forms of inhomogeneity, others more (e.g. Jupiter) others less. For this reason, studying the influence of inhomogeneities on the planetary signal seems a reasonable choice, when we are interested in the complete characterization of exoplanets.

In Chapters 3 and 4 we have presented a code to model the signal of inhomogeneous exoplanets and used it to look for the rainbow on exoplanets with liquid and ice water clouds. In both Chapters, our calculations were made using an Earth-like model. Our planet has a surface and an atmosphere with an Earth-like temperature–pressure (T–P) profile. Our code though can be extrapolated for the studying gaseous planets as well.

Since with the present day technology in the near future the first exoplanets that will be characterized through direct detections will be giant exoplanets, we thought it would be interesting to apply our code to giant planets as well and see to what extent inhomogeneities influence the total planetary signal and can be detected. For this reason we combined our code with that of Stam et al. (2004), to include different atmospheric chemical compositions and T–P profiles. The inhomogeneities we took this time into account (Sect. 5.4), were based on inhomogeneities met on the giant planets of our Solar System and were namely zonal and band formations across the planetary disk and spots.

Following Jupiter (Sato & Hansen 1979, Simon-Miller et al. 2001) we used ammonia ice clouds as the main constituents of our model belts and zones. In Sect. 5.4.1 we study the effect of the  $\text{NH}_3$  ice zones and belts on the total planetary signal at various wavelengths, as a function of the cloud top pressure of our belts. The base of our clouds is kept at 1 bar on both the zones and belts. The cloud top pressure of our zones is set at 0.1 bar. The cloud top pressure of our belts varies from 0.2 bar down to 0.5 bar. We compare our results with homogeneous giant planet models containing a cloud deck of  $\text{NH}_3$  ice with various cloud top pressures.

Our results indicate that multi-wavelength observations are important for the characterization of an exoplanet. In particular, while in one wavelength there may be more than one models fitting our “observation” the same will not hold for the other wavelengths.

In flux there are more than one homogeneous models that fit the inhomogeneous model ( $\Delta F \lesssim 1\%$ ). If we were observing an exoplanet with zones and belts

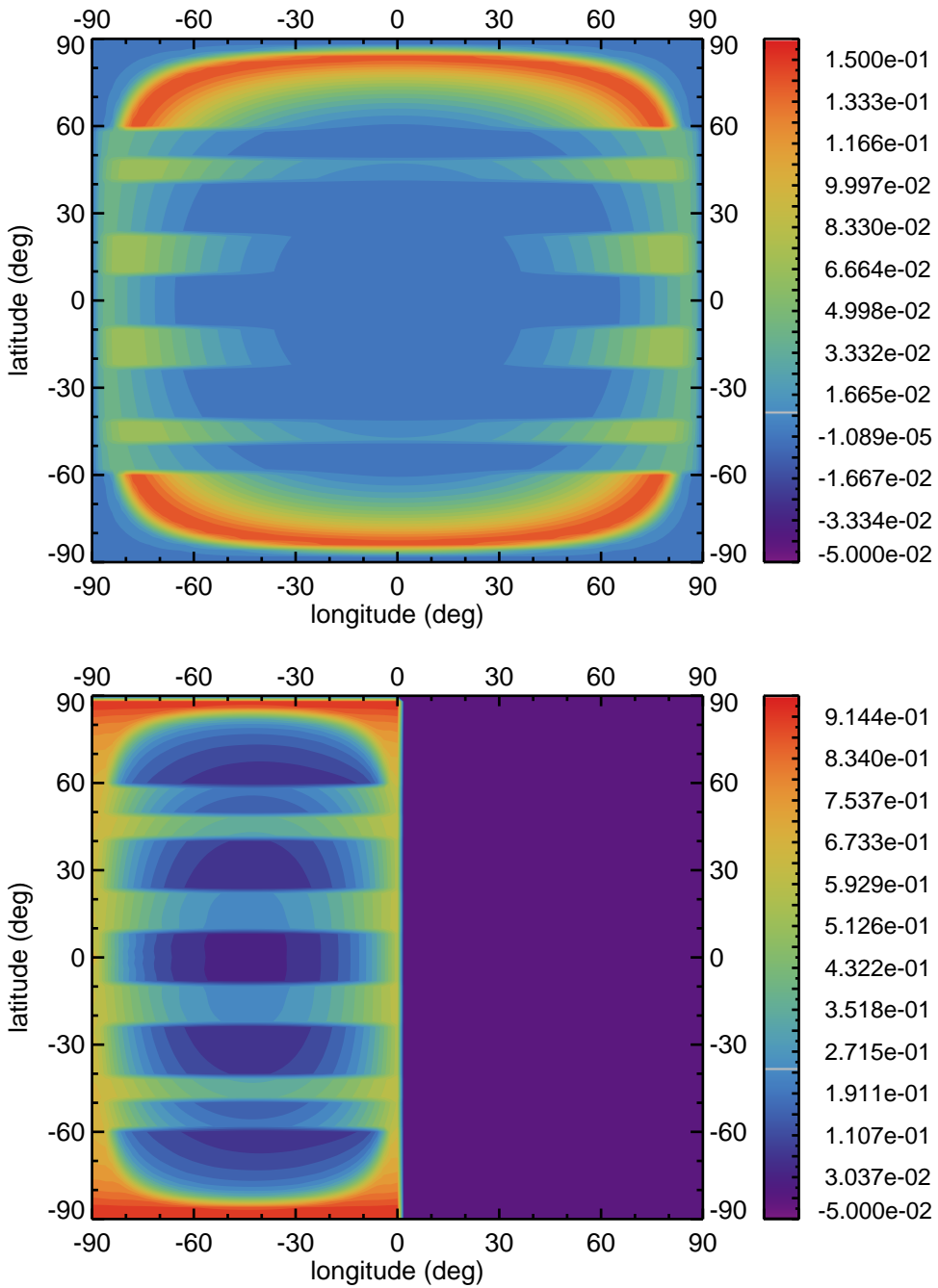
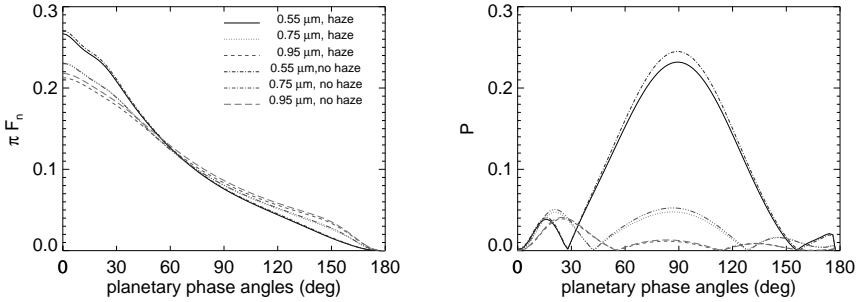


Figure 5.14: Same as in Fig. 5.13 but now for  $P$ .



**Figure 5.15:** Disk integrated  $\pi F_n$  and  $P$  as functions of  $\alpha$  for our jupiter like planets of Figs. 5.13 and 5.14 (black, solid line). Over-plotted are the disk integrated  $\pi F_n$  and  $P$  of our model planet at  $0.75 \mu\text{m}$  (red, dotted line) and  $0.95 \mu\text{m}$  (green, dashed line). For comparison we also plot the signals of our jovian planets without haze ( $0.55 \mu\text{m}$ : blue, dashed-dotted line,  $0.75 \mu\text{m}$ : grey, dashed-triple-dotted line and  $0.95 \mu\text{m}$ : magenta, long-dashed line).

similar to our model planet, we would not be able to characterize it based on flux-only measurements. The polarization, being sensitive to cloud top pressure (Knibbe et al. 2000), can help us distinguish among various models when flux cannot. In particular, in most cases  $P$  of our inhomogeneous model varies from the homogeneous models by more than 2% for  $\lambda = 0.55 \mu\text{m}$  and  $0.75 \mu\text{m}$ . At  $0.95 \mu\text{m}$   $P$  of our inhomogeneous model varies from  $P$  of the homogeneous zone model by less than 1%, making the separation between the two models impossible.

In case a giant planet has a spot-like feature like Jupiter's Great Red Spot or Neptune's Great Dark Spot it would be interesting to see if evidence for the existence of the spot survive in the disk-integrated planetary signal. For this reason in Sect. 5.4.2 we modelled a planet with zones and belts (following Simon-Miller et al. (2001)), and a spot-like feature containing  $\text{NH}_3$  ice clouds. We then vary the size and location of our spot on the planetary disk in order to study at which latitudes and what (relative) size must a spot have for an observer to be able to see its effect on the total planetary signal.

Our results show that a planet with a spot at mid to low latitudes that covers at least 2% of the planetary disk leaves a measurable signature on the planetary, disk-integrated  $P$  signal (see Figs. 5.11 and 5.12). In flux on the other hand,  $\Delta(\pi F_n)$  during a diurnal rotation of our model planet is less than 0.1% making the observation of the spot impossible.

Thus, in case an alien observer would observe our Solar System and could directly image Jupiter using both flux and polarization measurements depending on his position in relevance to the equator of the planet, he could get various information on the planetary composition. Given the fact that the Great Red Spot occupies a 4% to 7% of the planetary disk and is located close to the equator (around  $-20^\circ$  planetocentric coordinates (Fletcher et al. 2011)), the alien observer, when located close to the ecliptic plane, should be able to detect its signature on the total planetary signal. Of course, since Jupiter is quite a fast rotator the possibility of the alien observer to detect the existence of the Great Red Spot on the planetary disk, would largely depend on the necessary integration time.

An interesting feature of the giant planets of our Solar System, is the existence of haze on their poles, which leads to a large polarization signal on these planetary regions. We modelled our Jupiter-like planet's polar haze as aggregates (West & Smith 1991) with various refractive indexes and at three different wavelengths. Following Friedson et al. (2002) the refractive indexes used, where appropriate for hydrocarbons and/or PAHs.

The existence of polar hazes leaves a clear trace on the planetary maps. Especially the planetary  $P$ -map shows a strong wavelength and phase dependence. Our calculations at  $0.75 \mu\text{m}$  and for  $\alpha = 0^\circ$  show that our haze produce a fractional  $Q/F$  signal of  $\sim 6\%$ . This value is close to observations of Schmid et al. (2011) who find a  $Q/F$  of about 7%.

The disk integrated signal of our model planets holds no information on the existence of the haze in flux. In particular,  $\Delta(\pi F_n)$  between our haze-containing model and a model without haze is less than 0.3%.  $P$  at  $0.55 \mu\text{m}$  varies between the two models by  $\sim 1.3\%$ , allowing us to "see" the existence of the hazes on the exoplanet. At longer wavelengths  $\Delta P \lesssim 0.2\%$  and our disk integrated signal holds no information on the existence of haze on the planetary poles. Unfortunately, the existence of the polar hazes studied here, does not leave any distinctive trace in the shape of the flux or polarization curve of the planet as functions of the planetary phase angle, which probably indicates that the characterization of a similar planet would be degenerate.



# Observing the Earth as an exoplanet with LOUPE

---

Based on:

T. Karalidi, D. M. Stam, F. Snik, S. Bagnulo, W. B. Sparks and C. U. Keller, *Observing the Earth as an exoplanet with LOUPE, the Lunar Observatory for Unresolved Polarimetry of the Earth*, Planetary and Space Sciences, volume 74, p. 202–207, 2012

**Abstract** The detections of small, rocky exoplanets have surged in recent years and will likely continue to do so. To know whether a rocky exoplanet is habitable, we have to characterize its atmosphere and surface. A promising characterization method for rocky exoplanets is direct detection using spectropolarimetry. This method will be based on single pixel signals, because spatially resolving exoplanets is impossible with current and near-future instruments. Well-tested retrieval algorithms are essential to interpret these single pixel signals in terms of atmospheric composition, cloud and surface coverage. Observations of Earth itself provide the obvious benchmark data for testing such algorithms. The observations should provide signals that are integrated over the Earth's disk, that capture day and night variations, and all phase angles. The Moon is a unique platform from where the Earth can be observed as an exoplanet, undisturbed, all of the time. Here, we present LOUPE, the Lunar Observatory for Unresolved Polarimetry of Earth, a small and robust spectropolarimeter to observe our Earth as an exoplanet.

## 6.1 Introduction

Since the discovery of the first exoplanet (Mayor & Queloz 1995), more than 700 exoplanets have been detected as of today. Even though most of these exoplanets are gas giants, in recent years the number of detected smaller mass planets has surged (see e.g. Wordsworth et al. 2011). Indeed, according to (Cassan et al. 2012), about 62% of the Milky Way stars should have an Earth-like planet. A near-future detection of an Earth-sized exoplanet inside its star's habitable zone seems

inevitable. Whether or not an Earth-sized planet in a habitable zone is actually habitable, depends strongly on the composition and structure of its atmosphere. As an example, the Venusian surface is about  $500^{\circ}$  hotter than expected from Venus' orbital distance and albedo, thanks to an extremely strong greenhouse effect in its thick  $\text{CO}_2$  atmosphere. Hence, a characterization of the planetary atmosphere will be needed to address a planet's habitability.

Currently, atmospheres of exoplanets are being characterized using the so-called *transit method* (see e.g. Beaulieu et al. 2010, Miller-Ricci & Fortney 2010). This method is based on measurements of the wavelength dependence of starlight that filters through the upper layers of the planetary atmosphere during the primary transit (when the planet passes in front of the star), or of the planetary flux just before or after the secondary eclipse (during which the planet passes behind its star). The transit method is mostly applied to gaseous planets that orbit close to their star. Earth-sized exoplanets in the habitable zone of a solar-type star are too small to yield a strong enough signal for a spectroscopic characterization during transits (Kaltenegger & Traub 2009).

The best way to characterize the atmosphere and surface of an Earth-sized exoplanet, is through *direct detection*, using large ground-based telescopes such as the European Extremely Large Telescope (E-ELT) (Keller et al. 2010) or space telescopes with diameters of a few meters. With direct detection the light of a planet is measured separately from the stellar light (except for some background starlight). But even if we observe an exoplanet with a direct detection, the planet itself will be unresolved, i.e. it will appear as a single pixel. If the planet resembles the Earth, this single pixel holds information on oceans and continents, coverage by vegetation, desert, and, for example, snow and ice, all overlaid by various types of patchy clouds.

Polarimetry promises to play an important role in exoplanet research both for exoplanet detection and characterization. In particular, because the direct starlight is unpolarized (Kemp et al. 1987), while the starlight that is reflected by a planet will usually be polarized, polarimetry can increase the planet-to-star contrast ratio by 3 to 4 orders of magnitude (Keller et al. 2010), thus facilitating the detection of an exoplanet that might otherwise be lost in the glare of its parent star. Additionally, as in the case of Solar System planets (see e.g. Hansen & Hovenier 1974, Mishchenko & Travis 1997), polarimetry will help the characterization of planetary surfaces and atmospheres, because the polarization of the reflected starlight is very sensitive to the physical properties of an atmosphere and surface. In particular, it has been argued (Williams & Gaidos 2008) that polarimetry could help to detect the glint of starlight reflected on liquid surfaces, such as those of oceans, on exoplanets. Such a detection would be major step forward in the search for

life. Combining flux with polarimetric observations will also help to break retrieval degeneracies that flux-only measurements have (see e.g. Stam (2008) and Chapters 2 and 3). Finally, while measuring the state of *linear* polarization of reflected starlight helps to characterize a planetary atmosphere and surface, the degree of *circular* polarization of this light appears to be an indicator for the existence of life on a planet, since circular polarization, and in particular its wavelength dependence, is linked to homochirality of the complex molecules that are essential for life (Sparks et al. 2009b, Sterzik et al. 2010).

To decipher future signals of directly detected Earth-like exoplanets, numerical models that can simulate single pixel signals of exoplanets with inhomogeneous atmospheres and surfaces, are essential. Such models are essential for the design and optimization of telescope instruments and mission profiles (spectral bands, spectral resolution, integration times, revisiting times, etc.), and, once observations are available, they are a necessary tool to interpret the observations. There are a number of numerical models that are used to calculate signals of gaseous and terrestrial exoplanets, for reflected starlight and/or thermally emitted radiation (see e.g. Seager et al. (2000), Ford et al. (2001), Stam (2008), Tinetti et al. (2006a), Bailey (2007), Williams & Gaidos (2008) and Chapter 3). In order to validate the results of such numerical models, it is important to compare them against observations. The obvious test-case for numerical models for Earth-like exoplanets, is Earth itself. To fully validate these models, we need observations of the Earth as if it were an exoplanet, hence single pixel observations that cover the diurnal rotations of the Earth, and all phases of the Earth. And, ideally, the observations should cover different seasons to record the changes in surface albedos and weather patterns.

An excellent location for performing such observations and for building a benchmark dataset is the lunar surface facing the Earth. From there, we can observe the whole disk of the Earth, all of the time, at all phase angles, throughout the year. As we will argue in more detail in Sect. 6.3, such observations cannot be achieved by e.g. combining observations of Low Earth Orbit (LEO) satellites. In this Chapter, we present LOUPE, the Lunar Observatory for Unresolved Polarimetry of Earth. LOUPE is a small and robust spectropolarimeter that measures the flux and state of polarization of sunlight that is reflected by the Earth e.g. from ESA's Lunar Lander (Carpenter et al. 2012).

This Chapter is structured as follows. In Sect. 6.2, we present calculated flux and polarization spectra of a single pixel Earth. In Sect. 6.3, we summarize the advantages of observing the Earth from the moon. In Sect. 6.4, we describe the LOUPE instrument. Section 6.5, finally, contains the summary and our conclusions.

## 6.2 Flux and polarization spectra of the Earth as an exoplanet

### 6.2.1 Flux and polarization definitions

Sunlight that is reflected by a planet is described by a flux vector  $\pi\vec{F} = \pi[F, Q, U, V]$ , with  $\pi F$  the total flux,  $\pi Q$  and  $\pi U$  the linearly polarized fluxes and  $\pi V$  the circularly polarized flux (see e.g. Hansen & Travis 1974, Hovenier et al. 2004, Stam 2008). Each flux parameter depends on the wavelength  $\lambda$ , and has dimensions  $\text{W m}^{-2}\text{m}^{-1}$ . Linearly polarized fluxes  $\pi Q$  and  $\pi U$  are defined with respect to the plane through the center of the star, the planet and the observer (see Chapter 3). The degree of polarization  $P$  of the reflected sunlight is defined as the ratio of the polarized flux to the total flux, thus  $P = \sqrt{Q^2 + U^2 + V^2}/F$ . Specifically, the degree of linear polarization is defined as  $P_L = \sqrt{Q^2 + U^2}/F$ , and the degree of circular polarization as  $P_C = V/F$ .

### 6.2.2 Sample flux and linear polarization signals of the Earth

Figure 6.1 shows numerically calculated total fluxes  $\pi F$  and degrees of linear polarization  $P_L$  as functions of the wavelength  $\lambda$ . The Earth's phase angle,  $\alpha$ , is  $90^\circ$  (from the moon, one would see a 'half' Earth). The spectra have been calculated using the radiative transfer algorithm described in (Stam 2008), which assumes horizontally homogeneous model planets. We used four model planets, covered by sand, forest, ocean, or ice, combined with a cloud free or a completely cloudy atmosphere (composed of the model B cloud particles of Chapter 2) with an optical thickness of 10 (at  $0.55 \mu\text{m}$ ) and located between about 3 and 4 km. The forest and ice surfaces are treated as Lambertian reflectors, with albedos taken from the ASTER library. The ocean surface is completely flat and black with a Fresnel reflecting interface on top. The bi-directional and polarized reflection by the sand surface is modeled using an optically thick ( $\tau = 20$  at all  $\lambda$ ) layer of dust particles (Laan et al. 2009), with a single scattering albedo chosen such that the albedo agrees with that measured from an airplane above the Sahara (Bierwirth et al. 2009).

To model the spectra of the horizontally inhomogeneous Earth, we apply the weighted averages method (Stam 2008) using the total and polarized flux spectra of the horizontally homogeneous model planets. In Fig. 6.1, we have chosen the weighting factors such that they represent a case in which Africa and Eurasia are on the centre of the planetary disk and a case in which the Pacific ocean is on the centre. For comparison, the latter case is also shown with a cloud layer.

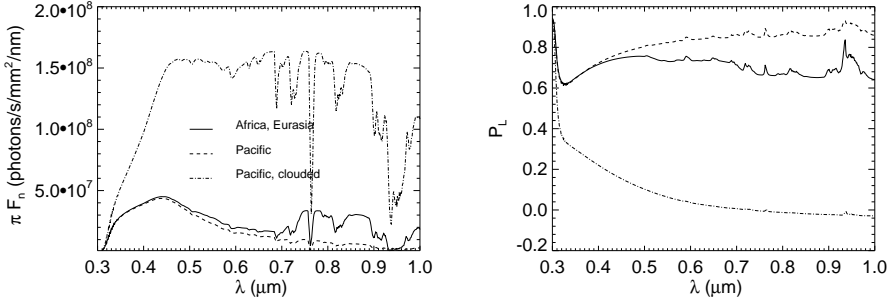


**Figure 6.1:** Calculated flux  $\pi F$  (left) and degree of linear polarization  $P_L$  (right) of sunlight reflected by the Earth as functions of  $\lambda$ , for  $\alpha = 90^\circ$ : with Africa and Eurasia in view and no clouds (solid lines), with the Pacific ocean in view and no clouds (dashed lines) and when completely cloudy (dashed-dotted lines).

For the solar flux that is incident on the Earth, we adopted the solar flux (in photons  $s^{-1} \text{ mm}^{-2} \text{ nm}^{-1}$ ) as measured on February 25th, 2008, by the GOME-2 spectrometer (Callies et al. 2000) on the Earth-observing MetOp satellite. The measured spectrum runs from 0.3  $\mu\text{m}$  to 0.8  $\mu\text{m}$ , and we extrapolated it smoothly towards 1.0  $\mu\text{m}$ .

The flux and polarization spectra of the cloud-free planets in Fig. 6.1 clearly show the traces of the Earth's surface and atmosphere. For a detailed explanation of the spectral features due to gaseous absorption by  $\text{O}_3$ ,  $\text{O}_2$ , and  $\text{H}_2\text{O}$ , see (see the explanation below (box A) or (Stam 2008)). Longwards of 0.7  $\mu\text{m}$ , the characteristic red-edge albedo feature of the vegetation (Seager et al. 2005) clearly shows up in  $\pi F$  when the continents are in full view:  $\pi F$  is higher by almost a factor of 5 (at 0.85  $\mu\text{m}$ ) than when the Pacific is in view (a small fraction of this increase will be due to the sand surface). The red-edge feature shows up as a decrease of  $P_L$  (of about 20% in absolute value) because an increase in surface albedo increases the amount of unpolarized light that is reflected towards the observer. Adding clouds to the model atmosphere increases  $\pi F$  strongly (except in the deepest gaseous absorption bands):  $\pi F$  is  $\sim 12$  times ( $\sim 23$  times) higher at  $\lambda = 0.65 \mu\text{m}$  (0.85  $\mu\text{m}$ ). At the same time, the clouds significantly decrease  $P_L$  at this phase angle ( $\alpha = 90^\circ$ ):  $\sim 80\%$  at  $\lambda = 0.65 \mu\text{m}$ . The model planets used in Fig. 6.1 are either cloudfree or completely cloudy. In reality, the Earth is only partly covered by clouds (with a range of optical thicknesses) and the real flux and polarization spectra will be mixtures of the spectra that are shown here.

In Fig. 6.2 we show  $\pi F$  and  $P_L$  at  $\lambda=550$  nm, as functions of phase angle  $\alpha$  for the model Earth that has a cloud coverage of about 42 % (the cloud properties are the same as in Fig. 6.1). The narrow features on top of the curves are due to the daily rotation of the planet as it orbits its star, showing ocean and/or continents through the holes in the clouds. The “bump” in the curves around  $\alpha = 38^\circ$  are due to the primary rainbow: sunlight that has been scattered by the cloud droplets once. Clearly, the rainbow is much more pronounced in  $P_L$  than in  $\pi F$ . Finding a rainbow in exoplanetary polarization signals will be a direct indication for the presence of liquid water droplets in the planetary atmosphere (for a more detailed description of rainbows on exoplanets, see Bailey 2007). The angular separation of the colors in exoplanetary rainbow could help to determine the cloud particle sizes (see Chapter 2).

The spectra in Figs. 6.1 and 6.2 do not include the contribution of sunlight that is scattered by the zodiacal dust surrounding the Earth. Sunlight scattered by this dust will usually be linearly polarized (see Renard et al. 1995), with a degree and direction of polarization that will depend on the phase angle, the wavelength, and on local variations in the dust particle properties. Since the dust is optically thin and dark (Renard et al. 1995), its contribution to the measured signal will depend strongly on the spatial resolution of the observations. When the instrument design allows spatially resolved observations (see Sect. 4), the signal of the zodiacal light could be measured separately from the Earth’s signal, and provide valuable benchmark data for (exo)zodiacal dust disk models. In the case of spatially unresolved observations (see Sect. 4), the contribution of the zodiacal dust to the total flux and polarization signal is expected to be negligible, because of the brightness of the Earth’s disk. Modelling of this contribution will be part of the future instrument studies.

### 6.2.3 Circular polarization

All known living material on Earth exhibits homo-chirality: sugars and nucleic acids occur exclusively in the right-handed form, and amino-acids and proteins in the left-handed form. Homo-chirality makes light scattered by organic material partially circularly polarized, and circular polarimetric spectra of various samples of biological material have been published (Wolstencroft et al. 2004, Sparks et al. 2009b, Sterzik et al. 2010). The reasons for homo-chirality are unknown, but if similar evolutionary scenarios naturally occur elsewhere in the universe, measuring  $P_C$  could be a unique tool for the detection of life on exoplanets. Since the Earth is the only planet we know that has life on it, Earth observations are the only way to empirically test this remote-sensing method. Some abiotic scattering

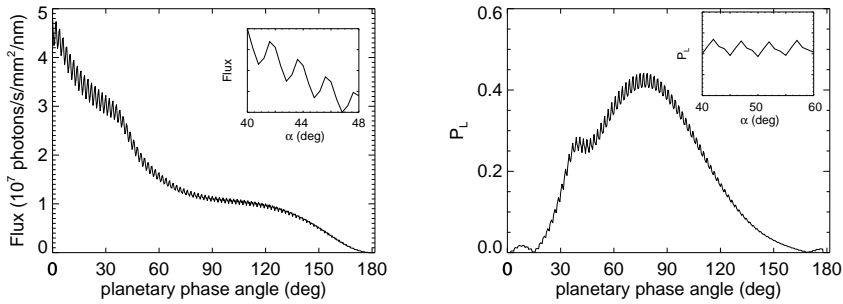


**Figure 6.2:** Calculated  $\pi F$  (left) and  $P_L$  (right) of sunlight reflected by a rotating model Earth with 42% cloud coverage as functions of  $\alpha$ , at 550 nm.

processes (e.g. by optically active atmospheric aerosols or minerals) may also give a measurable  $P_C$ , but as shown in (Sparks et al. 2009b) the wavelength dependence of these signals is very different from that of the circular polarization of biological material (Sparks et al. 2009a).

The degree of circular polarization produced by biological material is generally weak, on the order of  $10^{-3} - 10^{-4}$  (see Sparks et al. 2009b). Therefore, it would be very interesting to perform spatially resolved observations of the Earth, as this would allow us to study whether such signals can be measured locally (e.g. over the Amazonian rainforest) and whether they could be measurable in disk integrated signals.

### 6.3 The advantages of using the Moon as observation platform

In order to build a comprehensive database of benchmark data of the Earth as an exoplanet and to be able to fully test numerical algorithms for signal simulation and planet characterization, the requirements on the flux and polarization observations are as follows:

- 1) Each observation of the Earth should be (nearly) instantaneous, to observe different regions on the illuminated and visible part of the Earth simultaneously and hence to capture the effects of the differences in local solar zenith angles and viewing angles.

### A. The spectrum of Earth as an exoplanet

In Fig. 6.1 we plot the flux and polarization spectrum of a simplified Earth as if it were an exoplanet. The high-spectral resolution features that we see in both flux and polarization are due to gaseous absorption bands.

At the shortest wavelengths light is absorbed by the atmospheric  $O_3$ , causing a dip in the reflected flux and a corresponding increase in the degree of polarization around  $0.3 \mu\text{m}$ . Between  $\sim 0.5 \mu\text{m}$  and  $\sim 0.7 \mu\text{m}$  we notice, especially in the case we observe areas with high surface albedo (here, the case of Africa and Eurasia), a dip in the reflected flux, which is the so-called Chappuis absorption band of  $O_3$ . Around  $0.76 \mu\text{m}$  we notice a deep absorption band which is the famous oxygen A-band, the easiest identifiable  $O_2$  band in our atmosphere. The oxygen A-band is useful for the characterization of planetary atmospheres, since its depth compared to the continuum, can help us determine the cloud top heights in a planetary atmosphere (see e.g. Wu 1985, and references therein).

In polarization, we notice that the spectrum of our planet looks similar to that in flux, only now the absorption lines have transformed into “emission” lines, i.e. there is a local increase in the degree of polarization where an absorption line lies. The reason for this is that the absorption of light in a band decreases the amount of multiple scattered light and we see mostly light that is singly scattered ((normally) with a higher degree of polarization) in the atmosphere.

The general increase in polarization that we observe with wavelength in the non-cloudy cases is due to the decrease in the optical thickness of the atmosphere with wavelength, which leads to a small(er) amount of multiple scattering. In this way, in the case we observe the Pacific region, since the ocean surface is almost black the polarization reaches almost as high as the single scattering value of the atmosphere. In the case we observe the Africa–Eurasia area on the other hand, a number of photons will have managed to reach as low as the surface and get reflected. At the longer wavelengths, where the atmosphere is less opaque the number of photons that have managed to penetrate the atmosphere and reflect on the surface is (getting) comparable to the number of singly scattered photons on the upper atmosphere and the degree of polarization decreases.

- 2) Observations should cover the Earth's diurnal cycle, to capture the effects of different regions of the Earth emerging from the night, and disappearing over the limb (or the other way around), with the corresponding local changes in solar zenith and viewing angles.
- 3) The Earth should be observed at phase angles from  $\sim 0^\circ$  ('full Earth') to  $\sim 180^\circ$

('new Earth'), with steps small enough to capture characteristic angular features in the reflected  $\pi F$  and  $P$ , such as the glint of sunlight reflected by surface water and the rainbow of sunlight scattered in clouds.

4) The observations should ideally cover all seasons to capture the effects of changes in local solar zenith angles, polar nights, weather and cloud patterns, and surface albedos.

Thanks to the monthly orbit of the Moon around the Earth and the tidal locking of the Moon with respect to the Earth, a spectropolarimeter on the lunar surface could observe the whole Earth, during each day, at all phase angles (depending on the power source), and, in principle, throughout the seasons. Such whole Earth observations cannot be obtained from (existing) artificial satellites, such as Low Earth Orbit (LEO) remote-sensing satellites or geostationary satellites. LEO satellites observe local regions on the Earth, and would require several days to achieve global coverage. In addition, a certain location on Earth will always be observed under similar illumination and viewing geometries (apart for seasonal variations of the local solar zenith angle). Currently, only the POLDER Earth-observing satellite instrument has polarimetric capabilities (broadband, no spectropolarimetry). Geostationary satellites observe the same hemisphere of the Earth all of the time. While these satellites do capture the effects of the diurnal rotation and at the same time the phase angle changes of the Earth, they cannot observe different regions of the Earth, and their observations cannot teach us how to derive a global distribution of oceans and continents from single pixel measurements. There are currently no polarimeters onboard any geostationary satellite. A network of geostationary satellites could be used to capture the whole Earth. However, with such a network, it would not be possible to measure the effects of e.g. continents emerging from the night into the daylight or disappearing over the limb. In addition, to be able to compare total flux measurements from different satellites, every spectropolarimeter should be carefully internally calibrated.

Recent spectropolarimetric Earthshine observations (Sterzik et al. 2012), in which sunlight that has been reflected first by the Earth and then by the moon is measured with Earth-based instruments (see e.g. Qiu et al. 2003, Sterzik & Baguolo 2009) confirm that disk-integrated polarimetric observations are extremely sensitive to the visible surface and atmosphere of the Earth. At the same time, discrepancies between theoretical predictions and observations demonstrate that multi-epoch observations of the Earth are needed to constrain the models. The major drawback of Earthshine observations is that the properties of the lunar surface are not known well, especially when polarization is involved. This makes the modelling enormously more difficult than in the case of observations from space (including the Moon). Ground-based Earthshine observations are also hampered

by background contamination from the sunlit fraction of the Moon, and do not allow the same phase angle coverage (both in range and in angular resolution) and are unable to capture the full diurnal rotation.

Finally, a number of non-dedicated missions (e.g. Voyager 1, and more recently Deep Impact) have taken snapshots of the Earth.<sup>1</sup> These observations, while often providing interesting data, do not cover the diurnal rotation nor the phase angle range nor the seasonal effects. There have been no polarimetric observations performed by such missions.

A spectropolarimeter could be put onboard a specially designed satellite in an orbit that allows performing the required observations. That orbit would, however, probably closely resemble the orbit of the moon. Including the instrument on a Lunar Lander thus seems a straightforward and economical choice.

## 6.4 The LOUPE instrument

LOUPE, the Lunar Observatory for Unresolved Polarimetry of Earth shall fulfill the following requirements:

- It performs spectropolarimetric observations of the light from the Earth's disk (at least) at visible wavelengths (400–800 nm).
- The spectral resolution for the polarimetry shall be  $\sim 20$  nm, while the O<sub>2</sub>A band ( $\sim 0.76 \mu\text{m}$ ) is resolved in the flux spectrum. Limited spectropolarimetry can be performed within this and other bands.
- Data is collected on an hourly basis to resolve the Earth's rotation, and span at least a month to cover a full range of phase angles.
- The instrument is small and robust.

For the polarimetry, we explore two different scenarios:

1) *Linear spectropolarimetry only*. For this we adopt the spectral modulation approach (Snik et al. 2009). Using a combination of standard solid-state polarization optics (see Fig. 6.3), the total flux spectrum is multiplied by a sinusoidal modulation for which the amplitude scales with  $P_L$ , and the phase is determined by the angle of polarization. This novel polarimetric concept is being applied in the SPEX instruments. The SPEX prototype exhibits excellent polarimetric performance (van Harten et al. 2011).

---

<sup>1</sup>for a nice overview see: <http://planetary.org/explore/topics/earth/spacecraft.html>

2) *Linear and circular spectropolarimetry.* This implementation is more challenging as the data dimensionality is larger, and, moreover,  $P_C$  ( $\sim 10^{-4}$ ) is much smaller than the average  $P_L$  ( $\sim 10^{-4}$  versus  $\sim 0.1$ ). The spectral modulation approach in (Nordsieck 1974, Oka & Kato 1999) yields three modulation periods that contain information on the complete flux vector. The modulation approach introduced by (Sparks et al. 2012) yields similar modulations, but along the slit direction.

Various options can be identified for spatial resolution and pointing:

A) The instrument itself averages the light from the Earth's disk ( $\sim 2^\circ$  diameter). Because the disk is surrounded by black space, this requires only course pointing. The acceptance angle of the instrument should be wide enough to take lunar libration ( $\pm 8^\circ$ ) into account.

B) The instrument spatially resolves the Earth's disk to obtain data of e.g. just the Amazonian rainforest to maximize the circular polarization signal. Such spatial information can be attained by using a scanning slit or an integral field unit. In any case, accurate pointing and potentially scanning should be implemented. Averaging over the Earth's disk is then performed in the data pipeline. Spatially resolved measurements allow to measure the relatively weak signal of the zodiacal dust.

A sketch of the most basic implementation (1A: only linear spectropolarimetry and no spatial resolution) of LOUPE is presented in Fig. 6.3.

## 6.5 Summary and conclusions

We present LOUPE, the Lunar Observatory for Unresolved Polarimetry of Earth. LOUPE is a small and robust spectropolarimeter that can observe the Earth as if it were an exoplanet from a vantage point on the lunar surface. The Moon has a unique position with respect to Earth and can provide us with a unique platform from where we can observe the Earth as an exoplanet. From the Moon, LOUPE will be able to observe the whole disk of the Earth, all of the time, at most phase angles and throughout the year.

LOUPE measures the total flux and state (degree and direction) of polarization of sunlight that is reflected by the Earth. Polarimetry appears to be a strong tool for the characterization of exoplanets, allowing the retrieval of the composition and structure of a planet's atmosphere and surface (if present). In particular, the degree of linear polarization can give us information on the presence of liquid water clouds and the degree of circular polarization on the presence of life. LOUPE measurements would be used as a benchmark for future Earth-like exoplanet observations and to test numerical algorithms for the retrieval of planet properties from such observations.

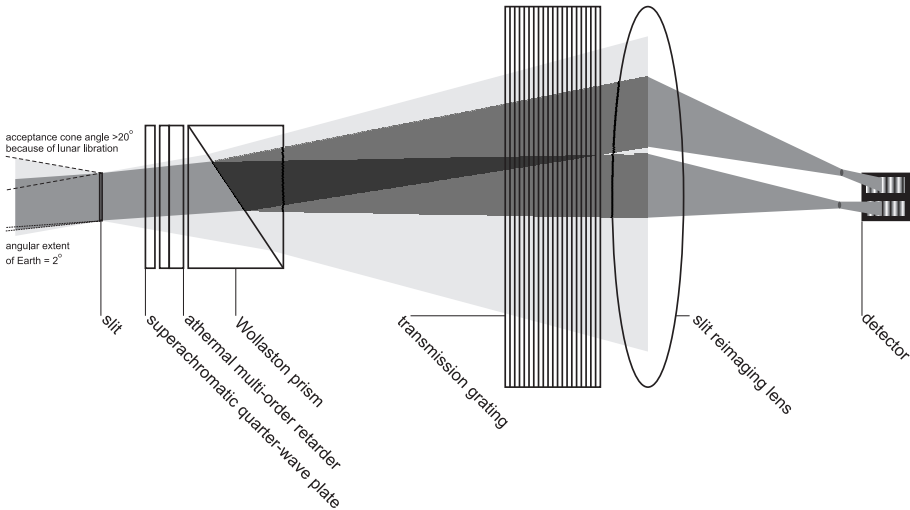


**Figure 6.3:** Schematic depiction of a potential implementation for LOUPE option 1A (only linear spectropolarimetry, no spatial resolution). The scale is approximately 1:1. The (wide-field) spectral polarization modulation optics are located behind the entrance slit. A Wollaston prism serves as a polarizing beam-splitter. A transmission grating or grism disperses the light, and a reimaging lens focuses the two spectra on the detector. An image of the Earth appears at the focal length of that lens. This instrument only needs to be roughly pointed towards the Earth as it accepts light from all angles within the range determined by the lunar libration.

## B. SPEX, the working force behind LOUPE

LOUPE, in its simplest configuration, when we are only interested in the linear polarization of Earth-as-an-exoplanet is working based on the concept of spectral polarization modulation of SPEX (Snik et al. 2009, van Harten et al. 2011).

Classical methods apply temporal or spatial modulation (or both), which demand moving parts (and thus a lot of energy, and risk of failure) and a lot of space (and high energy consumption in order to perform calibration of the system) respectively, while with SPEX we opt for low energy consumption and small volume. For this reason, for the polarization modulation of SPEX a new method was proposed, which takes into advantage the existence of a spectrograph in the system, and maps the polarization properties of the incoming signal onto the spectral dimension. The idea is to apply a “spectral modulation”, which is ideally achieved when a sinusoidal modulation of known periodicity is superimposed on top of the incoming spectrum with the amplitude and the phase of the modulation depending on the polarization characteristics of the incoming signal (in particular the amplitude depends on  $P$  and the phase on  $\chi$ ). SPEX encodes the degree and angle of linear polarization of the incoming (observed) signal in the sinusoidal form:  $I_{out}(\lambda) = (\frac{1}{2} + \frac{1}{2}P(\lambda)\cos(\frac{C(\lambda)}{\lambda} + 2\chi(\lambda, T)))I_{in}(\lambda)$ , where  $I_{in}$  is the incoming intensity and  $C(\lambda)$  depends on the retardance of the (multiple-order retarder of the) system (see Snik et al. 2009).

## Nederlandse samenvatting

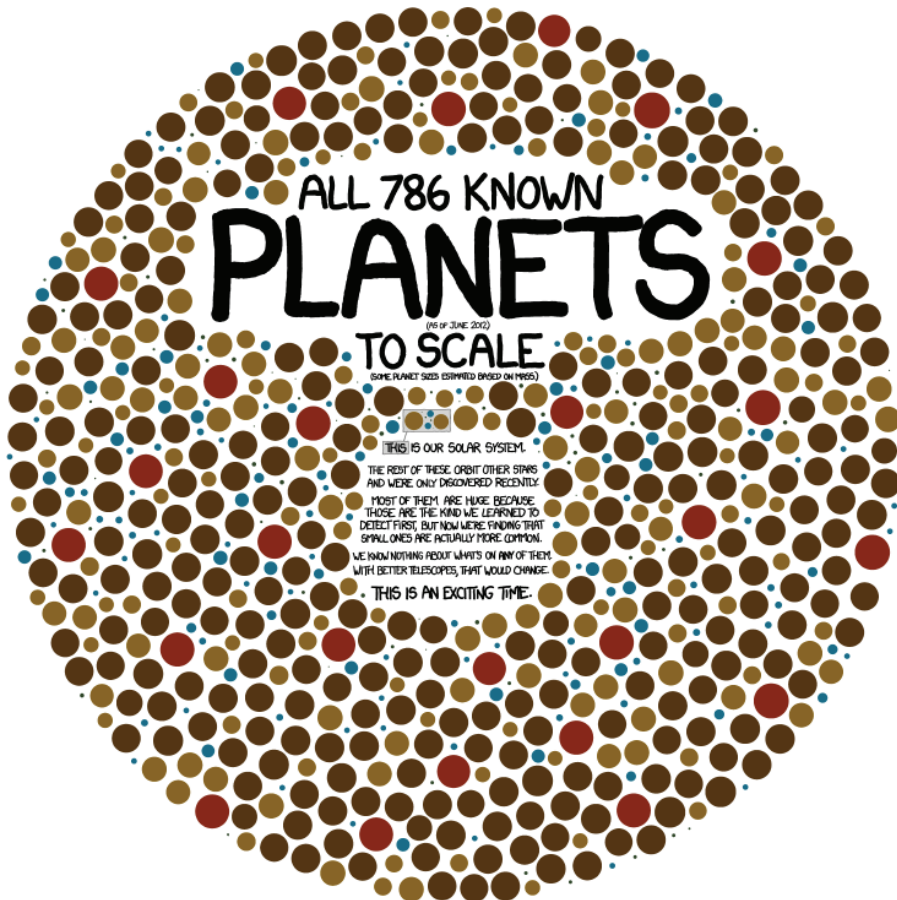
---

### 7.1 Exoplaneten, een korte geschiedenis

Dit proefschrift gaat over het modelleren en bestuderen van sterlicht dat gereflecteerd wordt door exoplaneten met verschillende micro- en macrofysische eigenschappen. Met de term “exoplaneet” bedoelen we een planeet die om een *andere* ster dan onze Zon draait. Het mogelijke bestaan van planeten buiten ons eigen zonnestelsel en de mogelijkheid van leven op zo’n planeet is een onderwerp dat de mensheid al duizenden jaren fascineert. Al rond de vierde eeuw voor het begin van onze jaartelling filosofeerden Democritus en Epicurus over het bestaan van andere planeten zoals de Aarde en de mogelijke verschillen. De mening van de invloedrijke Aristoteles dat er slechts één wereld kan bestaan (namelijk die van ons) zorgde er echter voor dat er eeuwenlang geen discussie meer plaatsvond over het onderwerp.

Het was de Nederlander Christiaan Huygens (1629–1695) die eeuwen later een filosofische discussie opschreef over het bestaan van andere planeten en de mogelijkheid voor het bestaan van leven op zo’n planeet. Inmiddels zijn we vier eeuwen verder en heeft de mensheid de mogelijkheid om de eerste exoplaneten te ontdekken. In 1992 was het Wolszczan & Frail (1992) die de eerste exoplaneet ontdekte. Deze exoplaneet draait echter om een pulsar: het zeer compacte eindproduct van een zware ster, met zo’n sterk magneetveld dat de omgeving van die planeet niet bepaald gunstig is voor leven zoals wij het kennen. Toen een paar jaar later Mayor & Queloz (1995) de eerste exoplaneet ontdekten die om een ster vergelijkbaar met onze Zon draait, begon er een nieuw tijdperk voor de sterrenkunde.

Sindsdien zijn er meer dan 770 exoplaneten ontdekt. Deze zijn schematisch weergegeven in Fig. 7.1. De meerderheid van deze planeten zijn zogenaamde gasreuzen: gasachtige planeten tot een paar keer zwaarder dan Jupiter, de zwaarste planeet in ons zonnestelsel. Ook roteren ze vaak in een erg nauwe baan rond hun ster. Gelukkig is dit slechts een “selectie-effect”: de methoden om exoplaneten te ontdekken waren in de eerste jaren veel gevoeliger om gasreuzen in een nauwe baan te ontdekken dan aardachtige planeten in een wijdere baan. Er is echter een grote kans dat astronomen de komende jaren een zusje van onze Aarde zullen vinden.



**Figuur 7.1:** We leven in een opwindende tijd waarin de ene na de andere planeet buiten ons zonnestelsel wordt ontdekt. Op dit moment, in minder dan 20 jaar tijd, zijn er meer dan 770 planeten ontdekt. De meeste van deze planeten zijn gasreuzen die een paar keer zwaarder zijn dan Jupiter. Gelukkig voor diegenen die graag een tweede Aarde willen ontdekken is dit slechts een selectie-effect, veroorzaakt door de gebruikte technieken en instrumenten die de eerste jaren zijn toegepast. Tekening van <http://www.xkcd.com>.

De meest gebruikte technieken om exoplaneten te ontdekken zijn indirect. We zien niet de exoplaneet zelf, maar de invloed op het signaal van de ster waar de planeet omheen draait. Deze invloed kan bijvoorbeeld gravitationeel zijn (de planeet beïnvloed het zwaartekrachtsveld van de ster) en dit kunnen we meten met de radieële snelheidsmethode (het meten van het "wiebelen" van een ster met behulp van een spectrum) of de microlens methode (het meten van helderheidsvariaties terwijl een zwaar object de ruimte-tijd vervormt). De exoplaneet kan ook voor of achter zijn ster langs bewegen, waarbij er kleine variaties in de helderheid van de ster optreden die we kunnen meten. Het is waarschijnlijk niet moeilijk om voor te stellen dat als een planeet zwaarder is en dichterbij zijn ster staat, zijn invloed op de ster groter is. Zo trekt de zwaartekracht van een zwaardere planeet harder aan de ster, waardoor het wiebelen van de ster makkelijker te meten is met een spectrum (via het Doppler effect). Als een planeet dichterbij zijn ster staat en dus een snellere omlooptijd heeft, treden de variaties vaker op en zijn deze dus makkelijker te zien. Een zusje van de Aarde die op dezelfde afstand van haar ster staat als de afstand tussen de Aarde en de Zon, zal echter maar een wiebel veroorzaken van 1 cm/sec en dat is op dit moment nog te weinig om te kunnen meten (de huidige grens ligt bij 1 m/sec).

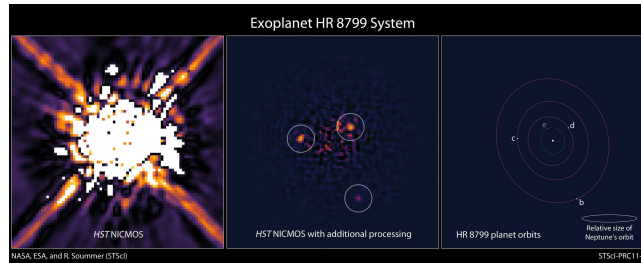
Terwijl het aantal ontdekte exoplaneten toeneemt, verschuift de interesse van de astronomen nu van het ontdekken naar het karakteriseren van exoplaneten. Het doel is nu vooral om meer te weten te komen over de omstandigheden op de reeds ontdekte exoplaneten: hebben ze een atmosfeer? Is er leven mogelijk? We weten uit onze ervaring met de planeten in ons zonnestelsel dat het bestaan van leven nauw verbonden is met het bestaan van water in de atmosfeer of aan het oppervlak van een planeet. Maar hoe ontdek je water op een planeet op vele lichtjaren afstand?

## 7.2 Het belang van polarisatie

De oplossing hiervoor is het direct waarnemen van exoplaneten en de polarisatie van het sterlicht dat zij reflecteren. Het licht van een ster zoals onze Zon is ongepolariseerd<sup>1</sup>, terwijl het licht dat een planeet reflecteert gepolariseerd is, vanwege de reflecties en verstrooiingen aan het oppervlak en/of in de atmosfeer. Dit bete-

---

<sup>1</sup>Natuurlijk licht, zoals zonlicht, bestaat uit electromagnetische golven die in alle richtingen trillen zonder een voorkeursrichting te hebben. Dit licht noemen we ongepolariseerd, of 0% gepolariseerd. Als deze golven tegen materie botsen, zoals bijvoorbeeld de moleculen in de atmosfeer van een planeet, of het oppervlak, krijgen de trillingen een voorkeursrichting. Dit noemen we (gedeeltelijk) gepolariseerd licht. In sommige gevallen, zoals bij een laser, trillen alle golven in één richting en spreken we van 100% gepolariseerd licht.

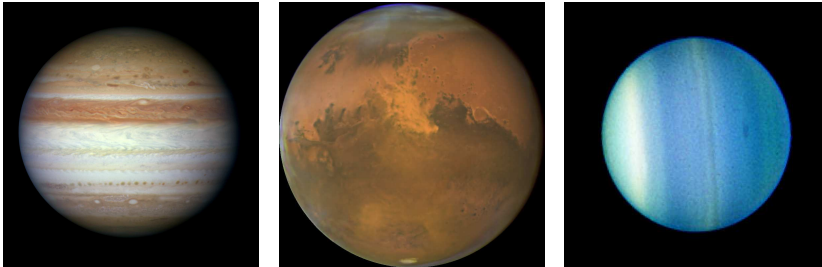


**Figuur 7.2:** Toen de Hubble Space Telescope in 1998 de linker foto nam, zagen astronomen niets opmerkelijks. Meer dan tien jaar later werden er echter drie exoplaneten zichtbaar nadat er nieuwe beeldbewerkingstechnieken werden toegepast op de oude data (middelste foto). De rechter foto laat de banen zien van vier exoplaneten die al met telescopen vanaf de grond waren ontdekt. De vierde planeet, “e” is niet te zien op de middelste foto omdat deze net aan de rand ligt van de coronograaf van de NICMOS camera. Copyright: NASA, ESA and R. Soummer (STScI).

kent dat we een exoplaneet makkelijker kunnen zien als we in gepolariseerd licht waarnemen en tegelijkertijd levert het gepolariseerde licht belangrijke informatie op die gebruikt kan worden om het oppervlak en de atmosfeer te karakteriseren. Soms hebben we het ook over de hoeveelheid *ongepolariseerd* licht. Dan spreken we in dit proefschrift over “flux”. In het ideale geval wordt de *combinatie* van flux en polarisatie gebruikt om een planeet volledig te karakteriseren.

Al meer dan een eeuw weten we hoe belangrijk het is om gepolariseerd licht te gebruiken om de atmosferen van planeten in ons zonnestelsel te bestuderen. In 1929 gebruikte de Fransman Lyot (Lyot 1929) de polarisatie van gereflecteerd licht van de atmosferen van Venus en Jupiter om hen te karakteriseren. Een paar decennia later ontdekten Hansen & Hovenier (1974) met behulp van polarisatie de chemische samenstelling en de grootte van de druppeltjes in de hoogste wolken van de atmosfeer van Venus en konden zij de hoogte van deze wolken bepalen.

Van de planeten in ons zonnestelsel kunnen we met behulp van telescopen verschillende gebieden op de planeetschijf onderscheiden. Dit is niet mogelijk voor exoplaneten. Een exoplaneet staat altijd zó ver weg dat het beeld slechts bestaat uit één pixel (zie ook Fig. 7.2). Hoe kunnen we dan toch zo’n planeet karakteriseren? Stam et al. (2004) en Stam (2008) hebben laten zien dat het gebruik van polarisatie ons helpt om meer over de samenstelling van dit “puntje” te leren.

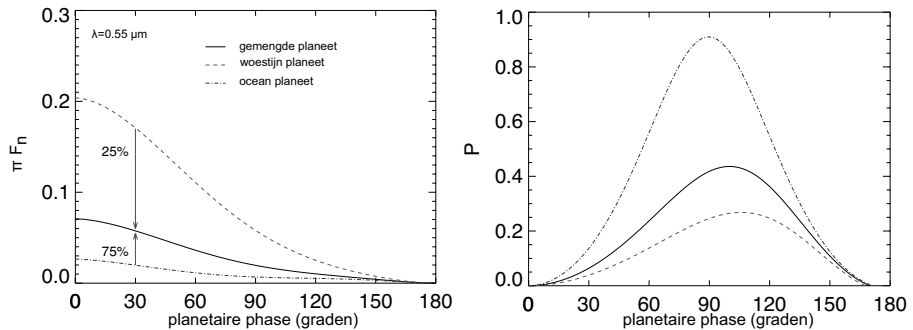


**Figuur 7.3:** Vrijwel alle planeten in ons zonnestelsel hebben inhomogene kenmerken. Jupiter (linker foto) en Neptunus (rechter foto) hebben bijvoorbeeld banden en wolken van ammonia en methaankristallen, Mars (middelste foto) heeft stofwolken, poolkappen, bergen en valleien. En we hebben natuurlijk oceanen en continenten op Aarde. Copyright (van links naar rechts): NASA, ESA, M.H. Wong (University of California, Berkeley), H.B. Hammel (Space Science Institute, Boulder, Colo.), A.A. Simon-Miller (Goddard Space Flight Center) en het Jupiter Impact Science Team; NASA, ESA, The Hubble Heritage Team (STScI/AURA), J. Bell (Cornell Univ.) en M. Wolff (Space Sci Inst.); NASA, ESA, L. Sromovsky en P. Fry (University of Wisconsin), H. Hammel (Space Science Institute), en K. Rages (SETI Institute).

### 7.3 Dit proefschrift

In dit proefschrift was het doel om de computercode van Stam (2008) aan te passen om de modellering van het polarimetrische signaal mogelijk te maken (voor meerdere golflengten) van inhomogene planeten, oftewel planeten waarbij het oppervlak of de atmosfeer uit verschillende aspecten bestaat, zoals continenten, oceanen en wolken (zie Hoofdstuk 3). Het ontbreken van inhomogeniteit was tot nu toe de grootste zwakte van de code, gezien het feit dat vrijwel alle planeten in ons zonnestelsel inhomogene kenmerken hebben (wolken van water, ijs, ammonia of stof, vlekken zoals de Grote Rode Vlek op Jupiter, of oceanen en continenten zoals op Aarde).

Voordat het werk voor dit proefschrift begon, bestond de techniek om het signaal van een inhomogene planeet te modelleren uit het naar ratio bij elkaar "optellen" van homogene planeten. Om bijvoorbeeld het signaal van een planeet te modelleren waarvan het oppervlak voor 75% bestaat uit oceanen en voor 25% uit een continent van zand, werd een oceaanneet (een planeet die helemaal bedekt is met water) en een woestijneet (een planeet die helemaal bedekt is met zand) gebruikt. Het signaal van de inhomogene planeet werd dan berekend door  $\frac{75}{100}$  van het signaal van de oceaanneet op te tellen bij  $\frac{25}{100}$  van de woestijneet (zie

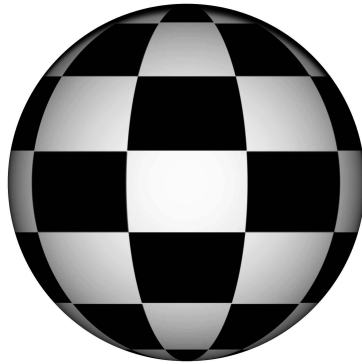


**Figuur 7.4:** Om het signaal van een inhomogene planeet te modelleren werd tot nu toe het signaal van homogene planeten gebruikt. Fracties van de homogene planeten werden bij elkaar opgeteld (links: flux, rechts: polarisatie), afhankelijk van de hoeveelheid oppervlak aanwezig op de inhomogene planeet.

Fig. 7.4).

Het gebruik van de nieuwe code heeft echter laten zien dat deze “optelmethode” alleen werkt bij planeten die bijna volledig homogeen zijn. Ook is de oude methode niet in staat om iets te zeggen over de lokatie van de inhomogeniteit. Het kan bijvoorbeeld geen onderscheid maken tussen kleine gebieden bij de evenaar of grote gebieden bij de polen. Dit komt omdat gebieden bij de evenaar groter lijken en dus een veel grotere bijdrage leveren aan het gereflecteerde signaal van een planeet dan gebieden bij de polen (denk bijvoorbeeld aan de afmetingen van de blokjes op een voetbal: die lijken naar de rand toe kleiner te worden, zie ook Fig. 7.5).

Een ander voorbeeld: veronderstel dat de planeet van Fig. 7.4 rond zijn ster draait met het continent van zand (25% van het zichtbare oppervlak) in het midden van de planeetschijf op het moment dat de planeet achter zijn ster staat (de volledige planeetschijf wordt dan verlicht, vergelijkbaar met volle maan). In deze situatie is de bijdrage van het continent groter dan de bijdrage van de oceaan en is het signaal *sterker* dan de voorspelling op basis van de optelmethode (want de optelmethode gaat uit van 75% oceaan over het gehele oppervlak en dus niet alleen langs de randen, om het continent heen). Als de planeet nu verder rond zijn ster draait kan het gebeuren dat het continent verborgen gaat aan de schaduwzijde van de planeet (denk aan het donkere, niet zichtbare deel van de maan tijdens een smalle maansikkel). Het verlichte, zichtbare deel van de planeet laat nu alleen oceaan zien, hetgeen een *zwakker* signaal oplevert dan we op basis van de optelme-



**Figuur 7.5:** Ook al zijn alle blokjes op deze bal precies hetzelfde, het lijkt alsof de blokjes in het midden groter zijn dan de blokjes aan de rand. Door ditzelfde “projectie-effect” wordt het signaal van een planeet vooral bepaald door de gebieden die dichtbij het centrum van het planeetschijf liggen (gezien vanaf de waarnemer).

thode zouden verwachten (want deze methode gaat nog steeds uit van een bijdrage van 25% zand, ook van de zichtbare smalle sikkels met alleen oceaan). Op deze manier geeft het optellen van homogene modellen altijd een onjuiste voorspelling en zal het dus lijden tot onjuiste conclusies bij het karakteriseren van inhomogene exoplaneten.

### 7.3.1 Op zoek naar de regenboog

Zoals we eerder hebben beschreven, verschuift de interesse van astronomen zich van de waarneming van nieuwe exoplaneten naar de karakterisatie van reeds waargenomen exoplaneten en het vinden van het “tweelingzusje” van onze Aarde: een planeet die precies op de juiste afstand om zijn ster draait zodat vloeibaar water en dus leven mogelijk is.

In ons zonnestelsel is het bestaan van leven zoals wij het kennen nauw verbonden met het bestaan van water in de atmosfeer en aan het oppervlak van de planeet. In onze zoektocht naar leven op andere planeten kan water dus een handig hulpmiddel zijn, vooral omdat het bestaan van water sporen achterlaat in het signaal van een planeet. Veel vloeibaar water aan het oppervlak, in de vorm van



**Figuur 7.6:** Links: schematische weergave van het pad dat het licht aflegt bij de vorming van een regenboog. Rechts: de regenboog die we zien als het regent terwijl de zon schijnt of als we bijvoorbeeld dicht bij een waterval staan bestaat uit de combinatie van kleine “regenbogen” die ontstaan door vele individuele, grote waterdruppels. Foto ter beschikking gesteld door Remco Scheepmaker.

een oceaan bijvoorbeeld, kan het sterlicht reflecteren als een spiegel. Terwijl de planeet rond zijn as draait zullen we bijvoorbeeld het ene moment de oceaan zien en het andere moment een continent. Dit zou de intensiteit van het ontvangen signaal zodanig kunnen veranderen dat we hiermee het bestaan van water aan het oppervlak kunnen aantonen (Williams & Gaidos 2008).

Een interessanter fenomeen dat we kunnen waarnemen bij een exoplaneet met water in de atmosfeer is de bekende regenboog. Een regenboog wordt veroorzaakt doordat zonlicht (of licht van een andere ster) door kleine waterdruppels schijnt. Als licht de druppel binnenkomt treedt er bij de overgang van lucht naar water breking van het licht op: het licht gaat onder een iets andere hoek verder, waarbij de hoek afhangt van de kleur van het licht. Hierdoor ontstaan de kleuren van de regenboog. Vervolgens reflecteert het licht aan de achterkant van de druppel en gaat het de druppel uit, waarbij er opnieuw breking optreedt (zie Fig. 7.6). Dit proces zorgt ervoor dat we de regenboog altijd zien onder een vaste hoek met de lichtbron, waarbij de exacte hoek afhangt van de brekingscoëfficiënt van het materiaal. Voor water is deze verstrooiingshoek ongeveer  $140^{\circ 2}$  (waarbij  $0^{\circ}$  recht vooruit betekent). Hierdoor zien we de regenboog altijd met de Zon in onze rug.

Onder de juiste omstandigheden is er soms een tweede (*secundaire*) regenboog binnen de eerste (*primaire*) regenboog te zien. De kleuren van deze tweede regenboog zijn omgekeerd (paars aan de buitenkant en rood aan de binnenkant), omdat

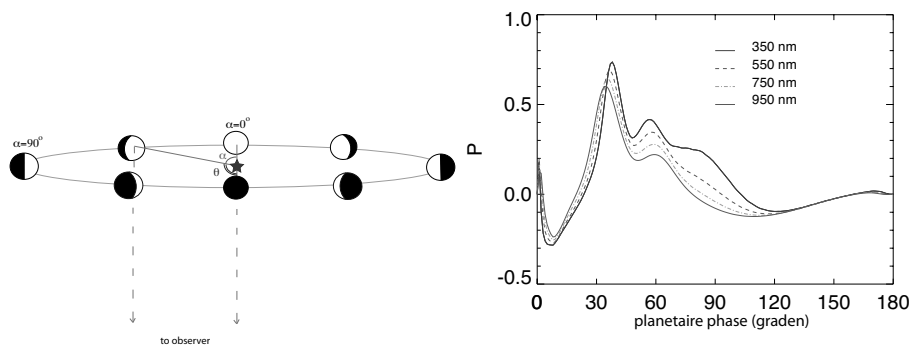
<sup>2</sup>De verstrooiingshoek ( $\theta$ ) is de supplementaire hoek van de planeetfase ( $\alpha$ ), oftewel:  $\alpha = 180^{\circ} - \theta$  (zie Fig. 7.7). De regenboog van een exoplaneet is daarom zichtbaar bij een planeetfase van  $40^{\circ}$ .

het licht nog een keer extra is gereflecteerd binnenin de waterdruppels. De reflecties kunnen zelfs nog vaker gebeuren en dan spreken van de *tertiaire* en zogenaamde *boventallige* regenbogen.

Vanwege de reflecties is het licht dat uit de waterdruppels komt gepolariseerd. Het licht van de primaire regenboog kan tot wel 96% gepolariseerd zijn en dat van de secundaire regenboog tot wel 90%. Deze grote graad van polarisatie maakt de regenboog tot een makkelijke doel bij het waarnemen van een exoplaneet.

Wat bedoelen we precies als we zeggen dat we de regenboog van een exoplaneet kunnen waarnemen? Terwijl een exoplaneet rond zijn ster draait, verandert de hoek van verstrooiing van het licht dat wij vanaf Aarde kunnen zien (zie Fig. 7.7). Als we een exoplaneet waarnemen die een planeetfase heeft van  $40^\circ$  (namelijk  $180^\circ-140^\circ$ ) en er zijn waterwolken in de atmosfeer van de planeet, zullen we dus een lokale verhoging zien in de graad van polarisatie van het gereflecteerde licht. Terwijl de planeet naar een grotere fasehoek draait neemt de graad van polarisatie weer af. Dit levert de piek op in de rechter figuur van Fig. 7.7. Als we de exoplaneet bij verschillende golflengten waarnemen, zullen we zien dat de positie van deze piek afhangt van de golflengte. We kijken dus naar de regenboog van de waterwolken op de exoplaneet. Het enige verschil met de regenboog die we allemaal kennen op Aarde, is de afmeting van de druppeltjes. De regenboog van een exoplaneet ontstaat door hele kleine druppeltjes in de wolken van de planeet, met een straal die vaak niet groter is dan  $10\mu\text{m}$  (oftewel 0.00001 meter). De regenboog op Aarde ontstaat daarentegen door veel grotere druppels.

In dit proefschrift laten we zien dat de regenboog in de meeste gevallen zichtbaar moet zijn in het signaal van de planeet. Als meer dan 10–20% (afhankelijk van de golflengte) van de planeetschijf bedekt is met wolken, kunnen wij het bestaan van deze wolken aantonen met het polarisatiesignaal van de regenboog. Als er ijswolken boven de waterwolken zweven blijft de regenboog bestaan totdat iets meer dan de helft van de waterwolken bedekt zijn met ijswolken. Dit betekent dat het zoeken naar de regenboog in het (polarisatie-)signaal van een exoplaneet één van de beste methoden is om water te vinden in de atmosfeer (en dus ook aan het oppervlak) van de planeet.



**Figuur 7.7:** Terwijl de (exo-)planeet rond zijn ster draait zien we telkens andere verstrooiingshoeken ( $\theta$ ). Als de atmosfeer van de planeet waterwolken heeft en op een positie staat met een fase van  $\alpha \sim 40^\circ$  (linker figuur), dan zien we een lokale verhoging in de graad van polarisatie van het licht dat de planeet reflecteert (rechter figuur). De precieze lokatie ( $\alpha$ ) van deze piek hangt af van de golflengte waarin wordt waargenomen. We zien dus eigenlijk de regenboog van de waterwolken op de exoplaneet.

## 7.4 Samenvatting van dit proefschrift

Dit proefschrift bevat de volgende hoofdstukken:

Hoofdstuk 1 is een introductie over exoplaneten. We geven een overzicht van de huidige stand van zaken in het vakgebied: de gebruikte waarneemmethoden, de technieken voor de karakterisatie en de daarmee verkregen eerste resultaten voor reeds waargenomen exoplaneten.

In Hoofdstuk 2 gebruiken we voor het eerst de computercode van Stam (2008) om het effect van bepaalde factoren op het regenboogsignaal van een (exo-)planeet te bestuderen. In het bijzonder kijken we naar het effect van verschillende micro- en macroscopische eigenschappen, zoals de afmetingen van de wolkendruppeltjes en de aanwezigheid van wolken die op een andere hoogte in de atmosfeer liggen.

De ervaringen met de computercode van Stam (2008) gebruiken we in Hoofdstuk 3 om de code zó aan te passen dat we ook inhomogene planeten kunnen modeleren. We testen of deze nieuwe code werkt, om er daarna de geldigheid van de “optelmethode” mee te testen. We vinden dat de optelmethode niet in staat is om het signaal van een exoplaneet juist te simuleren, tenzij de planeet bijna volledig homogeen is. Bij de karakterisatie van een exoplaneet zal het gebruik van de optelmethode in het algemeen dus tot onjuiste conclusies leiden.

In Hoofdstuk 4 gaan we met onze nieuwe code op zoek naar de regenboog in het gemodelleerde signaal van inhomogene exoplaneten. Eerst gebruiken we waterwolken die verschillende percentages van het oppervlak bedekken. We vinden dat bij een bedekking van minstens 10–20% (afhankelijk van de golflengte) het signaal van de planeet genoeg informatie bevat om het bestaan van de wolken aan te kunnen tonen. In die gevallen kunnen we dus de regenboog zien. Daarna gebruiken we meerdere lagen wolken, van vloeibaar water of van ijs, die in verschillende verhoudingen elkaar en het oppervlak bedekken. Onze resultaten laten zien dat zelfs als 52% van de waterwolken bedekt is met ijswolken de regenboog nog zichtbaar is in het polarisatiesignaal van de exoplaneet. Tot slot gebruiken we data van de MODIS satelliet om te onderzoeken of een buitenaards wezen dat naar onze Aarde kijkt het bestaan van wolken in de atmosfeer zou kunnen aantonen. Voor ons model van de Aarde gaan we uit van een bedekking van 66% met waterwolken en 36% met ijswolken, waarbij de ijswolken 45% van de waterwolken bedekken. Terwijl het flux (lichtsterkte) signaal geen tekenen laat zien van het bestaan van waterwolken, is de regenboog in het polarisatiesignaal duidelijk te zien. Hiermee zou een buitenaards wezen het bestaan van water in de aardse atmosfeer dus kunnen aantonen.

In Hoofdstuk 5 passen we onze code een klein beetje aan om ook gasachtige reuzenplaneten te kunnen modelleren. We onderzoeken de invloed van wolkenbanden, zones en vlekken, zoals ook te zien op Jupiter, de grootste gasachtige

planeet van ons eigen zonnestelsel. Onze resultaten laten zien dat deze structuren wel degelijk invloed hebben op het ontvangen signaal van een exoplaneet, al is niet altijd duidelijk onderscheid te maken tussen de verschillende structuren. Ook laten onze resultaten zien dat een buitenaards wezen op een verre planeet onder de juiste omstandigheden de Grote Rode Vlek op Jupiter zou kunnen aantonen.

Tot slot presenteren we in Hoofdstuk 6 LOUPE (Lunar Observatory for Unresolved Polarimetry of Earth). LOUPE is een idee voor een klein, licht instrument dat gebruikt kan worden om het signaal van de Aarde als een exoplaneet te bestuderen vanaf de Maan. Ons voorstel is om LOUPE mee te nemen naar de Maan met de toekomstige Lunar Lander missie van de Europese Ruimtevaartorganisatie ESA. Dankzij de unieke positie van de Maan ten opzichte van de Aarde kan LOUPE de veranderingen bestuderen in het zonlicht dat wordt gereflecteerd door de Aarde. De Aarde draait om haar as terwijl tegelijkertijd de Maan om de Aarde draait. Hierdoor komen verschillende structuren in beeld, terwijl ook de fase van de Aarde (zeg de schijngestalte) verandert. Als de missie meerdere maanden duurt, wordt het zelfs mogelijk om de invloed van seizoenen te zien op het signaal (in flux en polarisatie) van de Aarde als exoplaneet. Een instrument zoals LOUPE levert unieke gegevens op die gebruikt kunnen worden om onze modellen te controleren. Daarnaast kunnen deze gegevens gebruikt worden voor de toekomstige karakterisatie van aardachtige exoplaneten en de zoektocht naar water en leven op andere planeten.

# Περίληψη

---

## 8.1 Μια σύντομη ανασκόπηση.

Σε αυτήν τη διδακτορική διατριβή ασχολούμαστε με τη δημιουργία μοντέλων και τη μελέτη του αστρικού φωτός που ανακλάται απο εξωπλανήτες με διάφορα φυσικά χαρακτηριστικά. Με τον όρο εξωπλανήτη, όπως φανερώνει και το όνομά του, εννοούμε έναν πλανήτη ο οποίος περιστρέφεται γύρω απο ένα άστρο εκτός του Ηλίου μας.

Η ύπαρξη πλανητών πέραν του Ηλιακού μας συστήματος και η πιθανότητα ύπαρξης ζωής σε αυτούς, ήταν ένα αντικείμενο που απασχολούσε την ανθρωπότητα εξ' αρχαιοτάτων χρόνων. Ήδη τον τέταρτο προ Χρηστού αιώνα ο Δημόκριτος και ο Επίκουρος αναφερόντουσαν στην ύπαρξη πλανητών είτε όμοιων είτε ανόμοιων με τον δικό μας. Η αυθεντία του Αριστοτέλη ο οποίος πίστευε ότι δεν μπορεί να υπάρχει άνω του ενός κόσμου (του δικού μας) επισκίασε για αρκετούς αιώνες τις όποιες περαιτέρω φιλοσοφικές σκέψεις στο θέμα. Αρκετούς αιώνες αργότερα ο Christiaan Huygens (1629–1695 π.Χ.) είναι ο πρώτος που θα προχωρήσει σε μια καταγεγραμμένη φιλοσοφική συζήτηση περι της ύπαρξης άλλων πλανητών και της πιθανότητας ύπαρξης ζωής σε αυτούς. Θα πρέπει να περάσουν όμως εκατονταετίες μέχρι η ανθρωπότητα να έχει στη διάθεσή της τα κατάλληλα μέσα προκειμένου να ανακαλύψει τον πρώτο εξωπλανήτη.

Έτσι, μόλις το 1992 οι Wolszczan & Frail (1992) κατάφεραν να ανακαλύψουν τον πρώτο εξωπλανήτη, ο οποίος περιστρεφόταν γύρω απο έναν pulsar, βρισκόταν δηλαδή σε ένα περιβάλλον καθόλου φιλικό για την ύπαρξη ζωής (τουλάχιστον όπως εμείς την γνωρίζουμε). Όταν λίγο αργότερα οι Mayor & Queloz (1995) ανακάλυπταν τον πρώτο εξωπλανήτη που περιστρέφεται γύρω απο ένα άστρο όμοιο με τον Ήλιο μας, ξεκινούσε μια νέα εποχή για την αστρονομία. Έκτοτε πάνω από 770 εξωπλανήτες έχουν ανακαλυφθεί, οι περισσότεροι εκ των οποίων είναι γίγαντες πλανήτες, με μάζες πολλαπλάσιες αυτής του Δία, και περιστρέφονται σε πολύ κοντινές αποστάσεις γύρω απ' το μητρικό τους άστρο. Όπως αναφέρει και το κομμάτι της Εικόνας 8.1, ευτυχώς για τους αστρονόμους

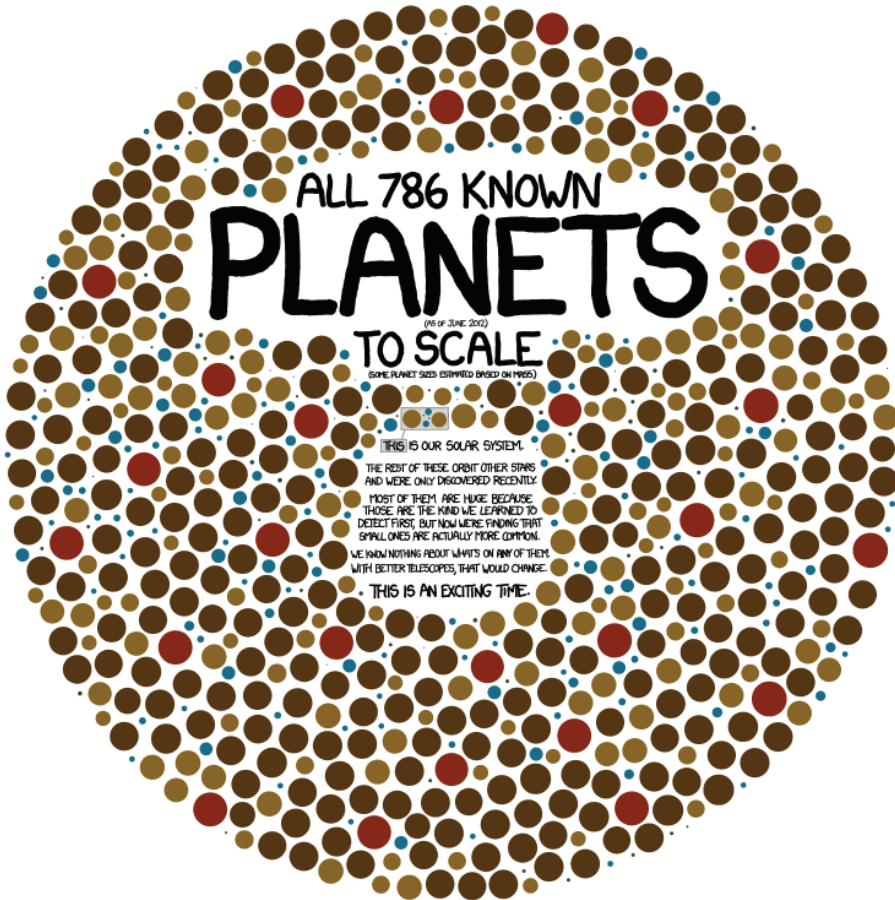


**Figure 8.1:** Ζούμε σε μια συναρπαστική εποχή κατά την οποία ανακαλύπτουμε τον ένα μετά τον άλλο πλανήτη εκτός του Ηλιακού μας Συστήματος. Μέχρι σήμερα, σε λιγότερα από 20 χρόνια έχουμε ανακαλύψει πάνω από 770 πλανήτες. Οι περισσότεροι απ' αυτούς είναι γιγάντιοι, αέριοι πλανήτες με μάζες πολλαπλάσιες αυτής του Δία. Ευτυχώς για όσους ενδιαφερόμαστε να βρούμε τη δίδιμη αδελφή της Γης μας αυτό οφείλεται καθαρά στις μεθόδους που χρησιμοποιήσαμε τα πρώτα χρόνια. Κόμικ απ' το: [xkcd.com](http://xkcd.com)

που ενδιαφέρονται να βρουν τη δίδιμη αδελφή της Γης μας, το φαινόμενο αυτό δεν έχει κάποια φυσική υπόσταση, αλλά είναι απλά μία αδυναμία των παρατηρησιακών μεθόδων και οργάνων που χρησιμοποιήθηκαν τα πρώτα χρόνια.

Πιο συγκεκριμένα, οι μέθοδοι που χρησιμοποιούμε σήμερα για να εντοπίσουμε τους εξωπλανήτες είναι όλες 'έμμεσες', με άλλα λόγια δεν βλέπουμε ποτέ τον ίδιο τον εξωπλανήτη, αλλά βλέπουμε την επίδραση που έχει η ύπαρξη του στο σήμα που λαμβάνουμε απ' το μητρικό του άστρο. Η επίδραση αυτή προέρχεται είτε από την βαρυτική αλληλεπίδραση μεταξύ του πλανήτη και του άστρου (μέθοδος ακτινικής ταχύτητας, μέθοδος βαρυτικής μικροεστίασης), είτε από την 'γεωμετρική' αλληλεπίδραση τους, δηλαδή η τροχιά του πλανήτη γύρω απ' το μητρικό του άστρο είναι τέτοια που μπορούμε να παρατηρήσουμε τη διάβαση του πλανήτη μπροστά (ή πίσω) απ' το δίσκο του μητρικού αστέρα. Έτσι, όσο πιο μεγάλη είναι η μάζα του πλανήτη και όσο πιο κοντά βρίσκεται στο μητρικό του άστρο, τόσο πιο μεγάλη θα είναι και η επίδραση του στο σήμα του μητρικού άστρου. Παραδείγματος χάριν, ένας βαρύτερος πλανήτης θα οδηγήσει σε μεγαλύτερη ταλάντωση του μητρικού άστρου, και λόγω του φαινομένου Doppler το σήμα του μητρικού άστρου θα αλλάζει εντονότερα, διευκολύνοντας την παρατήρηση της ύπαρξης του εξωπλανήτη. Μια δεύτερη Γη όμως, που περιστρέφεται γύρω απ' το μητρικό της άστρο στην ίδια απόσταση που περιστρέφεται η Γη μας γύρω απ' τον Ήλιο, θα είχε μια τόσο μικρή επίδραση στο σήμα του εξω-Ήλιου ( $\sim 1 \text{ cm/sec}$ ) που θα ήταν αδύνατο να την παρατηρήσουμε με τα σημερινά μέσα (με ακρίβειες της τάξης του  $\sim 1 \text{ m/sec}$ ).

Καθώς ο αριθμός των ανακαλυπτόμενων εξωπλανητών αυξάνεται, η προσοχή των αστροφυσικών αρχίζει και στρέφεται σταδιακά απ' την απλή παρατήρηση τους, στην προσπάθεια χαρακτηρισμού τους. Στόχος μας πλέον είναι να μάθουμε πώς είναι αυτοί οι πλανήτες. Έχουν ατμόσφαιρα; Έχουν τις προϋποθέσεις για να συντηρίσουν ζωή; Ειδικά όσον αφορά το τελευταίο ερώτημα, η εμπειρία μας από τους πλανήτες του Ηλιακού μας Συστήματος μας έχει δείξει ότι η ύπαρξη ζωής είναι άρρηκτα συνδεδεμένη με την ύπαρξη νερού στην ατμόσφαιρα και την επιφάνεια ενός πλανήτη. Πώς όμως θα μπορούσαμε να βρούμε νερό σε ένα πλανήτη που βρίσκεται αρκετά έτη φωτός μακριά μας;

## 8.2 Η σημαντική συνεισφορά της πόλωσης του φωτός στην μελέτη των εξωπλανητών.

Η λύση στο πρόβλημα μας έρχεται μέσω της μεθόδου της άμεσης παρατήρησης των εξωπλανητών και τη μελέτη της πόλωσης του φωτός που ανακλούν. Πιο συγκεκριμένα, το φως που ακτινοβολεί το μητρικό άστρο ενός πλανήτη (όταν το

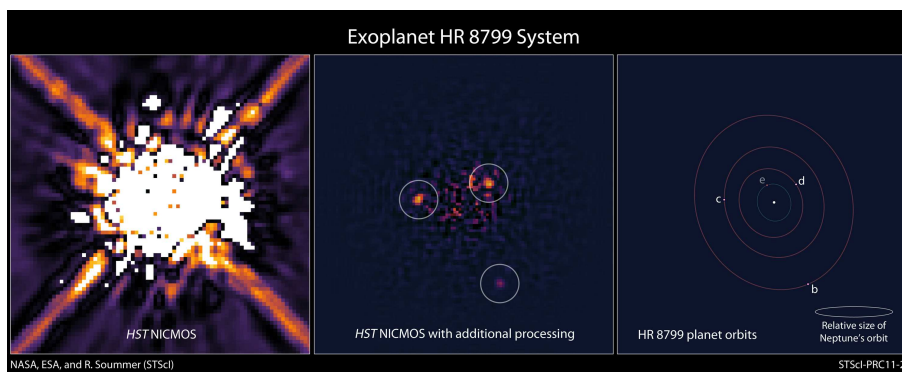


**Figure 8.2:** Όταν το 1998 το Hubble πήρε τη φωτογραφία που βλέπουμε στα αριστερά, οι αστρονόμοι δεν είδαν κάτι το ασυνήθιστο. Μια δεκαετία μετά, το 2009 και κατόπιν το 2011, μετά απο μία επίπονη ‘ανασκαφή’ στα αρχεία του Hubble, οι αστρονόμοι κατάφεραν να ανακαλύψουν τρεις εξωπλανήτες (μεσαία φωτογραφία). Ο τέταρτος εξωπλανήτης του συστήματος δεν φαίνεται στην εικόνα καθώς βρίσκεται στα όρια του κορονογράφου της NICMOS. Credit: NASA, ESA and R. Soummer (STScI).

άστρο δεν είναι πολύ ενεργό) δεν εμφανίζει καθόλου πόλωση<sup>1</sup> ενώ το φως που ανακλάται απο τον πλανήτη, λόγω μιας σειράς ανακλάσεων και σκεδάσεων που υπόκειται στην ατμόσφαιρα και την επιφάνεια του πλανήτη, είναι (μερικώς) πολωμένο. Αν λοιπόν παρατηρήσουμε το εξωπλανητικό σύστημα με τη βοήθεια πολωτικών οργάνων, αφενός μεν θα μπορέσουμε να διακρίνουμε πιο εύκολα τον (εξω-) πλανήτη μας και αφετέρου δε θα μπορέσουμε να αποκτήσουμε σημαντικές πληροφορίες για τον χαρακτηρισμό του πλανήτη.

Η σημασία της χρήσης του πολωμένου φωτός για τη μελέτη της ατμόσφαιρας των πλανητών του Ηλιακού μας Συστήματος είναι γνωστή πάνω απο ένα αιώνα. Ήδη το 1929 ο Lyot (Lyot 1929) χρησιμοποίησε την παρατήρηση του πολωμένου φωτός που ανακλάται απο τις ατμόσφαιρες του Δία και της Αφροδίτης προκειμένου να τις χαρακτηρίσει. Μερικές δεκαετίες αργότερα οι

<sup>1</sup>Το φυσικό φως, το φως για παράδειγμα που ακτινοβολεί ο Ήλιος μας, αποτελείται απο φωτόνια τα οποία ταλαντεύονται προς διάφορες κατευθύνσεις χωρίς καμμία συγκεκριμένη προτίμηση. Αν για κάποιο λόγο αυτά τα φωτόνια συγκρουστούν με κάποιο υλικό, όπως π.χ. τα μόρια ή τα σύννεφα της ατμόσφαιρας ενός πλανήτη, την επιφάνειά του κλπ, θα αποκτήσουν κάποια προτιμώμενη κατεύθυνση ταλάντωσης και τότε το φως είναι (μερικώς) πολωμένο. Σε κάποιες περιπτώσεις μάλιστα, όπως στα laser, μπορεί όλα τα φωτόνια να ταλαντεύονται κατα την ίδια διεύθυνση και τότε έχουμε πλήρως πολωμένο φως.

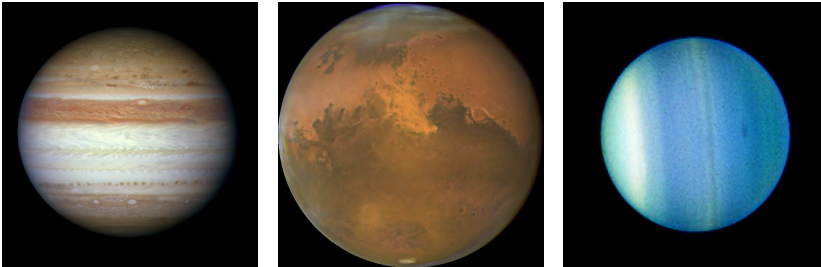


**Figure 8.3:** Σχεδόν όλοι οι πλανήτες του Ηλιακού μας Συστήματος επιδεικνύουν κάποια μορφή ανομοιομορφίας. Ζώνες και ταινίες στο Δία (αριστερή φωτογραφία), νέφη κρυστάλλων αμμωνίας και μεθανίου στο Δία και στον Ποσειδώνα (δεξιά φωτογραφία), νέφη σκόνης στον Άρη (μεσαία φωτογραφία), ωκεανοί και ήπειροι στη Γη. Credits (from left to right): NASA, ESA, M.H. Wong (University of California, Berkeley), H.B. Hammel (Space Science Institute, Boulder, Colo.), A.A. Simon-Miller (Goddard Space Flight Center), and the Jupiter Impact Science Team; NASA, ESA, The Hubble Heritage Team (STScI/AURA), J. Bell (Cornell Univ.) and M. Wolff (Space Sci Inst.); NASA, ESA, L. Sromovsky and P. Fry (University of Wisconsin), H. Hammel (Space Science Institute), and K. Rages (SETI Institute).

Hansen & Hovenier (1974) κατάφεραν να βρουν την χημική σύσταση και το μέγεθος των σταγονιδίων των σύννεφων που βρίσκονται στα ανώτερα στρώματα της ατμόσφαιρας της Αφροδίτης, όπως επίσης και το ύψος των σύννεφων στην ατμόσφαιρα.

Η ειδοποιός διαφορά μεταξύ των πλανητών του Ηλιακού μας Συστήματος και τον εξωπλανητών είναι ότι ενώ στην πρώτη περίπτωση μπορούμε να διαχωρίσουμε (ακόμη και με ένα μικρό τηλεσκόπιο) διάφορες περιοχές του πλανητικού δίσκου, στην δεύτερη περίπτωση όλος ο (εξω-)πλανητικός δίσκος δεν είναι παρά ένα σημείο, μια τελεία στην εικόνα μας (δες Εικόνα 8.2). Οπότε γεννάται αμέσως το ερώτημα, πως μπορούμε να χαρακτηρίσουμε ένα πλανήτη όταν όλος καταλαμβάνει μόλις ένα σημείο (pixel) στην εικόνα μας; Οι Stam et al. (2004) και Stam (2008) έδειξαν ότι ακόμη και σε αυτήν την περίπτωση, τουλάχιστον όσον αφορά τους ομογενείς πλανήτες, το πολωμένο κομμάτι του φωτός που ανακλάται απ' τον πλανήτη μπορεί να μας δώσει πληροφορίες για τη σύσταση του.

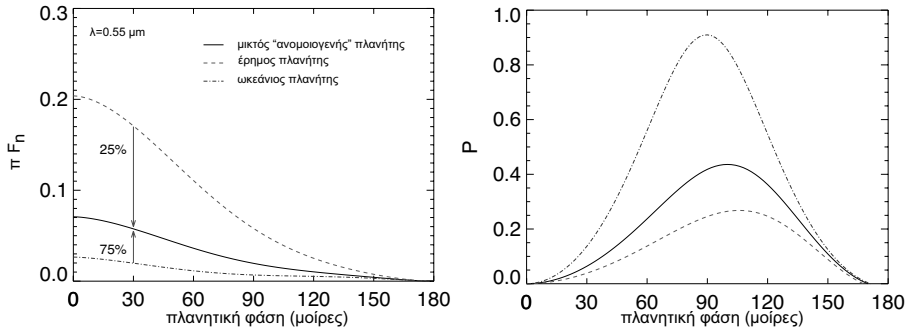


**Figure 8.4:** Μέχρι πρότινος προκειμένου να δημιουργήσουμε το σήμα ενός ανομοιογενή πλανήτη χρησιμοποιούσαμε ομοιογενείς πλανήτες το σήμα των οποίων προσθέταμε ανάλογα με το ποσοστό το οποίο κάθε στοιχείο καταλάμβανε στον ανομοιογενή πλανήτη.

### 8.3 Μοντέλα για την μελέτη των εξωπλανητών.

Σε αυτήν τη διδακτορική διατριβή βασικός μας στόχος ήταν η προσαρμογή του κώδικα της Stam (2008) ώστε να μπορεί να μοντελοποιήσει το φως που ανακλάται από έναν ανομοιογενή πλανήτη (δες Κεφάλαιο 3). Δεδομένου ότι όλοι οι πλανήτες του Ηλιακού μας Συστήματος παρουσιάζουν κάποια μορφή ανομοιογένειας (π.χ. σύννεφα νερού, πάγου, σκόνης ή παγοκρυστάλλων αμωννίας ή μεθανίου, κηλίδες όπως ο Δίας ή ο Ποσειδώνας, ζώνες ή ταινίες όπως ο Δίας, ωκεανοί και ήπειροι όπως η Γη κλπ, δες Εικόνα 8.3), η μέχρι πρότινος αδυναμία του κώδικα να διαχειριστεί σωστά αυτές τις περιπτώσεις ήταν ίσως το μόνο του (βασικό) ελάττωμα.

Μέχρι πρότινος, προκειμένου να δημιουργήσουμε το σήμα ενός ανομοιογενή πλανήτη χρησιμοποιούσαμε το σήμα ομοιογενών πλανητών τα οποία εν συνεχεία προσθέταμε προκειμένου να παράγουμε το σήμα του ανομοιογενή πλανήτη. Έτσι για παράδειγμα για να δημιουργήσουμε το σήμα ενός πλανήτη του οποίου η επιφάνεια καλύπτεται από ωκεανό και έχει μια ήπειρο-έρημο που καλύπτει το 25% της επιφάνειας του, χρησιμοποιούμε το σήμα ενός ωκεάνιου-πλανήτη (ενός πλανήτη που καλύπτεται μόνο από νερό) και ενός πλανήτη-έρημο (ενός πλανήτη που καλύπτεται μόνο από σκόνη) και προσθέτουμε  $\frac{75}{100}$  (σήμα πλανήτη-ωκεανού) +  $\frac{25}{100}$  (σήμα πλανήτη-έρημου) για να δημιουργήσουμε 'θεωρητικά' το σήμα του ανομοιογενή εξωπλανήτη μας (δες Εικόνα 8.4).

Στην πραγματικότητα όπως μας έδειξε η χρήση του νέου μας κώδικα βέβαια, κάτι τέτοιο ισχύει μόνο στην περίπτωση που οι ανομοιογένειες στον πλανήτη είναι τόσο μεγάλης κλίμακας, που θα μπορούσαμε να τον θεωρήσουμε και ομοιογενή. Σε κάθε άλλη περίπτωση, η αδυναμία αυτής της μεθόδου να ξέρει που βρίσκεται η κάθε 'ανομοιογένεια' στον πλανήτη οδηγεί σε σφάλματα στην εκτίμηση μας. Αυτό συμβαίνει επειδή για παράδειγμα περιοχές που βρίσκονται κοντά στο κέντρο του πλανητικού δίσκου θα συνεισφέρουν παραπάνω στο πλανητικό σήμα από περιοχές που βρίσκονται κοντά στους πόλους (αρκεί να σκεφτούμε πως αλλάζει το μέγεθος των εξαγώνων μιας μπάλας ποδοσφαίρου που βλέπουμε από απόσταση καθώς παρατηρούμε κατά μήκος της, δεξ και Εικόνα 8.5).

Ας υποθέσουμε για απλοποίηση ότι ο (ανομοιογενής) εξωπλανήτης της Εικόνας 8.4 βρίσκεται σε σύγχρονη τροχιά γύρω απ' το μητρικό του άστρο και ότι η ηπειρος βρίσκεται στο κέντρο του πλανητικού δίσκου όταν ο πλανήτης είναι πίσω απ' το μητρικό του άστρο (πλανητική φάση  $0^\circ$ ). Αρχικά η συνεισφορά της ηπείρου στο πλανητικό σήμα θα είναι αρκετά πιο σημαντική απ' του ωκεανού και το σήμα του πλανήτη μας θα είναι ισχυρότερο απ' το σήμα του πλανήτη-μείγμα της Εικόνας 8.4. Καθώς ο πλανήτης περιστρέφεται γύρω απ' το μητρικό του άστρο, όλο και μεγαλύτερο μέρος της ηπείρου θα περνάει στη μη ορατή πλευρά και το κέντρο του (ορατού και φωτισμένου) πλανητικού δίσκου θα κινείται προς τις ωκεάνιες περιοχές του πλανήτη οπότε και σταδιακά το σήμα του πλανήτη θα είναι πιο αδύναμο απ' το σήμα του πλανήτη-μείγμα της Εικόνας 8.4.

Η 'μείξη' λοιπόν των ομοιογενών μοντέλων θα μας δίνει συνεχώς λανθασμένο (είτε πολύ πιο αδύναμο είτε πολύ πιο ισχυρό) σήμα και αν το χρησιμοποιήσουμε σαν 'οδηγό' για τον ακριβή χαρακτηρισμό του εξωπλανήτη που παρατηρούμε θα οδηγηθούμε (αναπόφευκτα) σε λάθος συμπεράσματα. Τα αποτελέσματα μας βέβαια, μας δείχνουν ότι η μείξη ομοιογενών μοντέλων μπορεί μας δώσει μια πρώτη 'αίσθηση' για τη φύση των ανομοιογενειών που συναντάμε στον παρατηρούμενο εξωπλανήτη. Έτσι, μιας και ο νέος κώδικας μας είναι αρκετά αργός, ιδανικά, μπορούμε να χρησιμοποιούμε αρχικά τον ομοιογενή κώδικα προκειμένου να πάρουμε μια πρώτη ιδέα για τη φύση των ανομοιογενειών που συναντάμε στον πλανήτη και κατόπιν τον ανομοιογενή κώδικα προκειμένου να χαρακτηρίσουμε πλήρως τον εξωπλανήτη μας.

### 8.3.1 Ψάχνοντας το ουράνιο τόξο

Όπως προαναφέραμε, στη σημερινή εποχή το ενδιαφέρον των αστρονόμων αρχίζει σταδιακά και στρέφεται απ' την απλή ανακάλυψη των εξωπλανητών

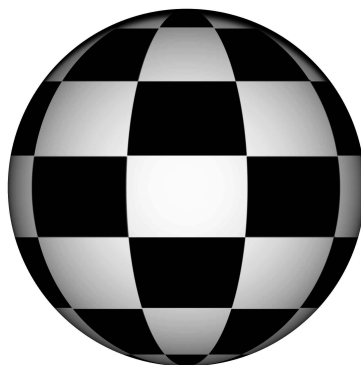


**Figure 8.5:** Αν και η μπάλα είναι φτιαγμένη από παραλληλόγραμμα ίδιων διαστάσεων, παρατηρούμε ότι τα παραλληλόγραμμα στο κέντρο της μπάλας φαίνονται μεγαλύτερα από αυτά στις άκρες. Λόγω αυτού του φαινομένου, το σήμα ενός πλανήτη καθορίζεται (συνήθως) κυρίως από τις ιδιότητες των περιοχών του πλανήτη που βρίσκονται πιο κοντά στο κέντρο του πλανητικού δίσκου όπως τον αντιλαμβάνεται ο παρατηρητής.

στην προσπάθεια χαρακτηρισμού τους και στην προσπάθεια εύρεσης της δίδυμης αδελφής της Γης μας. Ενός πλανήτη ο οποίος θα βρίσκεται στην κατάλληλη απόσταση απ' το μητρικό του άστρο και θα μπορεί να συντηρήσει ζωή.

Η ύπαρξη ζωής όπως την γνωρίζουμε στο Ηλιακό μας Σύστημα είναι συνυφασμένη με την ύπαρξη νερού στην ατμόσφαιρα και την επιφάνεια του πλανήτη. Στην προσπάθειά μας προς αναζήτηση ζωής το νερό μπορεί να αποδειχθεί ένας εξαιρετικός σύμμαχος, καθώς η ύπαρξη του στην επιφάνεια και την ατμόσφαιρα ενός πλανήτη μπορεί να αφίσει έντονα τα ίχνη της στο πλανητικό σήμα. Οι μεγάλες ποσότητες νερού στην επιφάνεια ενός πλανήτη (π.χ. υπό την μορφή ωκεανού) μπορούν να ανακλάσουν το φως του μητρικού του άστρου σαν καθρέπτης. Έτσι, καθώς ο πλανήτης περιστρέφεται γύρω απ' τον άξονά του και άλλοτε θα βλέπουμε π.χ. ωκεάνια επιφάνεια και άλλοτε ηπείρους, η ένταση του φωτός που ανακλάται από τον πλανήτη θα αλλάζει συνεχώς επιτρέποντάς μας ίσως να 'δούμε' την ύπαρξη του νερού στην επιφάνεια του πλανήτη (Williams & Gaidos 2008).

Ένα πιο ενδιαφέρον φαινόμενο το οποίο μπορούμε να παρατηρήσουμε στους



**Figure 8.6:** Αριστερα: Καλλιτεχνική απεικόνιση του δρόμου τον οποίο ακολουθεί μια ακτίνα λευκού φωτός μέχρι να γίνει μέρος του ουράνιου τόξου. Δεξιά: Το ουράνιο τόξο που βλέπουμε κατα τη διάρκεια μιας βροχής ή όταν π.χ. είμαστε κοντά σε ένα καταράκτη δημιουργείται απο το συνδιασμό μικρών 'ουράνιων τόξων' απο πολλές σταγόνες. Φωτογραφία του Remco Scheepmaker.

εξωπλανήτες όταν έχουν νερό στην ατμόσφαιρά τους, είναι το γνωστό μας ουράνιο τόξο. Το ουράνιο τόξο δημιουργείται όταν το φως απο τον Ήλιο (ή ένα άλλο άστρο) εισέρχεται στις σταγόνες νερού στα σύννεφα της ατμόσφαιρας. Καθώς διέρχεται απο το ένα υλικό (αέρα) στο άλλο (νερό), το λευκό φως υπόκειται διάθλαση και 'σπάει' στα γνωστά μας χρώματα του ουράνιου τόξου (ανεστραμμένα). Στη συνέχεια το φως ανακλάται στο πίσω μέρος της σταγόνας, τα χρώματα αποκτούν τη 'σωστή' τους σειρά και καθώς επιστρέφει προς την πλευρά εισόδου του θα υποστεί ξανά διάθλαση και θα δημιουργήσει το γνωστό μας ουράνιο τόξο στον ουρανό (Εικόνα 8.6). Λόγω της διαδικασίας που απαιτείται για τη δημιουργία του ουράνιου τόξου μπορούμε να το παρατηρήσουμε πάντα σε συγκεκριμένη γωνία από τον ήλιο η οποία εξαρτάται απ' το δείκτη διάθλασης του υλικού το οποίο διαθλά το φως. Για το νερό η γωνία αυτή είναι στις περίπου  $140^{\circ}$ <sup>2</sup> γι' αυτό βλέπουμε πάντα το ουράνιο τόξο όταν έχουμε τον ήλιο στην πλάτη μας.

Μερικές φορές μπορεί να παρατηρήσουμε, αν οι συνθήκες είναι κατάλληλες, και ένα δεύτερο ουράνιο τόξο, μέσα απο το το γνωστό μας, του οποίου τα χρώματα είναι ανεστραμμένα (πρώτα βλέπουμε το ιώδες και στο τέλος το

<sup>2</sup>Η γωνία σκέδασης του φωτός ( $\theta$ ) μπορεί να δειχθεί ότι είναι παραπληρωματική της πλανητικής φάσης ( $\alpha$ ), δηλαδή  $\alpha = 180^{\circ} - \theta$  (δες Εικόνα 8.7). Για το λόγο αυτό το ουράνιο τόξο απο έναν εξωπλανήτη όπως θα δουμε σε λίγο, μπορούμε να το δούμε για πλανητικές φάσεις κοντά στις  $40^{\circ}$ .

κόκκινο). Το ουράνιο αυτό τόξο δημιουργείται απο φως το οποίο έχει ανακλαστεί και δεύτερη φορά μέσα στις σταγόνες νερού πριν να βγει εκτός τους (εξού και τα ανεστραμμένα χρώματα σε σχέση με το γνωστό μας τόξο). Το ουράνιο αυτό τόξο ονομάζεται *δευτερεύον* για να διαχωριστεί απο το *πρωτεύον* και πλέον γνωστό σε όλους μας ουράνιο τόξο. Η διαδικασία των ανακλάσεων μέσα στη σταγόνα μπορεί να επαναληφθεί περισσότερες των δύο φορές, δημιουργώντας το *τριτεύον* και τα λεγόμενα *υπεράριθμα τόξα*.

Λόγω των ανακλάσεων το φως όταν εξέρχεται από τις σταγόνες θα είναι πολωμένο. Συγκεκριμένα μπορεί να δειχθεί ότι το φως του πρωτεύοντος ουράνιου τόξου μπορεί να είναι μέχρι και 96% πολωμένο<sup>3</sup> ενώ το δευτερεύον μπορεί να είναι μέχρι και 90% πολωμένο. Ο υψηλός βαθμός πόλωσης του ουράνιου τόξου το καθιστά ορατό ακόμη και στην περίπτωση που παρατηρούμε έναν εξωπλανήτη.

Αλλά, τί εννοούμε όταν λέμε 'βλέπουμε' το ουράνιο τόξο ενός εξωπλανήτη; Καθώς ένας εξωπλανήτης περιστρέφεται γύρω απ' το μητρικό του άστρο, η γωνία σκέδασης του φωτός που παρατηρούμε αλλάζει (δες Εικόνα 8.7). Έτσι, παρατηρώντας έναν εξωπλανήτη γύρω στις 40° (=180°-140°) πλανητική φάση, εάν ο πλανήτης έχει σύννεφα νερού στην ατμόσφαιρά του, θα μπορέσουμε να δούμε το βαθμό πόλωσης του φωτός να αυξάνει τοπικά, και καθώς ο πλανήτης κινείται προς μεγαλύτερες πλανητικές φάσεις να ξαναμειώνεται. Αν η παρατήρηση μας γίνεται σε διάφορα μήκη κύματος, θα δούμε ότι η πλανητική φάση στην οποία εμφανίζεται αυτό το 'γόνατο' αλλάζει με το μήκος κύματος (δες Εικόνα 8.7). Ουσιαστικά λοιπόν, βλέπουμε το ουράνιο τόξο που δημιουργείται απο τα σύννεφα του εξωπλανήτη. Η μόνη διαφορά με το γνωστό μας ουράνιο τόξο είναι οτι ενώ αυτό σχηματίζεται απο την αλληλεπίδραση του φωτός με μεγάλες σταγόνες νερού, το ουράνιο τόξο των εξωπλανητών δημιουργείται απο την αλληλεπίδραση του φωτός με μικρά σταγονίδια νερού των οποίων η ακτίνα πολλές φορές δεν ξεπερνάει τα 10μm (0.00001 μέτρα).

Όπως δείχνουμε στην διδακτορική αυτή διατριβή, το ουράνιο τόξο 'επιβιώνει' στο σήμα ενός πλανήτη στις περισσότερες περιπτώσεις. Έτσι όταν πάνω απο το 10% με 20% (ανάλογα με το μήκος κύματος στο οποίο παρατηρούμε τον εξωπλανήτη) της επιφάνειας ενός πλανήτη καλύπτεται απο σύννεφα, αυτά είναι ικανά να επηρεάσουν το σήμα του και να δούμε το (πρωτεύον) ουράνιο τόξο. Ακόμη και σε δύσκολες περιπτώσεις, όπως όταν σύννεφα παγοκρυστάλλων βρίσκονται πάνω απο τα σύννεφα του πλανήτη, το σήμα του ουράνιου τόξου

---

<sup>3</sup>Το πόσο πολωμένο είναι το φως το μετράμε με το βαθμό πόλωσης, ο οποίος κυμαίνεται απο 0% έως 100%. Όταν έχουμε φυσικό φως τα φωτόνια ταλαντεύονται προς όλες τις διευθύνσεις χωρίς καμμία προτίμηση και το φως μας είναι 0% πολωμένο, ενώ όταν όλα τα φωτόνια ταλαντεύονται σε μία διεύθυνση όπως σε ένα laser το φως είναι 100% πολωμένο.

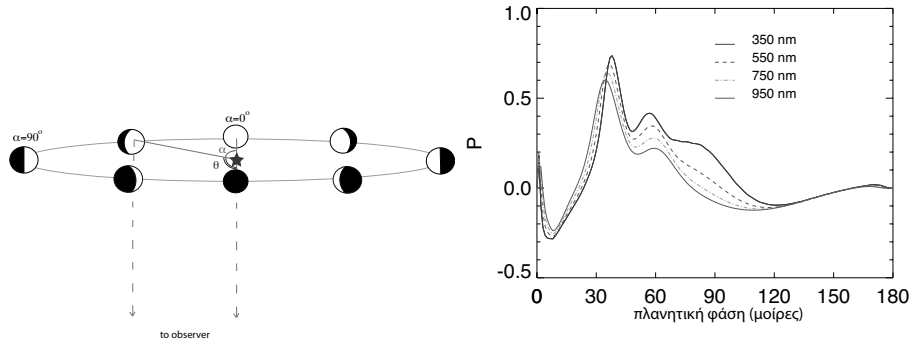


**Figure 8.7:** Καθώς ο πλανήτης περιστρέφεται γύρω απ' το μητρικό του άστρο προς μεγαλύτερες πλανητικές φάσεις ( $\alpha$ ), βλέπουμε διαφορετικές γωνίες σκέδασης ( $\theta$ ) του φωτός απο τον πλανήτη. Έτσι, εάν η ατμόσφαιρά του έχει σύννεφα νερού όταν  $\alpha \sim 40^\circ$  θα δούμε μια αύξηση στο βαθμό πόλωσης του φωτός. Η ακριβής γωνία που παρατηρείται αυτή η αύξηση αλλάζει με το μήκος κύματος που παρατηρούμε. Ουσιαστικά βλέπουμε το ουράνιο τόξο των σύννεφων του εξωπλανήτη.

μπορεί να φανεί ακόμη και αν πάνω απο τα μισά σύννεφα καλύπτονται απο σύννεφα πάγου. Το γεγονός αυτό καθιστά την αναζήτηση του ουράνιου τόξου ίσως έναν απ' τους πρωτεύοντες στόχους μας εάν ενδιαφερόμαστε να βρούμε νερό στην ατμόσφαιρα (και άρα και την επιφάνεια) ενός εξωπλανήτη.

**Αυτή η διδακτορική διατριβή αποτελείται απο τα εξής μέρη:**

Στο Κεφάλαιο 1 παρουσιάζουμε μια μικρή εισαγωγή στον τομέα της παρατήρησης και μοντελοποίησης των εξωπλανητών. Συγκεκριμένα παρουσιάζουμε τις μεθόδους που χρησιμοποιούνται σήμερα για την ανακάλυψη εξωπλανητών, τις αδυναμίες και τα προτερήματα της κάθε μεθόδου και τον αριθμό των εξωπλανητών που έχουμε ανακαλύψει μέχρι σήμερα με αυτήν. Κατόπιν δίνουμε μια περιγραφή των μεθόδων που χρησιμοποιούνται σήμερα για τον χαρακτηρισμό των εξωπλανητών. Τέλος περιγράφουμε την σημασία του πολωμένου φωτός για την ανακάλυψη εξωπλανητών και για τον χαρακτηρισμό τους.

Στο Κεφάλαιο 2 παρουσιάζουμε για πρώτη φορά τον προϋπάρχοντα κώδικα της Stam (2008) και τον χρησιμοποιούμε προκειμένου να μελετήσουμε την επίδραση διαφόρων παραμέτρων στο ουράνιο τόξο ενός πλανήτη. Έτσι, μελετάμε διάφορα σύννεφα νερού, με διαφορετικές τόσο μικροσκοπικές όσο και μακροσκοπικές ιδιότητες και το πως αυτές επιδρούν στο πλανητικό σήμα.

Στο Κεφάλαιο 3 έχοντας πλέον αποκτήσει οικειότητα με τον προϋπάρχοντα κώδικα τον διαφοροποιούμε ώστε να μπορεί να μοντελοποιήσει ανομοιογενείς πλανήτες. Αφού ελέγξουμε πρώτα ότι ο κώδικάς μας όντως λειτουργεί όπως πρέπει, προχωράμε στο να ελέγξουμε το κατά πόσον η μέθοδος που χρησιμοποιούταν μέχρι πρότινος για την δημιουργία του σήματος ενός ανομοιογενή πλανήτη (μέθοδος στατιστικής μύξης σημάτων ομοιογενών πλανητών) μας δίνει σωστά αποτελέσματα. Όπως αποδεικνύεται η μέθοδος της μύξης ομοιογενών μοντέλων λειτουργεί μόνο όταν ο εξωπλανήτης μας είναι σχεδόν ομοιογενής. Σε κάθε άλλη περίπτωση η χρήση της παλαιάς μεθόδου μπορεί να μας οδηγήσει σε λανθασμένα συμπεράσματα για την (ποσοτική) σύσταση του εξωπλανήτη, αν και σε αρκετές περιπτώσεις μπορεί να μας δώσει μια ποιοτική αίσθηση για τη φύση των ανομοιογενειών που συναντάμε στον πλανήτη.

Στο Κεφάλαιο 4 χρησιμοποιούμε τον νέο μας κώδικα για να ψάξουμε το ουράνιο τόξο σε διάφορα μοντέλα ανομοιογενών πλανητών. Αρχικά χρησιμοποιούμε μόνο σύννεφα νερού τα οποία καλύπτουν ολόένα και αυξανόμενο ποσοστό του πλανήτη μας. Τα αποτελέσματά μας, μας δείχνουν ότι όταν ένας πλανήτης καλύπτεται τουλάχιστον κατά 10% με 20% (ανάλογα με το μήκος κύματος στο οποίο παρατηρούμε) απο σύννεφα νερού, η ύπαρξη τους πρέπει να είναι εμφανής μέσω του ουράνιου τόξου που δημιουργούν. Κατόπιν τοποθετούμε ένα δεύτερο στρώμα συννέφων πάνω απ' τα σύννεφα νερού, είτε της ίδιας φύσης είτε σύννεφα πάγου, και αλλάζουμε τις ιδιότητες των δυο στρωμάτων συννέφων καθώς και το ποσοστό αλληλοκάλυψής τους (δηλαδή το ποιο ποσοστό συννέφων πάγου βρίσκεται πάνω απο ένα σύννεφο νερού). Βλέπουμε ότι ακόμη και όταν σχεδόν τα μισά απο τα σύννεφά μας καλύπτονται

απο ένα σύννεφο πάγου η ύπαρξη των σύννεφων νερού είναι ακόμη ορατή στο πολωμένο φως του εξωπλανήτη μας (μέσω του ουράνιου τόξου πάντα). Τέλος χρησιμοποιώντας δεδομένα απ' τον δορυφόρο MODIS μελετάμε το σήμα της Γης σαν να ήταν εξωπλανήτη. Απο τις προσομοιώσεις μας φαίνεται ότι το ουράνιο τόξο επιβιώνει στο (πολωμένο) σήμα του εξωπλανήτη Γη, τουτέστιν ένας εξωγήινος που θα παρατηρούσε με τα κατάλληλα μέσα τη Γη μας, θα μπορούσε να δει την ύπαρξη σύννεφων στην ατμόσφαιρά της.

Στο Κεφάλαιο 5 χρησιμοποιούμε τον κώδικά μας, λίγο παραλλαγμένο, προκειμένου να μελετήσουμε την επίδραση ανομοιογενειών στο σήμα γιγάντιων, αέριων πλανητών. Έτσι, μια σειρά απο φαινόμενα όπως η ύπαρξη ζωνών ή ταινιών, η ύπαρξη κηλίδων και διαφόρων ειδών ομίχλης (haze) μελετώνται με στόχο να δούμε το κατα πόσον αφήνουν παρατηρήσιμα σημάδια στο σήμα ενός εξωπλανήτη. Τα αποτελέσματά μας δείχνουν ότι πολλά απο αυτά τα χαρακτηριστικά αφήνουν σημάδια στο ανακλώμενο φως, αν και σε κάποιες περιπτώσεις ίσως υπάρχει ένας εκφυλισμός, δηλαδή πάνω απο μια ανομοιογένεια θα μπορούσε να είναι υπαίτια για την ίδια αλλαγή στο σήμα που παρατηρούμε. Τα αποτελέσματά μας δείχνουν τέλος ότι υπο κατάλληλες συνθήκες ένας εξωγήινος παρατηρητής ίσως μπορούσε να διακρίνει την ύπαρξη της Μεγάλης Ερυθράς Κηλίδας στο Δία.

Τέλος στο Κεφάλαιο 6 παρουσιάζουμε το LOUPE (Lunar Observatory for Unresolved Polarimetry of Earth). Το LOUPE είναι ένα μικρό και ελαφρύ όργανο ικανό να μελετήσει απο τη Σελήνη τη Γη σαν να ήταν εξωπλανήτη. Λόγω της μοναδικής θέσης που έχει η Σελήνη σε σχέση με τη Γη μας, το LOUPE ενσωματωμένο σε μια αποστολή στη Σελήνη, θα μπορούσε να μελετήσει τις αλλαγές στο ανακλώμενο φως απο τη Γη καθώς αυτή περιστρέφεται γύρω απο τον άξονά της (ημέρα), κατα τη διάρκεια ενός μήνα (καθώς η Γη μας αλλάζει φάσεις απο μια Νέα Γη σε μια ολόφωτη Γη (σαν την Πανσέληνο) ) και, εφόσον η αποστολή θα μπορούσε να διαρκέσει μεγαλύτερο χρονικό διάστημα, κατα την αλλαγή των εποχών ενός έτους. Τα δεδομένα που θα αποκτούσαμε απο μια τέτοια αποστολή θα αποτελούσαν μια βάση ελέγχου των μοντέλων μας (η οποία μέχρι στιγμής δεν υπάρχει, ιδίως όταν ενδιαφερόμαστε για κατοικήσιμους πλανήτες) και αναφοράς/ σύγκρισης όταν στο εγγύς μέλλον παρατηρήσουμε τον πρώτο εξωπλανήτη που βρίσκεται στην κατάλληλη θέση σε σχέση με το μητρικό του άστρο για να μπορεί να έχει νερό και ζωή.



# Bibliography

---

- Adam, J. A. 2002, *Physics Reports*, 356, 229 (cited on pages 16, 17, and 41)
- Atreya, S. K., Wong, A. S., Baines, K. H., Wong, M. H., & Owen, T. C. 2005, *Planetary and Space Science*, 53, 498 (cited on page 119)
- Baglin, A., Auvergne, M., Barge, P., et al. 2006, in *ESA Special Publication*, Vol. 1306, *ESA Special Publication*, ed. M. Fridlund, A. Baglin, J. Lochard, & L. Conroy, 33 (cited on pages 4, 84, and 113)
- Bailey, J. 2007, *Astrobiology*, 7, 320 (cited on pages 16, 43, 86, 108, 139, and 142)
- Baines, K. H., Carlson, R. W., & Kamp, L. W. 2002, *Icarus*, 159, 74 (cited on page 119)
- Bates, D. R. 1984, *Planetary and Space Science*, 32, 785 (cited on page 36)
- Beaulieu, J.-P., Bennett, D. P., Fouqué, P., et al. 2006, *Nature*, 439, 437 (cited on page 56)
- Beaulieu, J. P., Kipping, D. M., Batista, V., et al. 2010, *Monthly Notices of the Royal Astronomical Society*, 409, 963 (cited on pages 56 and 138)
- Berdugina, S. V., Berdyugin, A. V., Fluri, D. M., & Piirola, V. 2008, *Astrophysical Journal Letters*, 673, L83 (cited on page 85)
- Berdugina, S. V., Berdyugin, A. V., Fluri, D. M., & Piirola, V. 2011, *Astrophysical Journal Letters*, 728, L6 (cited on page 85)
- Beuzit, J.-L., Feldt, M., Dohlen, K., et al. 2006, *The Messenger*, 125, 29 (cited on page 20)
- Bierwirth, E., Wendisch, M., Ehrlich, A., et al. 2009, *Tellus Series B Chemical and Physical Meteorology B*, 61, 252 (cited on page 140)
- Borucki, W. J., Koch, D. G., Basri, G., et al. 2011, *Astrophysical Journal*, 728, 117 (cited on page 6)
- Broggi, M., Snellen, I. A. G., de Kok, R. J., et al. 2012, *Nature*, 486, 502 (cited on page 85)
- Brown, R. A. 2005, *Astrophysical Journal*, 624, 1010 (cited on page 107)
- Callies, J., Corpaccioli, E., Eisinger, M., Hahne, A., & Lefebvre, A. 2000, *ESA Bull.*, 102, 28 (cited on page 141)

- Carpenter, J. D., Fisackerly, R., De Rosa, D., & Houdou, B. 2012, *Planetary and Space Science* (cited on page 139)
- Cash, W. & New Worlds Study Team. 2010, in *Astronomical Society of the Pacific Conference Series*, Vol. 430, *Astronomical Society of the Pacific Conference Series*, ed. V. Coudé Du Foresto, D. M. Gelino, & I. Ribas, 353–+ (cited on pages 20, 29, and 56)
- Cassan, A., Kubas, D., Beaulieu, J.-P., et al. 2012, *Nature*, 481, 167 (cited on pages 6 and 137)
- Cess, R. D., Kwon, T. Y., Harrison, E. F., et al. 1992, *Journal of Geophysical Research*, 97, 7613 (cited on page 26)
- Chapman, E. G., Gustafson, Jr., W. I., Easter, R. C., et al. 2009, *Atmospheric Chemistry & Physics*, 9, 945 (cited on pages 27 and 50)
- Charbonneau, D., Berta, Z. K., Irwin, J., et al. 2009, *Nature*, 462, 891 (cited on page 55)
- Collett, E. 1992, *Polarized light. Fundamentals and applications* (Optical Engineering, New York: Dekker, —c1992) (cited on page 13)
- Cowan, N. B., Agol, E., Meadows, V. S., et al. 2009, *Astrophysical Journal*, 700, 915 (cited on page 84)
- Daimon, M. & Masumura, A. 2007, *Applied Optics*, 46, 3811 (cited on page 35)
- Dave, J. V. 1969, *Applied Optics*, 8, 155 (cited on page 38)
- de Haan, J. F., Bosma, P. B., & Hovenier, J. W. 1987, *Astronomy & Astrophysics*, 183, 371 (cited on pages 32, 58, 60, 61, 63, 88, and 117)
- de Mooij, E. J. W., Brogi, M., de Kok, R. J., et al. 2012, *Astronomy & Astrophysics*, 538, A46 (cited on page 85)
- de Pater, I. & Lissauer, J. J. 2001, *Planetary Sciences*, ed. de Pater, I. & Lissauer, J. J. (cited on page 119)
- de Rooij, W. A. & van der Stap, C. C. A. H. 1984, *Astronomy & Astrophysics*, 131, 237 (cited on pages 36, 91, and 119)
- del Toro Iniesta, J. C. 2003, *Introduction to Spectropolarimetry* (Introduction to Spectropolarimetry, by Jose Carlos del Toro Iniesta, pp. 244. ISBN 0521818273. Cambridge, UK: Cambridge University Press, April 2003.) (cited on page 13)
- Deming, D., Fraine, J. D., Sada, P. V., et al. 2012, *Astrophysical Journal*, 754, 106 (cited on page 84)
- Deming, D., Knutson, H., Agol, E., et al. 2011, *Astrophysical Journal*, 726, 95 (cited on page 85)
- Deschamps, P.-Y., Breon, F.-M., Leroy, M., et al. 1994, *IEEE Transactions on Geoscience and Remote Sensing*, 32, 598 (cited on page 106)
- Désert, J.-M., Bean, J., Miller-Ricci Kempton, E., et al. 2011, *Astrophysical Journal Letters*, 731, L40 (cited on page 8)

- Dohlen, K., Langlois, M., Saisse, M., et al. 2008, in Society of Photo-Optical Instrumentation Engineers (SPIE) Conference Series, Vol. 7014, Society of Photo-Optical Instrumentation Engineers (SPIE) Conference Series (cited on pages 84, 85, and 114)
- Ehrenreich, D., Hébrard, G., Lecavelier des Etangs, A., et al. 2007, *Astrophysical Journal Letters*, 668, L179 (cited on page 85)
- Eleftheratos, K., Zerefos, C. S., Zanis, P., et al. 2007, *Atmospheric Chemistry & Physics Discussions*, 7, 93 (cited on page 102)
- Fischer, J. & Grassl, H. 1991, *Journal of Applied Meteorology*, 30, 1245 (cited on page 27)
- Fletcher, L. N., Orton, G. S., Rogers, J. H., et al. 2011, *Icarus*, 213, 564 (cited on page 135)
- Ford, E. B., Seager, S., & Turner, E. L. 2001, *Nature*, 412, 885 (cited on pages 9, 18, 57, 62, 84, 115, and 139)
- Fresnel, A. 1819, *Memoire sur la diffraction de la lumiere* (da p. 339 a p. 475 : 1 tav. f.t.; AQ 210) (cited on page 10)
- Friedson, A. J., Wong, A.-S., & Yung, Y. L. 2002, *Icarus*, 158, 389 (cited on pages 115, 121, and 135)
- Garay, M. J., de Szoeko, S. P., & Moroney, C. M. 2008, *Journal of Geophysical Research (Atmospheres)*, 113, 18204 (cited on page 27)
- Gibson, J., Welch, W. J., & de Pater, I. 2005, *Icarus*, 173, 439 (cited on page 119)
- Goloub, P., Herman, M., Chepfer, H., et al. 2000, *Journal of Geophysical Research*, 105, 14747 (cited on pages 26, 28, 33, 54, 86, 106, and 109)
- Goode, P. R., Qiu, J., Yurchyshyn, V., et al. 2001, *Geophysical Research Letters*, 28, 1671 (cited on page 84)
- Gould, A. & Loeb, A. 1992, *Astrophysical Journal*, 396, 104 (cited on page 4)
- Hammel, H. B., Lockwood, G. W., Mills, J. R., & Barnet, C. D. 1995, *Science*, 268, 1740 (cited on page 128)
- Hammel, H. B., Sromovsky, L. A., Fry, P. M., et al. 2009, *Icarus*, 201, 257 (cited on page 128)
- Han, Q., Rossow, W. B., & Lacis, A. A. 1994, *Journal of Climate*, 7, 465 (cited on pages 27, 33, 91, and 100)
- Hansen, J. E. & Hovenier, J. W. 1974, *Journal of Atmospheric Sciences*, 31, 1137 (cited on pages 8, 9, 29, 38, 40, 58, 85, 115, 125, 138, 152, and 165)
- Hansen, J. E. & Travis, L. D. 1974, *Space Science Reviews*, 16, 527 (cited on pages 8, 9, 14, 28, 30, 33, 34, 35, 36, 37, 38, 39, 40, 43, 58, 59, 72, 85, 87, 91, 115, 116, 118, 119, 120, and 140)
- Hess, M. 1998, *Journal of Quantitative Spectroscopy & Radiative Transfer*, 60, 301 (cited on pages 91, 92, 93, 102, 107, and 110)

- Hess, M. & Wiegner, M. 1994, *Applied Optics*, 33, 7740 (cited on pages 91, 92, 93, 102, and 107)
- Heymsfield, A. J. & Platt, C. M. R. 1984, *Journal of Atmospheric Sciences*, 41, 846 (cited on page 91)
- Hovenier, J. W. 1970, *Astronomy & Astrophysics*, 7, 86 (cited on page 30)
- Hovenier, J. W. & Stam, D. M. 2007, *Journal of Quantitative Spectroscopy & Radiative Transfer*, 107, 83 (cited on page 42)
- Hovenier, J. W., Van der Mee, C., & Domke, H. 2004, *Astrophysics and Space Science Library*, Vol. 318, *Transfer of polarized light in planetary atmospheres : basic concepts and practical methods* (cited on pages 28, 30, 36, 59, 60, 87, 116, and 140)
- Hovenier, J. W. & van der Mee, C. V. M. 1983, *Astronomy & Astrophysics*, 128, 1 (cited on page 60)
- Huitson, C. M., Sing, D. K., Vidal-Madjar, A., et al. 2012, *Monthly Notices of the Royal Astronomical Society*, 422, 2477 (cited on page 8)
- Ingersoll, A. P., Dowling, T. E., Gierasch, P. J., et al. 2004, *Dynamics of Jupiter's atmosphere*, ed. F. Bagenal, T. E. Dowling, & W. B. McKinnon, 105–128 (cited on page 118)
- Kaltenegger, L. & Sasselov, D. 2011, *Astrophysical Journal Letters*, 736, L25 (cited on page 5)
- Kaltenegger, L. & Traub, W. A. 2009, *Astrophysical Journal*, 698, 519 (cited on pages 6, 56, 85, and 138)
- Kaltenegger, L., Traub, W. A., & Jucks, K. W. 2007, *Astrophysical Journal*, 658, 598 (cited on page 26)
- Kasper, M., Beuzit, J.-L., Verinaud, C., et al. 2010, in *Society of Photo-Optical Instrumentation Engineers (SPIE) Conference Series*, Vol. 7735, *Society of Photo-Optical Instrumentation Engineers (SPIE) Conference Series* (cited on pages 20 and 114)
- Kasting, J. F., Whitmire, D. P., & Reynolds, R. T. 1993, *Icarus*, 101, 108 (cited on page 26)
- Keller, C. U. 2006, in *Presented at the Society of Photo-Optical Instrumentation Engineers (SPIE) Conference*, Vol. 6269, *Society of Photo-Optical Instrumentation Engineers (SPIE) Conference Series* (cited on page 28)
- Keller, C. U., Schmid, H. M., Venema, L. B., et al. 2010, in *Presented at the Society of Photo-Optical Instrumentation Engineers (SPIE) Conference*, Vol. 7735, *Society of Photo-Optical Instrumentation Engineers (SPIE) Conference Series* (cited on pages 5, 7, 20, 21, 28, 57, and 138)
- Kemp, J. C., Henson, G. D., Steiner, C. T., & Powell, E. R. 1987, *Nature*, 326, 270 (cited on pages 6, 28, 31, 61, 88, and 138)
- Kim, D. & Ramanathan, V. 2008, *Journal of Geophysical Research (Atmospheres)*, 113, 2203 (cited on page 26)

- Klouda, G. A., Lewis, C. W., Rasmussen, R. A., et al. 1996, *Environmental Science & Technology*, 30, 1098 (cited on page 26)
- Knibbe, W. J. J., de Haan, J. F., Hovenier, J. W., et al. 2000, *Journal of Quantitative Spectroscopy & Radiative Transfer*, 64, 173 (cited on pages 125 and 134)
- Kobayashi, T. & Adachi, A. 2009, EGU General Assembly 2009, held 19-24 April, 2009 in Vienna, Austria, p.11842, 11, 11842 (cited on page 51)
- Koch, D. G., Borucki, W., Webster, L., et al. 1998, in Presented at the Society of Photo-Optical Instrumentation Engineers (SPIE) Conference, Vol. 3356, Society of Photo-Optical Instrumentation Engineers (SPIE) Conference Series, ed. P. Y. Bely & J. B. Breckinridge, 599–607 (cited on pages 4, 84, and 113)
- Laan, E. C., Volten, H., Stam, D. M., et al. 2009, *Icarus*, 199, 219 (cited on page 140)
- Léger, A., Grasset, O., Fegley, B., et al. 2011, *Icarus*, 213, 1 (cited on page 55)
- Lenoble, J. 1993, Atmospheric radiative transfer (cited on page 10)
- Leroy, J. L. 2001, *The Polarization of Light and Astronomical Observation Advances in Astronomy and Astrophysics Series*, Vol. 4 (Gordon and Breach Publishing) (cited on page 11)
- Liou, K. N. & Takano, Y. 2002, *Geophysical Research Letters*, 29, 090000 (cited on page 43)
- Litvinov, P., Hasekamp, O., Cairns, B., & Mishchenko, M. 2010, *Journal of Quantitative Spectroscopy & Radiative Transfer*, 111, 529 (cited on page 10)
- Lyot, B. 1929, *Annales de l'Observatoire de Paris, Section de Meudon*, 8 (cited on pages 8, 114, 152, and 164)
- Macintosh, B., Graham, J., Palmer, D., et al. 2006, in Society of Photo-Optical Instrumentation Engineers (SPIE) Conference Series, Vol. 6272, Society of Photo-Optical Instrumentation Engineers (SPIE) Conference Series (cited on page 20)
- Macintosh, B. A., Graham, J. R., Palmer, D. W., et al. 2008, in Society of Photo-Optical Instrumentation Engineers (SPIE) Conference Series, Vol. 7015, Society of Photo-Optical Instrumentation Engineers (SPIE) Conference Series (cited on pages 84, 85, and 114)
- Macke, A., Mueller, J., & Raschke, E. 1996, *Journal of Atmospheric Sciences*, 53, 2813 (cited on page 91)
- Mackowski, D. W. & Mishchenko, M. I. 2011, *Journal of Quantitative Spectroscopy & Radiative Transfer*, 112, 2182 (cited on page 121)
- Madhusudhan, N. & Burrows, A. 2012, *Astrophysical Journal*, 747, 25 (cited on page 58)
- Magono, C. & Lee, C. W. 1966, *Journal of the Faculty of Science, Hokkaido University* (cited on page 91)
- Malek, E. 2007, AGU Fall Meeting Abstracts, A18+ (cited on page 26)

- Marley, M. S., Gelino, C., Stephens, D., Lunine, J. I., & Freedman, R. 1999, *Astrophysical Journal*, 513, 879 (cited on page 26)
- Marley, M. S., Saumon, D., & Goldblatt, C. 2010, *Astrophysical Journal Letters*, 723, L117 (cited on page 85)
- Marshak, A., Wen, G., Coakley, J. A., et al. 2008, *Journal of Geophysical Research (Atmospheres)*, 113, 14 (cited on page 89)
- Martin, G. M., Johnson, D. W., & Spice, A. 1994, *Journal of Atmospheric Sciences*, 51, 1823 (cited on page 33)
- Martin, S. 2004, *An Introduction to Ocean Remote Sensing* (cited on page 15)
- Matcheva, K. I., Conrath, B. J., Gierasch, P. J., & Flasar, F. M. 2005, *Icarus*, 179, 432 (cited on page 27)
- Mayor, M., Bonfils, X., Forveille, T., et al. 2009, *Astronomy & Astrophysics*, 507, 487 (cited on page 6)
- Mayor, M. & Queloz, D. 1995, *Nature*, 378, 355 (cited on pages 2, 3, 4, 26, 55, 83, 113, 137, 149, and 161)
- McClatchey, R. A., Fenn, R., Selby, J. E. A., Volz, F., & Garing, J. S. 1972, AFCRL-72.0497 (US Air Force Cambridge research Labs) (cited on pages 32, 33, 70, and 89)
- Meakin, P. 1983, *Physical Review A (General Physics)*, 27, 1495 (cited on page 123)
- Miller-Ricci, E. & Fortney, J. J. 2010, *Astrophysical Journal Letters*, 716, L74 (cited on pages 56 and 138)
- Minnis, P., Heck, P. W., Young, D. F., Fairall, C. W., & Snider, J. B. 1992, *Journal of Applied Meteorology*, 31, 317 (cited on page 33)
- Mishchenko, M. I. 1990, *Icarus*, 84, 296 (cited on pages 58, 85, and 115)
- Mishchenko, M. I. 1993, *Astrophysical Journal*, 411, 351 (cited on page 9)
- Mishchenko, M. I., Rosenbush, V. K., Kiselev, N. N., et al. 2010, *ArXiv e-prints* (cited on pages 28 and 92)
- Mishchenko, M. I. & Travis, L. D. 1997, *Journal of Geophysical Research*, 102, 16989 (cited on page 138)
- Montañés-Rodríguez, P., Pallé, E., Goode, P. R., & Martín-Torres, F. J. 2006, *Astrophysical Journal*, 651, 544 (cited on pages 84 and 115)
- Nadal, F. & Breon, F.-M. 1999, *IEEE Transactions on Geoscience and Remote Sensing*, 37, 1709 (cited on pages 10 and 15)
- Natraj, V., Spurr, R. J. D., Boesch, H., Jiang, Y., & Yung, Y. L. 2007, *Journal of Quantitative Spectroscopy & Radiative Transfer*, 103, 245 (cited on page 21)
- Nordsieck, K. H. 1974, *Publications of the Astronomical Society of the Pacific*, 86, 324 (cited on page 147)
- Oakley, P. H. H. & Cash, W. 2009, *Astrophysical Journal*, 700, 1428 (cited on pages 29, 57, 62, and 84)

- O'Dell, C. W., Connor, B., Bösch, H., et al. 2011, *Atmospheric Measurement Techniques Discussions*, 4, 6097 (cited on page 10)
- Oka, K. & Kato, T. 1999, *Optics Letters*, 24, 1475 (cited on page 147)
- Pallé, E., Ford, E. B., Seager, S., Montañés-Rodríguez, P., & Vazquez, M. 2008, *Astrophysical Journal*, 676, 1319 (cited on pages 84 and 115)
- Pallé, E., Goode, P. R., Montañés-Rodríguez, P., & Koonin, S. E. 2004, *Science*, 304, 1299 (cited on page 84)
- Pepe, F., Mayor, M., Queloz, D., et al. 2004, *Astronomy & Astrophysics*, 423, 385 (cited on pages 84 and 114)
- Peralta, J., Hueso, R., & Sánchez-Lavega, A. 2007, *Icarus*, 190, 469 (cited on page 27)
- Perrin, M. D., Graham, J. R., Larkin, J. E., et al. 2010, in *Society of Photo-Optical Instrumentation Engineers (SPIE) Conference Series*, Vol. 7736, *Society of Photo-Optical Instrumentation Engineers (SPIE) Conference Series* (cited on page 20)
- Pope, R. M. & Fry, E. S. 1997, *Applied Optics*, 36, 8710 (cited on page 35)
- Pour Biazar, A., McNider, R. T., Doty, K., & Cameron, R. 2007, *AGU Fall Meeting Abstracts*, D740+ (cited on page 26)
- Povel, H. P., Keller, C. U., & Yadigaroglu, I.-A. 1994, *Applied Optics*, 33, 4254 (cited on page 20)
- Qiu, J., Goode, P. R., Pallé, E., et al. 2003, *Journal of Geophysical Research (Atmospheres)*, 108, 4709 (cited on page 145)
- Ramanathan, V., Barkstrom, B. R., & Harrison, E. F. 1989, *Physics Today*, 42, 22 (cited on page 26)
- Renard, J. B., Lévassieur-Regourd, A. C., & Dumont, R. 1995, *Astronomy & Astrophysics*, 304, 602 (cited on page 142)
- Rodenhuis, M., Canovas, H., Jeffers, S., & Keller, C. 2011, in *Astronomical Society of the Pacific Conference Series*, Vol. 449, *Astronomical Society of the Pacific Conference Series*, ed. P. Bastien, 33 (cited on page 7)
- Roelfsema, R., Gisler, D., Pragt, J., et al. 2011, in *Society of Photo-Optical Instrumentation Engineers (SPIE) Conference Series*, Vol. 8151, *Society of Photo-Optical Instrumentation Engineers (SPIE) Conference Series* (cited on pages 84, 85, and 114)
- Romanescu, C., Marschall, J., Kim, D., Khatiwada, A., & Kalogerakis, K. S. 2010, *Icarus*, 205, 695 (cited on page 119)
- Saar, S. H. & Seager, S. 2003, in *Astronomical Society of the Pacific Conference Series*, Vol. 294, *Scientific Frontiers in Research on Extrasolar Planets*, ed. D. Deming & S. Seager, 529–534 (cited on pages 29, 57, 58, 85, and 115)
- Sato, M. & Hansen, J. E. 1979, *Journal of Atmospheric Sciences*, 36, 1133 (cited on pages 119 and 132)

- Schmid, H. M., Joos, F., Buenzli, E., & Gisler, D. 2011, *Icarus*, 212 (cited on pages 114, 130, and 135)
- Seager, S., Spergel, D., Scowen, P., et al. 2009, in *Bulletin of the American Astronomical Society*, Vol. 41, American Astronomical Society Meeting Abstracts #213, 458.08 (cited on page 20)
- Seager, S., Turner, E. L., Schafer, J., & Ford, E. B. 2005, *Astrobiology*, 5, 372 (cited on pages 9, 15, and 141)
- Seager, S., Whitney, B. A., & Sasselov, D. D. 2000, *Astrophysical Journal*, 540, 504 (cited on pages 29, 57, 58, 85, 115, and 139)
- Segal, Y. & Khain, A. 2006, *Journal of Geophysical Research (Atmospheres)*, 111, 15204 (cited on page 33)
- Simon-Miller, A. A., Banfield, D., & Gierasch, P. J. 2001, *Icarus*, 154, 459 (cited on pages 114, 119, 128, 132, and 134)
- Smith, P. H. & Tomasko, M. G. 1984, *Icarus*, 58, 35 (cited on page 114)
- Snellen, I. A. G., de Kok, R. J., de Mooij, E. J. W., & Albrecht, S. 2010a, *Nature*, 465, 1049 (cited on page 8)
- Snellen, I. A. G., de Mooij, E. J. W., & Burrows, A. 2010b, *Astronomy & Astrophysics*, 513, A76 (cited on pages 8 and 85)
- Snik, F., Karalidi, T., & Keller, C. U. 2009, ArXiv e-prints (cited on pages 146 and 148)
- Sparks, W. B., Germer, T. A. and MacKenty, J., & Snik, F. 2012, *Applied Optics* (cited on page 147)
- Sparks, W. B., Hough, J., Germer, T. A., et al. 2009a, *Proceedings of the National Academy of Science*, 106, 7816 (cited on page 143)
- Sparks, W. B., Hough, J. H., Kolokolova, L., et al. 2009b, *Journal of Quantitative Spectroscopy & Radiative Transfer*, 110, 1771 (cited on pages 139, 142, and 143)
- Spinhirne, J. D., Boers, R., & Hart, W. D. 1989, *Journal of Applied Meteorology*, 28, 81 (cited on page 100)
- Sromovsky, L. A. 2005, *Icarus*, 173, 284 (cited on page 21)
- Sromovsky, L. A., Hammel, H. B., de Pater, I., et al. 2012, *Icarus*, 220, 6 (cited on page 128)
- Stam, D. M. 2003, in *ESA Special Publication*, Vol. 539, *Earths: DARWIN/TPF and the Search for Extrasolar Terrestrial Planets*, ed. M. Fridlund, T. Henning, & H. Lacoste, 615–619 (cited on pages 29, 58, 85, and 115)
- Stam, D. M. 2008, *Astronomy & Astrophysics*, 482, 989 (cited on pages 9, 18, 19, 26, 29, 30, 31, 32, 34, 43, 57, 58, 59, 61, 76, 81, 85, 86, 87, 88, 115, 117, 139, 140, 141, 152, 153, 159, 165, 166, and 172)
- Stam, D. M., De Haan, J. F., Hovenier, J. W., & Stammes, P. 1999, *Journal of Geophysical Research*, 104, 16843 (cited on page 118)

- Stam, D. M., de Rooij, W. A., Cornet, G., & Hovenier, J. W. 2006a, *Astronomy & Astrophysics*, 452, 669 (cited on pages 31, 57, 58, 59, 60, 62, 75, 79, 87, 88, and 117)
- Stam, D. M. & Hovenier, J. W. 2005, *Astronomy & Astrophysics*, 444, 275 (cited on pages 18, 59, 62, 87, and 116)
- Stam, D. M., Hovenier, J. W., & Waters, L. B. F. M. 2004, *Astronomy & Astrophysics*, 428, 663 (cited on pages 19, 28, 29, 32, 57, 58, 85, 115, 117, 118, 119, 132, 152, and 165)
- Stam, D. M., Laan, E., Selig, A., Hoogeveen, R., & Hasekamp, O. 2006b, in *European Planetary Science Congress 2006*, 607–+ (cited on page 11)
- Stephens, G. L. & Platt, C. M. R. 1987, *Journal of Applied Meteorology*, 26, 1243 (cited on page 100)
- Stephens, G. L., Vane, D. G., Tanelli, S., et al. 2008, *Journal of Geophysical Research (Oceans)*, 113, 0 (cited on page 27)
- Sterzik, M., Bagnulo, S., Azua, A., et al. 2010, *The Messenger*, 142, 25 (cited on pages 139 and 142)
- Sterzik, M. F. & Bagnulo, S. 2009, in *Astronomical Society of the Pacific Conference Series*, Vol. 420, *Bioastronomy 2007: Molecules, Microbes and Extraterrestrial Life*, ed. K. J. Meech, J. V. Keane, M. J. Mumma, J. L. Siefert, & D. J. Werthimer, 371 (cited on page 145)
- Sterzik, M. F., Bagnulo, S., & Palle, E. 2012, *Nature*, 483, 64 (cited on pages 21, 76, and 145)
- Tinetti, G. 2006, *Origins of Life and Evolution of the Biosphere*, 36, 541 (cited on pages 18, 84, and 115)
- Tinetti, G. & Griffith, C. A. 2010, in *Astronomical Society of the Pacific Conference Series*, Vol. 430, *Astronomical Society of the Pacific Conference Series*, ed. V. Coudé Du Foresto, D. M. Gelino, & I. Ribas, 115–+ (cited on page 85)
- Tinetti, G., Meadows, V. S., Crisp, D., et al. 2006a, *Astrobiology*, 6, 34 (cited on page 139)
- Tinetti, G., Meadows, V. S., Crisp, D., et al. 2006b, *Astrobiology*, 6, 881 (cited on pages 56, 57, 62, 84, and 114)
- Tinetti, G., Rashby, S., & Yung, Y. L. 2006c, *Astrophysical Journal Letters*, 644, L129 (cited on page 26)
- Tinetti, G., Vidal-Madjar, A., Liang, M.-C., et al. 2007, *Nature*, 448, 169 (cited on page 8)
- Todorov, K. O., Deming, D., Knutson, H. A., et al. 2012, *Astrophysical Journal*, 746, 111 (cited on page 8)
- Tomasko, M. G., Doose, L. R., Dafoe, L. E., & See, C. 2009, *Icarus*, 204, 271 (cited on pages 58, 85, and 115)

- Turnbull, M. C., Traub, W. A., Jucks, K. W., et al. 2006, *Astrophysical Journal*, 644, 551 (cited on page 21)
- van de Hulst, H. C. 1957, *Light Scattering by Small Particles* (*Light Scattering by Small Particles*, New York: John Wiley & Sons, 1957) (cited on pages 16, 36, and 37)
- van de Kamp, P. 1969a, *Astronomical Journal*, 74, 757 (cited on page 2)
- van de Kamp, P. 1969b, *Astronomical Journal*, 74, 238 (cited on page 2)
- van Deelen, R., Hasekamp, O. P., van Diedenhoven, B., & Landgraf, J. 2008, *Journal of Geophysical Research (Atmospheres)*, 113, 12204 (cited on pages 27 and 33)
- van Diedenhoven, B., Hasekamp, O. P., & Landgraf, J. 2007, *Journal of Geophysical Research (Atmospheres)*, 112, 15208 (cited on pages 34, 35, and 91)
- van Harten, G., Snik, F., Rietjens, J. H. H., et al. 2011, in *Society of Photo-Optical Instrumentation Engineers (SPIE) Conference Series*, Vol. 8160, *Society of Photo-Optical Instrumentation Engineers (SPIE) Conference Series* (cited on pages 146 and 148)
- Wark, D. Q. & Mercer, D. M. 1965, *Applied Optics*, 4, 839 (cited on page 27)
- Weigelt, A., Hermann, M., van Velthoven, P. F. J., et al. 2009, *Journal of Geophysical Research (Atmospheres)*, 114, 1204 (cited on page 27)
- West, R. A., Baines, K. H., Friedson, A. J., et al. 2004, *Jovian clouds and haze*, ed. F. Bagenal, T. E. Dowling, & W. B. McKinnon, 79–104 (cited on page 118)
- West, R. A., Hart, H., Hord, C. W., et al. 1983, *Journal of Geophysical Research*, 88, 8679 (cited on pages 9 and 114)
- West, R. A. & Smith, P. H. 1991, *Icarus*, 90, 330 (cited on pages 9, 114, 118, 119, 120, 123, 129, and 135)
- Wiktorowicz, S. J. 2009, *Astrophysical Journal*, 696, 1116 (cited on page 85)
- Williams, D. M. & Gaidos, E. 2008, *Icarus*, 195, 927 (cited on pages 8, 9, 18, 85, 110, 138, 139, 156, and 168)
- Wolstencroft, R. D., Tranter, G. E., & Le Pevelen, D. D. 2004, in *IAU Symposium*, Vol. 213, *Bioastronomy 2002: Life Among the Stars*, ed. R. Norris & F. Stootman, 149 (cited on page 142)
- Wolszczan, A. & Frail, D. A. 1992, *Nature*, 355, 145 (cited on pages 2, 149, and 161)
- Wong, A.-S., Lee, A. Y. T., Yung, Y. L., & Ajello, J. M. 2000, *Astrophysical Journal Letters*, 534, L215 (cited on page 115)
- Wong, M. H., Bjoraker, G. L., Smith, M. D., Flasar, F. M., & Nixon, C. A. 2004, *Planetary and Space Science*, 52, 385 (cited on page 119)
- Wordsworth, R. D., Forget, F., Selsis, F., et al. 2011, *Astrophysical Journal Letters*, 733, L48 (cited on page 137)
- Wu, M.-L. C. 1985, *Journal of Applied Meteorology*, 24, 539 (cited on pages 16 and 144)
- Yamamoto, G. & Wark, D. Q. 1961, *Journal of Geophysical Research*, 66, 3596 (cited on page 27)

- Zugger, M. E., Kasting, J. F., Williams, D. M., Kane, T. J., & Philbrick, C. R. 2010, *Astrophysical Journal*, 723, 1168 (cited on pages 57, 85, and 115)
- Zugger, M. E., Kasting, J. F., Williams, D. M., Kane, T. J., & Philbrick, C. R. 2011, *Astrophysical Journal*, 739, 55 (cited on page 85)



# Acknowledgments

---

Four exciting years have past, during which I have gathered more knowledge and experience than I could ever have imagined. During this trip of knowledge there are many people that have contributed each on his own way to the completion of this dissertation.

First of all, I would like to thank Daphne for trusting me and giving me the opportunity to do my PhD using her model and expertise these past four years. With her guidance I came in contact with the exciting world of modelling (exo-)planetary signals and most importantly their polarisation. We have spent together numerous hours testing the code, and performing matrix multiplications (of course) by hand, maybe the first point where I realised why most researchers avoid studying polarisation even though they all recognise its importance!

Then of course I would like to thank Joop. His guidance and help in some of the papers of this thesis has been a huge inspiration for me, and have helped me improve my knowledge of the field. I feel honored to be able to include in this thesis papers where my co-author is one of the fathers of our field, having already used polarisation to characterise planets of our Solar System even before I was born and having opened the way for us nowadays.

A special word of thank you also goes to Christoph, for his help in all the technical details of this thesis and for giving me the opportunity to get experience on teaching assistance.

When as a masters student, walking down the corridor of the Astronomical Institute of Utrecht on a summery day, after a short discussion with Frans we agreed to do my master thesis on SPEX for Mars, I never knew where that would lead me. Frans, thanks for getting me in the world of polarisation!

Rob, even though you have been away from Utrecht for quite some time now, you have still provided useful help many times, either to my linguistic challenges or to my paper and coding questions. Thanks for all of that, and for all the fun times we have spent drinking nice wines and beer and watching football together or in parallel (even though I know you mostly don't agree with my choices of teams I support!).

Throughout my PhD I have been working in SRON in Utrecht, in the Earth and Planetary Sciences division. Since most of my work concerns Earth-like exoplanets my working in an environment with experts on Earth's atmosphere has helped me a lot and from all the people here I have gained a lot of useful knowledge and experience that I have used during my PhD. So, to all of EPS: thank you!

Richard and Pieter (even though you are not part of EPS anymore) I would like to thank you for helping me with the cluster and making most of this thesis possible. Truus and Anita, thanks for helping with booking the tickets and hotels for every conference I had to go to. Remco, thanks for all the helpful talks on exoplanets and three dimensional geometries! Thijs, thanks for all the times you have helped me with my IDL problems. Paul, thanks for helping with the colours in IDL and the poster printer. Pieter, Sandrine and Ralf, thanks for getting me and Remco in the second "passion" that I developed during this PhD, sport climbing!

Apart from work, EPS is of course also a place to have fun! Andreas, Arjen, Dani, Dinand, Sandrine, Tobias, Toncho thanks for all the nice evenings we have had together with lots of nice food and drinks (and of course football!). Andreas and Dinand, thanks for all the fun times in the office. Without you I would never know the legendary music of Heino and the Hoff! And of course, for all the fun "observation" times usually during the boring hours the codes were running on the cluster!

I would also like here to thank some of my professors from my bachelor years, who have guided me on my first steps in science. Professors Mary Kontiza, Xenophon Moussas and Helen Mavromichalaki, thank you for all your guidance and inspiration during my first years in science.

A thank you also goes to Carla, Henjo, Wendy and Mark for their support and interest during these past four years, even though many times what I did could sound a bit complicated and my choice of words to describe it a bit confusing...A special kiss and a hug goes to Stijn. You were born during the first year of this work and every one of your birthdays reminded me that I was a year closer to writing this thesis. I hope you always keep liking good food and music!

A very, very, very big thank you goes to Yuli, my best friend and support during all these years away from Greece. Yuli, thanks for all the hours we have spent chatting, even some times when we were not supposed to be (see, in the classroom). Thanks for all the fun times either in Greece or here and for all the nice hand-made jewellery that has brightened up everyday of my PhD years! Hopefully, by the time this is printed you are also done with your studies and then we can have a double feast .

Remco, thanks for all the support and discussions throughout the years of my PhD, and even before that. Thanks for all the nice times, trips and adventures we have had together so far and I am definitely looking forward to more! Also thanks for translating my dutch summary into proper dutch.

Last but not least, I would like to thank my parents and my brother. Thanks for all your love and support and always providing me with the means to fulfil my dreams. Finally, dad thanks for buying that small telescope when I was about 5 years old and showing me that night, so many years ago, how different the sky is from what our eyes only can see. That small telescope was my first window to the beautiful world of astronomy and my inspiration to be here today.

# Curriculum Vitae

---

Theodora Karalidi was born on August 31<sup>st</sup> 1983 in Amarousio (Marousi) of Attiki, Greece. In 1989 she started her education at the 15<sup>th</sup> primary school of Nea Smirni, Athens, Greece. In 1995 she attended the 7<sup>th</sup> secondary school of Nea Smirni and in 1996 she moved to the 5<sup>th</sup> secondary school of Nea Smirni. In 1998 she proceeded to the 5<sup>th</sup> lyceum of Nea Smirni, at which she successfully took the Panhellenic exams in 2001 to enter the Physics department of the University of Athens.

Following a course on Cosmic Rays, she started a project on the cosmic ray modulation during the 23<sup>rd</sup> solar cycle in collaboration with prof. dr. H. (Helen) Mavromichalaki and E. (Vagelis) Paouris. This work resulted in a publication in *Solar Physics* (Mavromichalaki et al., 2007). In 2005 she visited the Astronomical Institute of Utrecht University with a Leonardo Da Vinci scholarship. There she worked for three months with prof. dr. H.J.G.L.M. (Henny) Lamers on a study of *The mass function of star clusters in our Galaxy and M81, the mass of the most massive cluster*, after which she returned to the University of Athens. She received her Bachelor's degree in Physics in 2006 with a thesis on *The Luminosity and Mass Functions of Star Clusters in the Milky Way galaxy and the Magellanic Clouds*, which was performed under supervision of prof. dr. M. (Mary) Kontizas.

In 2006 she went back to Utrecht University to continue her studies in the Master's program of the Astronomical Institute. She received her Master's degree in Astrophysics in 2008 with a thesis on *Polarimetry with SPEX – the Spectropolarimeter for Planetary EXploration* under supervision of dr. ir. F. (Frans) Snik, dr. D. M. (Daphne) Stam and prof. dr. C. U. (Christoph) Keller. During this research she performed both a theoretical and a laboratory study of SPEX.

In 2008 she started her PhD research in the group of Daphne Stam at SRON Netherlands Institute for Space Research, co-supervised by Christoph Keller (Leiden University). The results of this research are presented in this book. During this research she assisted teaching the Master's course *Planets and Exoplanets* of Daphne Stam and Christoph Keller at Utrecht University. She presented her work at conferences and workshops in Paris, Barcelona, Exeter, Flagstaff, Heidelberg, Madrid, Dalfsen, Groningen and Amsterdam. She will defend her thesis on April 23<sup>rd</sup> 2013.

